NASA/TM–2017-219613

Experimental Investigation of Roughness Effects on Transition Onset and Turbulent Heating Augmentation on a Hemisphere at Mach 6 and Mach 10

Brian R. Hollis
Langley Research Center, Hampton, Virginia

May 2017

NASA STI Program . . . in Profile

Since its founding, NASA has been dedicated to the advancement of aeronautics and space science. The NASA scientific and technical information (STI) program plays a key part in helping NASA maintain this important role.

The NASA STI program operates under the auspices of the Agency Chief Information Officer. It collects, organizes, provides for archiving, and disseminates NASA's STI. The NASA STI program provides access to the NTRS Registered and its public interface, the NASA Technical Reports Server, thus providing one of the largest collections of aeronautical and space science STI in the world. Results are published in both non-NASA channels and by NASA in the NASA STI Report Series, which includes the following report types:

- TECHNICAL PUBLICATION. Reports of completed research or a major significant phase of research that present the results of NASA Programs and include extensive data or theoretical analysis. Includes compilations of significant scientific and technical data and information deemed to be of continuing reference value. NASA counter-part of peer-reviewed formal professional papers but has less stringent limitations on manuscript length and extent of graphic presentations.

- TECHNICAL MEMORANDUM. Scientific and technical findings that are preliminary or of specialized interest, e.g., quick release reports, working papers, and bibliographies that contain minimal annotation. Does not contain extensive analysis.

- CONTRACTOR REPORT. Scientific and technical findings by NASA-sponsored contractors and grantees.

- CONFERENCE PUBLICATION. Collected papers from scientific and technical conferences, symposia, seminars, or other meetings sponsored or co-sponsored by NASA.

- SPECIAL PUBLICATION. Scientific, technical, or historical information from NASA programs, projects, and missions, often concerned with subjects having substantial public interest.

- TECHNICAL TRANSLATION. English-language translations of foreign scientific and technical material pertinent to NASA's mission.

Specialized services also include organizing and publishing research results, distributing specialized research announcements and feeds, providing information desk and personal search support, and enabling data exchange services.

For more information about the NASA STI program, see the following:

- Access the NASA STI program home page at http://www.sti.nasa.gov

- E-mail your question to help@sti.nasa.gov

- Phone the NASA STI Information Desk at 757-864-9658

- Write to:
  NASA STI Information Desk
  Mail Stop 148
  NASA Langley Research Center
  Hampton, VA 23681-2199

NASA/TM–2017-219613

Experimental Investigation of Roughness Effects on Transition Onset and Turbulent Heating Augmentation on a Hemisphere at Mach 6 and Mach 10

Brian R. Hollis
Langley Research Center, Hampton, Virginia

National Aeronautics and
Space Administration

Langley Research Center
Hampton, Virginia 23681-2199

May 2017

Available from:

NASA STI Program / Mail Stop 148
NASA Langley Research Center
Hampton, VA 23681-2199
Fax: 757-864-6500

Table of Contents

List of Tables

List of Figures

Abstract

An experimental investigation of the effects of distributed surface roughness on boundary-layer transition and turbulent heating has been conducted. Hypersonic wind tunnel testing was performed using hemispherical models with surface roughness patterns simulating those produced by heat shield ablation. Global aeroheating and transition onset data were obtained using phosphor thermography at Mach 6 and Mach 10 over a range of roughness heights and free stream Reynolds numbers sufficient to produce laminar, transitional and turbulent flow. Upstream movement of the transition onset location and increasing heating augmentation over predicted smooth-wall levels were observed with both increasing roughness heights and increasing free stream Reynolds numbers. The experimental heating data are presented herein, as are comparisons to smooth-wall heat transfer distributions from computational flow-field simulations. The transition onset data are also tabulated, and correlations of these data are presented.

Nomenclature

Symbols

H_0	tunnel total (reservoir) enthalpy
H_{AW}	adiabatic wall enthalpy
H_W	wall enthalpy
H_{300K}	wall enthalpy at 300 K
h	measured heat-transfer film coefficient
h_{FR}	Fay-Riddell theory heat-transfer film coefficient
h	measured roughness height
h_{mean}	measured mean roughness height
k	effective roughness height
k_{PVxx}	effective peak-to-valley roughness height for *xx*% exceedance height
M_∞	free stream Mach number
p	effective roughness weighting factor
p_∞	free stream pressure
q	heat transfer rate
Re_θ	boundary-layer momentum thickness Reynolds number
$Re_{\theta,TR}$	boundary-layer momentum thickness Reynolds number at transition
Re_∞	unit free stream Reynolds number
s/R	normalized surface running length from nose
T_e	boundary-layer edge temperature
T_w	wall temperature
T_∞	free stream temperature
U_e	boundary-layer edge velocity
U_k	velocity at roughness height
U_∞	free stream velocity
x, y, z	Cartesian coordinates
β	angular position measured from nose tip
μ_e	boundary-layer edge viscosity
μ_k	viscosity at roughness height
μ_∞	free stream viscosity
ρ_e	boundary-layer edge density
ρ_k	density at roughness height
ρ_∞	free stream density
θ	boundary-layer momentum thickness
σ_h	standard deviation of measured roughness height
σ_{rough}	standard deviation of h/h_{FR} due to roughness

Subscripts and Superscripts

∞	wind tunnel free stream condition
0	wind tunnel stagnation or reservoir condition
e	boundary layer edge condition
k	roughness height condition
PV	peak-to-valley surface roughness distance

RMS root mean square
TR transition location
w model wall condition

Acronyms

ASTM	American Society for Testing and Materials
CFD	Computational Fluid Dynamics
IHEAT	Imaging for Hypersonic Experimental Aerothermodynamic Testing
LAL	Langley Aerothermodynamic Laboratories
LaRC	Langley Research Center
PANT	PAssive Nosetip Technology
LAURA	Langley Aerothermodynamic Upwind Relaxation Algorithm
SLA	Stereo-Lithographic Apparatus
TPS	Thermal Protection System

Introduction

This report details an experimental dataset on the effects of distributed surface roughness on boundary-layer transition and heating augmentation. The data were obtained through hypersonic wind tunnel testing of a set of generic hemisphere models with roughness patterns that simulate those produced by the ablation of a reentry vehicle's Thermal Protection System (TPS). Global heat-transfer distributions and boundary-layer transition onset locations are presented herein as the basis for future, detailed analysis.

Background

"Roughness" is a generic term in aerospace literature that can encompass different types of surface features, as illustrated in Figure 1 and Figure 2. Roughness can be divided into two general types, discrete and distributed. Discrete roughness includes surface features such as: attachment-point cavities, recessed or protruding compression pads; steps or gaps between heat shield tiles; and physical damage to a TPS. Distributed roughness includes features such as: regular patterns resulting from ablation of hexcomb-structure TPS; irregular deflection of a flexible TPS under aerodynamic loading; or the random "sand-grain" distribution resulting from ablation of a monolithic TPS.

Data on the effects of surface roughness are valuable because the roughness of an entry vehicle's TPS can promote earlier boundary-layer transition and produce higher turbulent heating (and shear) levels than would be expected based on an idealized, smooth-wall analysis. However, due to the complexities of roughness effects, a vehicle's TPS is typically designed using analytical, computational and/or experimental techniques that are based on the assumption of a smooth surface. The effects of roughness on the aerothermodynamic environment are then included through approximate engineering correlations and methods.

The focus of this test program is on obtaining data on the effects of distributed sand-grain type roughness on a generic, blunt body geometry, i.e., a hemisphere. These data are primarily intended for use in the development and/or validation of engineering correlations for the effects of distributed roughness on boundary-layer transition and turbulent heat transfer. These data can also serve as the basis

for development and/or validation of higher-fidelity, numerical flow-field simulation models for roughness effects.

Experimental Tools and Methods

Wind tunnel testing was conducted on 6.00-inch diameter hemispherical models with a wide range of surface roughness heights, including (nominally) smooth surfaces. Global surface heating and boundary-layer transition data were obtained on these models using phosphor thermography in the 20-Inch Mach 6 Air and 31-Inch Mach 10 Air Tunnels of the NASA Langley Aerothermodynamic Laboratories (LAL).

Wind Tunnel Model Fabrication

Hemispherical models with a range of surface roughness heights were fabricated for this study. The fabrication process for a rough-surface model follows that for smooth models, as documented in Ref. 1, with an additional steps to add roughness to the surface. The first step in fabrication of a smooth-surface model is the production of a rapid-prototype, resin pattern of the geometry in a stereo-lithographic apparatus (SLA) machine. The pattern is then hand-worked to a smooth surface finish to remove any SLA manufacturing artifacts. A multiple-piece injection mold (from which the resin model can easily be removed) is then built around the resin pattern. The resin pattern is then removed and wax is injected into the mold to form a wax pattern. Next, a new two-piece shell mold is built around the wax pattern, and then the wax is burned out of the shell mold. A silica ceramic model is then slip-cast in the shell mold. Then, the ceramic model is removed from the shell mold, dried, and sintered. The finished ceramic model is then back-filled with a hydraulically setting magnesia ceramic for strength and support and mounted on a stainless steel cylindrical sting. Finally, the model is coated with a mixture of phosphors that luminesce under ultraviolet lighting.

In the fabrication of a roughness model, an adhesive coating is applied to the smooth SLA resin pattern and then the pattern is dipped into a container filled with precision-manufactured, spherical glass particles. The particles adhere to the SLA resin pattern to form a distributed, sand-grain type roughness over the entire surface. The pattern is then hand-worked as necessary to remove any obvious surface irregularities (i.e., clumps of glass spheres). Also, particles are removed from an approximately 1-inch region at the end of the model to ensure that roughness elements do not bind in the mold during the casting process. A rough-surface ceramic model is then fabricated from the roughened pattern following the remaining steps detailed above for smooth-surface models. These steps are illustrated in Figure 3 with photographs (for a similar spherical-cap geometry model, not the current hemispherical models) of a smooth-surface SLA resin pattern, an SLA pattern with applied roughness elements, and the final cast-ceramic model with roughness.

The model surface roughness was created using precision-manufactured, spherical glass particles ranging in size from 2.5 mil to 68.9 mil[1]. The spherical glass particle diameters are specified according to an ASTM standard (Ref. 2) that defines the mesh sieve opening size through which the particle can pass. A listing of the models and ASTM mesh sizes is given in Table 1 and photographs of each model are shown in Figure 4 through Figure 11.

A nominal roughness height for each ASTM mesh size is based on the assumption that for a uniform array of elements in contact with each other, the height is equal to the vertical distance from the top of an

[1] The “mil” unit will be used in the discussion of roughness heights rather than inches or SI units in deference to historical literature on surface roughness.

element to the point of contact with the adjacent element – that is the roughness height is equal to the glass particle radius. This height measurement is referred to as the nominal "peak-to-valley" roughness. The characterization of the actual "as-built" roughness height, which differs from the specified nominal value, will be presented below in the "Roughness Height Characterization" section.

Roughness Height Characterization

Scan data acquisition and processing

The surface roughness data presented previously in Table 1 represent ideal values based on the sizes of the particles used in the fabrication of each model. However, the characterization of the actual "as-built" roughness was more complex and was based on a statistical analysis of the surface height distributions. The differences between the ideal and as-built roughness geometries are illustrated in Figure 12. In the ideal geometry, the roughness is defined by perfectly-formed hemispherical elements in a single, flat, layer. However, in reality, the process of binding the glass particles to the surface, forming the mold, and then casting the ceramic model, introduces random imperfections in the surface.

To determine roughness characterization parameters, laser scans were made of flat, 4-in. x 4-in. square sample plates for each of the ASTM roughness sizes to obtain a data cloud of *x*-*y*-*z* points. These flat plates were used in place of the actual hemisphere models owing to the difficulty of performing a scan over a curved surface. The stated, ideal scan resolution of the system was ~ ±2.00 mil, however, the actual achieved resolution was approximately ±4.00 mil. Margins of 0.5 in. on the sides of the plates were specified to avoid any edge effects and so the actual scan area was 3 in. by 3 in. square. The data cloud was then triangulated to form a continuous surface representation and the height (*z*) coordinate was shifted to put the average height of all points at zero.

Profile line-cuts were extracted from the global data sets at various stations to show the height distribution of scan data points. The global surface scan data and representative profile line-cuts are shown for each ASTM mesh size sample in Figure 13 - Figure 18. In the line plots, the dashed blue lines represent the nominal diameter and height of the roughness element and the symbols represent the scan data point locations. As can be seen from these figures, for the larger roughness sizes, several data points were obtained on each roughness element, while for the smaller roughness sizes, the data point spacing was on the order of the roughness element diameter (e.g., 4.17 mil diameter for 140-Mesh and 2.48 mil diameter for the 240-Mesh). Therefore, while data and analyses for these smaller mesh sizes will be presented herein, these data are not considered to be quantitatively reliable.

Statistical Analysis of Roughness Height

In previous distributed roughness studies (e.g., Ref. 3-4), the peak-to-valley roughness height has been identified as a key parameter in correlation of roughness data. Peaks and valleys of adjacent roughness elements were determined manually from examination of the profile line-cut data and a statistical database of "as-built" peak-to-valley heights was created. The statistical approach is required because the application of roughness elements, fabrication of molds, and final casting of the ceramic models introduces random deviations from the nominal peak-to-valley roughness height, which is simply the radius of the spherical glass particles. For each profile, the exceedance, which is defined as the percentage of data points in a set greater than a specified value, was computed from the database. The exceedance height distributions obtained from scans of each sample plate are plotted in Figure 19. Also shown are Gaussian curve fits to these data of the form:

$$\% \text{ exceedance} = 100 \times \exp\left\{-0.5\left[\frac{\left(h - h_{mean}/2\right)}{\sigma_h}\right]^2\right\} \quad (1)$$

The exceedance height distributions are replotted in terms of the normalized roughness height (h/h_{mean}) in Figure 20. As seen in the two figures, the exceedance distributions approximate the Gaussian distribution that would be expected from a large sample set with random deviations.

An important factor in the analysis of the peak-to-valley data, which is sometimes neglected, is the difference between the peak-to-valley height determined from a profile and the actual or "effective" height. Because a given profile line does not necessarily pass through the exact center of each roughness element, the measured peak-to-valley roughness height, denoted by h, may be less than the effective roughness height, denoted by k. Additionally, for other types of roughness elements (e.g., rods, cones and fence elements or fabric weave, honeycomb and random ablation patterns), the relationship between measured and effective height can have a complex dependence on element geometry, alignment and spacing. For the current data set, in which the roughness is nominally represented as a tightly-packed array of hemispherical elements, it has been shown by Dirling (Ref. 5), that the *mean* measured height *(h)* is equal to a factor of $\pi/4$ times the *mean* effective roughness (k). More generally, the relationship between mean measured and effective heights for hemispherical, conical and rectangular elements is given by:

$$\bar{h} = \bar{k} \times \bar{p}\text{: where } \bar{p} = \begin{cases} \pi/4 & \text{hemispherical element} \\ 1/2 & \text{conical element} \\ 1 & \text{rectangular element} \end{cases} \quad (2)$$

For the purposes of this study, it is assumed that this relationship for the mean values holds for any arbitrary exceedance percentile value. Values of the 30$^{\text{th}}$ and 50$^{\text{th}}$ percentiles have been reported in the literature, and herein values for the 50$^{\text{th}}$, 30$^{\text{th}}$, 15$^{\text{th}}$ and 5$^{\text{th}}$ percentiles of the effective peak-to-valley roughness heights are reported. These values were derived from the measured roughness height distributions of Figure 19 and are listed in Table 2.

The relationship between the as-built, effective heights to the nominal heights for the 50$^{\text{th}}$, 30$^{\text{th}}$, 15$^{\text{th}}$ and 5$^{\text{th}}$ percentile exceedances is shown in Figure 21. For the larger ASTM Mesh sizes (10, 20 and 40-mesh), the ratios of effective to nominal heights are approximately the same for each exceedance percentile, varying from ~0.5 for the 50$^{\text{th}}$ percentile to ~1.0 for the 5$^{\text{th}}$ percentile. However, the ratio of effective to nominal height begins to increase rapidly with decreasing mesh size for the smaller ASTM mesh sizes (80, 140, and 230-Mesh). For the smallest, ASTM 230-Mesh sizes, the ratio of effective to nominal height varies from ~1.6 for the 50$^{\text{th}}$ percentile to 2.7 for the 5$^{\text{th}}$ percentile. Absent other information, these results would suggest that the smaller mesh size models had much larger as-built roughness heights than specified. However, as noted earlier, the nominal roughness sizes for these models were on the order of the ideal image resolution of the scanning system used to obtain the data. It was therefore concluded that, while the data may indicate that the smaller mesh size model roughness heights were larger than intended, it was not possible to absolutely quantify the differences.

An overall RMS roughness height also was determined from the global scan data for each sample plate and these values are also given in Table 2. In contrast to the peak-to-valley roughness values, the RMS value was based on all surface data points regardless of their location with respect to the peaks and

valleys of individual elements. The RMS values are useful in relating the current data set to prior studies in which statistical peak-to-valley data were not provided. It has been shown (e.g., Refs. 3, 4) that an approximate relationship holds between RMS and peak-to-valley exceedance parameters that allows for conversion between the two types of measurements. In Ref. 4, Jackson stated that the "significant" peak-to-valley roughness was equal to 3.6 times the RMS value. Unfortunately, the term "significant" was not explicitly defined, although in Ref. 3, Batt later concluded that the "significant" value was equal to the 30^{th} percentile exceedance height. A reanalysis conducted for the current report of the limited roughness profile data available from Ref. 4 suggests that Batt's conclusion was tenuous and that Jackson's "significant" values could just as easily be equated to the 50^{th} percentile roughness height. However, it is possible that Batt had access to more of the original data set than has been published and drew conclusions based on those data.

Regardless of the definition of "significant" for the Ref. 4 data set, examination of the current data set does confirm that an approximate log-linear relationship between the effective peak-to-valley and RMS heights holds, as shown in Figure 22. Here, the effective peak-to-valley and RMS values for each ASTM mesh size are plotted on a log-log-scale. Different fits can be generated depending on the peak-to-valley exceedance height specified, but in all cases, the approximate log-linear relationship holds. In Batt's analysis, the 30^{th} percentile exceedance height was found to be 3.6 times the RMS height. For the current data set, a factor of 3.3772 times the RMS was determined, which compares favorably to Batt's result.

Wind Tunnel Test Program

Four wind tunnel tests were performed at the Langley Aerothermodynamics Laboratory (LAL) in support of this program: two high unit Reynolds number tests in the 20-Inch Mach 6 Air Tunnel and two low unit Reynolds number tests in the 31-Inch Mach 10 Air Tunnel. These facilities are described in brief below and more detailed information on the LAL can be found in Refs. 6 -7.

Data were obtained at Mach 6 for six unit Reynolds numbers from $Re_\infty = 3.0\times10^6$/ft to 8.3×10^6/ft and at Mach 10 for four unit Reynolds numbers from $Re_\infty = 0.5\times10^6$/ft to 2.0×10^6/ft. Conditions are listed in Table 3 and Table 4 for Tests 6975 and 6998 in the 20-Inch Mach 6 Air Tunnel and in Table 5 and Table 6 for Tests 487 and 501 in the 31-Inch Mach 10 Air Tunnel. Entries in these tables are sorted first by model and then by free stream unit Reynolds number. The heat-transfer film coefficient (h_{FR}) values listed in these tables are based on Fay-Riddell (Ref. 8) calculations for the 3.00-in. radius of the models at cold-wall (300 K) conditions. The enthalpy difference is defined as the difference between the free stream total enthalpy and the wall enthalpy at 300K ($\Delta H_{tot} = H_0 - H_{300K}$). Additionally, an approximate hot-wall temperature (based on the value at the nose) is listed; this value was used in the computations to provide a more accurate prediction of boundary-layer transition parameters, which are dependent on the wall temperature.

NASA LaRC 20-Inch Mach 6 Air Tunnel

The NASA LaRC 20-Inch Mach 6 Air Tunnel (Figure 23 - Figure 24) is a blow-down facility in which heated, dried, and filtered air is used as the test gas. The tunnel has a two-dimensional contoured nozzle that opens into a 20.5 in × 20.0 in test section. The tunnel is equipped with a bottom-mounted injection system with a -5-deg to +55-deg pitch range and ±5-deg yaw range that can transfer a model from a sheltered model box to the tunnel centerline in less than 0.5 sec. Run times of up to 15 minutes are possible in this facility, although for the current aeroheating study, run times of only a few seconds were required. The nominal reservoir conditions of this facility produce perfect-gas free stream flows with

Mach numbers between 5.8 and 6.1 and unit Reynolds numbers of 0.5×10^6/ft to 8.3×10^6/ft. With its wide Reynolds number operating range capable of producing laminar, transitional, or turbulent flow on most geometries, this tunnel is primarily used for heat-transfer and boundary-layer transition studies.

NASA LaRC 31-Inch Mach 10 Air Tunnel

The NASA LaRC 31-Inch Mach 10 Air Tunnel (Figure 25 - Figure 26) is a perfect-gas, blow-down facility that uses dried, filtered air as the working fluid. The tunnel has been calibrated for reservoir conditions varying from 150 psi to 1450 psi at an operating temperature of 1850 deg-R, which produces free-stream unit Reynolds numbers from 0.25×10^6/ft to 2.2×10^6/ft. The nozzle is water-cooled, has a three-dimensional contour, and ends with 1.07 in. × 1.07 in. square throat. The 31 in × 31 in square test section features abundant optical access (side, top, and bottom windows) for visual imaging techniques and has a side-mounted injection system with a -45-deg to +45-deg pitch range and ±5-deg yaw range. The test core varies from approximately 12 in × 12 in at the lowest unit Reynolds number to 14 in × 14 in at the highest unit Reynolds number. This tunnel has the highest Mach number of the LAL facilities and is mainly employed in aerodynamic and fluid-mechanics studies. The high stagnation temperature of the facility also makes it suitable for aftbody/wake heating studies where the temperature rise is much lower than on the forebody

Data Acquisition, Reduction, Uncertainty and Presentation

Data Acquisition

Aeroheating data were obtained using the two-color, relative-intensity, global thermographic phosphor method (Ref. 9) and reduced using the IHEAT (Imaging for Hypersonic Experimental Aerothermodynamic Testing) code (Ref. 10). In this method, a model is illuminated by ultraviolet light sources that produce temperature-dependent fluorescence of the phosphor coating. Images of the model are taken in the tunnel before and during a run using a three-color, charge-coupled device camera and the images are processed to determine heat-transfer distributions.

Because of optical access limitations in both facilities, it was not possible to position a camera such that the entire surface of the model could be imaged. An illustration of the camera field-of-view for the 20-Inch Mach 6 Air Tunnel is shown in Figure 27 (the field-of-view was similar in the 31-Inch Mach 10 Air Tunnel). Data were obtained on the "top" half (relative to camera location) of the hemisphere model, including the stagnation region, but the bottom half of the model was out of the field-of-view.

Data Reduction

The IHEAT code uses calibrations to convert the intensity data from each image pixel to temperatures. Heat-transfer film coefficients are then determined by assuming a step function in heat transfer beginning at injection of the model into the tunnel, which corresponds to a parabolic temperature-time history. Heat-transfer data from IHEAT are typically reported in terms of ratio h/h_{FR}, where h_{FR} is the heat-transfer film coefficient resulting from a Fay-Riddell computation for a reference hemisphere of specified radius (in this case the 3.00-in. hemispherical radius). The heat-transfer film coefficient is defined in terms of enthalpy as:

$$h = q/\Delta H_{tot} = q/\left(H_{AW} - H_W\right) = q/\left(H_0 - H_W\right) \tag{3}$$

In the calculation of the heat-transfer film coefficient, it is assumed that, for a blunt-body, the adiabatic wall enthalpy H_{AW} is equal to the free stream total enthalpy of the tunnel, H_0. This heat transfer coefficient definition provides a theoretically near-constant value over the course of a run since the decrease in time of the heat transfer rate in the numerator as the model surface becomes hotter is balanced by the decrease of the enthalpy-difference term in the denominator.

The two-dimensional (2-D) image data obtained from IHEAT are corrected for optical perspective effects and mapped to a three-dimensional (3-D) surface model for that geometry. To accomplish this mapping, perspective, translational, and rotational transformations are first performed on the 3-D surface model until its 2-D projection matches that of the 2-D image data. The image data are then assigned transformed (x, y, z) coordinates based on interpolation between the image and surface geometry, and then the transformation is inverted to obtain an orthographic, 3-D heating distribution map.

Experimental Uncertainty

The experimental uncertainty for convective heat transfer measurements on *smooth* models in the LAL facilities are quantified as a function of uncertainties resulting from: the data acquisition method (±10%); flow quality and test-condition repeatability (±5%); and the accuracy of the 3D mapping process (±10%), which results in an overall root-sum-squared value of ±15%. Experience with this technique indicates that these values are usually conservative and as will be shown later, the predicted and measured heating distributions were in close agreement (generally less than ±5%) for laminar, smooth-wall cases.

However, in the current study, the quantification of experimental uncertainty was considerably more complex due to the presence of the distributed roughness elements. While the roughness element heights were assigned statistically-derived global values representative of the distribution over the entire model surface (as discussed in the next section), the local element heights exhibited random deviations from the global values. As a result of these deviations, boundary-layer transition locations and turbulent heating augmentation levels were not necessarily uniform around the circumference of the axisymmetric hemisphere models. As illustrated in Figure 28, transition generally occurred at an approximately constant radial location allowing for the definition of a mean transition front, but random, irregular surface elements also produced transitional "wedge" heating patterns upstream of the mean transition location.

Because of these roughness influences on uncertainty, it was concluded that analysis and presentation of the data in the usual manner of extracting a single, center-line profile from the image data for each run would provide a poor representation of the results. Instead, taking advantage of the axisymmetric nature of the hemisphere models and the resulting flow field, the entire global image data set for each run was used by analyzing the heating and transition effects in terms of s/R. Thus, instead of basing the analysis on the ~250 data points from a typical centerline profile, the ~65,500 data points from an entire image are employed, resulting in a more statistically accurate representation of the observed trends in the data.

Because of the variations in heating and transition onset by the random height variations and the flow-field variation over each element, the nominally axisymmetric heating distributions can exhibit varying amounts of scatter, depending on the roughness element size distribution and test condition. To aid in the interpretation of these data, locally-weighted, least-square curve fits were generated for each run in terms of h/h_{FR} vs. s/R that better illustrate the trends in the data set. Then, the overall standard deviation, σ_{rough} of the differences in heating levels between each data point and the curve-fit value were determined for each run to provide a measure of the "uncertainty" due to roughness effects. The term "uncertainty" is qualified because while some of the data scatter observed can be attributed to a true uncertainty – i.e., the

statistical variation in roughness over the surface introduced by the model fabrication process – there is also a nonrandom component that is a function of roughness element size and free stream Reynolds number. In general, values of σ_{rough} were small for low Reynolds and small element sizes and large for higher Reynolds numbers and larger element sizes. These standard deviations will be presented for all runs in the "Experimental Data and Analysis" section.

Another factor to be considered is the definition of the "transition onset" location. From a flow physics standpoint, transition onset is defined as the point where smooth, laminar flow in the boundary layer begins to break down. This location can, in theory, be determined through flow field imaging and/or diagnostic techniques (e.g., high-frequency pressure measurements, laser velocimetry). However, in this study, the only measurements available are of the surface temperature and (through data reduction) surface heating distribution. For such measurements, the differences between levels for laminar flow and for flow at transition onset are generally too subtle to permit precise definition of the onset location (except cases such as for very large roughness elements for which the transition distance from laminar to turbulent flow approaches zero).

In lieu of a precise measurement of the transition location, transition onset is defined herein through a common approach in which an "effective" or "apparent" point is determined through the "tangent-slope-intercept" method. As shown in Figure 29, the effective transition onset location is identified as the point where a line drawn tangent to the slope of the heat-transfer distribution curve (which is a fit to the entire surface data set) through the transition region intercepts the nominal, laminar distribution level. While this method does not provide the true transition onset location (at which fluctuations in the boundary-layer flow began), it is consistent with common practice for determining the roughness-induced transition location via surface-based measurement techniques. This method also permits a more consistent means of identifying a relevant transition parameter since identification of the small rise in heating levels at the actual transition onset location would be highly susceptible to error through surface measurement techniques alone. Transition onset data from this test program will be presented in the "Experimental Data and Analysis" section.

Computational Tools and Methods

Flow field predictions were performed using the LAURA (Langley Aerothermodynamic Upwind Relaxation Algorithm) code (Refs. 11-12) to generate heating values for comparisons with the experimental data. LAURA is a three-dimensional, finite-volume solver that includes perfect-gas and nonequilibrium chemistry options, a variety of turbulence models, and ablation and radiative transport capabilities. In this study, the perfect-gas air option was used and both laminar and turbulent solutions were generated. Turbulent cases were computed using the Cebeci-Smith algebraic model with transition onset specified at the nose, corresponding to fully-turbulent flow over the entire geometry. Solutions were computed on an axisymmetric grid with 90 streamwise and 64 surface normal cells using grid adaption to align the grid outer boundary with the shock and to cluster cells near the surface to produce wall cell Reynolds numbers on the order of 1 to 10. Free stream conditions were set to the nominal wind tunnel conditions for each run as given in Table 3 - Table 6

For the wall temperature boundary condition, a deviation in the normal practice of setting this value to a "cold-wall" ambient temperature (because of the usually small variation in heat-transfer coefficient with temperature) was employed. Literature on roughness effects indicates dependence of transition onset location on the ratio of boundary-layer edge temperature to wall temperature T_e/T_w. To approximately account for this effect (which was expected to be small for these test conditions), the computations were

performed using a uniform "hot-wall" wall temperature equal to that measured for each run at the stagnation point. These values varied between 350 K to 415 K at Mach 6 and 380 K to 425 K at Mach 10 (or greater, but this value is the upper limit for reliable temperature measurement via the phosphor thermography technique), depending on roughness height and test condition.

Experimental Data and Analysis

Overview of Data Set

The data from all runs (in both tunnels) is presented first in order to provide an overview of the complete data set and illustrate the characteristics and quality of the data. A limited analysis of the data follows this overview, but detailed analysis and development of models for roughness effects on transition and turbulent heating are beyond the scope of this data release report.

The data from the Mach 6 runs are shown in Figure 30 - Figure 125 and the data for the Mach 10 runs are shown in Figure 126 - Figure 183. The figures are ordered for each Mach number by roughness height and then by the test Reynolds number for each height. Two figures are shown for each run; a high-resolution version of the 3-D mapped global image data is presented in the first figure and a line plot of these data in terms of h/h_{FR} vs. s/R, along with the locally-weighted least-square fits, is presented in the second figure. In the line plots, error bars corresponding to the standard deviation of heating due to roughness height variations, $\sigma_{rough,}$ are also shown.

In some of these line-plots (e.g., Figure 39 and Figure 41), the presence of isolated heating spikes, due to phosphor coating damage or larger roughness elements that are outliers from the statistical height distribution, may create apparently significant scatter in the data plots. However, in these plots, only every 10^{th} point of the ~65,500 point data set was plotted in order to keep the plots legible. Nearly all of these unplotted points fall near the least-square fits atop those points already plotted. As result of this sparse plotting, the few outlier points are more visually significant than they actually are statistically.

As illustrated by these figures, the roughness effects data set spans the entire range of boundary-layer phenomena from laminar flow at the lowest Reynolds numbers and smallest roughness heights to completely turbulent at the highest Reynolds numbers and largest roughness heights. At a constant Reynolds number, increasing roughness height serves to both move the transition point upstream toward the nose and to augment the turbulent heating levels.

Data Quality

In terms of the general quality of the data, several features warrant discussion. The first is the presence of circumferential asymmetries in heating levels and transition onset locations for certain cases. These deviations are mostly due to the random variations in the roughness height over the surface of the model that result from the fabrication process, as discussed earlier. Another source of asymmetry is due to random, discrete damage to a model's phosphor coating resulting from either handling of the model during installation or wear over the course of multiple runs. An example of discrete, local asymmetries is the smooth-model data from the Mach 6, 7.5×10^6/ft and 8.3×10^6/ft Reynolds number cases (Test 6975, Runs 7 and 8) shown in Figure 38 - Figure 41. For these nominally smooth-surface, laminar flow cases, several isolated streaks of higher heating can be seen, which are indicative of small imperfections in the phosphor coating. An example of more widespread heating and transition onset asymmetries due to variation in roughness height over the model surface is the 40-Mesh model data from the Mach 6,

3.0×10^6/ft and 3.9×10^6/ft Reynolds number cases (Test 6975, Runs 15 and 16) shown in Figure 78 - Figure 81. It is noteworthy that the higher Reynolds number data for this model show much less scatter; this is because at the higher Reynolds number, when the boundary-layer flow more naturally trends toward turbulence, the effects of small surface deviations on the transition location were smaller than at lower Reynolds numbers, when the flow is borderline transitional. For both of these examples, the data scatter due to variations in the transition onset location illustrates the statistical reliability of basing the analysis on the least-square data fits for all the data from each case rather than using only a single profile line-cut.

Another data quality issue is the data loss due to temperature limitations on the phosphor thermography system. The ideal limit (the actual limit is a function of model illumination) of the current system is a surface temperature of approximately 425 K, above which the data are not considered to be reliable and are not retained. In the global image figures, areas where the surface temperature exceeded the temperature limit are rendered in black to indicate lack of data. In the 20-Inch Mach 6 Air Tunnel, this temperature limiting occurred only in very small regions near the nose on the 10-Mesh and 20-Mesh models at the higher Reynolds numbers (Figure 110, Figure 118, Figure 120, Figure 122). However, in the 31-Inch Mach 10 Air Tunnel, the stagnation temperature is considerably higher, and as a result some data loss due to temperature limiting occurred on almost every run. At the lowest Reynolds number with the smallest roughness (230-Mesh model at 0.5×10^6/ft in Figure 126) only a few pixels of data were lost, while at the highest Reynolds number with the largest roughness (10-Mesh at 2.0×10^6/ft in Figure 182) almost no usable data were obtained. For these Mach 10 runs, all data were cut off ahead of the s/R location where $T_w > 425$ in order to provide a cleaner image with a clearly defined boundary on the reliable data.

It can also be seen in the images for larger roughness element cases that a discontinuous drop in heating occurs near the trailing edge ($s/R > 1.2$) of the hemisphere. This discontinuity corresponds to the change from a rough surface to a smooth surface. As noted in the "Wind Tunnel Model Fabrication" section, no roughness elements were applied to this region of the ceramic models in order to ensure that the models did not bind during removal from the casting molds. However, since the boundary-layer edge on a hemisphere is supersonic ahead of this point, the upstream heating and transition measurements were not affected.

Reynolds Number and Roughness Height Effects on Heating and Transition

The effects of Reynolds number on the heating levels and boundary-layer transition onset locations are illustrated next for each roughness height in Figure 184 - Figure 222. Three figures are provided for each case: in the first figure, global heating images are shown for each roughness height (ordered left-to-right, top-to-bottom in terms of increasing Reynolds number); in the second and third figures, line plots of h/h_{FR} vs. s/R are shown both with all the data points (second figure) to illustrate the scatter in the data and with only the locally-weighted, least-squares fits (third figure) to highlight trends in the data.

In these line-plots, the CFD predictions for smooth-wall, laminar and turbulent heating levels are also shown. Because the heat-transfer film coefficient ratio, h/h_{FR}, remains nearly constant with Reynolds number, only the lowest Reynolds number laminar prediction is shown for each case. But since this invariance does not hold for turbulent flow, turbulent predictions are shown for each Reynolds number. As noted previously, transition was specified at the nose for these solutions and so the predictions are for fully-turbulent flow over the entire geometry, which was not necessarily consistent with the actual data.

The same data are shown in the next group of figures, but they are reordered to show the effects of roughness height on transition and heating at each Reynolds number. In Figure 223 - Figure 252, three figures are shown for each case: in the first figure, global heating images are shown for each Reynolds number condition (ordered left-to-right, top-to-bottom in terms of increasing roughness height); in the second and third figures, line plots of h/h_{FR} vs. s/R are shown both with all the data points (second figure for each case) to illustrate the scatter in the data and with only the locally-weighted, least-squares fits (third figure for each case) to highlight trends in the data. Smooth-wall, laminar and fully-turbulent CFD predictions are also shown in the line plots for each case.

In these line-plots for roughness and Reynolds number effects, the laminar CFD predictions that are shown allow for baseline assessment of the computational accuracy through comparisons with the low-Reynolds number, small roughness cases for which transition did not occur. In general, good agreement between data and predictions was observed for all laminar cases. However, the turbulent predictions are shown only for illustrative purposes since the fully-turbulent, smooth-wall computations did not account for roughness effects on transition location or heating augmentation.

Roughness and Reynolds-number effects on transition and heating follow expected trends. As Reynolds number is increased, the transition onset location moves upstream toward the stagnation point of the hemisphere. The transition onset location also moves upstream as roughness height is increased and the measured rough-wall turbulent heating levels grow increasingly greater than the predicted smooth-wall turbulent heating levels.

Transition Onset Data Correlation

Transition onset data (for those runs where transition occurred) are provided in Table 7 for the Mach 6 tests and Table 8 for the Mach 10 tests. As discussed in the "Experimental Uncertainty" section, these values represent the effective transition locations as determined from the tangent-slope-intercept method analysis of the least-square curve fits to the global image data. The wall temperatures at the onset locations are also listed.

While the development of transition models is outside the scope of this work, the data are presented in terms of two common transition onset correlations in order to provide a basis for comparison with historical data sets. These correlations are the Passive Nosetip Transition (PANT) test program correlation developed from a series of rough-surface wind tunnel data sets (Ref. 4, 13) in the U.S. Navy's Naval Ordnance Laboratory Tunnel #8 in the 1970s and the ballistics range transition correlation based originally on data obtained (Ref. 14) during the 1970s in the Air Force's Arnold Engineering Development Center Ballistic Range/Track G and later supplemented (Ref. 15) by data from the NASA Ames Research Center Hypervelocity Free-Flight Aerodynamics Facility.

These wind-tunnel based and ballistics-range based correlations for transition onset are given by:

$$\mathrm{Re}_{\theta,TR} = 215\left[\left(k/\theta\right)\times\left(T_e/T_w\right)\right]^{(-0.7)} \tag{4}$$

and

$$\mathrm{Re}_{\theta,TR}\left(\mu_e/\mu_w\right) = 250\left[\left(\rho_k U_k k\right)/\left(\rho_e U_e \theta\right)\right]^{(-1.0)} \tag{5}$$

There has been considerable discussion in the literature (e.g., Ref. 3) about the applicability of these

correlations. In brief, when wind tunnel data are cast in terms of the ballistics range correlation, the agreement is not as good and the same holds for representation of ballistics range data in terms of the wind tunnel correlation. The current test program thus provides a third, independent source of transition onset data, which may be useful in reconciling these first two data sets. As shown in Figure 253 for the wind tunnel correlation and Figure 254 for the ballistics range correlation, the current data are reasonably well represented by either correlation method, although neither method provides a perfect fit to the data.

The largest differences between the correlations and the data are evident for the large roughness model (20-Mesh and 10-Mesh) data, which diverge sharply from the correlations. This result is not surprising, given that the roughness heights for these models are generally greater than the boundary-layer height and as such, are outside the range of applicability of these boundary-layer property based correlations. There are additional complications when dealing with these data points. The first issue is grid resolution. The computational grids were adapted to provide clustering *within* the boundary layer in order to capture the strong gradients in that region. But since these large roughness element peaks fall *outside* the boundary layer, the grid resolution is coarser there and thus the flow field information from the point used to evaluate the correlation variables is less accurate. Another issue for large roughness heights is the proximity of transition onset to the stagnation point. In the stagnation region, the flow field gradients are large, and thus a small uncertainty in transition onset identification can produce large errors. Additionally, most Navier-Stokes CFD codes (such as LAURA) are prone to stability and convergence issues in the stagnation region, which are mitigated through various numerical methods that can affect the accuracy of the solution, and thus of the boundary-layer parameters used in the correlations. For these reasons, the large roughness heights ($k > \delta$) should not be used in the development of correlations and the existing correlations should not be expected to provide accurate results for such conditions. The inclusion of these data in Figure 253 and Figure 254 provides a demonstration of the limits of such correlations.

Roughness Heating Augmentation

In this report, analysis of the heating augmentation due to roughness is limited to the expected observation that heating levels increase with roughness height. This limitation is due to the complexities of the problem and the goal of releasing this data set as a basis for further analysis. For any given roughness-height / Reynolds-number / body-point-location, the heating augmentation with respect to smooth-wall laminar or turbulent predictions can be determined through reference to the data and figures presented herein. However, the development of engineering correlations or numerical models for simulation of these data depend on not just modeling the effects of roughness on heating, but also modeling the effects of roughness on transition onset; that is, it is not possible to accurately predict heating levels without being able to first predict the transition onset location. As discussed in the previous section, the current transition onset dataset can be approximately modeled using historical correlations developed for either ballistics range data or wind tunnel data, but these correlations are not consistent with each other. Rather than developing heating augmentation models incorporating one or the other of these transition onset models, or developing a new transition onset model, this problem is deferred to future analysis and the incorporation of additional data to better resolve the discrepancies in historical datasets and models.

Summary and Conclusions

The effects of distributed surface roughness on boundary-layer transition and turbulent heating have been investigated through hypersonic wind tunnel testing of hemispherical models with roughness patterns simulating those of a heat shield with an ablated TPS. Heating and transition onset data were

obtained at Mach 6 and Mach 10 over a range of roughness heights and free stream Reynolds numbers sufficient to produce laminar, transitional and turbulent flow.

Least-square curve fits of the nominally axisymmetric heating distributions in terms of h/h_{FR} vs. s/R were generated to reduce data scatter and better illustrate trends. Comparisons of these curve-fits with smooth-wall heating predictions demonstrated that both increasing roughness height and increasing free stream Reynolds number produced an upstream movement of the transition onset location, as well as increasing augmentation of the heating levels above predicted, smooth-wall values.

A method was presented for generating statistically-based estimates of distributed surface roughness heights based on measurements of the peak-to-valley heights of roughness elements. The roughness height estimates were used along with boundary-layer properties from flow field solutions to correlate the transition onset data in terms of two historical correlation methods. The current transition onset data were reasonably well correlated in terms of either method.

References

1. Buck, G. M., "Rapid Model Fabrication and Testing for Aerospace Vehicles," AIAA Paper 2000-0826, 38th AIAA Aerospace Sciences Meeting and Exhibit, Reno, NV, January 10-13, 2000.
2. ASTM E11-01, Standard Specification for Wire Cloth and Sieves for Testing Purposes, ASTM International, West Conshohocken, PA, 2001.
3. Batt, R. G. and Legner, H. H., "A Review of Roughness-Induced Nosetip Transition," *AIAA Journal*, Vol. 21, No. 1, January 1983, pp. 7-22.
4. Jackson, M. D., "Passive Nosetip Technology (PANT) Program. Volume 15: Roughness Induced Transition on Blunt Axisymmetric Bodies – Data Report," Space and Missile Systems Organization TR-74-86-Vol-XV, April 1974.
5. Dirling, R. B., "On the Relationship Between Material Variability and Surface Roughness," AIAA Paper 1977-0402, 18th Structural Dynamics and Materials Conference, San Diego, CA, March 21-23, 1977.
6. Berger, K., Rufer, S., Hollingsworth, K. and Wright, S., "NASA Langley Aerothermodynamic Laboratory: Hypersonic Testing Capabilities," AIAA Paper 2015-1337, 53rd AIAA Aerospace Sciences Meeting, Kissimmee, FL, January 5-9, 2015.
7. Hollis, B. R., Berger, K. T., Berry, S. A., Brauckmann, G. J., et al, "Entry, Descent, and Landing Aerothermodynamics: NASA Langley Experimental Capabilities and Contributions," AIAA Paper 2014-1154, AIAA 52nd Aerospace Science Meeting, National Harbor, MD, January 13-17, 2014.
8. Fay, J. A., and Riddell, F. R., "Theory of Stagnation Point Heat Transfer in Dissociated Air," *Journal of Aeronautical Sciences*, Vol. 25, No. 2., February 1958, pp. 73-85.
9. Buck, G. M., "Surface Temperature/Heat Transfer Measurement Using a Quantitative Phosphor Thermography System," AIAA Paper 91-0064, 29th Aerospace Sciences Meeting, Reno, NV, January 7-10, 1991.
10. Merski, N. R., "Global Aeroheating Wind-Tunnel Measurements Using Improved Two-Color Phosphor Thermography Methods," *Journal of Spacecraft and Rockets*, Vol. 36, No. 2, March-April 1999, pp. 160-170.
11. Gnoffo, P. A., "An Upwind-Biased, Point-Implicit Algorithm for Viscous, Compressible Perfect-Gas Flows," NASA TP-2953, February 1990.

12. Mazaheri, A., Gnoffo, P. A., Johnston, C. O., and Kleb, B., "LAURA User's Manual: 5.5-65135," NASA TM-2013-217800, February 2011.

13. Bishop, W. M., "Transition Induced by Distributed Roughness on Blunt Bodies in Supersonic Flow," Space and Missile Systems Organization TR-76-146, October 1976.

14. Reda, D. C., "Correlation of Nosetip Boundary-Layer Transition Measured in Ballistics-Range Experiments," *AIAA Journal*, Vol. 19, No. 3, March 1981, pp. 329-339.

15. Wilder, M. C., Reda, D. C., and Prabhu, D. K., "Transition Experiments on Blunt Bodies with Roughness in Hypersonic Free Flight in Carbon Dioxide," AIAA Paper 2015-1738, 53rd AIAA Aerospace Sciences Meeting, Kissimmee, FL, 2015.

Table 1. Wind tunnel model list.

Model ID	Model Geometry	Model Diameter (in)	ASTM Mesh Designation	Spherical glass particle diameter (mil)	Nominal element height (mil)
10-Mesh	Hemisphere	6.00	ASTM-10	68.90	34.45
20-Mesh	Hemisphere	6.00	ASTM-20	33.58	16.79
30-Mesh	Hemisphere	6.00	ASTM-30	23.60	11.80
40-Mesh	Hemisphere	6.00	ASTM-40	16.73	8.37
80-Mesh	Hemisphere	6.00	ASTM-80	7.09	3.54
140-Mesh	Hemisphere	6.00	ASTM-140	4.17	2.09
230-Mesh	Hemisphere	6.00	ASTM-230	2.48	1.24

Table 2. Roughness data from sample plate scans.

Model ID	Nominal element height (mil)	# of profile-line points	50 % Effective height k_{PV50} (mil)	30 % Effective height k_{PV30} (mil)	15 % Effective height k_{PV15} (mil)	5 % Effective height k_{PV05} (mil)	Measured RMS height (mil)
10-Mesh	34.45	66	21.48	25.78	30.15	36.03	7.873
20-Mesh	16.79	81	8.49	10.19	14.18	16.93	2.380
30-Mesh*	11.80	N/A	6.59	8.13	10.94	12.83	1.993
40-Mesh	8.37	65	3.83	5.13	6.23	6.86	1.430
80-Mesh	3.54	89	3.40	4.38	5.09	6.47	1.181
140-Mesh	2.09	105	2.73	3.38	3.96	4.65	1.102
230-Mesh	1.24	96	1.94	2.30	2.71	3.32	0.683

* No scan data for 30-Mesh, values are estimated

Table 3. 20-Inch Mach 6 Air Tunnel Test 6975 run matrix.

Run	Model	Re_∞ (1/ft)	M_∞	T_∞ (K)	ρ_∞ (kg/m^3)	U_∞ (m/s)	ΔH (MJ/kg)	h_{FR} (kg/m^2-s)	$T_{w,approx}$ (K)
2	Baseline	3.03E+06	5.99	62.5	4.71E-02	948.7	2.12E+05	2.16E-01	360
5	Baseline	3.88E+06	6.01	63.3	6.05E-02	957.2	2.21E+05	2.48E-01	372
1	Baseline	5.04E+06	6.02	63.2	7.84E-02	957.5	2.21E+05	2.82E-01	375
6	Baseline	6.63E+06	6.04	62.6	1.02E-01	954.6	2.17E+05	3.21E-01	386
7	Baseline	7.46E+06	6.04	62.5	1.15E-01	953.6	2.17E+05	3.40E-01	386
8	Baseline	8.34E+06	6.03	58.6	1.25E-01	918.1	1.79E+05	3.41E-01	376
39	230-mesh	3.03E+06	5.99	62.5	4.71E-02	948.7	2.12E+05	2.16E-01	365
41	230-mesh	3.88E+06	6.01	63.3	6.05E-02	957.2	2.21E+05	2.48E-01	373
40	230-mesh	5.04E+06	6.02	63.2	7.84E-02	957.5	2.21E+05	2.82E-01	378
42	230-mesh	6.63E+06	6.04	62.6	1.02E-01	954.6	2.17E+05	3.21E-01	396
43	230-mesh	7.46E+06	6.04	62.5	1.15E-01	953.6	2.17E+05	3.40E-01	405
44	230-mesh	8.34E+06	6.03	58.6	1.25E-01	918.1	1.79E+05	3.41E-01	390
27	140-mesh	3.03E+06	5.99	62.5	4.71E-02	948.7	2.12E+05	2.16E-01	359
28	140-mesh	3.88E+06	6.01	63.3	6.05E-02	957.2	2.21E+05	2.48E-01	373
29	140-mesh	5.04E+06	6.02	63.2	7.84E-02	957.5	2.21E+05	2.82E-01	381
30	140-mesh	6.63E+06	6.04	62.6	1.02E-01	954.6	2.17E+05	3.21E-01	399
31	140-mesh	7.46E+06	6.04	62.5	1.15E-01	953.6	2.17E+05	3.40E-01	405
32	140-mesh	8.34E+06	6.03	58.6	1.25E-01	918.1	1.79E+05	3.41E-01	391
33	80-mesh	3.03E+06	5.99	62.5	4.71E-02	948.7	2.12E+05	2.16E-01	363
34	80-mesh	3.88E+06	6.01	63.3	6.05E-02	957.2	2.21E+05	2.48E-01	375
35	80-mesh	5.04E+06	6.02	63.2	7.84E-02	957.5	2.21E+05	2.82E-01	389
36	80-mesh	6.63E+06	6.04	62.6	1.02E-01	954.6	2.17E+05	3.21E-01	405
37	80-mesh	7.46E+06	6.04	62.5	1.15E-01	953.6	2.17E+05	3.40E-01	411
38	80-mesh	8.34E+06	6.03	58.6	1.25E-01	918.1	1.79E+05	3.41E-01	395
15	40-mesh	3.03E+06	5.99	62.5	4.71E-02	948.7	2.12E+05	2.16E-01	353
16	40-mesh	3.88E+06	6.01	63.3	6.05E-02	957.2	2.21E+05	2.48E-01	371
17	40-mesh	5.04E+06	6.02	63.2	7.84E-02	957.5	2.21E+05	2.82E-01	385
18	40-mesh	6.63E+06	6.04	62.6	1.02E-01	954.6	2.17E+05	3.21E-01	395
19	40-mesh	7.46E+06	6.04	62.5	1.15E-01	953.6	2.17E+05	3.40E-01	399
20	40-mesh	8.34E+06	6.03	58.6	1.25E-01	918.1	1.79E+05	3.41E-01	376
9	20-mesh	3.03E+06	5.99	62.5	4.71E-02	948.7	2.12E+05	2.16E-01	381
10	20-mesh	3.88E+06	6.01	63.3	6.05E-02	957.2	2.21E+05	2.48E-01	398
11	20-mesh	5.04E+06	6.02	63.2	7.84E-02	957.5	2.21E+05	2.82E-01	404
12	20-mesh	6.63E+06	6.04	62.6	1.02E-01	954.6	2.17E+05	3.21E-01	407
13	20-mesh	7.46E+06	6.04	62.5	1.15E-01	953.6	2.17E+05	3.40E-01	411
14	20-mesh	8.34E+06	6.03	58.6	1.25E-01	918.1	1.79E+05	3.41E-01	396
21	10-mesh	3.03E+06	5.99	62.5	4.71E-02	948.7	2.12E+05	2.16E-01	380
22	10-mesh	3.88E+06	6.01	63.3	6.05E-02	957.2	2.21E+05	2.48E-01	394
23	10-mesh	5.04E+06	6.02	63.2	7.84E-02	957.5	2.21E+05	2.82E-01	405
24	10-mesh	6.63E+06	6.04	62.6	1.02E-01	954.6	2.17E+05	3.21E-01	414
25	10-mesh	7.46E+06	6.04	62.5	1.15E-01	953.6	2.17E+05	3.40E-01	410
26	10-mesh	8.34E+06	6.03	58.6	1.25E-01	918.1	1.79E+05	3.41E-01	401

Table 4. 20-Inch Mach 6 Air Tunnel Test 6998 run matrix.

Run	Model	Re_∞ (1/ft)	M_∞	T_∞ (K)	ρ_∞ (kg/m^3)	U_∞ (m/s)	ΔH (MJ/kg)	h_{FR} (kg/m^2-s)	$T_{w,approx}$ (K)
13	30-mesh	2.10E+06	5.96	61.9	3.25E-02	939.5	2.03E+05	1.77E-01	347
12	30-mesh	3.03E+06	5.99	62.5	4.71E-02	948.7	2.12E+05	2.16E-01	359
11	30-mesh	3.88E+06	6.01	63.3	6.05E-02	957.2	2.21E+05	2.48E-01	370
10	30-mesh	5.04E+06	6.02	63.2	7.84E-02	957.5	2.21E+05	2.82E-01	388
14	30-mesh	6.63E+06	6.04	62.6	1.02E-01	954.6	2.17E+05	3.21E-01	390
15	30-mesh	7.46E+06	6.04	62.5	1.15E-01	953.6	2.17E+05	3.40E-01	399

Table 5. 31-Inch Mach 10 Air Tunnel Test 487 run matrix.

Run	Model	Re_∞ (1/ft)	M_∞	T_∞ (K)	ρ_∞ (kg/m^3)	U_∞ (m/s)	ΔH (MJ/kg)	h_{FR} (kg/m^2-s)	$T_{w,approx}$ (K)
28	230-mesh	4.85E+05	9.67	51.7	4.21E-03	1392.8	7.21E+05	1.02E-01	380
9	230-mesh	5.31E+05	9.68	51.8	4.61E-03	1396.5	7.26E+05	1.07E-01	383
29	230-mesh	9.98E+05	9.80	50.5	8.45E-03	1395.0	7.23E+05	1.45E-01	409
8	230-mesh	1.03E+06	9.81	51.5	8.83E-03	1410.0	7.45E+05	1.50E-01	415
30	230-mesh	1.51E+06	9.89	50.1	1.27E-02	1400.6	7.30E+05	1.79E-01	>425
11	230-mesh	1.57E+06	9.90	50.4	1.32E-02	1406.2	7.38E+05	1.83E-01	>425
10	230-mesh	2.02E+06	9.96	50.4	1.68E-02	1413.8	7.49E+05	2.08E-01	>425
27	230-mesh	2.02E+06	9.96	49.2	1.66E-02	1396.5	7.23E+05	2.04E-01	>425
18	40-mesh	4.70E+05	9.66	50.9	4.06E-03	1382.3	7.06E+05	9.95E-02	369
19	40-mesh	9.92E+05	9.80	50.7	8.42E-03	1397.8	7.27E+05	1.45E-01	404
20	40-mesh	1.54E+06	9.89	49.6	1.28E-02	1394.0	7.20E+05	1.79E-01	422
26	40-mesh	2.00E+06	9.96	49.6	1.66E-02	1401.5	7.31E+05	2.04E-01	>430
22	20-mesh	5.03E+05	9.67	50.8	4.33E-03	1381.4	7.04E+05	1.03E-01	386
23	20-mesh	1.07E+06	9.82	48.1	8.87E-03	1362.0	6.75E+05	1.44E-01	410
21	20-mesh	1.57E+06	9.90	48.9	1.30E-02	1384.3	7.06E+05	1.78E-01	>425
25	20-mesh	2.05E+06	9.96	48.8	1.68E-02	1390.6	7.15E+05	2.04E-01	>425
17	10-mesh	4.60E+05	9.66	51.6	4.00E-03	1391.1	7.19E+05	9.95E-02	389
13	10-mesh	5.31E+05	9.68	51.8	4.61E-03	1397.2	7.27E+05	1.07E-01	>425
16	10-mesh	1.02E+06	9.81	49.8	8.54E-03	1386.3	7.10E+05	1.45E-01	>425
14	10-mesh	1.03E+06	9.81	51.5	8.83E-03	1409.8	7.45E+05	1.50E-01	>425
12	10-mesh	1.55E+06	9.90	50.8	1.31E-02	1411.1	7.46E+05	1.83E-01	>425
15	10-mesh	2.03E+06	9.96	50.2	1.69E-02	1410.8	7.44E+05	2.08E-01	>425

Table 6. 31-Inch Mach 10 Air Tunnel Test 501 run matrix.

Run	Model	Re_∞ (1/ft)	M_∞	T_∞ (K)	ρ_∞ (kg/m^3)	U_∞ (m/s)	ΔH (MJ/kg)	h_{FR} (kg/m^2-s)	$T_{w,approx}$ (K)
10	40-mesh	5.58E+05	9.69	51.5	4.83E-03	1394.4	7.23E+05	7.93E+00	360
11	40-mesh	1.07E+06	9.82	51.0	9.08E-03	1403.3	7.35E+05	1.11E+01	392
12	40-mesh	1.52E+06	9.89	50.3	1.28E-02	1404.4	7.36E+05	1.32E+01	416
4	30-mesh	5.58E+05	9.69	51.5	4.83E-03	1394.4	7.23E+05	7.93E+00	372
5	30-mesh	1.07E+06	9.82	51.0	9.08E-03	1403.3	7.35E+05	1.11E+01	404
9	30-mesh	1.52E+06	9.89	50.3	1.28E-02	1404.4	7.36E+05	1.32E+01	414
6	20-mesh	5.58E+05	9.69	51.5	4.83E-03	1394.4	7.23E+05	7.93E+00	374
7	20-mesh	1.07E+06	9.82	51.0	9.08E-03	1403.3	7.35E+05	1.11E+01	407
8	20-mesh	1.52E+06	9.89	50.3	1.28E-02	1404.4	7.36E+05	1.32E+01	412

Table 7. 20-Inch Mach 6 Air Tunnel transition onset data.

Re_∞ (1/ft)	Model	Test	Run	$T_{w,TR}$ (K)	β_{TR} (deg)	$(s/R)_{TR}$
2.10E+06	30	6998	13	345	25.16	0.4391
3.03E+06	10	6975	21	380	2.83	0.0495
3.03E+06	20	6975	9	381	8.00	0.1395
3.03E+06	30	6998	12	357	16.00	0.2793
3.03E+06	40	6975	15	353	32.42	0.5659
3.88E+06	20	6975	10	398	4.06	0.0708
3.88E+06	30	6998	1	364	11.72	0.2046
3.88E+06	40	6975	16	371	20.38	0.3557
5.04E+06	20	6975	11	404	1.37	0.0238
5.04E+06	30	6998	10	370	9.48	0.1655
5.04E+06	40	6975	17	385	14.48	0.2528
5.04E+06	80	6975	35	389	24.62	0.4297
6.63E+06	30	6998	14	384	7.01	0.1223
6.63E+06	40	6975	18	395	12.22	0.2133
6.63E+06	80	6975	36	405	16.77	0.2927
6.63E+06	140	6975	30	399	26.25	0.4581
6.63E+06	230	6975	42	396	31.56	0.5508
7.46E+06	30	6998	15	390	6.27	0.1094
7.46E+06	40	6975	19	399	11.22	0.1958
7.46E+06	80	6975	37	411	14.99	0.2616
7.46E+06	140	6975	31	405	23.55	0.4110
7.46E+06	230	6975	43	405	26.25	0.4581
8.34E+06	30	6998	16	376	5.78	0.1008
8.34E+06	40	6975	20	376	10.72	0.1871
8.34E+06	80	6975	38	395	13.22	0.2308
8.34E+06	140	6975	32	391	21.43	0.3740
8.34E+06	230	6975	44	390	25.43	0.4438

Table 8. 31-Inch Mach 10 Air Tunnel transition onset data.

Re_∞ (1/ft)	Model	Test	Run	$T_{w,TR}$ (K)	β_{TR} (deg)	$(s/R)_{TR}$
1.03E+06	10	487	14	420	24.35	0.4250
1.02E+06	10	487	16	385	26.52	0.4628
1.57E+06	20	487	21	380	27.34	0.4772
1.52E+06	20	501	8	380	27.34	0.4772
1.52E+06	30	501	9	380	30.98	0.5408

Cavities and protrusions

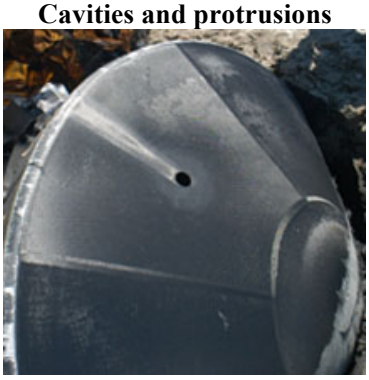

a) Genesis heat shield attachment point cavities

Tile/panel steps and gaps

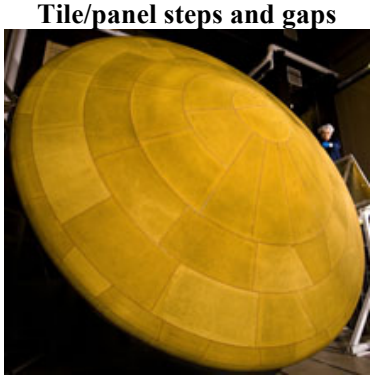

b) TPS panels on MSL heat shield

Physical Damage

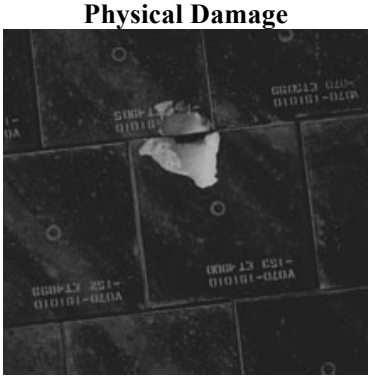

c) Damage to Orbiter tiles

Figure 1. Discrete surface roughness types.

Pattern

a) Hexcomb cavities from ablation of Apollo TPS

Flexible TPS

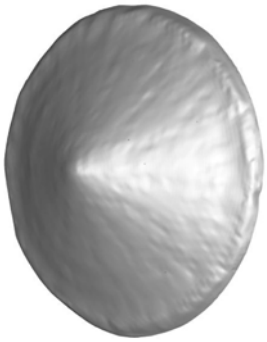

b) Scan data of flexible TPS under aerodynamic load

Sand-grain

c) Ablation of monolithic TPS on Stardust heat shield

Figure 2. Distributed surface roughness types.

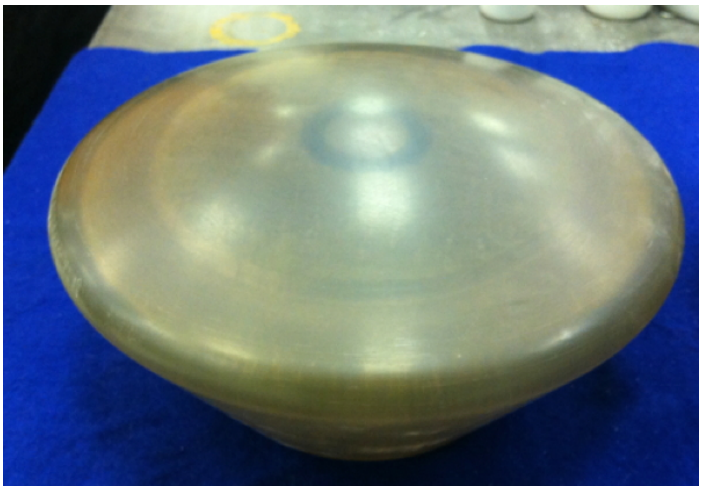

a) Smooth surface SLA resin pattern (hemispherical cap model)

b) SLA pattern with roughness elements epoxied in place

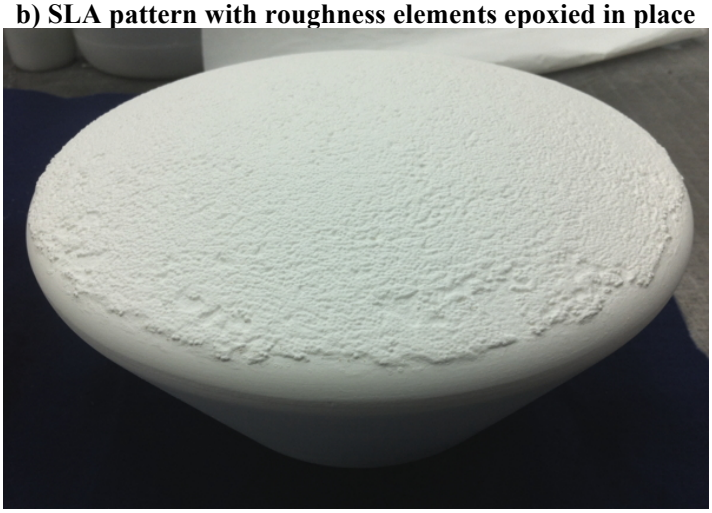

c) Cast ceramic model with roughness

Figure 3. Roughness model fabrication steps.

a) Oblique View

b) Side View

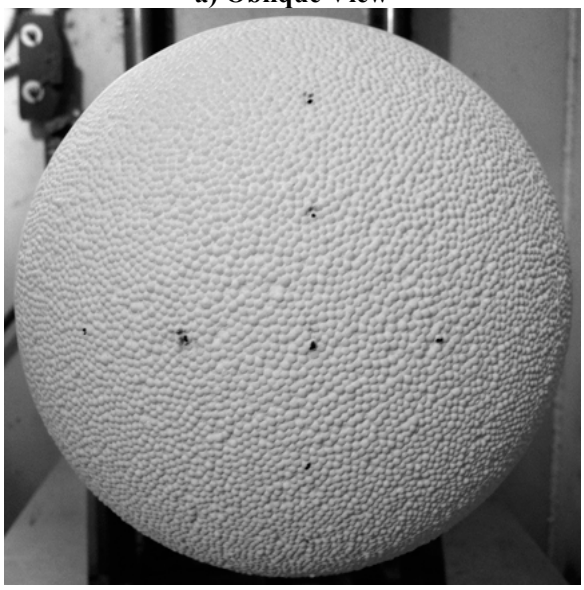

c) Front View

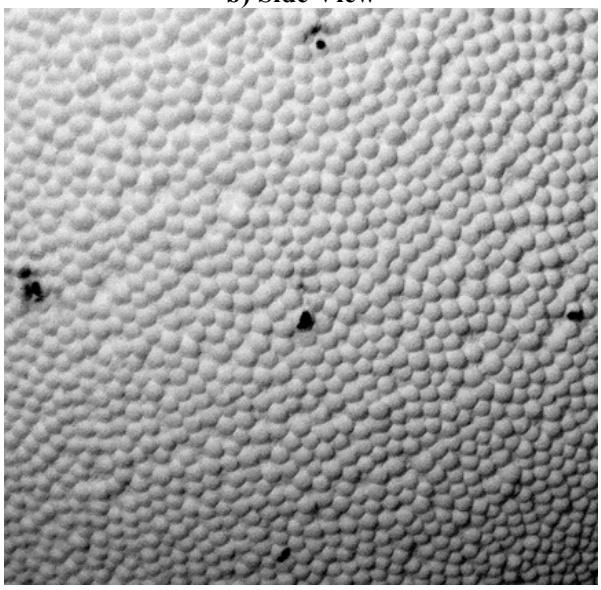

d) Close-up View

Figure 4. 10-Mesh hemisphere model photographs.

a) Oblique View

b) Side View

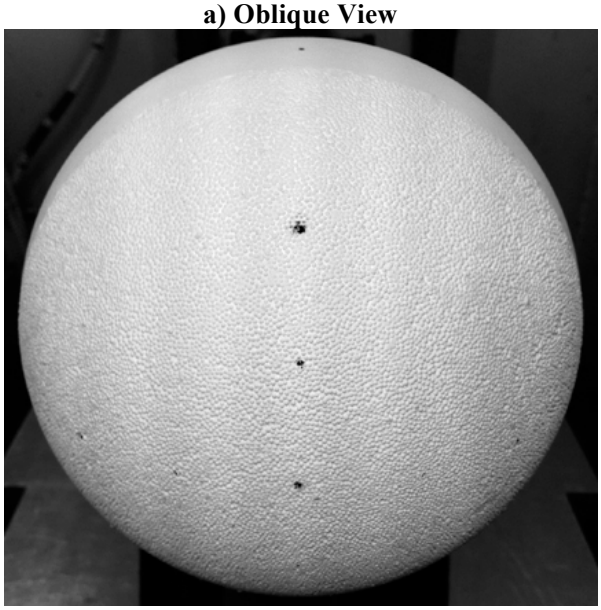

c) Front View

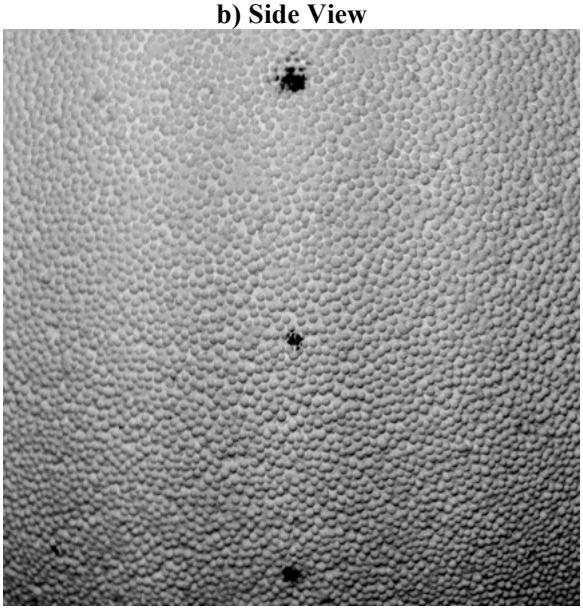

d) Close-up View

Figure 5. 20-Mesh hemisphere model photographs.

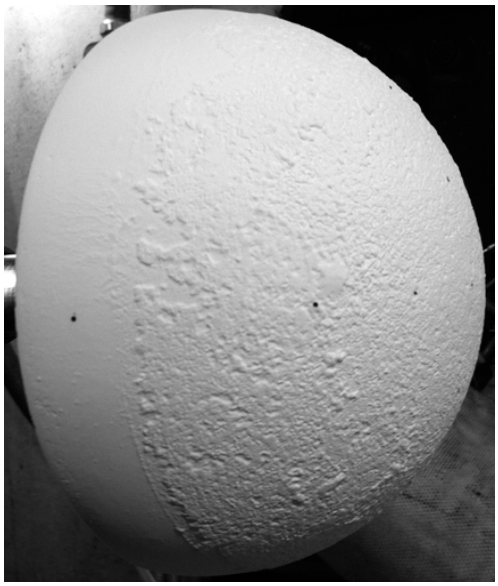

a) Oblique View

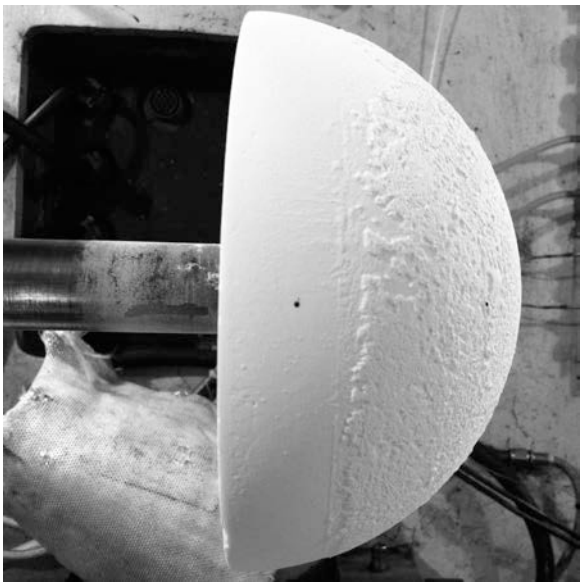

b) Side View

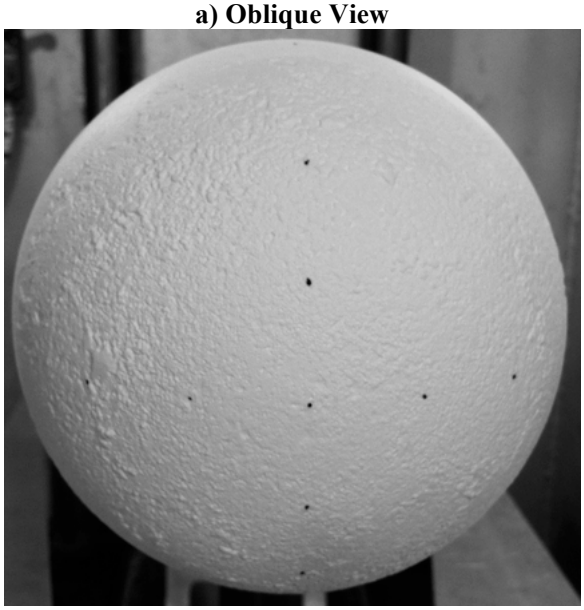

c) Front View

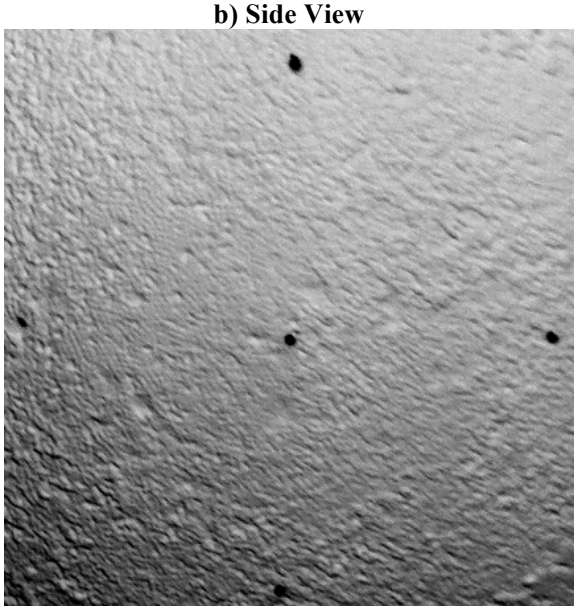

d) Close-up View

Figure 6. 30-Mesh hemisphere model photographs.

a) Oblique View

b) Side View

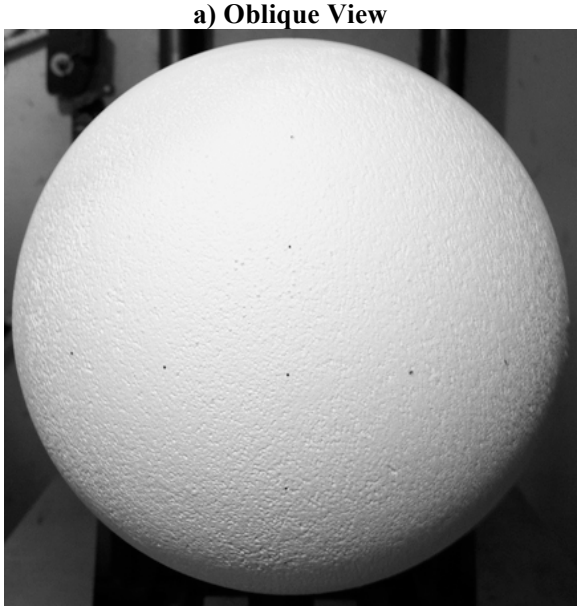

c) Front View

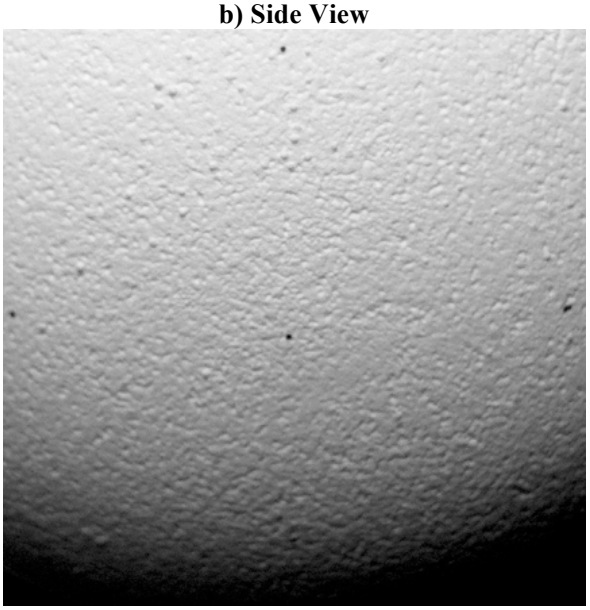

d) Close-up View

Figure 7. 40-Mesh hemisphere model photographs.

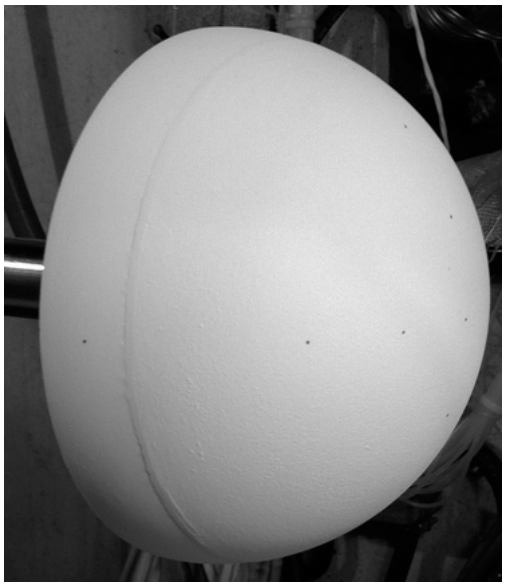

a) Oblique View

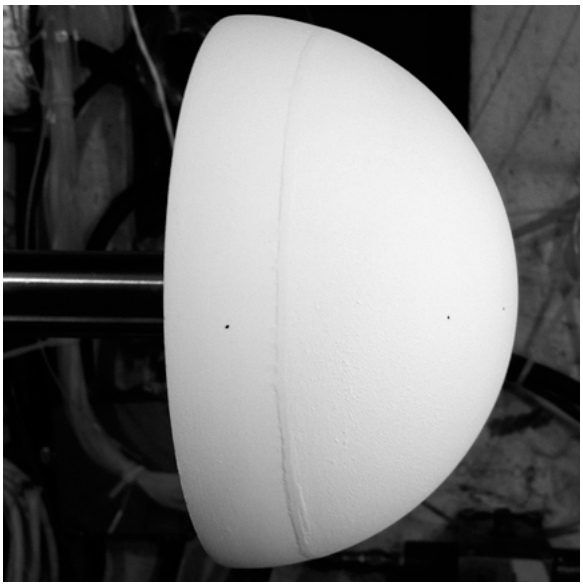

b) Side View

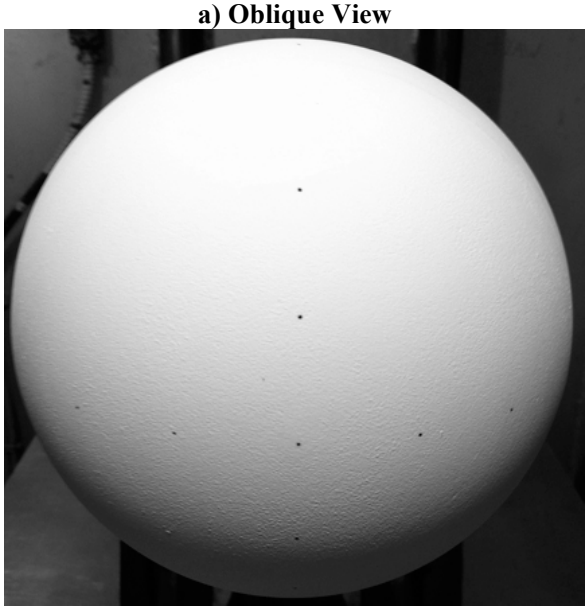

c) Front View

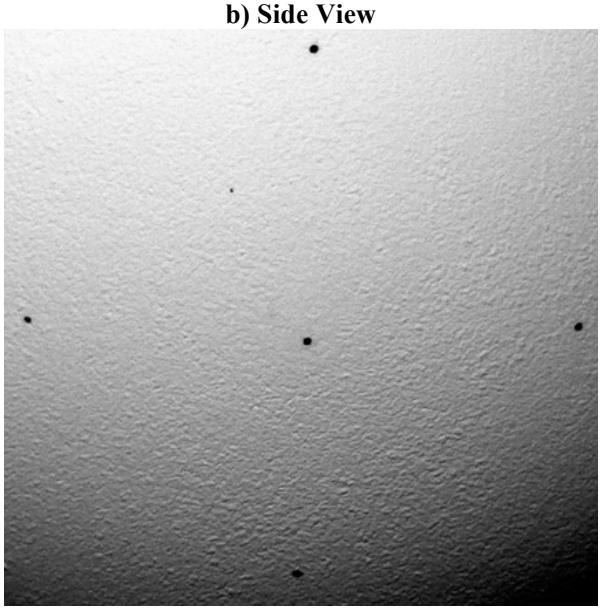

d) Close-up View

Figure 8. 80-Mesh hemisphere model photographs.

a) Oblique View

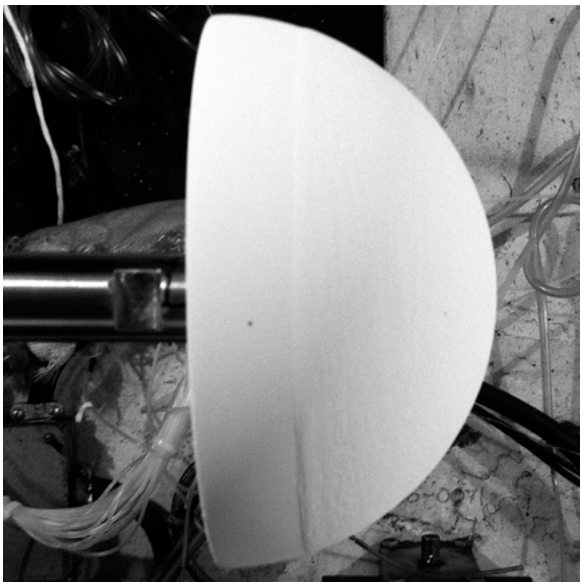

b) Side View

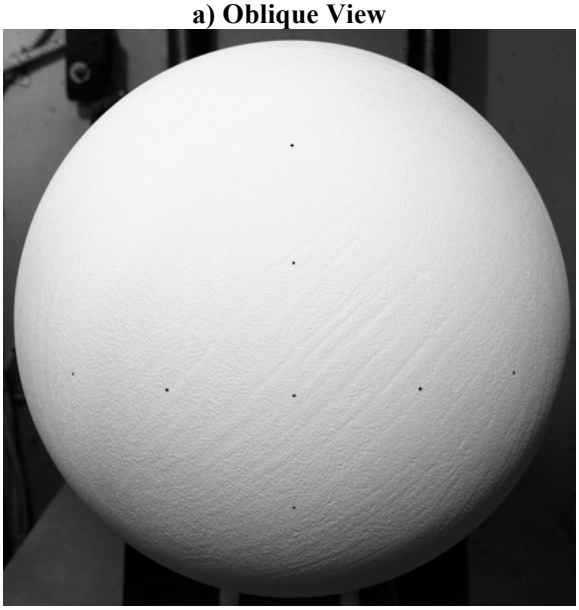

c) Front View

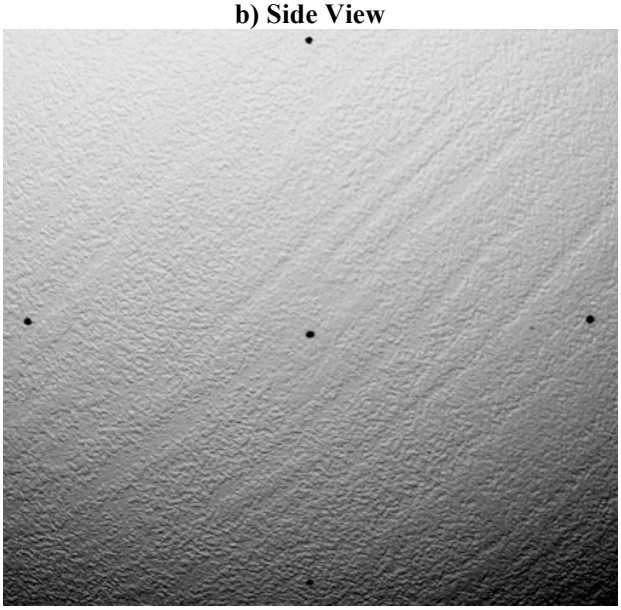

d) Close-up View

Figure 9. 140-Mesh hemisphere model photographs.

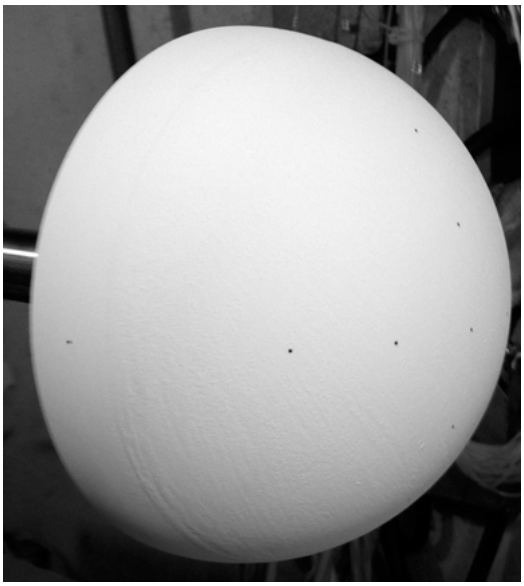

a) Oblique View

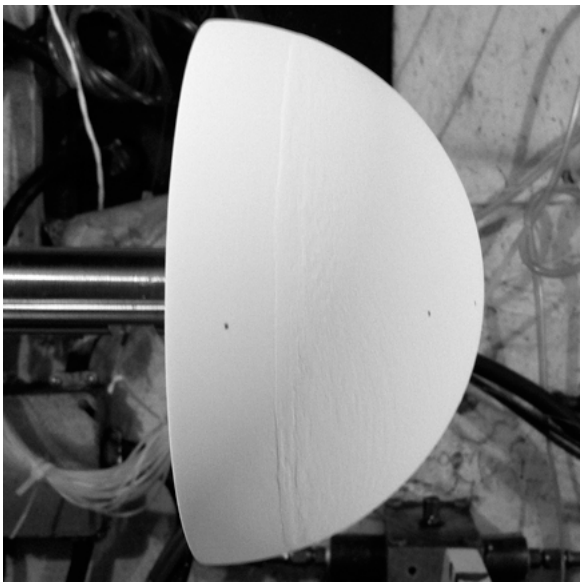

b) Side View

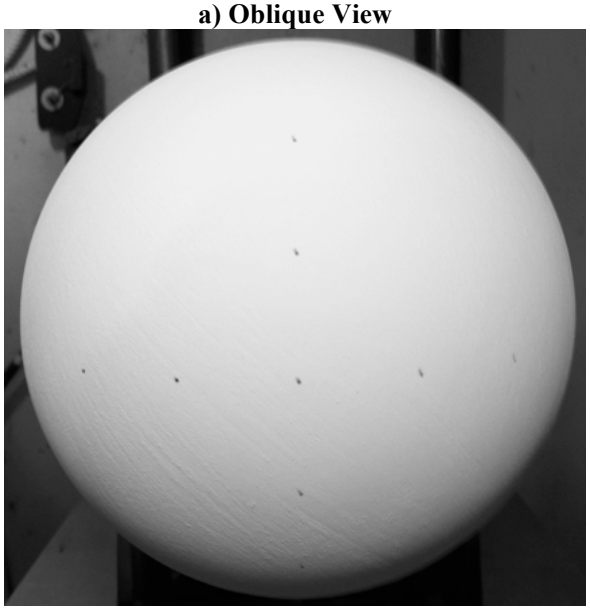

c) Front View

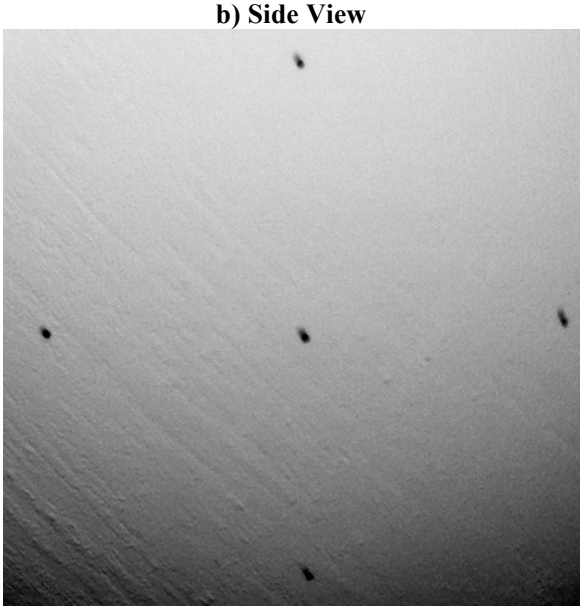

d) Close-up View

Figure 10. 230-Mesh hemisphere model photographs.

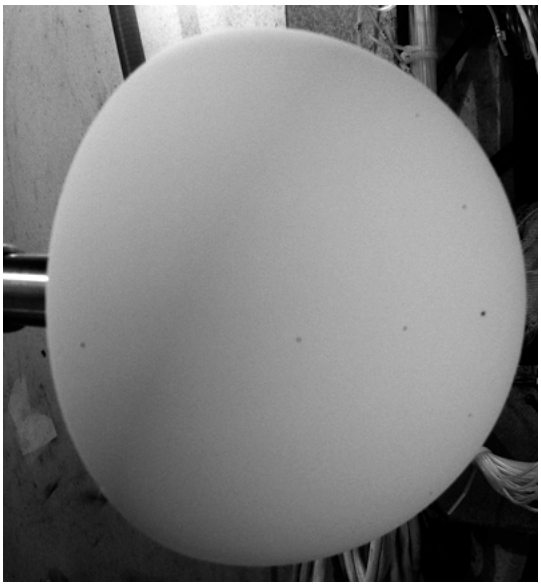

a) Oblique View

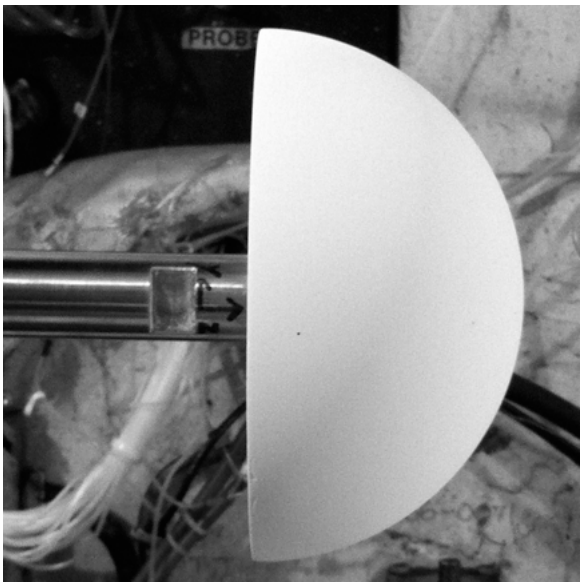

b) Side View

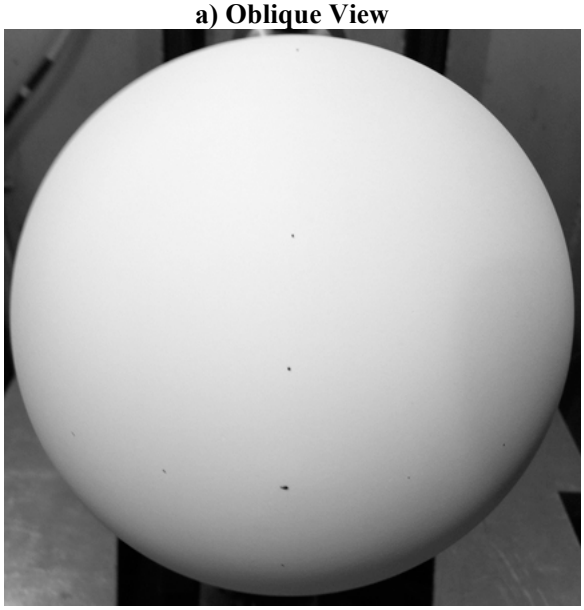

c) Front View

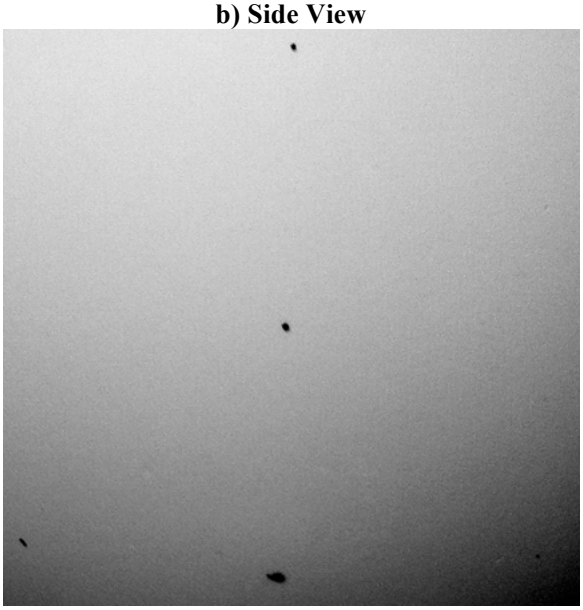

d) Close-up View

Figure 11. Smooth hemisphere model photographs.

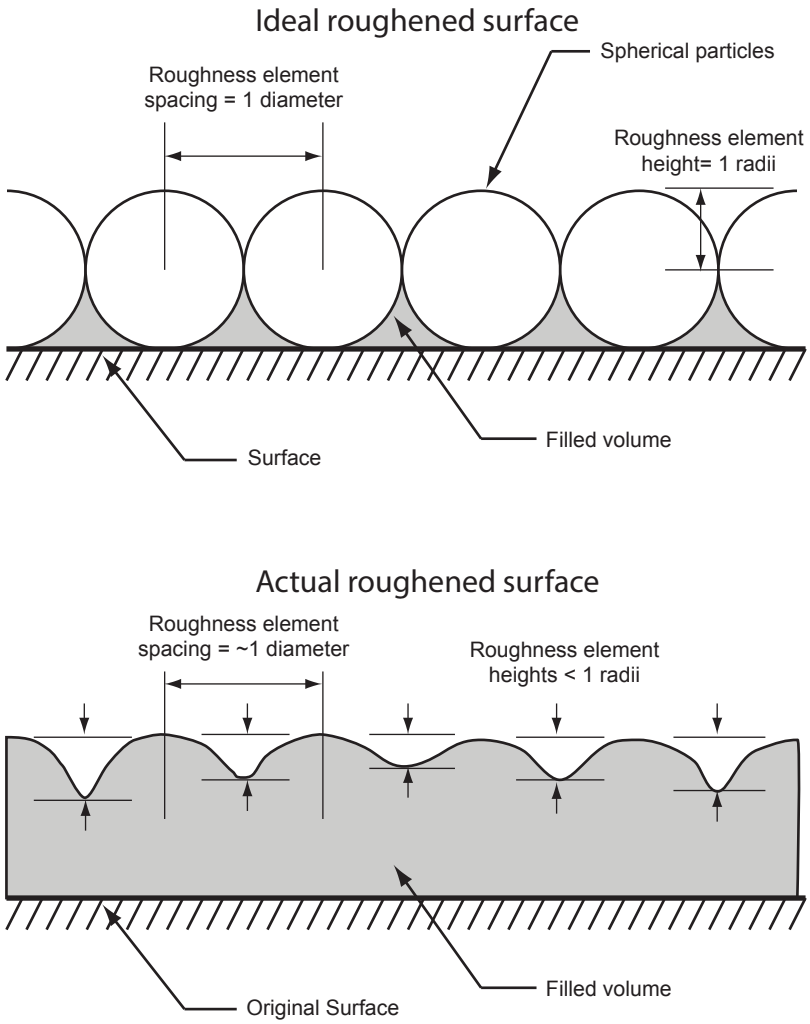

Figure 12. Illustration of ideal and actual surface roughness.

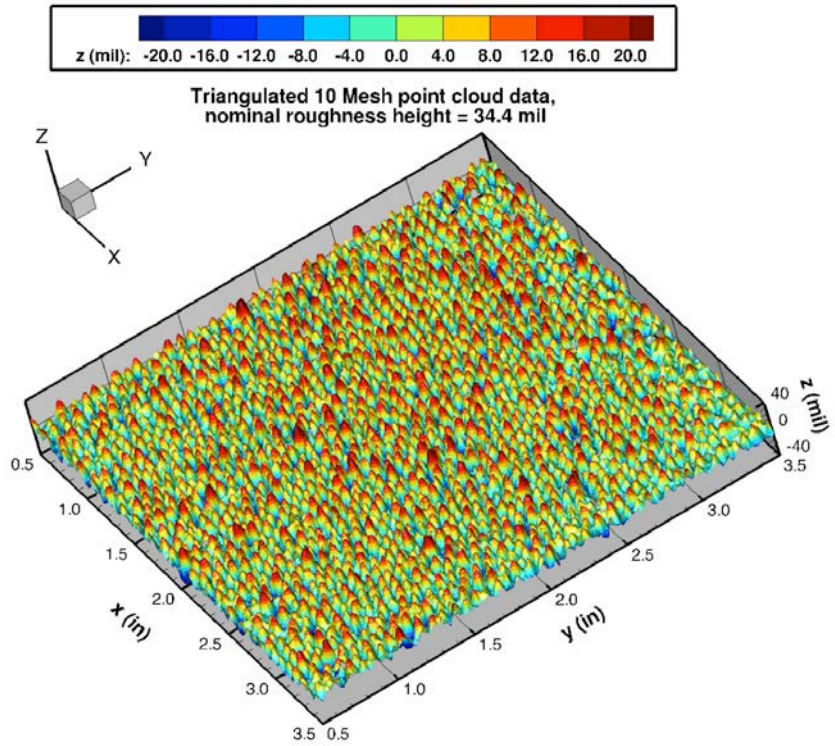

a) Triangulated point-cloud data

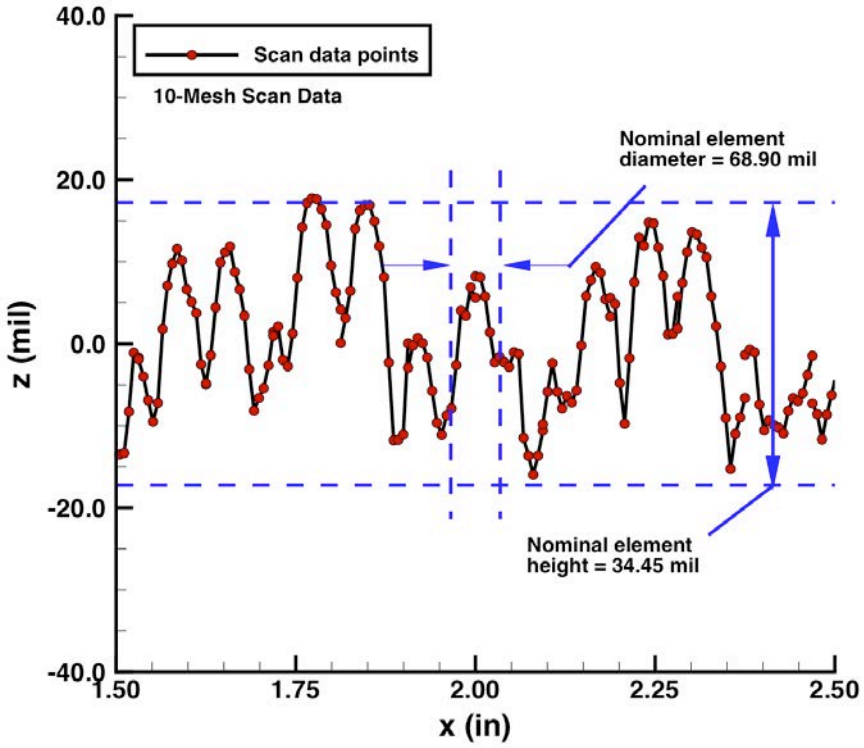

b) Profile line-cut

Figure 13. 10-Mesh sample plate scan data.

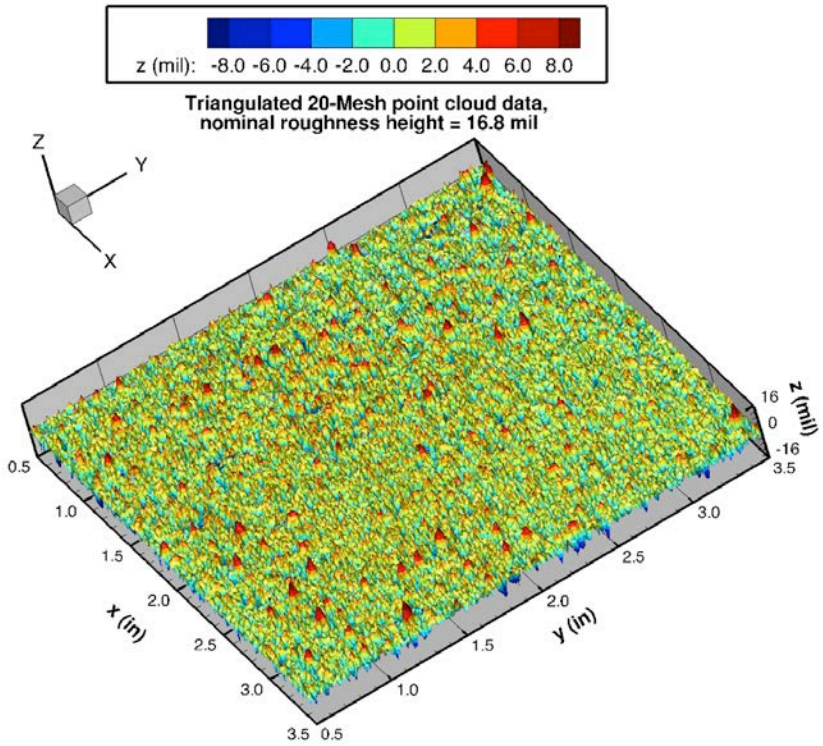

a) Triangulated point-cloud data

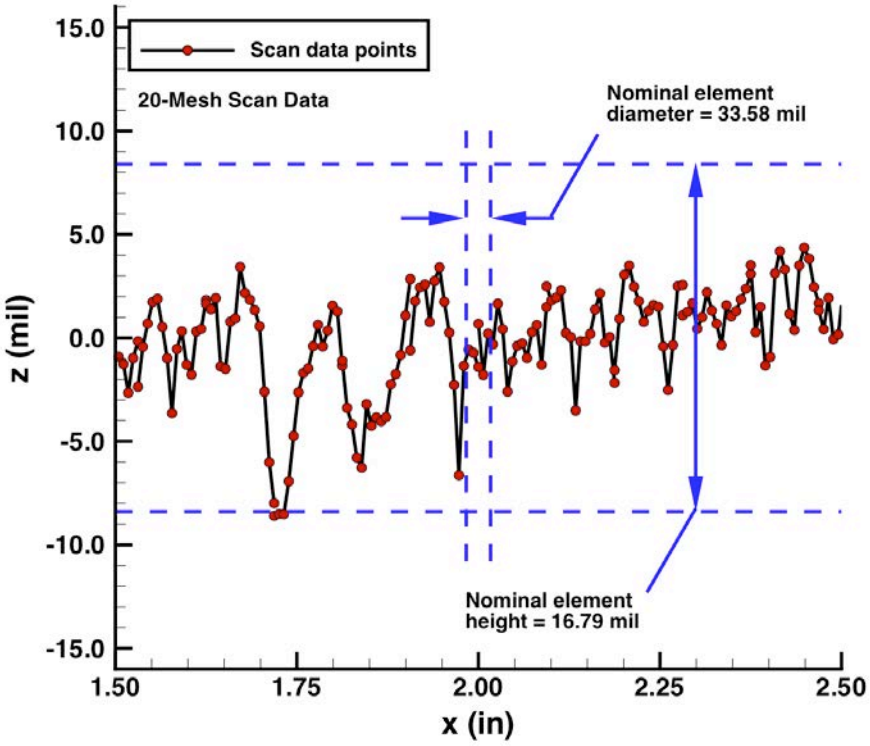

b) Profile line-cut

Figure 14. 20-Mesh sample plate scan data.

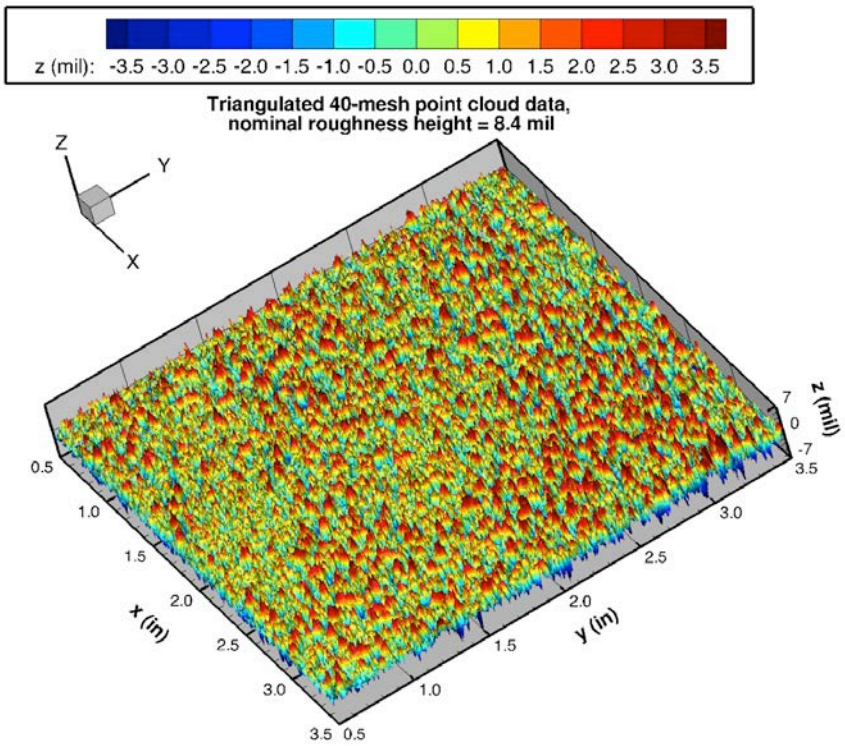

a) Triangulated point-cloud data

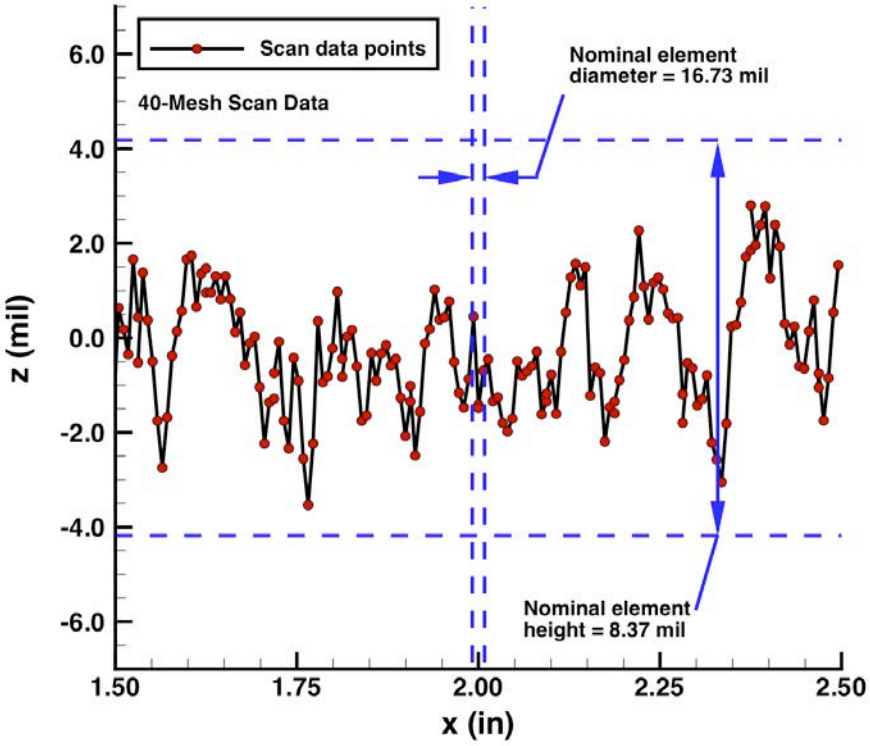

b) Profile line-cut

Figure 15. 40-Mesh sample plate scan data.

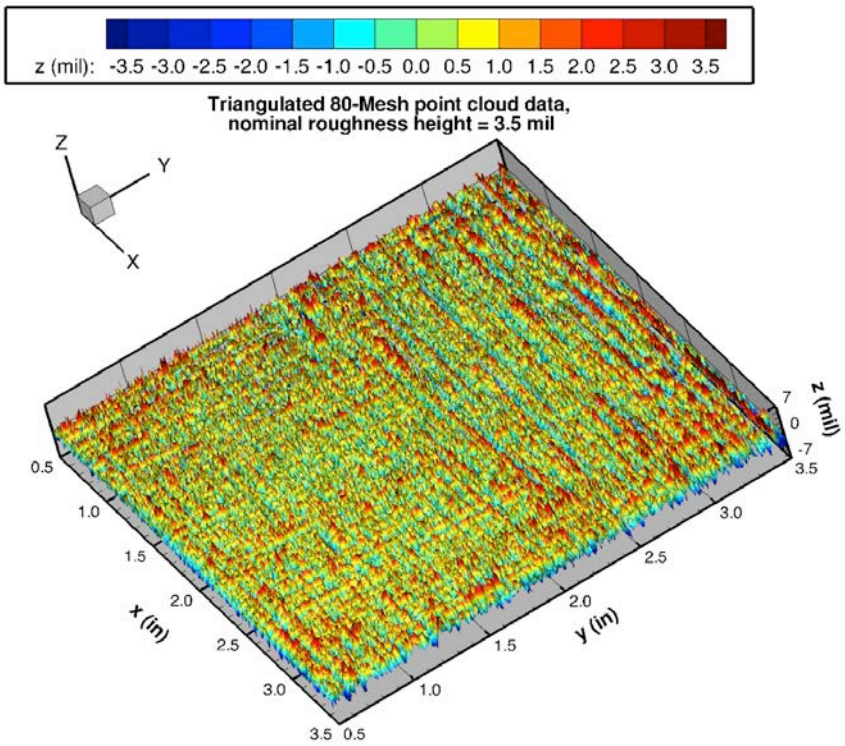

a) Triangulated point-cloud data

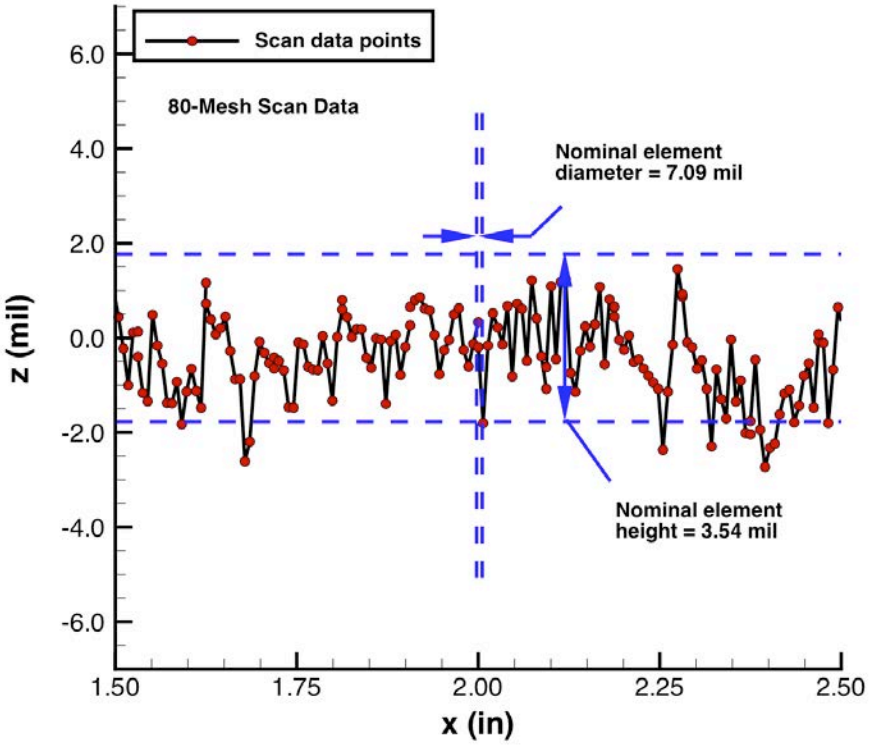

b) Profile line-cut

Figure 16. 80-Mesh sample plate scan data.

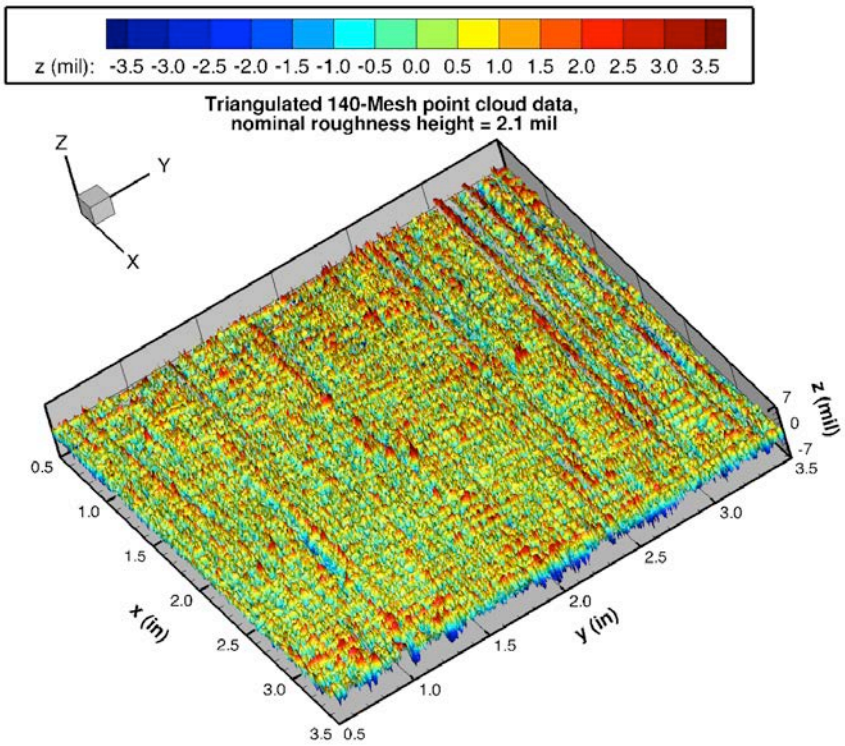

a) Triangulated point-cloud data

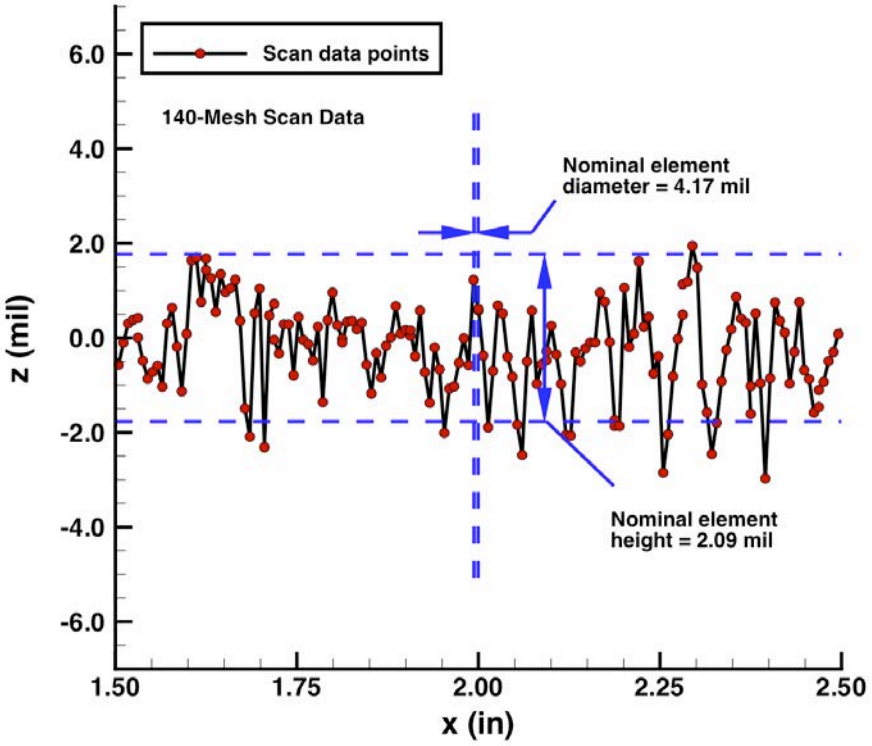

b) Profile line-cut

Figure 17. 140-Mesh sample plate scan data.

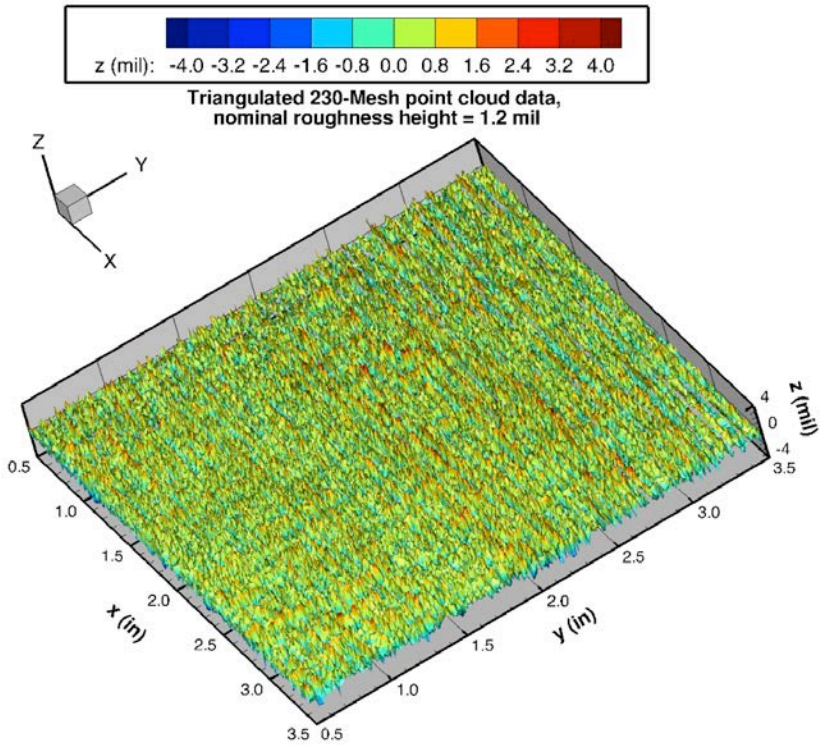

a) Triangulated point-cloud data

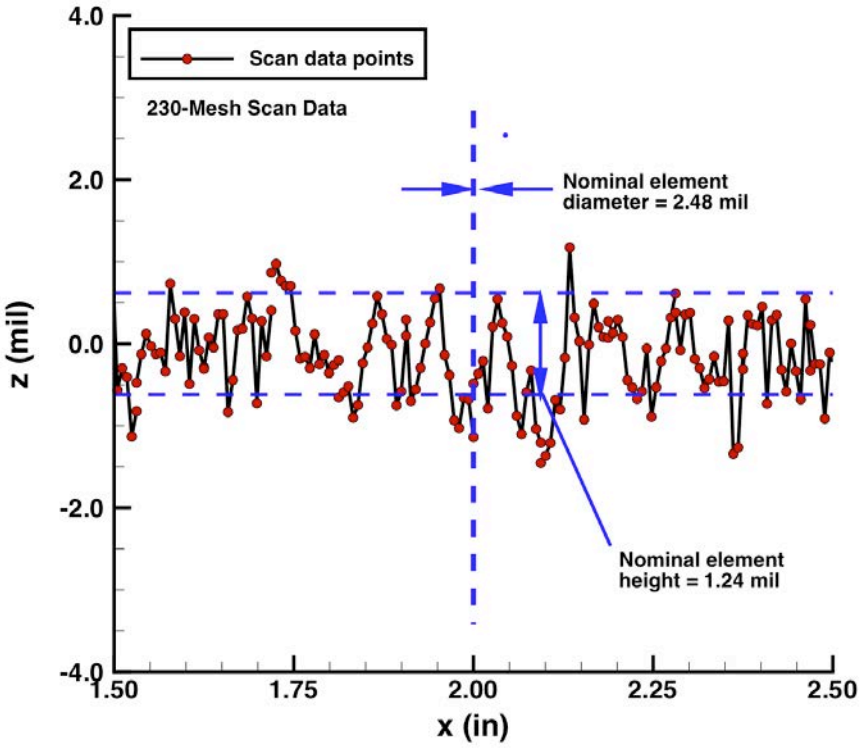

b) Profile line-cut

Figure 18. 230-Mesh sample plate scan data.

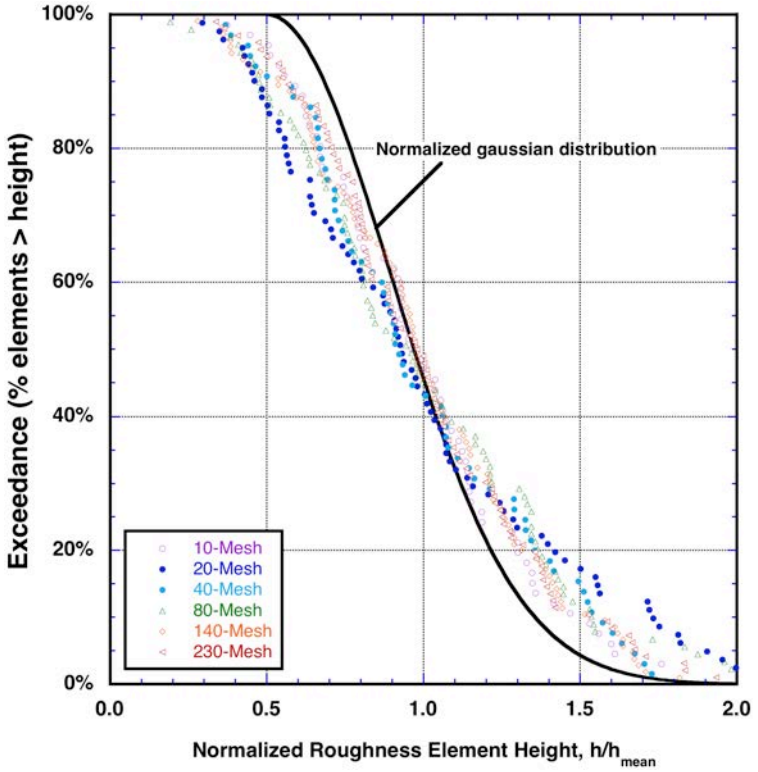

Figure 19. Roughness height probability of exceedance distributions.

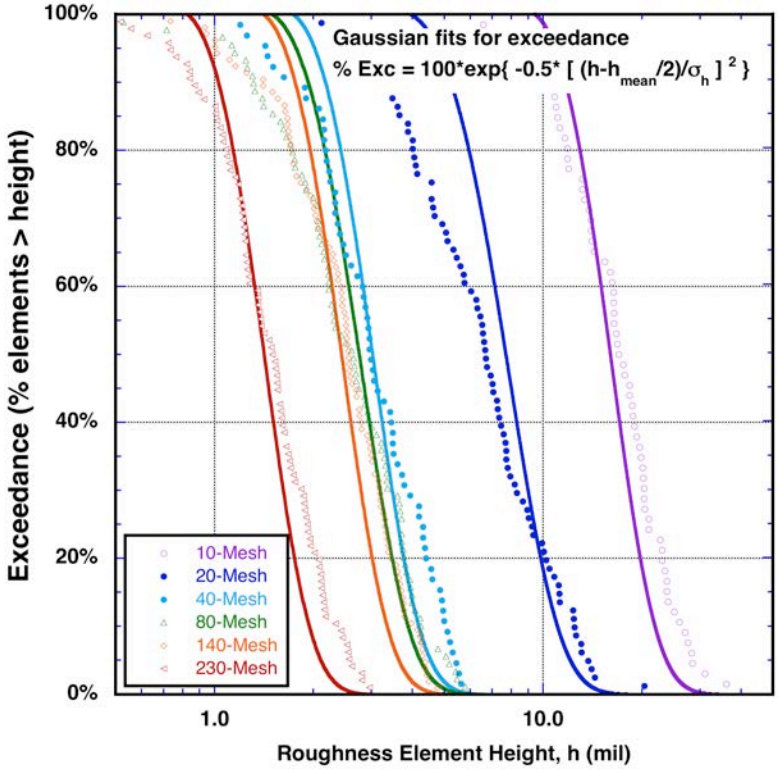

Figure 20. Normalized exceedance distributions.

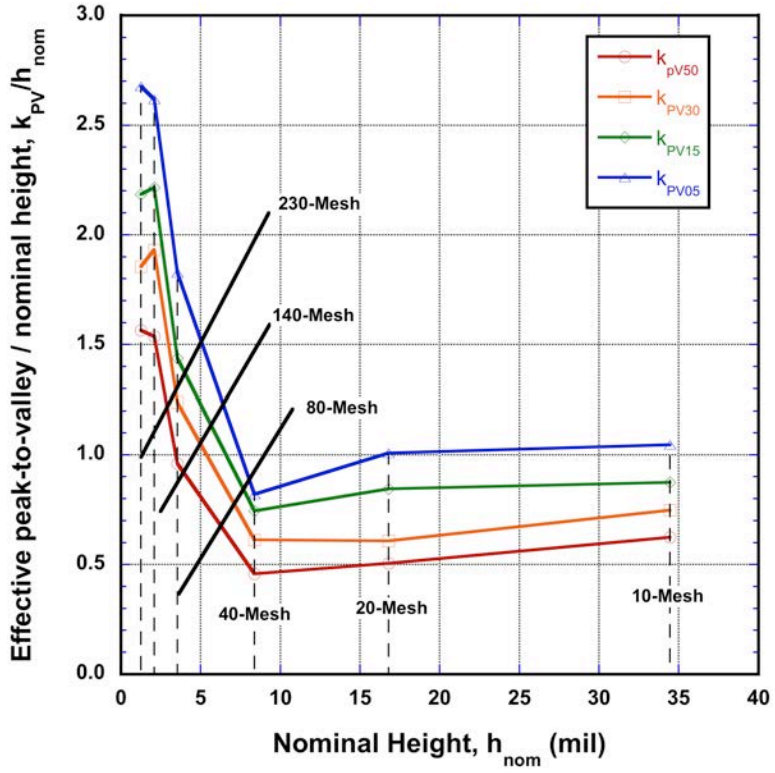

Figure 21. Comparison of effective and nominal roughness heights.

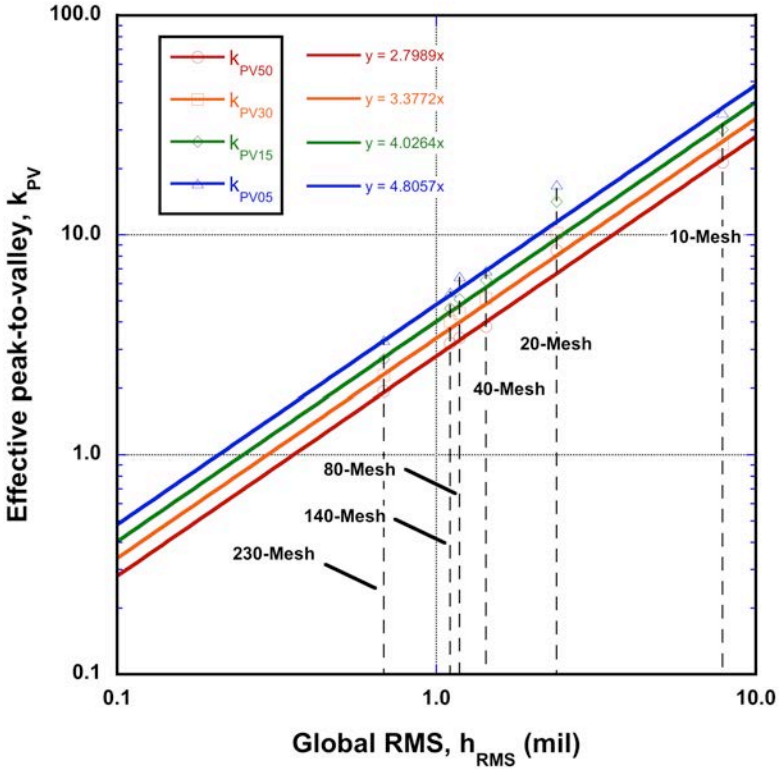

Figure 22. Relationship between effective roughness heights and measured RMS heights.

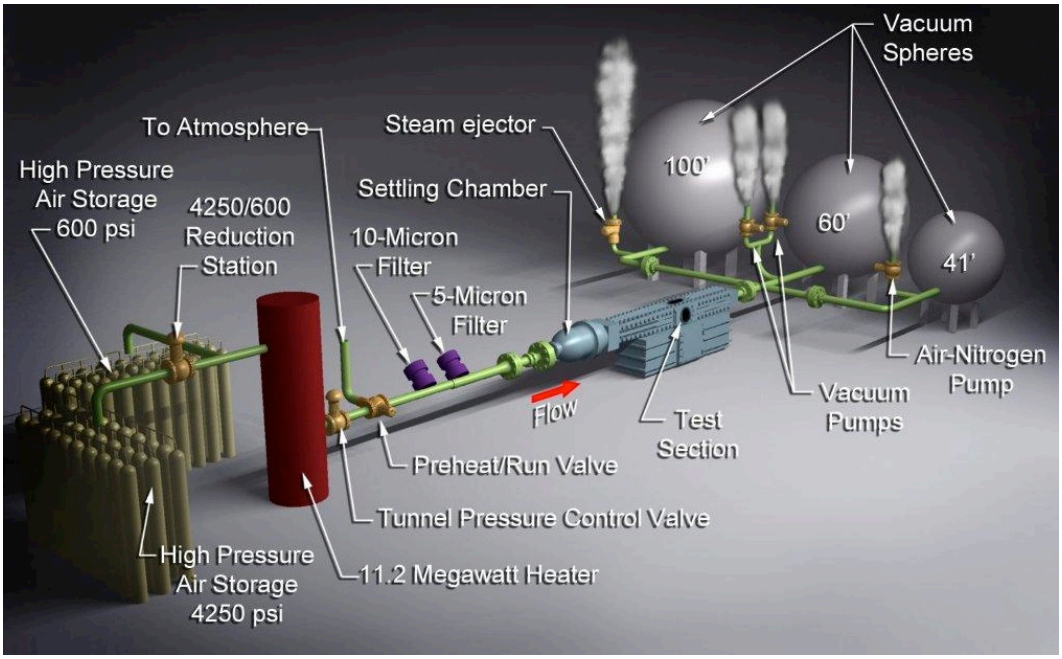

Figure 23. Schematic of Langley Research Center 20-Inch Mach 6 Air Tunnel.

Figure 24. Langley Research Center 20-Inch Mach 6 Air Tunnel test section with model.

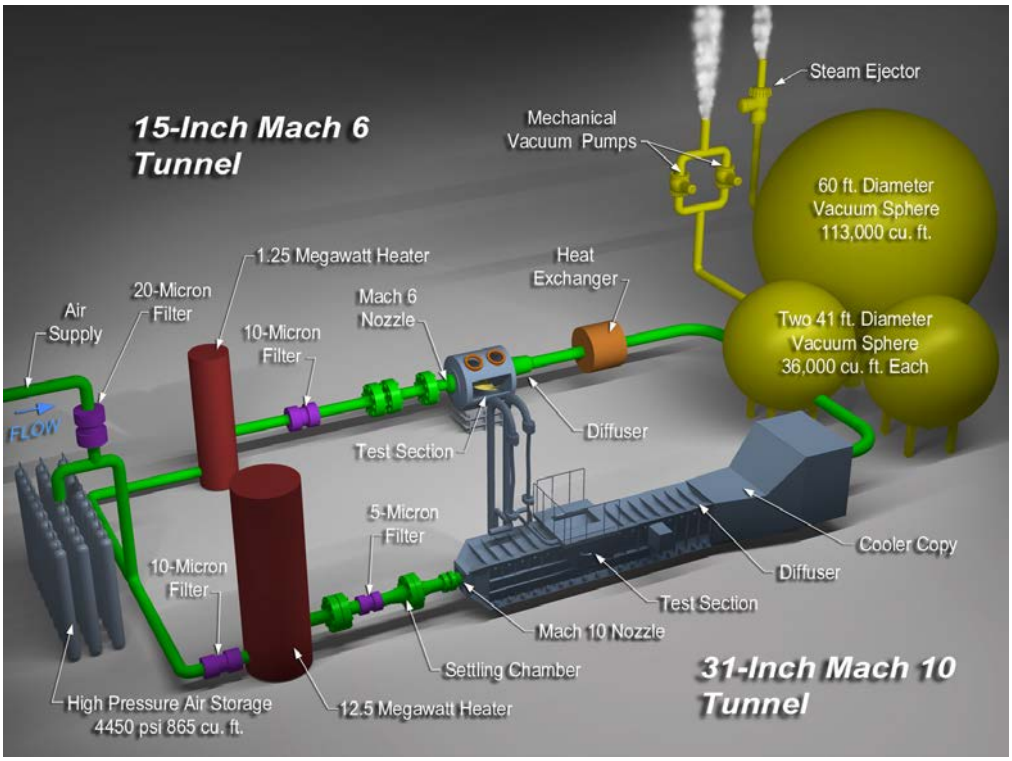

Figure 25. Schematic of Langley Research Center 31-Inch Mach 10 Air Tunnel.

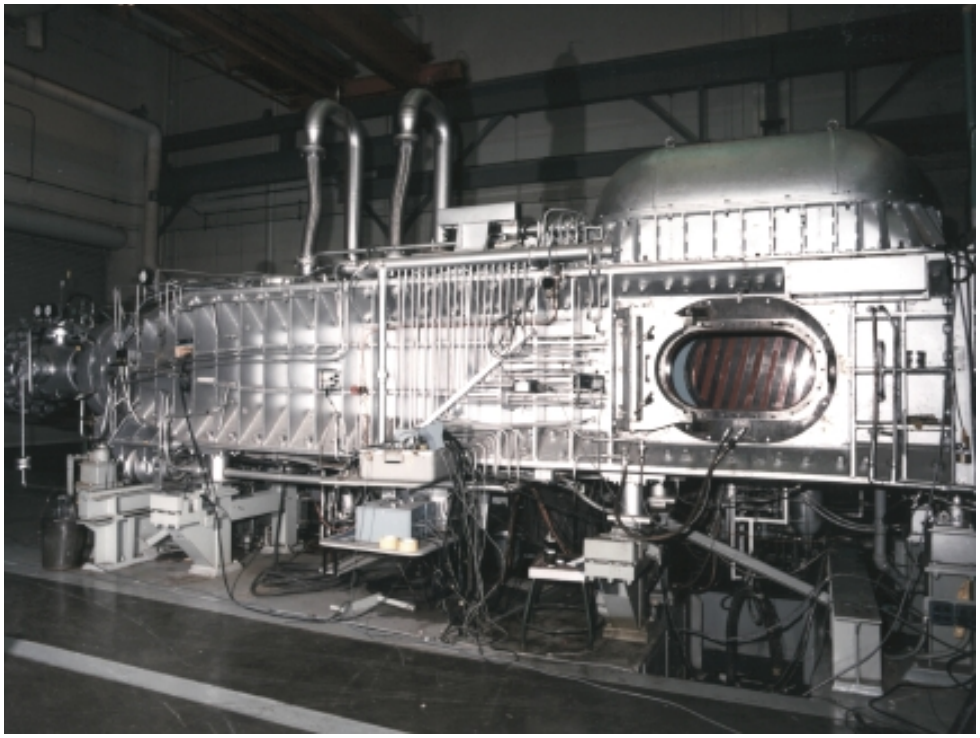

Figure 26. Langley Research Center 31-Inch Mach 10 Air Tunnel.

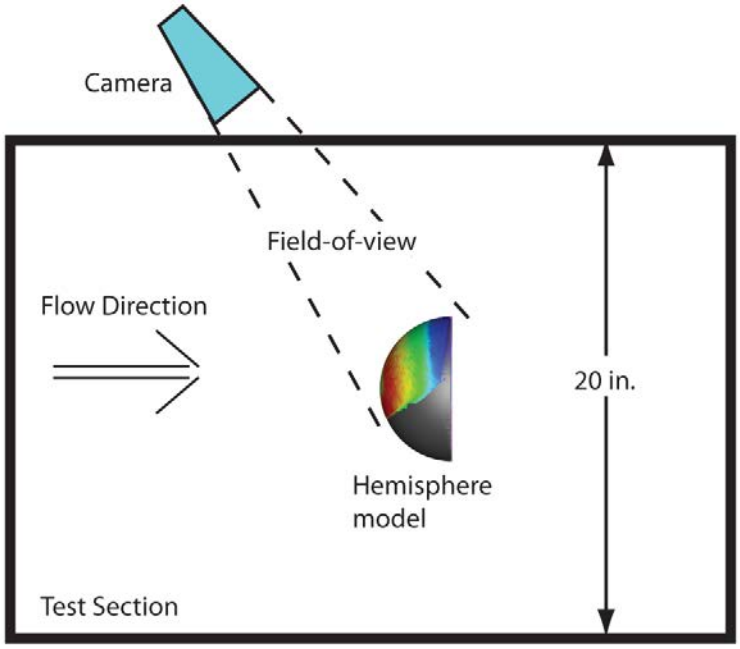

Figure 27. Illustration of camera field-of-view for hemisphere model in 20-Inch Mach 6 Air Tunnel.

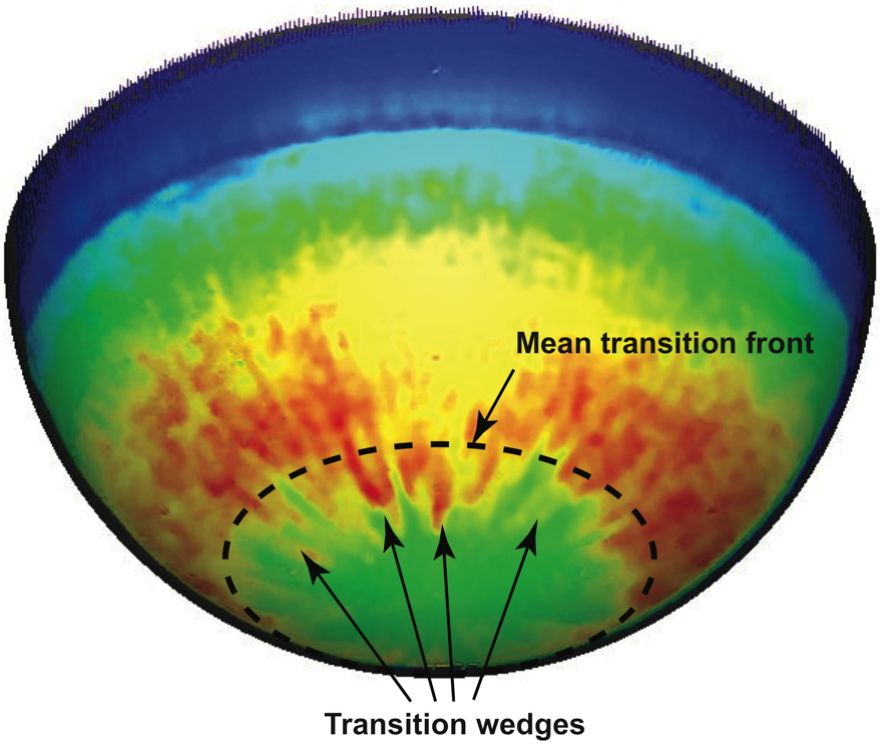

Figure 28. Comparison of irregular transition wedges vs. mean transition front.

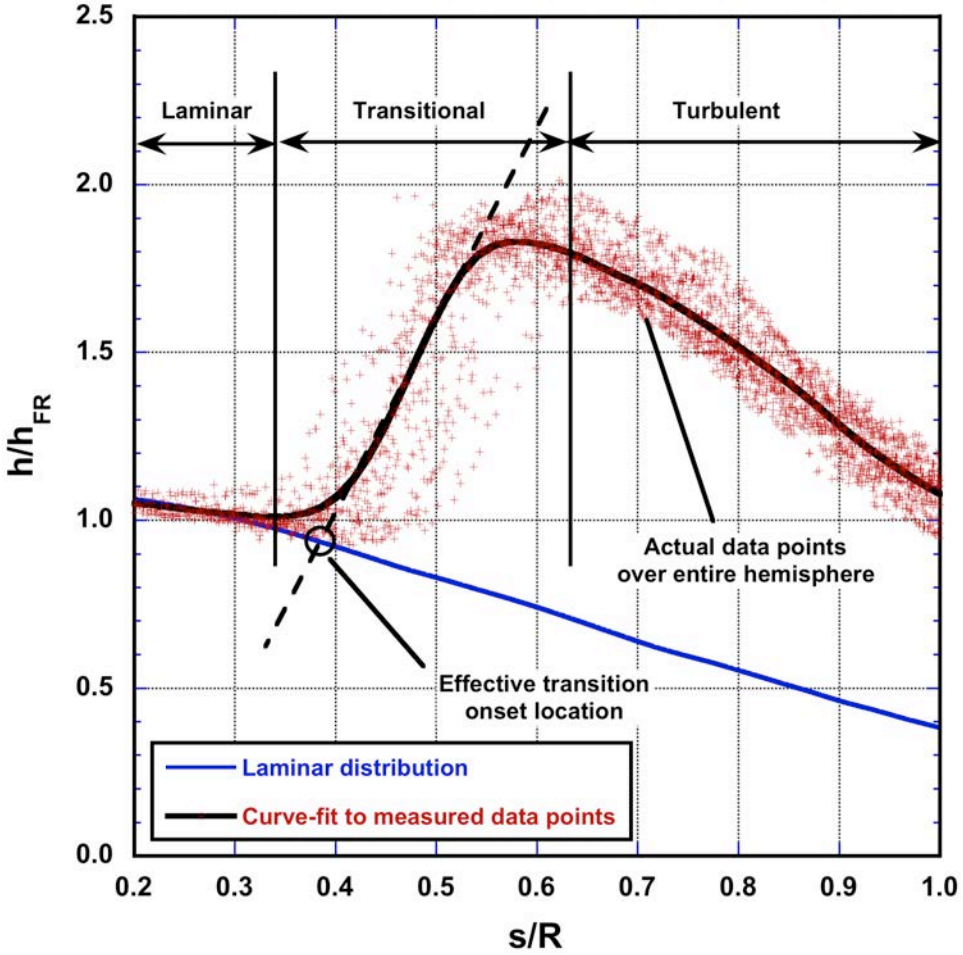

Figure 29. Tangent-slope-intercept method for determination of effect transition onset location.

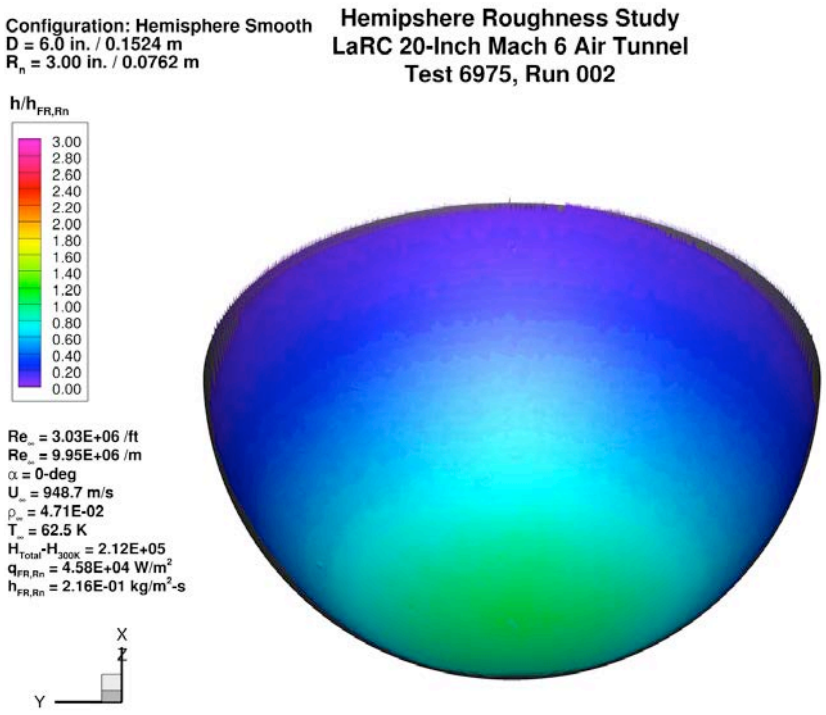

Figure 30. Test 6975, Run 02: Mach 6, $Re_\infty = 3.0\times10^6$/ft, smooth model, global heating image.

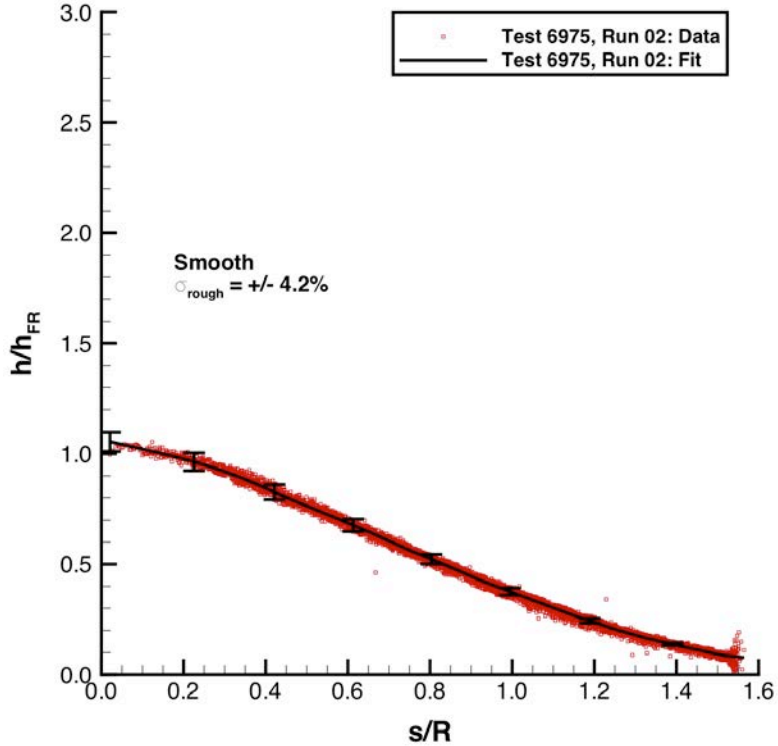

Figure 31. Test 6975, Run 02: Mach 6, $Re_\infty = 3.0\times10^6$/ft, smooth model, heating data and fit.

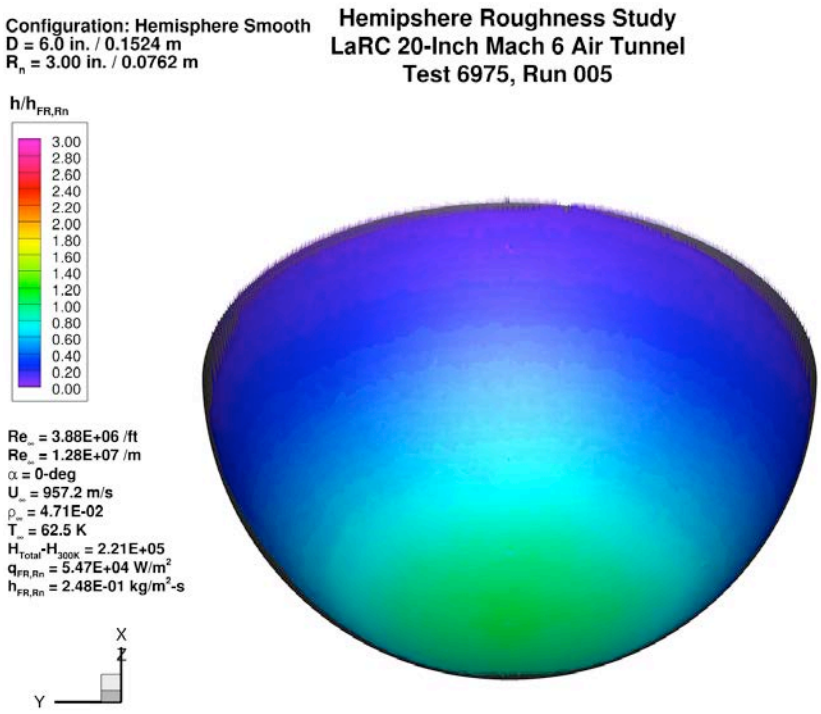

Figure 32. Test 6975, Run 05: Mach 6, $Re_\infty = 3.9\times10^6$/ft, smooth model, global heating image.

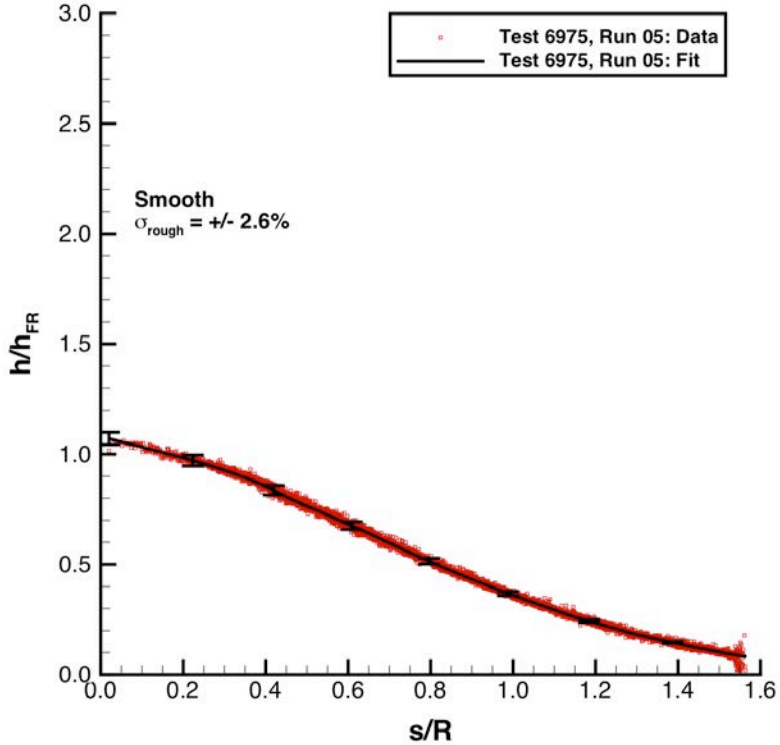

Figure 33. Test 6975, Run 05: Mach 6, $Re_\infty = 3.9\times10^6$/ft, smooth model, heating data and fit.

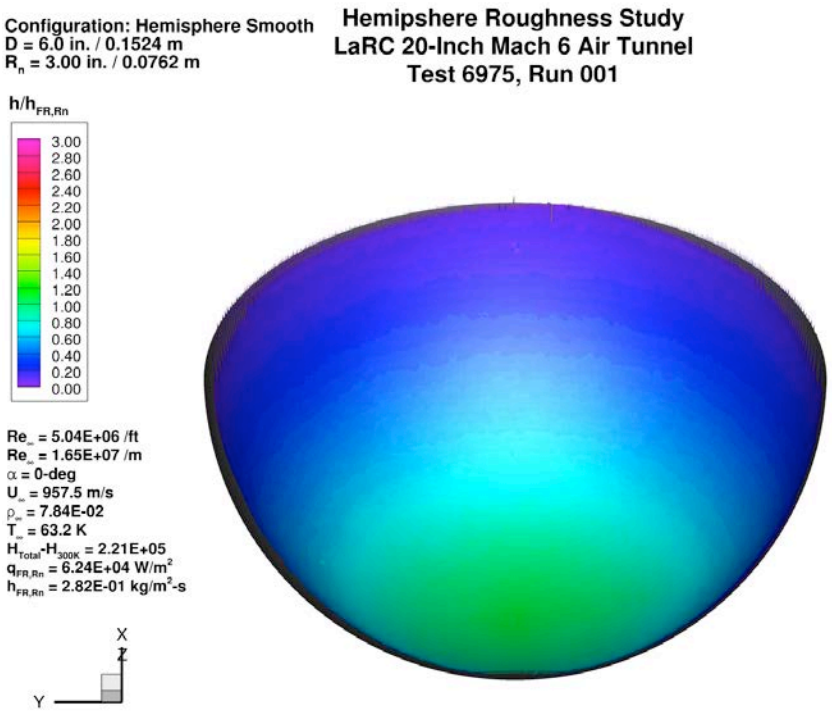

Figure 34. Test 6975, Run 01: Mach 6, $Re_\infty = 5.0\times10^6$/ft, smooth model, global heating image.

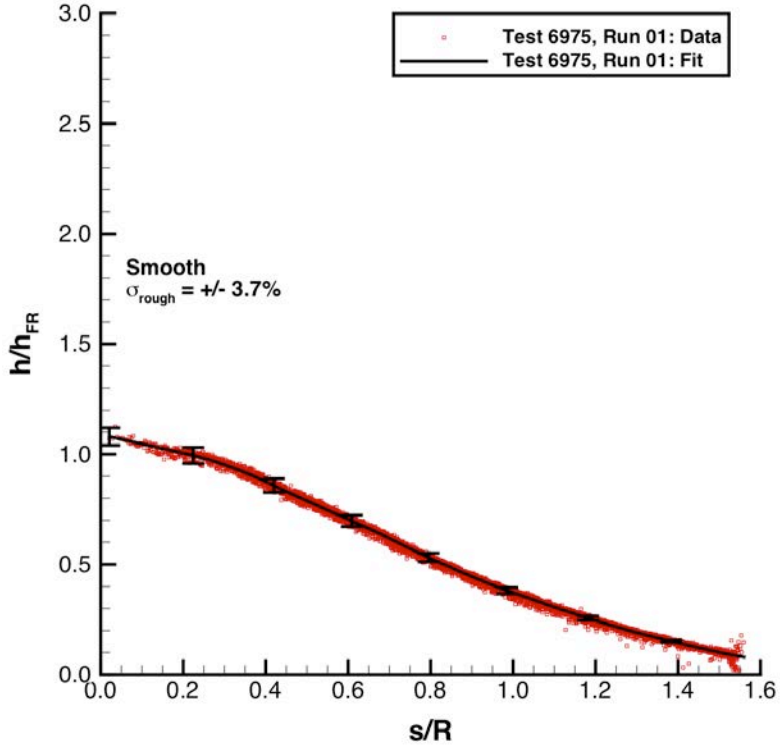

Figure 35. Test 6975, Run 01: Mach 6, $Re_\infty = 5.0\times10^6$/ft, smooth model, heating data and fit.

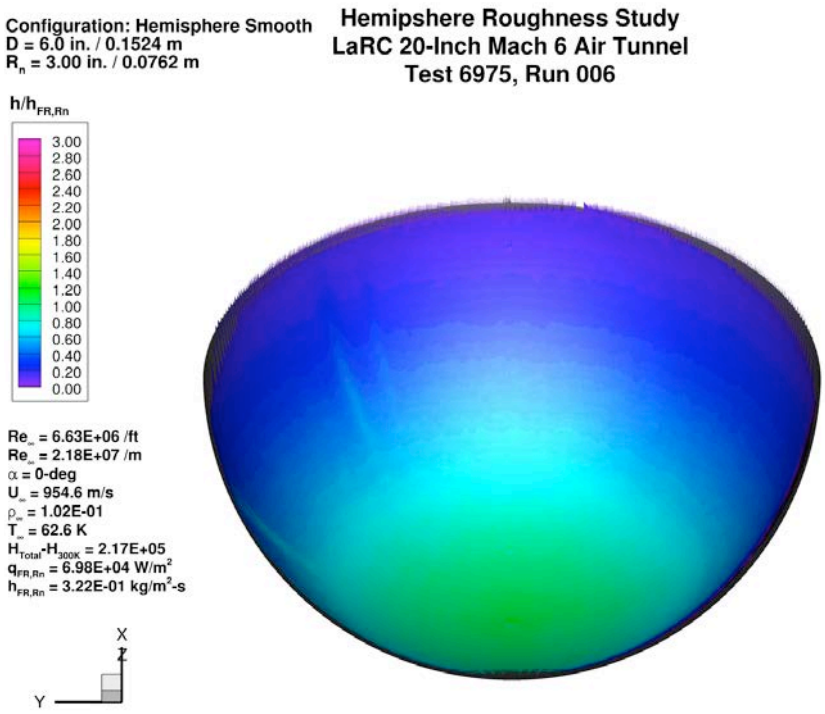

Figure 36. Test 6975, Run 06: Mach 6, $Re_\infty = 6.6\times10^6$/ft, smooth model, global heating image.

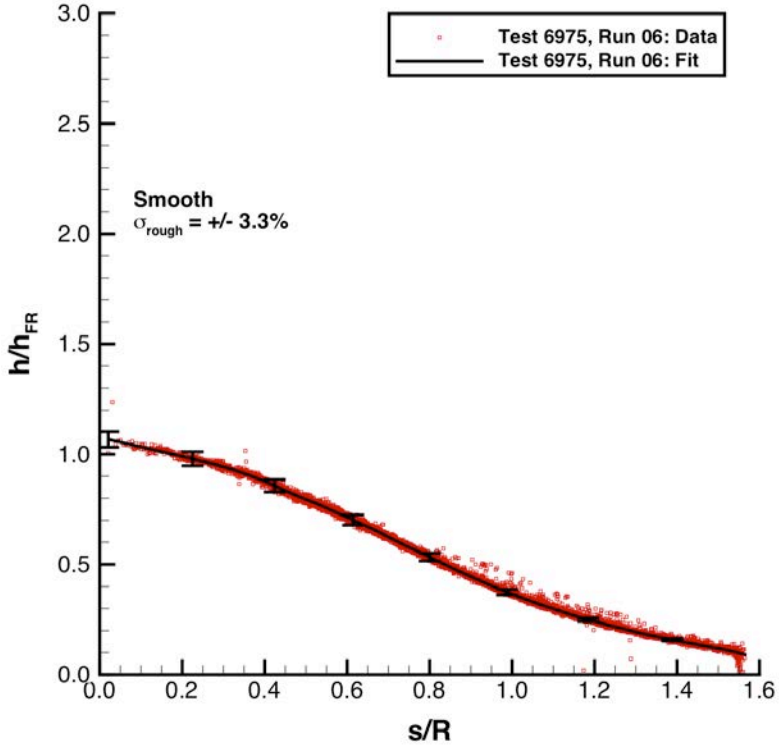

Figure 37. Test 6975, Run 06: Mach 6, $Re_\infty = 6.6\times10^6$/ft, smooth model, heating data and fit.

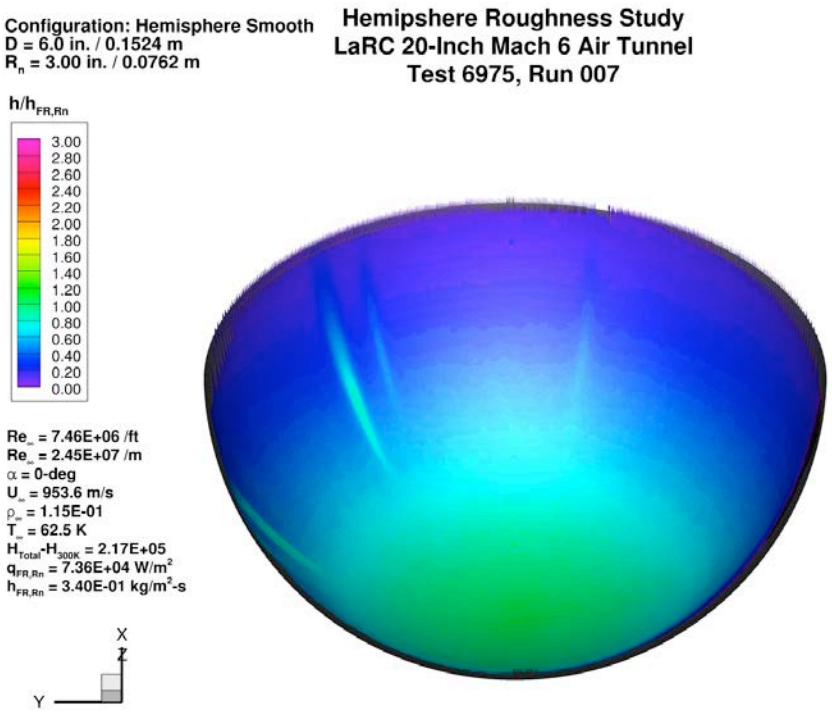

Figure 38. Test 6975, Run 07: Mach 6, $Re_\infty = 7.5\times10^6$/ft, smooth model, global heating image.

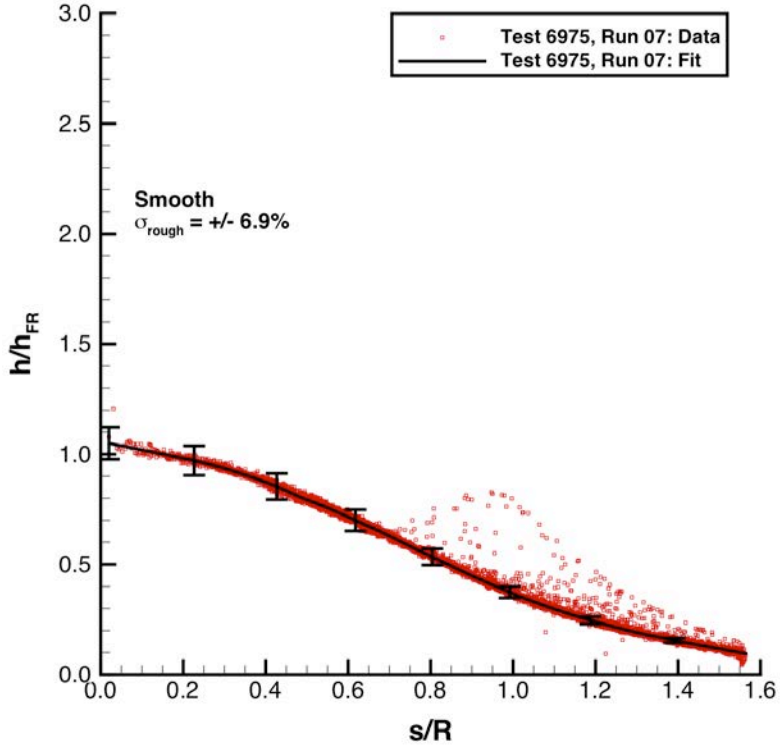

Figure 39. Test 6975, Run 07: Mach 6, $Re_\infty = 7.5\times10^6$/ft, smooth model, heating data and fit.

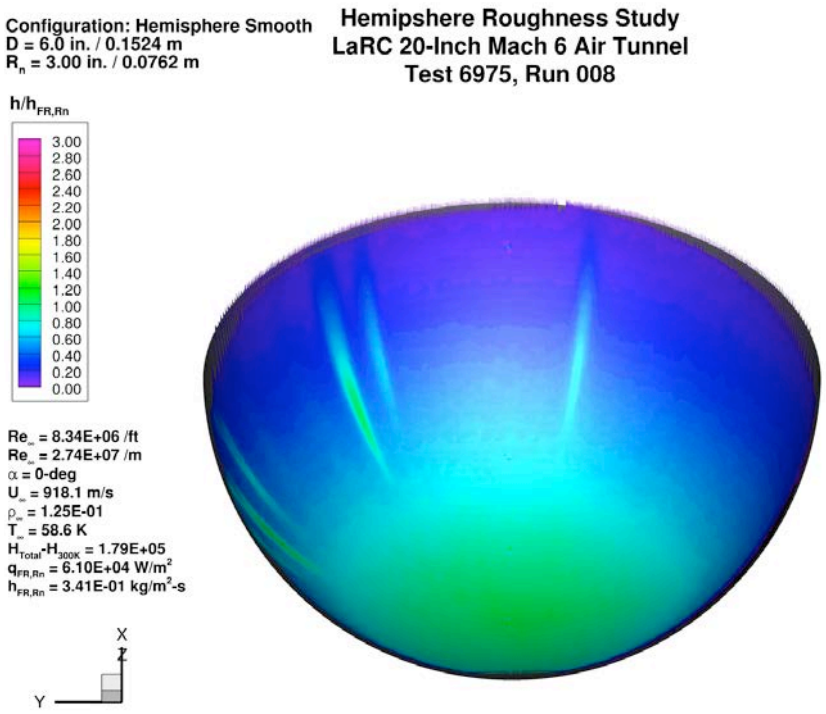

Figure 40. Test 6975, Run 08: Mach 6, $Re_\infty = 8.3\times10^6$/ft, smooth model, global heating image.

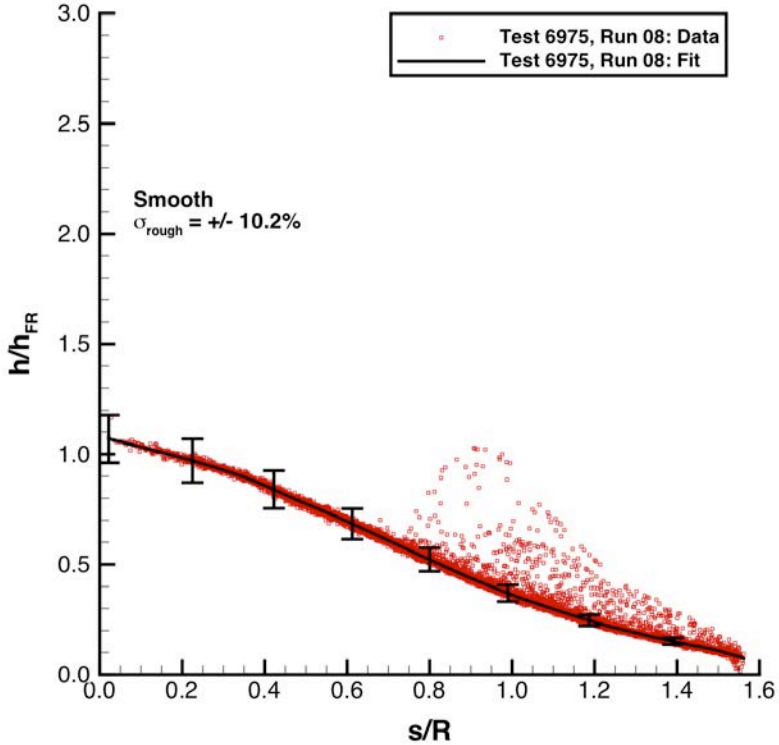

Figure 41. Test 6975, Run 08: Mach 6, $Re_\infty = 8.3\times10^6$/ft, smooth model, heating data and fit.

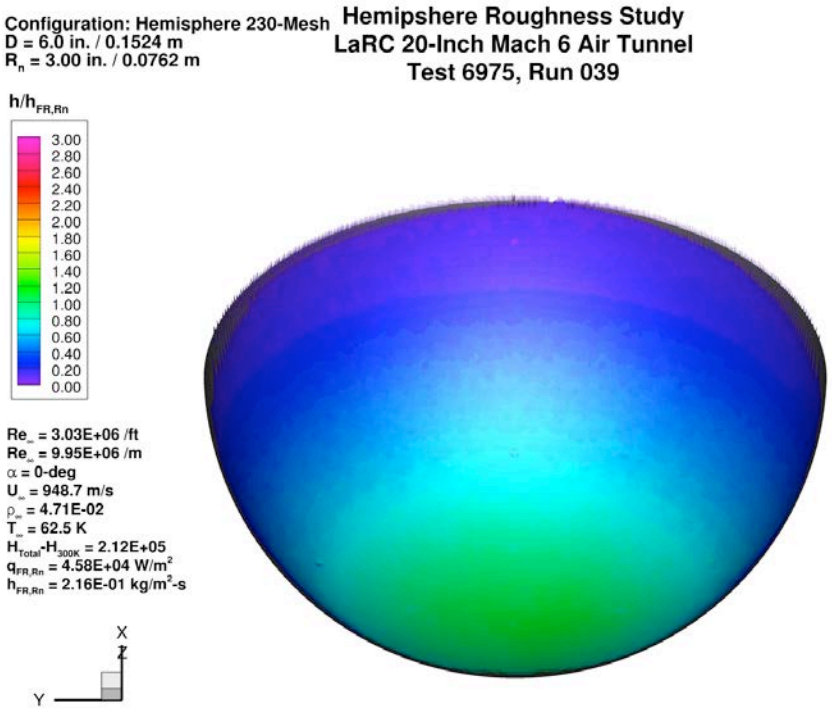

Figure 42. Test 6975, Run 39: Mach 6, $Re_\infty = 3.0\times10^6$/ft, 230-Mesh model, global heating image.

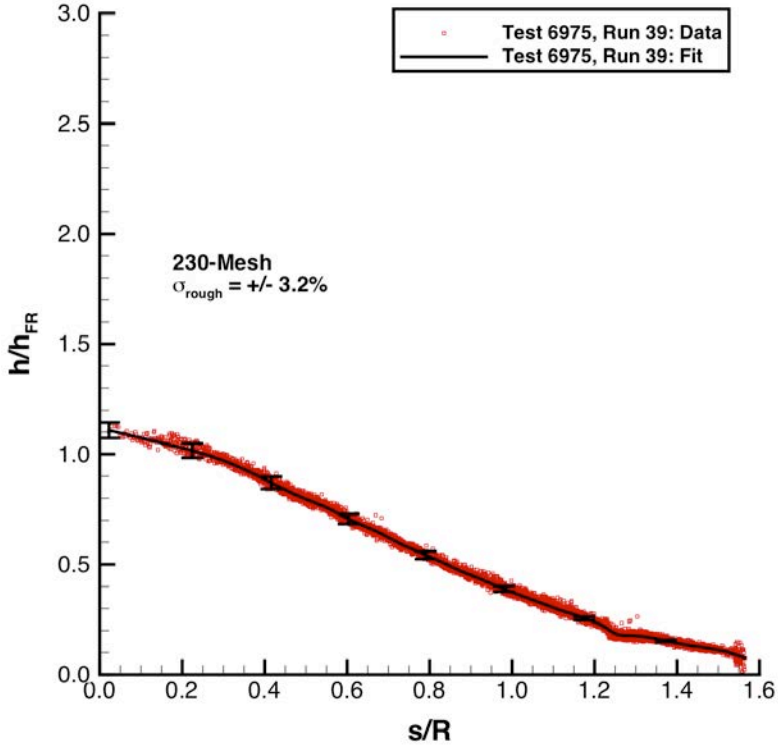

Figure 43. Test 6975, Run 39: Mach 6, $Re_\infty = 3.0\times10^6$/ft, 230-Mesh Model, heating data and fit.

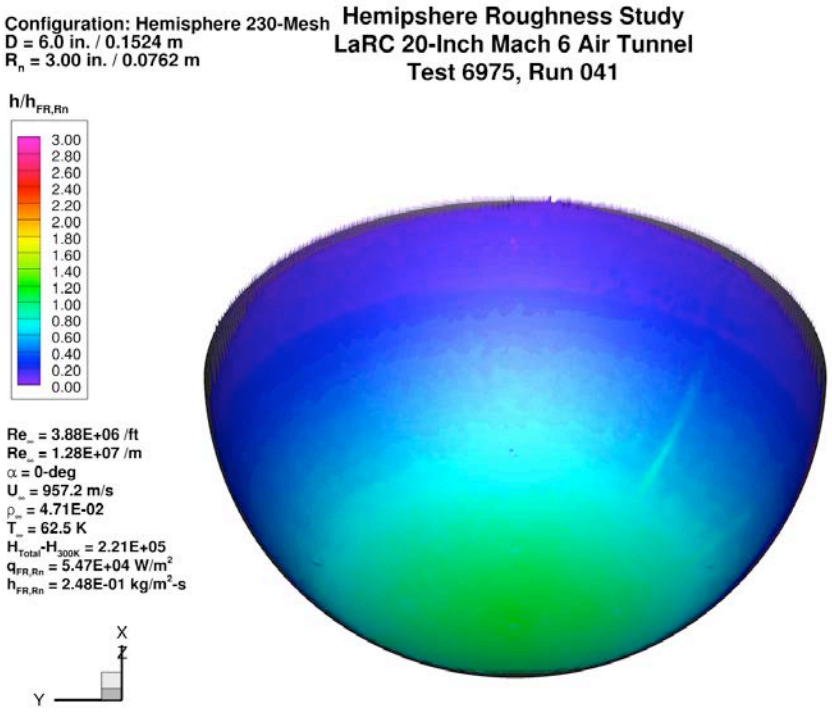

Figure 44. Test 6975, Run 41: Mach 6, $Re_\infty = 3.9\times10^6$/ft, 230-Mesh Model, global heating image..

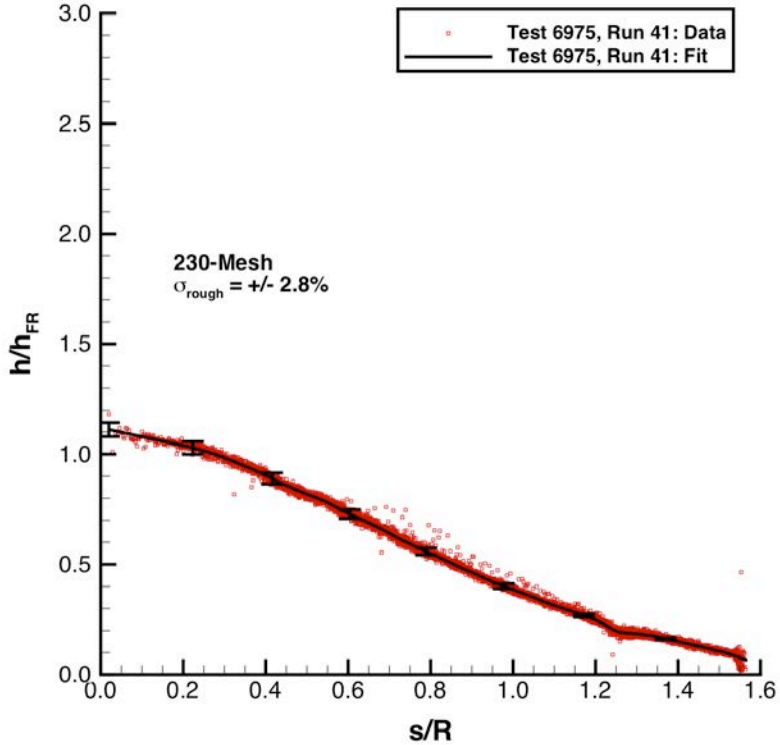

Figure 45. Test 6975, Run 41, Mach 6, $Re_\infty = 3.9\times10^6$/ft, 230-Mesh Model, heating data and fit.

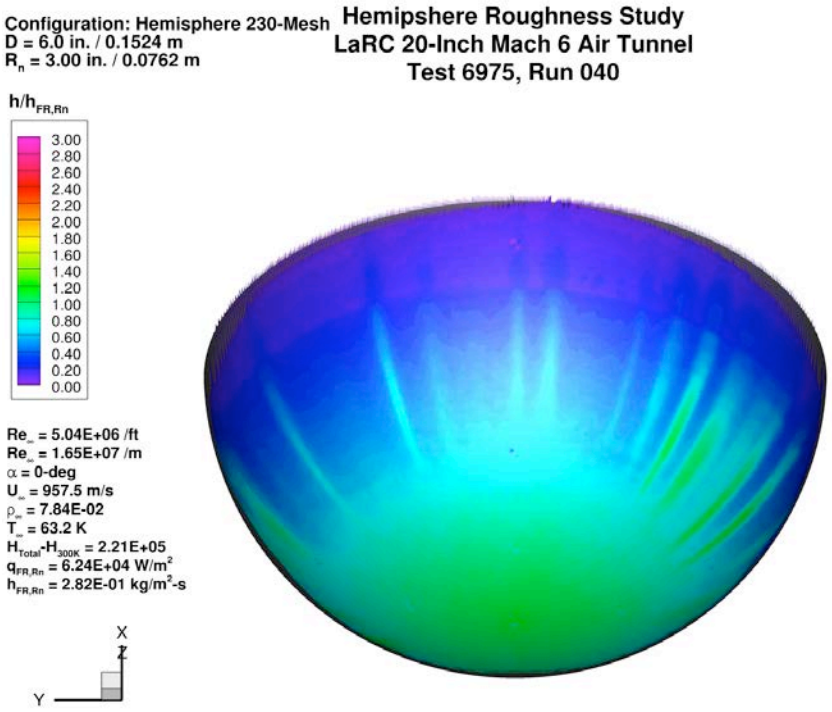

Figure 46. Test 6975, Run 40: Mach 6, $Re_\infty = 5.0\times10^6$/ft, 230-Mesh model, global heating image.

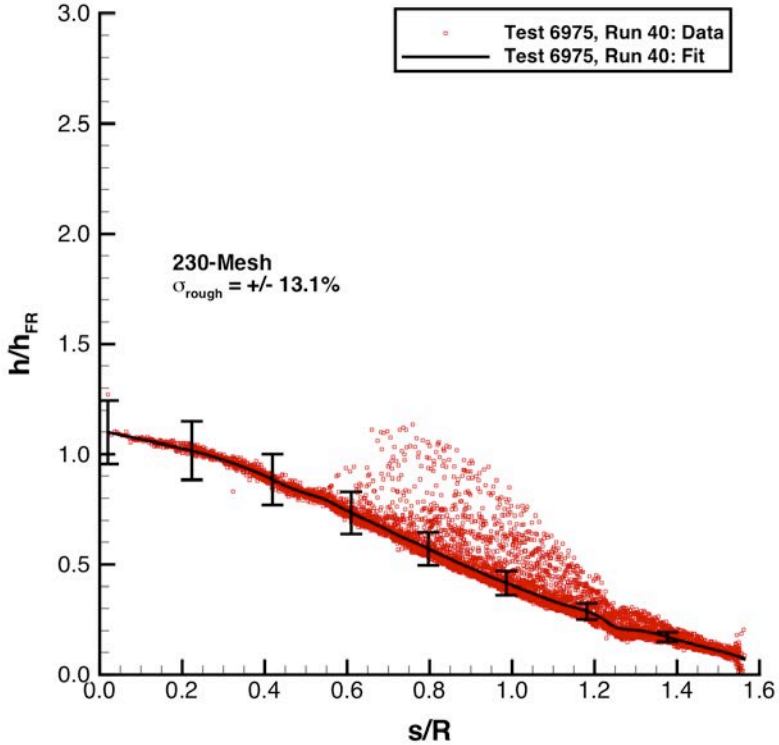

Figure 47. Test 6975, Run 40: Mach 6, $Re_\infty = 5.0\times10^6$/ft, 230-Mesh model, heating data and fit.

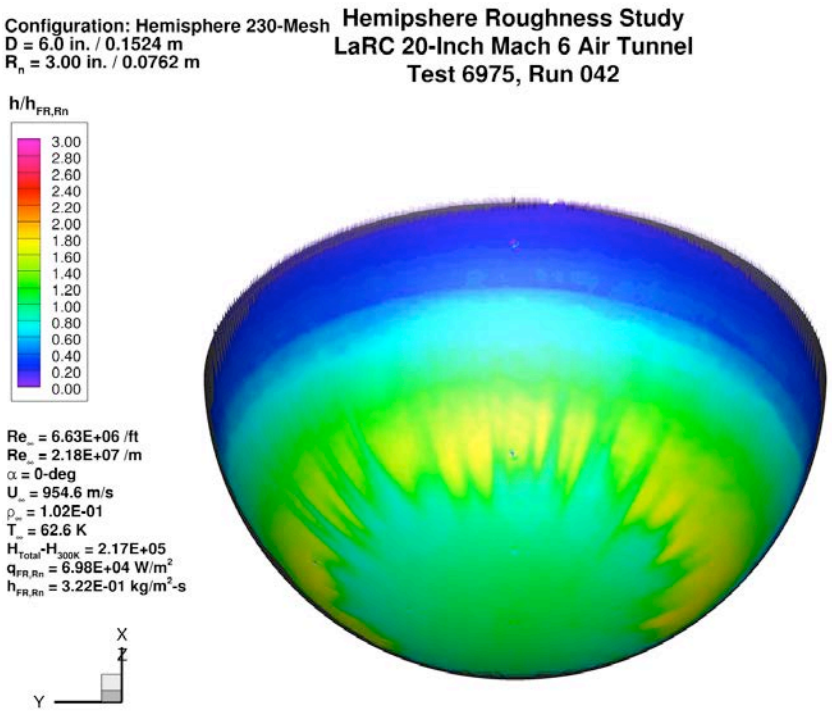

Figure 48. Test 6975, Run 42: Mach 6, $Re_\infty = 6.6\times10^6$/ft, 230-Mesh model, global heating image.

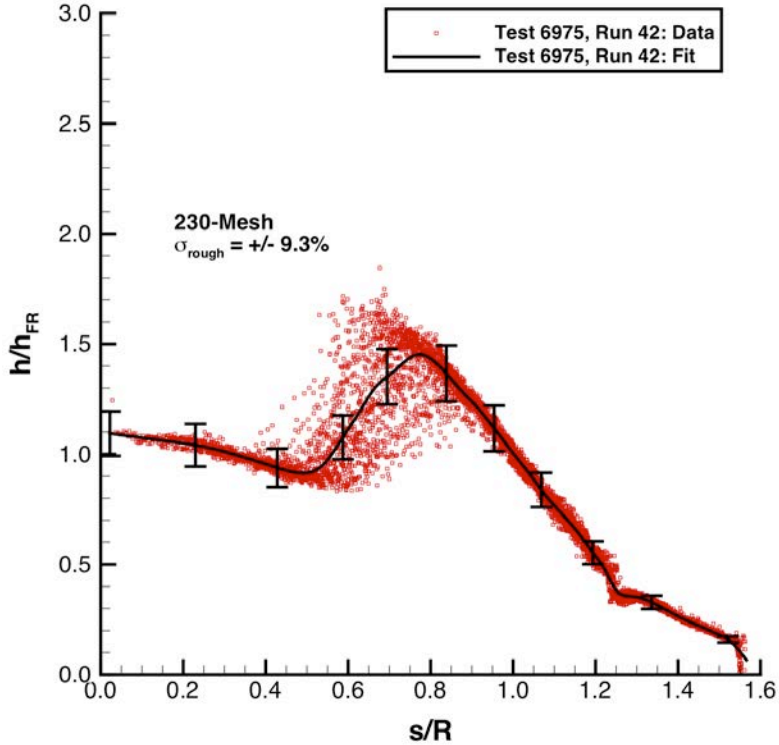

Figure 49. Test 6975, Run 42: Mach 6, $Re_\infty = 6.6\times10^6$/ft, 230-Mesh model, heating data and fit.

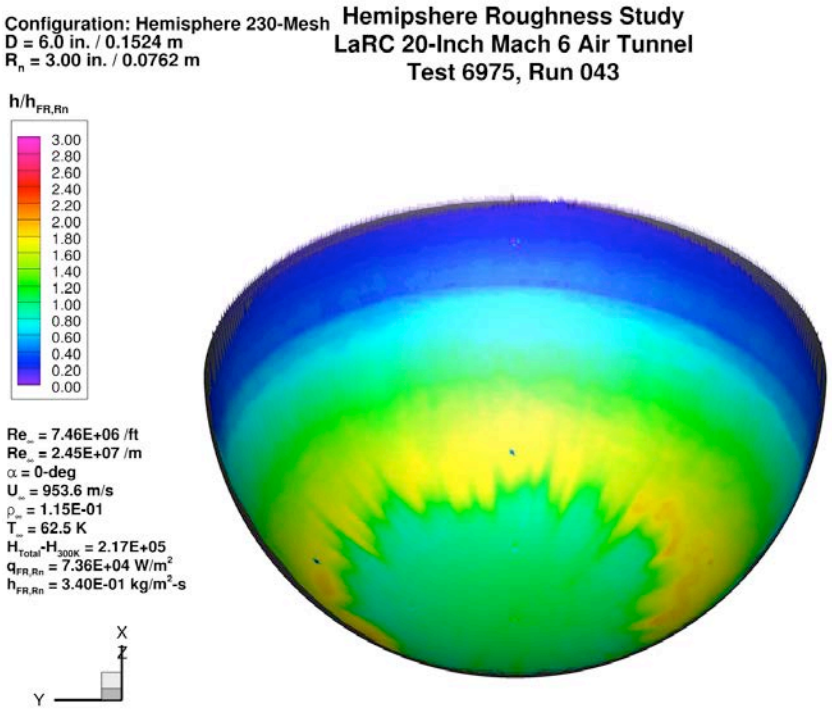

Figure 50. Test 6975, Run 43: Mach 6, $Re_\infty = 7.5\times10^6$/ft, 230-Mesh model, global heating image.

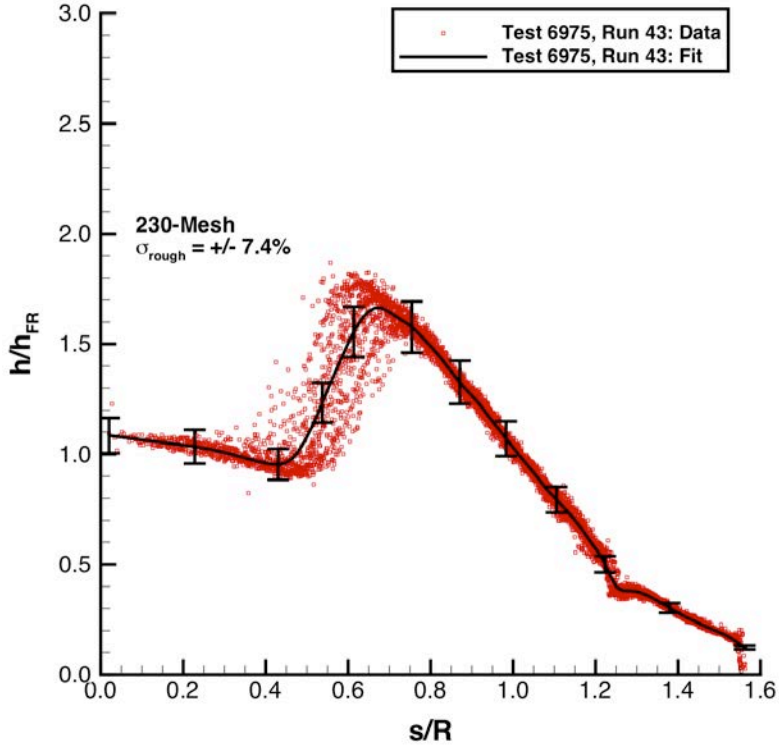

Figure 51. Test 6975, Run 43: Mach 6, $Re_\infty = 7.5\times10^6$/ft, 230-Mesh model, heating data and fit.

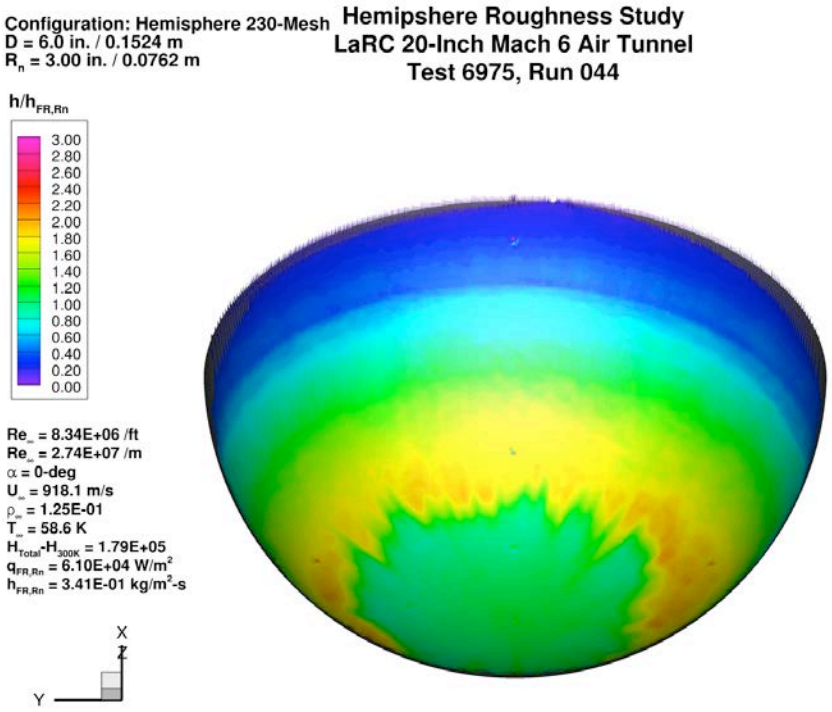

Figure 52. Test 6975, Run 44: Mach 6, $Re_\infty = 8.3\times10^6$/ft, 230-Mesh model, global heating image.

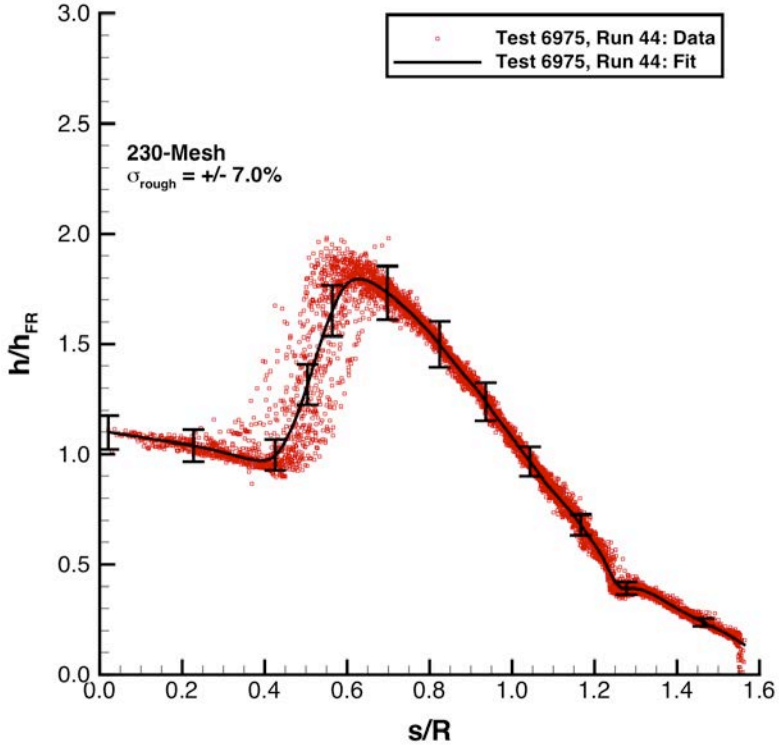

Figure 53. Test 6975, Run 44: Mach 6, $Re_\infty = 8.3\times10^6$/ft, 230-Mesh model, heating data and fit.

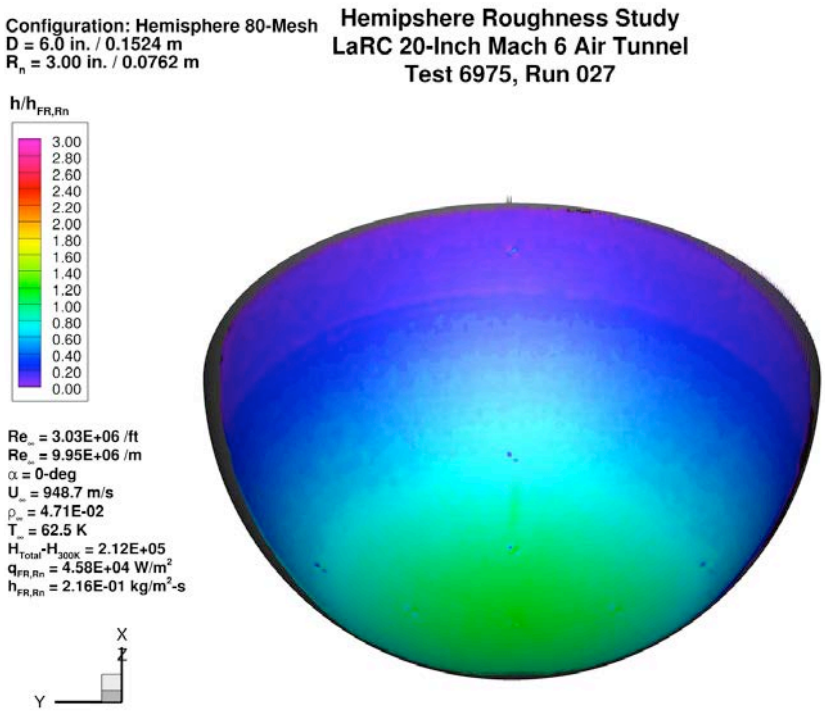

Figure 54. Test 6975, Run 27: Mach 6, $Re_\infty = 3.0\times10^6$/ft, 140-Mesh model, global heating image.

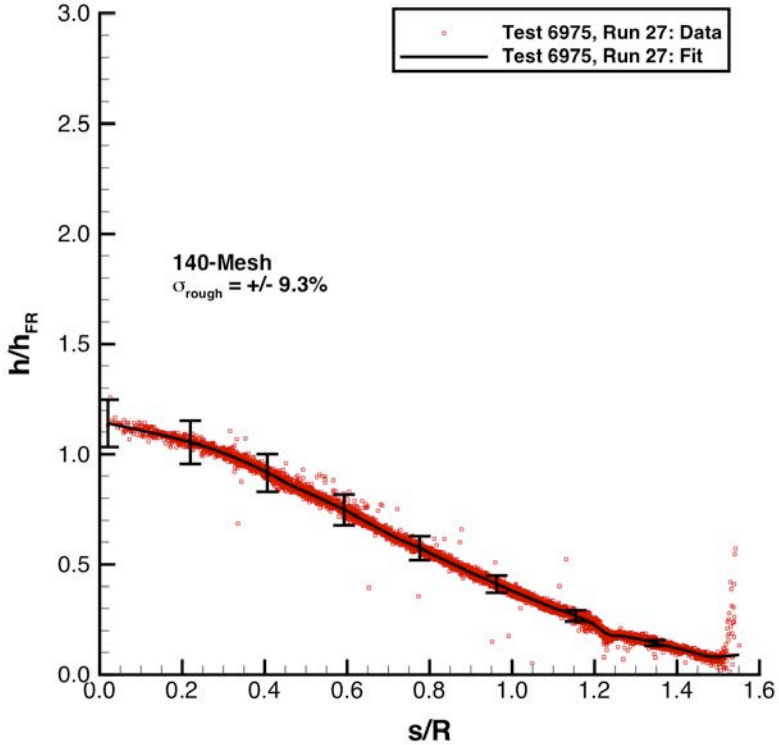

Figure 55. Test 6975, Run 27: Mach 6, $Re_\infty = 3.0\times10^6$/ft, 140-Mesh model, heating data and fit.

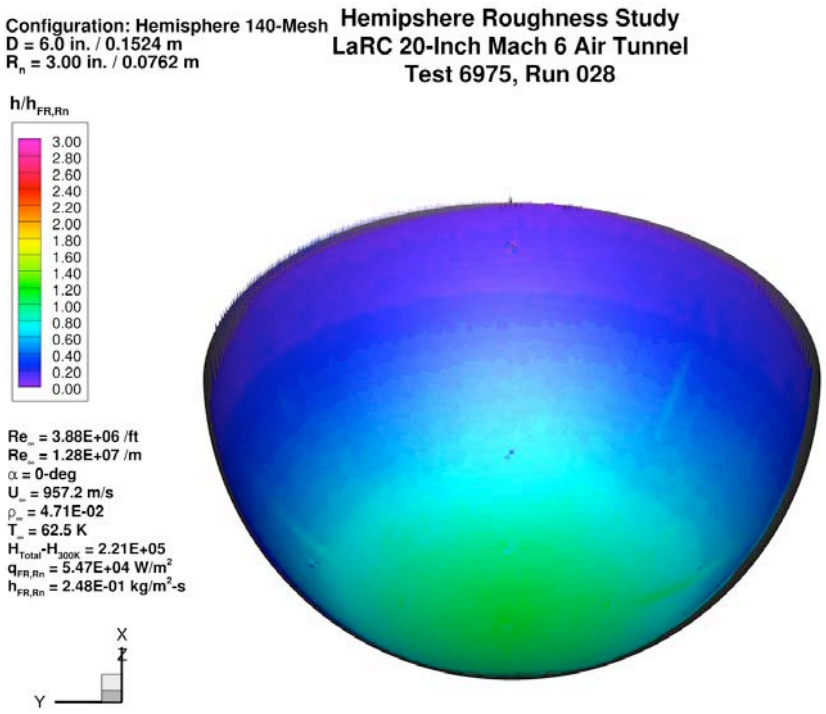

Figure 56. Test 6975, Run 28: Mach 6, $Re_\infty = 3.9\times10^6$/ft, 140-Mesh model, global heating image.

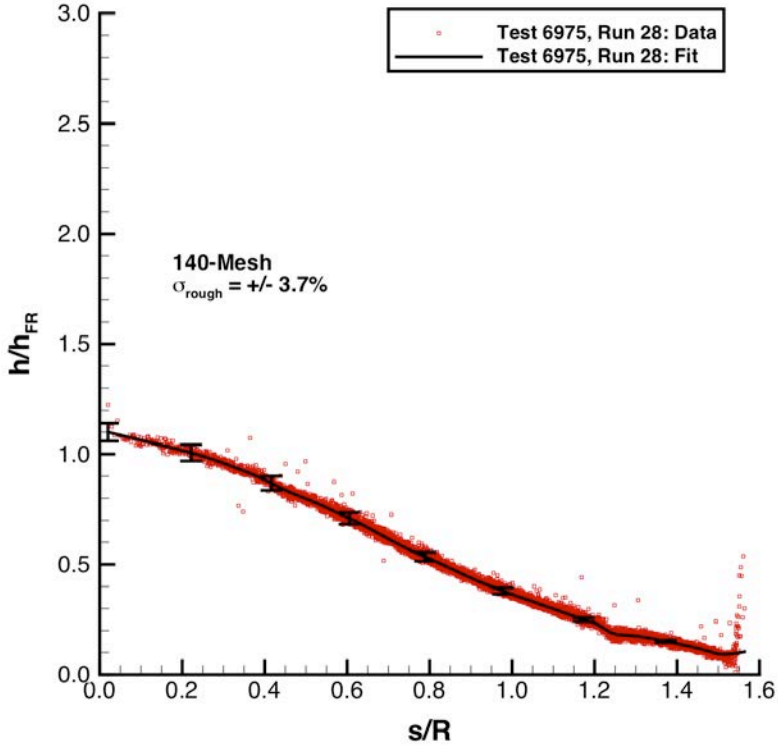

Figure 57. Test 6975, Run 28: Mach 6, $Re_\infty = 3.9\times10^6$/ft, 140-Mesh model, heating data and fit.

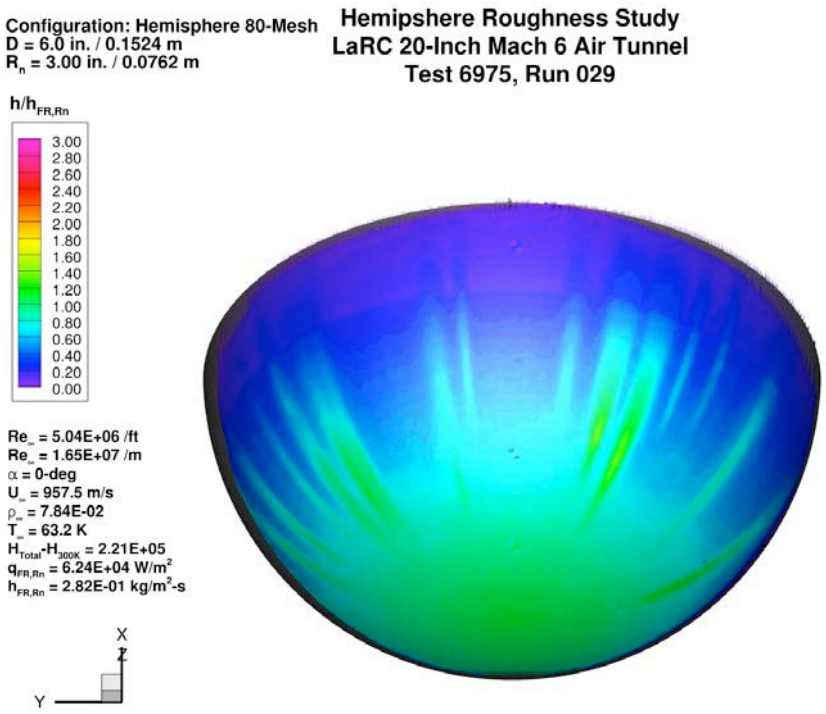

Figure 58. Test 6975, Run 29: Mach 6, $Re_\infty = 5.0\times10^6$/ft, 140-Mesh model, global heating image.

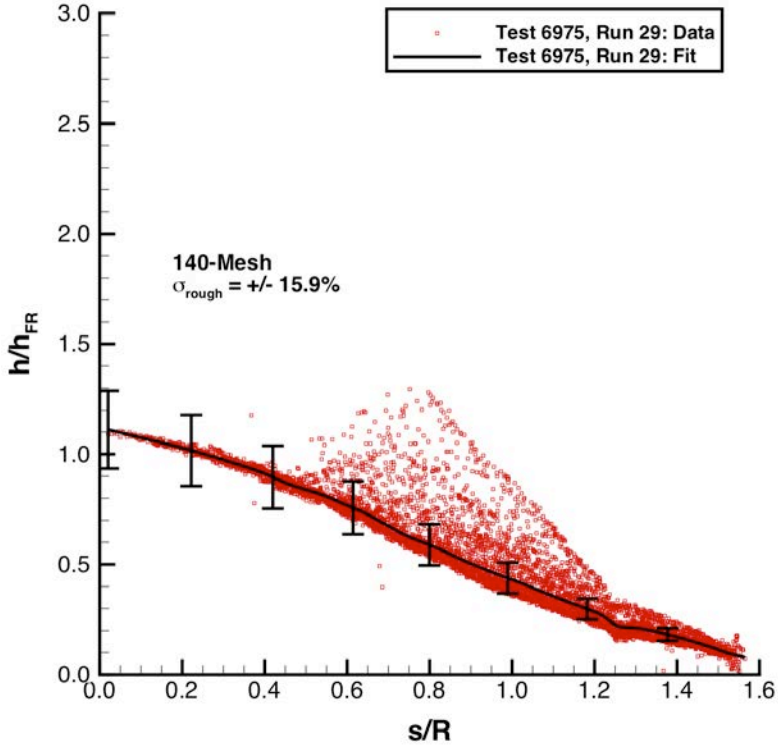

Figure 59. Test 6975, Run 29: Mach 6, $Re_\infty = 5.0\times10^6$/ft, 140-Mesh model, heating data and fit.

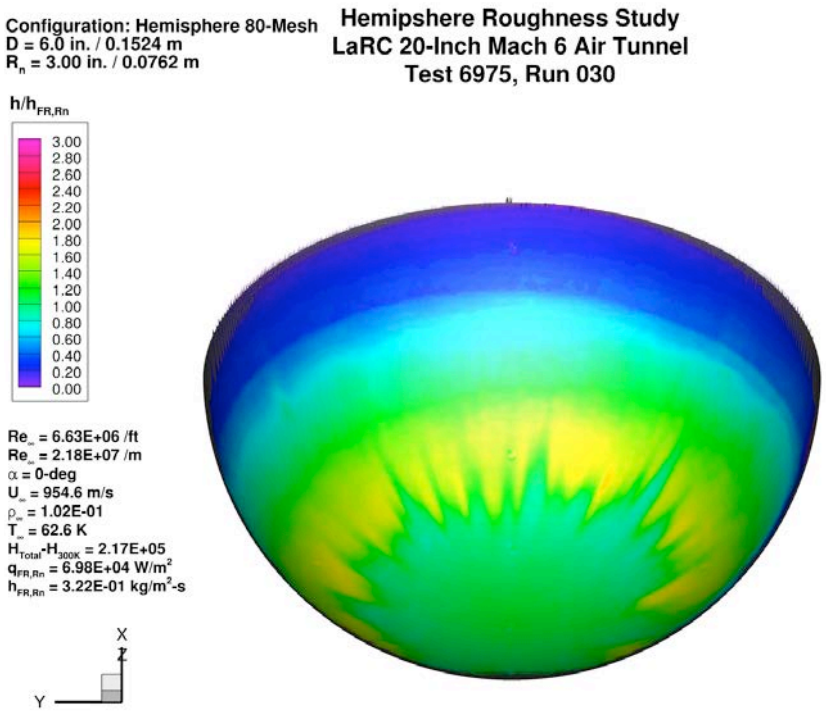

Figure 60. Test 6975, Run 30: Mach 6, $Re_\infty = 6.6\times10^6$/ft, 140-Mesh model, global heating image.

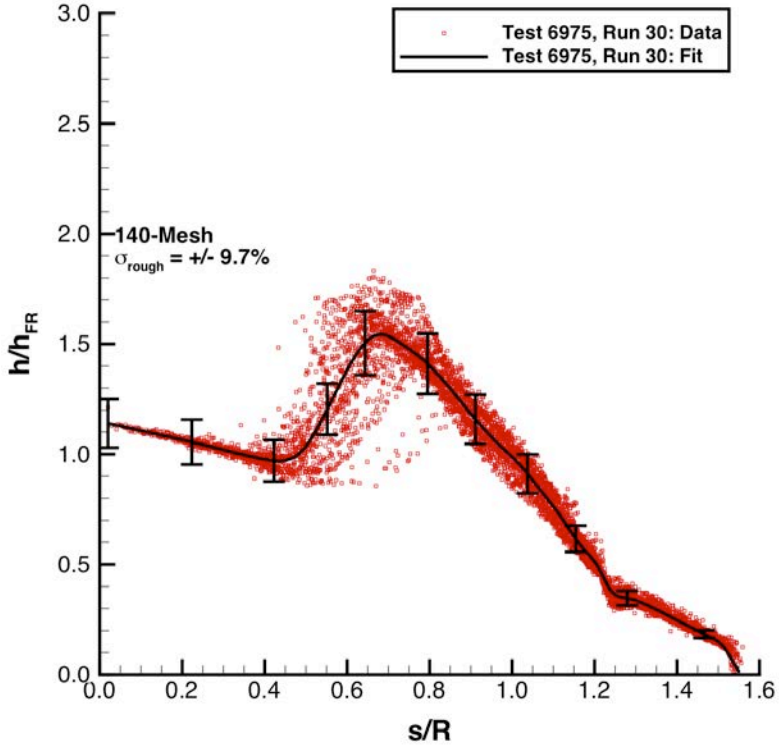

Figure 61. Test 6975, Run 30: Mach 6, $Re_\infty = 6.6\times10^6$/ft, 140-Mesh model, heating data and fit.

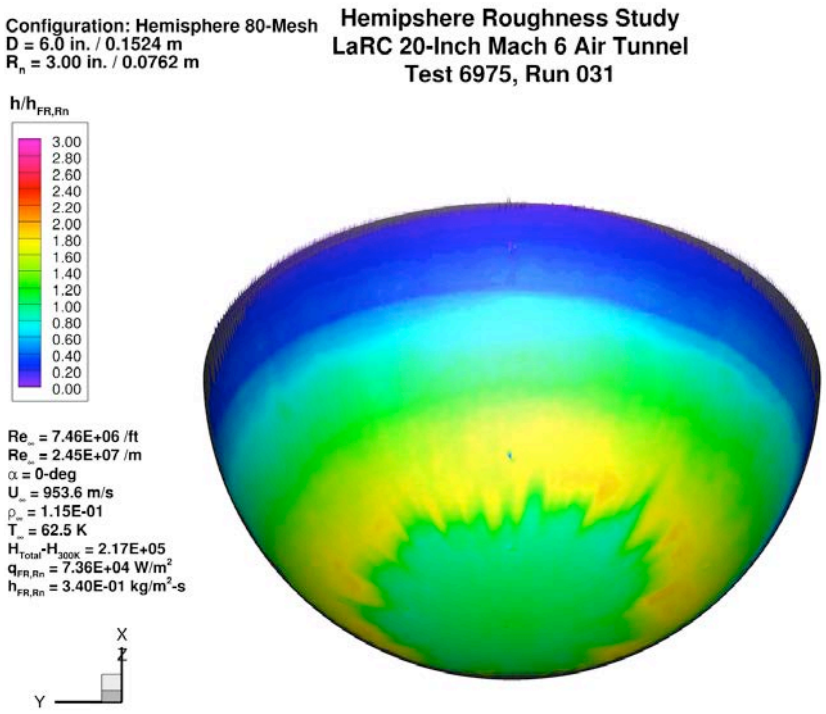

Figure 62. Test 6975, Run 31: Mach 6, $Re_\infty = 7.5\times10^6$/ft, 140-Mesh model, global heating image.

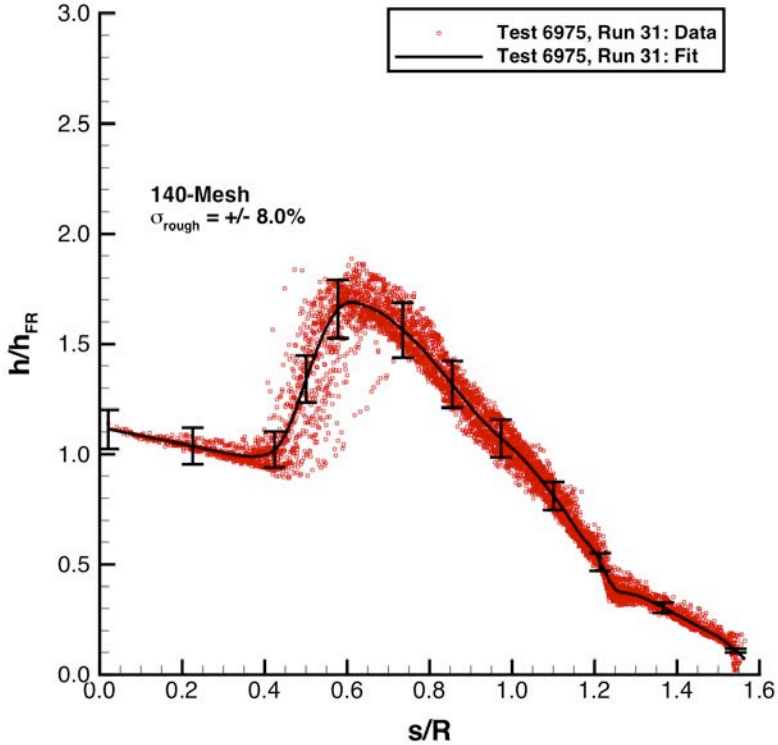

Figure 63. Test 6975, Run 31: Mach 6, $Re_\infty = 7.5\times10^6$/ft, 140-Mesh model, heating data and fit.

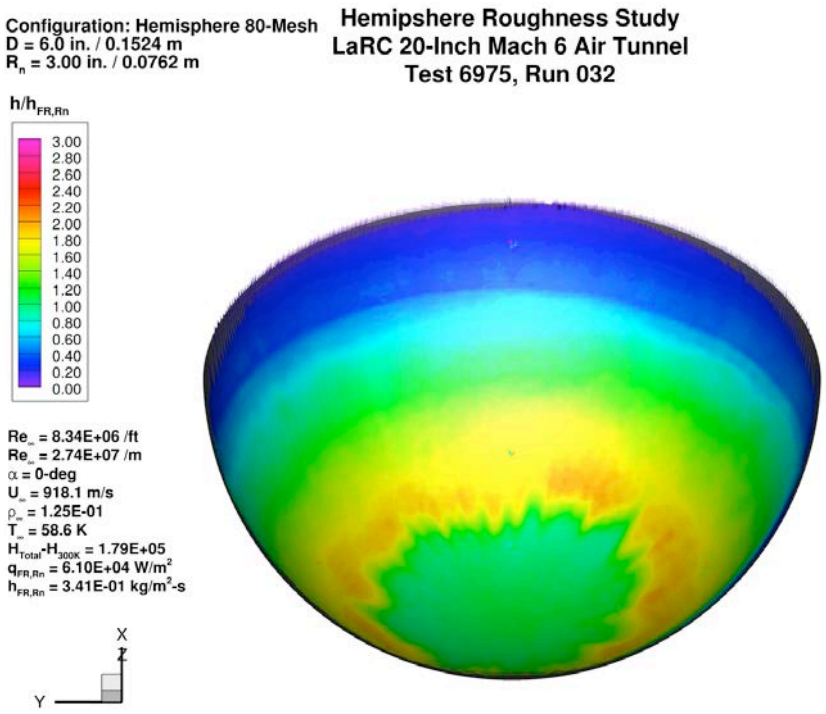

Figure 64. Test 6975, Run 32: Mach 6, $Re_\infty = 8.3\times10^6$/ft, 140-Mesh model, global heating image.

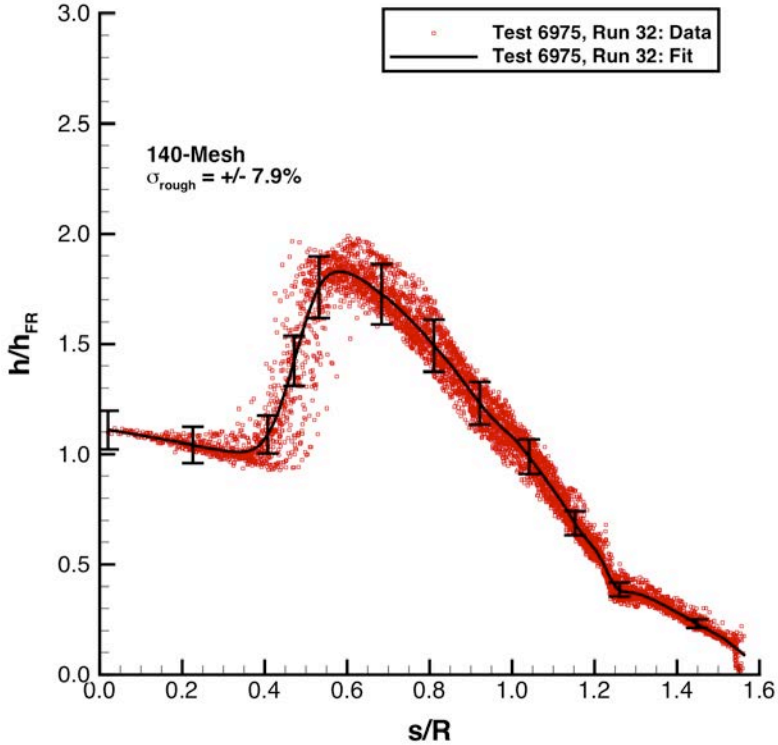

Figure 65. Test 6975, Run 32: Mach 6, $Re_\infty = 8.3\times10^6$/ft, 140-Mesh model, heating data and fit.

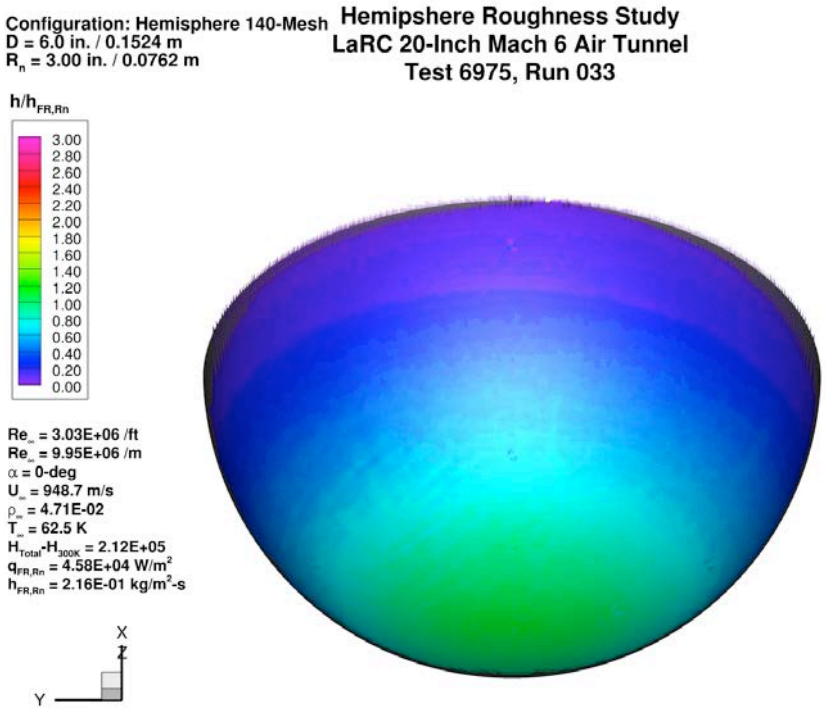

Figure 66. Test 6975, Run 33: Mach 6, $Re_\infty = 3.0\times10^6$/ft, 80-Mesh model, global heating image.

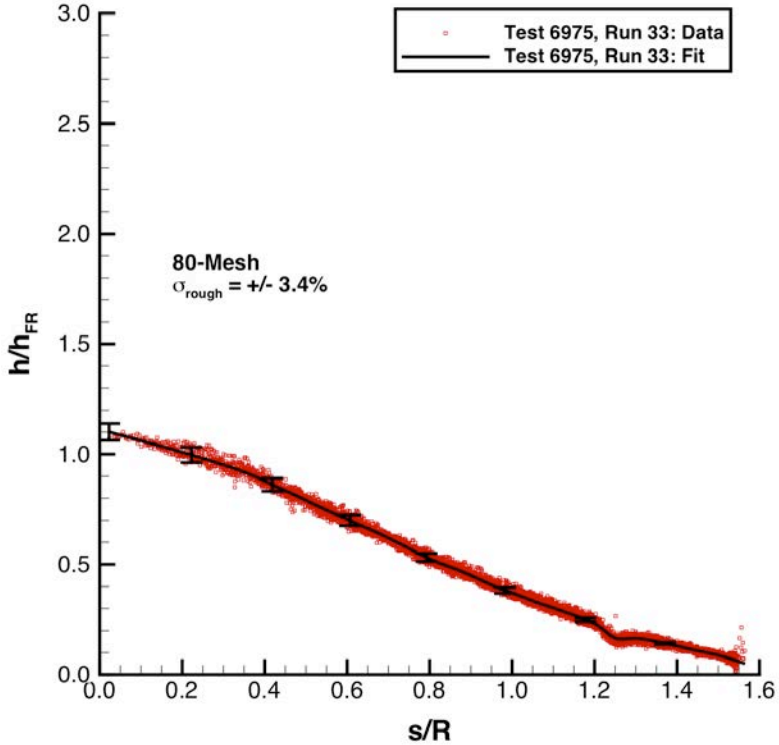

Figure 67. Test 6975, Run 33: Mach 6, $Re_\infty = 3.0\times10^6$/ft, 80-Mesh model, heating data and fit.

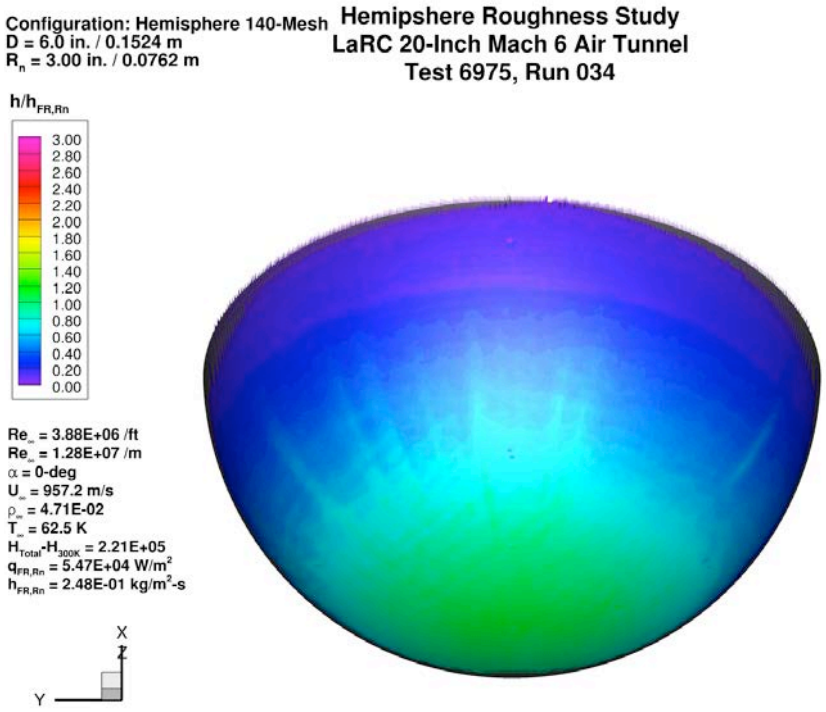

Figure 68. Test 6975, Run 34: Mach 6, $Re_\infty = 3.9\times10^6$/ft, 80-Mesh model, global heating image.

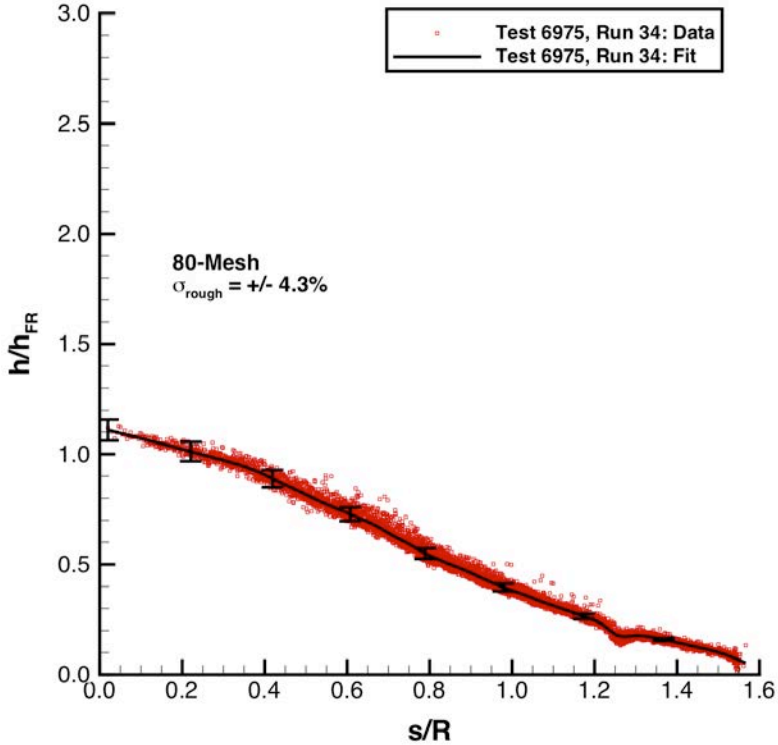

Figure 69. Test 6975, Run 34: Mach 6, $Re_\infty = 3.9\times10^6$/ft, 80-Mesh model, heating data and fit.

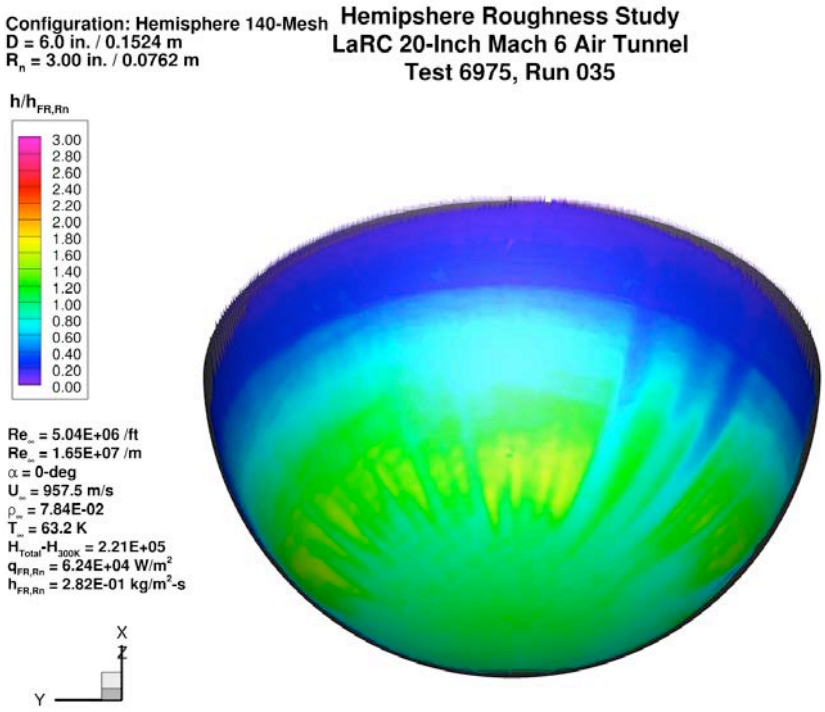

Figure 70. Test 6975, Run 35: Mach 6, $Re_\infty = 5.0\times10^6$/ft, 80-Mesh model, global heating image.

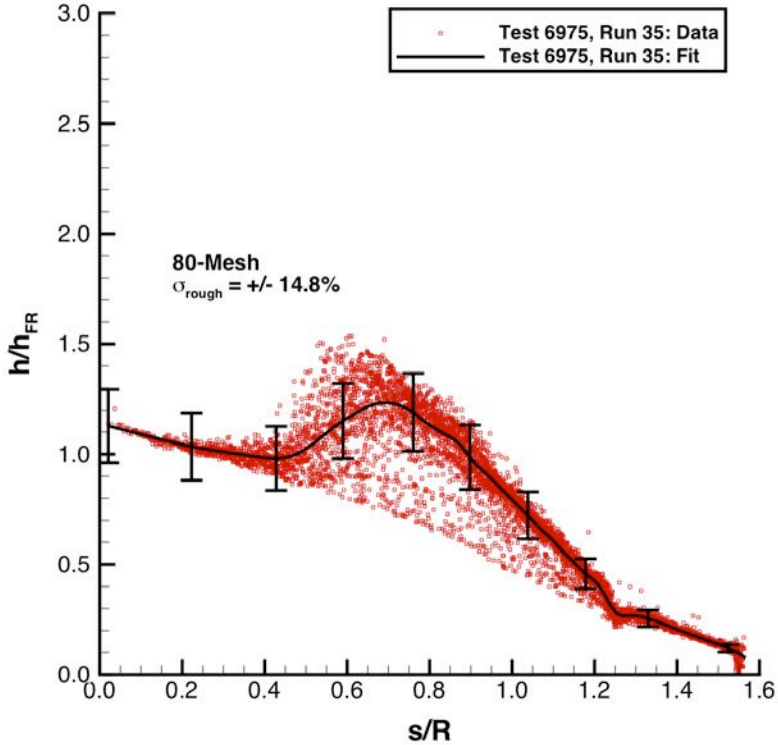

Figure 71. Test 6975, Run 35: Mach 6, $Re_\infty = 5.0\times10^6$/ft, 80-Mesh model, heating data and fit.

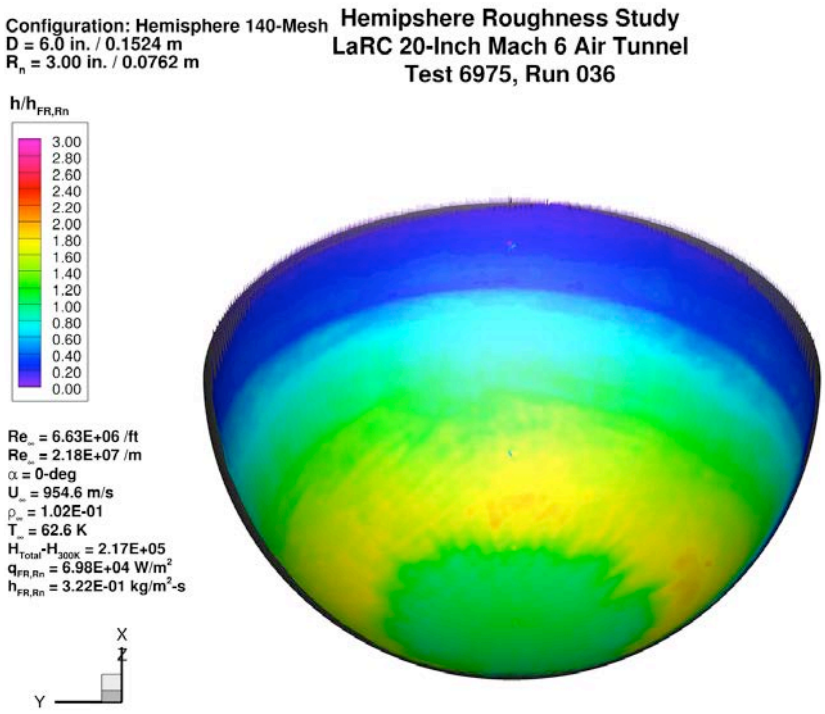

Figure 72. Test 6975, Run 36: Mach 6, $Re_\infty = 6.6\times10^6$/ft, 80-Mesh model, global heating image.

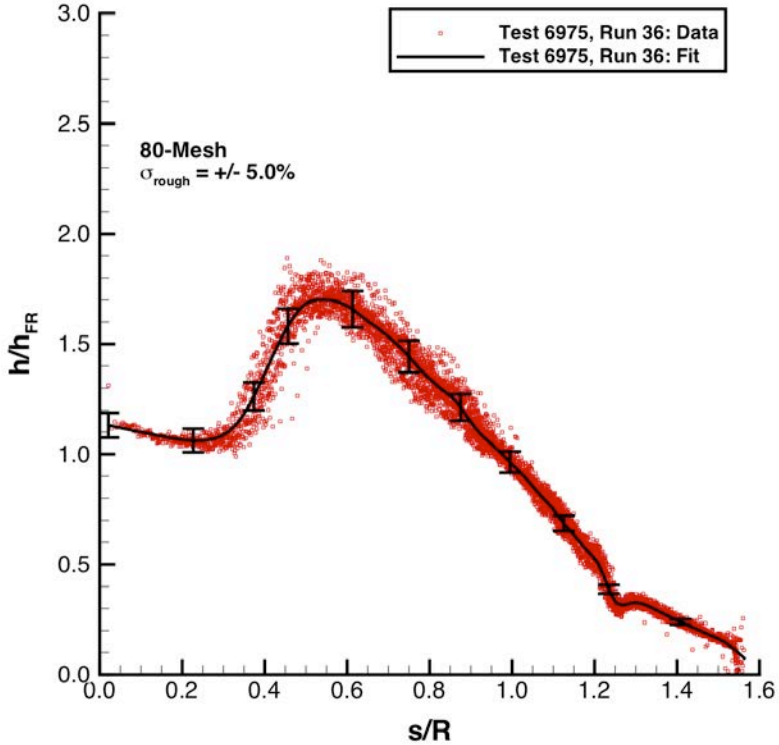

Figure 73. Test 6975, Run 36: Mach 6, $Re_\infty = 6.6\times10^6$/ft, 80-Mesh model, heating data and fit.

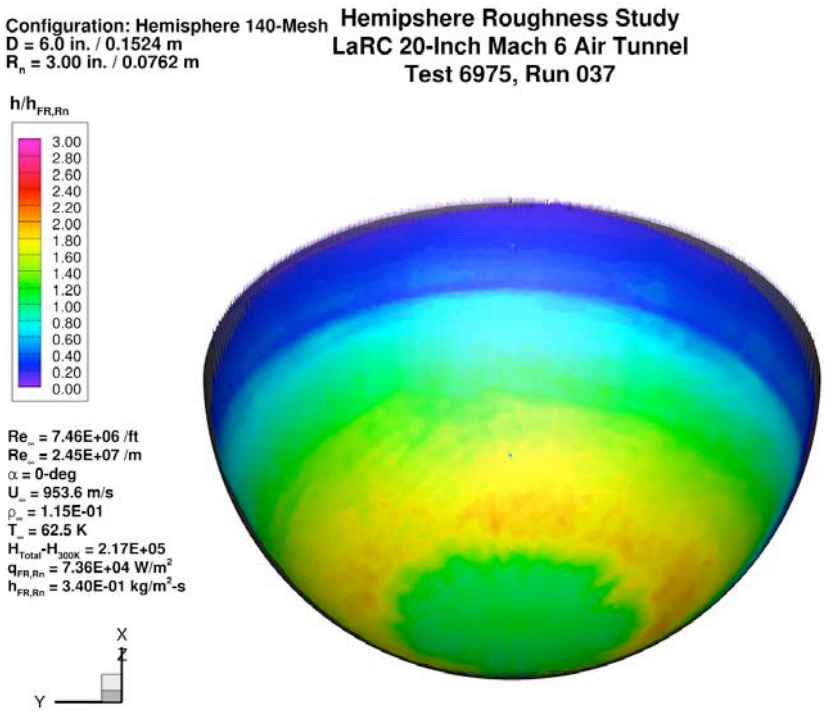

Figure 74. Test 6975, Run 37: Mach 6, $Re_\infty = 7.5\times10^6$/ft, 80-Mesh model, global heating image.

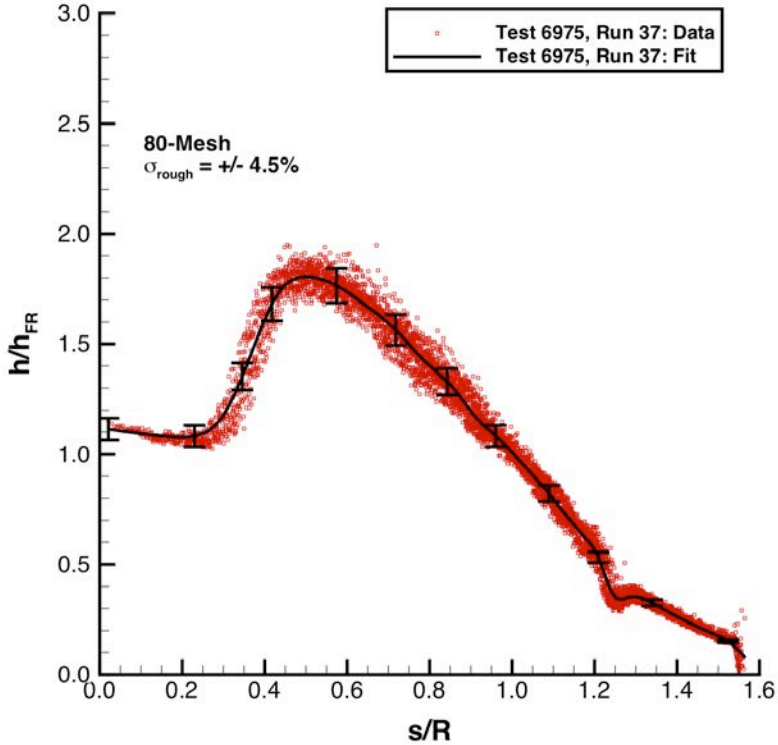

Figure 75. Test 6975, Run 37: Mach 6, $Re_\infty = 7.5\times10^6$/ft, 80-Mesh model, heating data and fit.

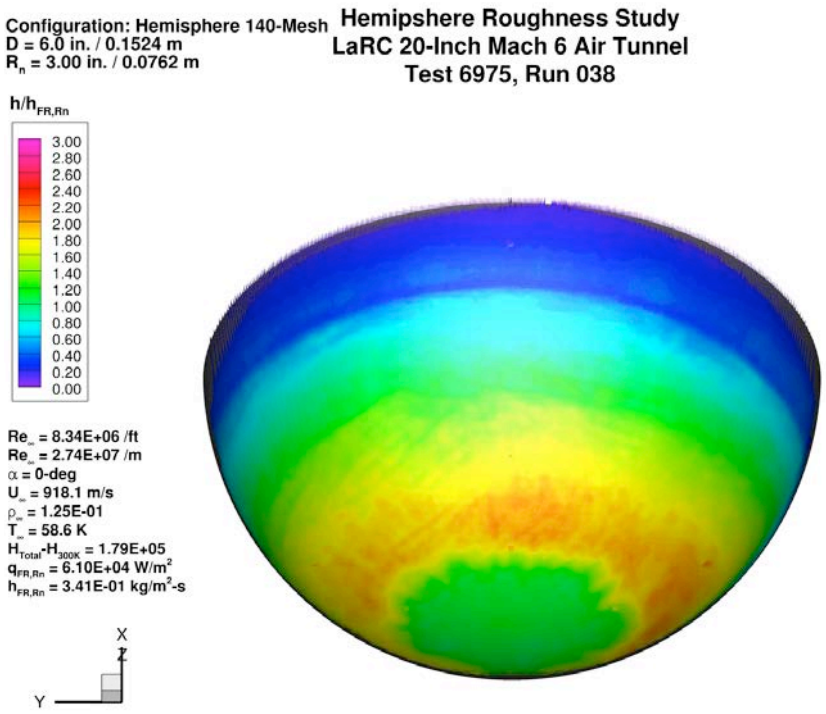

Figure 76. Test 6975, Run 38: Mach 6, $Re_\infty = 8.3\times10^6$/ft, 80-Mesh model, global heating image.

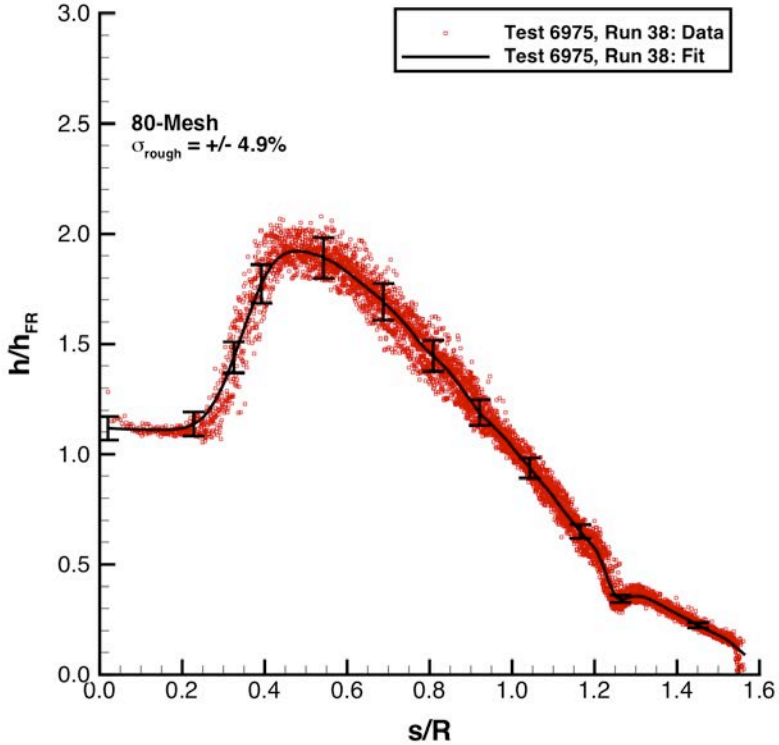

Figure 77. Test 6975, Run 38: Mach 6, $Re_\infty = 8.3\times10^6$/ft, 80-Mesh model, heating data and fit.

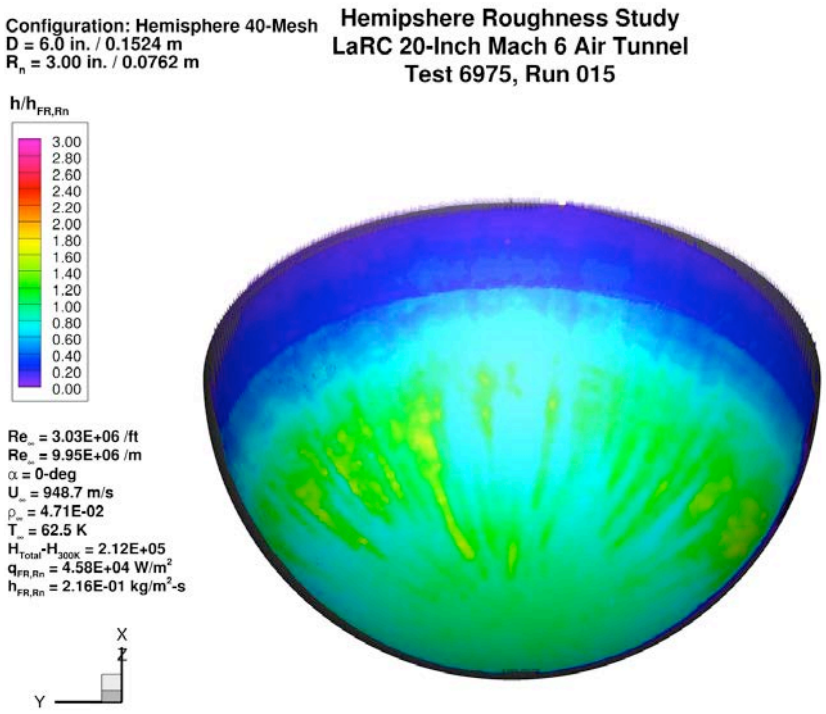

Figure 78. Test 6975, Run 15: Mach 6, $Re_\infty = 3.0\times10^6$/ft, 40-Mesh model, global heating image.

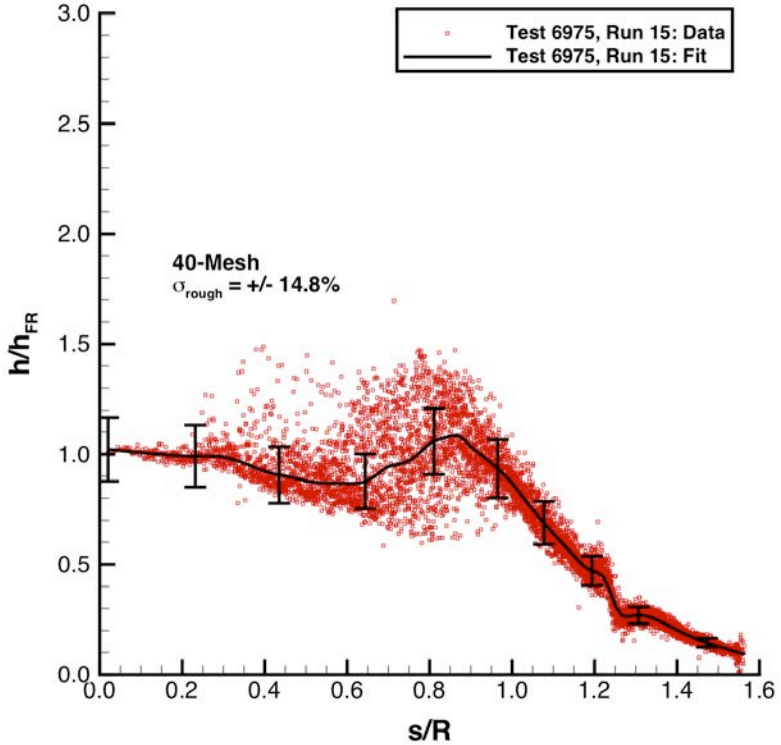

Figure 79. Test 6975, Run 15: Mach 6, $Re_\infty = 3.0\times10^6$/ft, 40-Mesh model, heating data and fit.

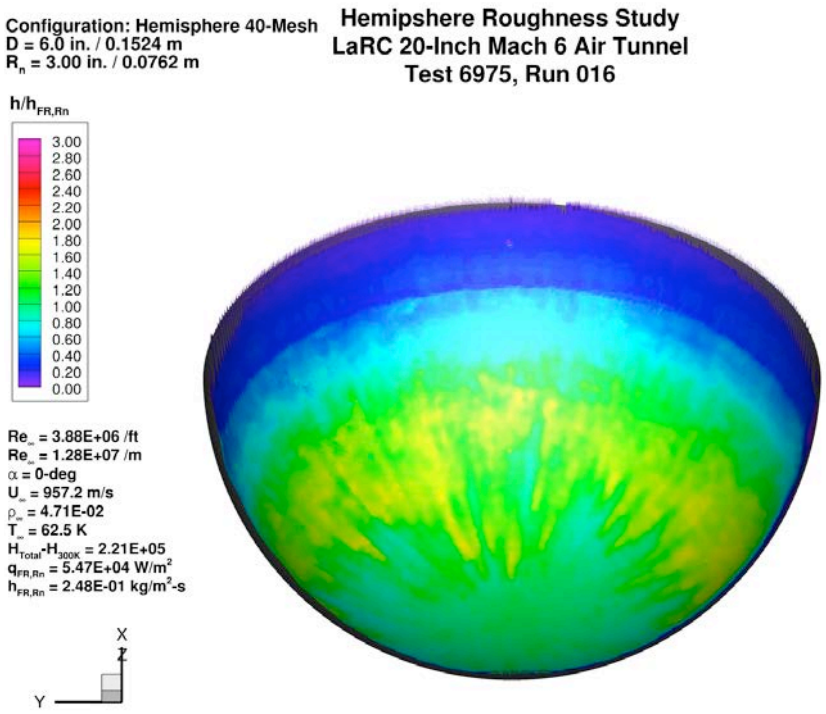

Figure 80. Test 6975, Run 16: Mach 6, $Re_\infty = 3.9\times10^6$/ft, 40-Mesh model, global heating image.

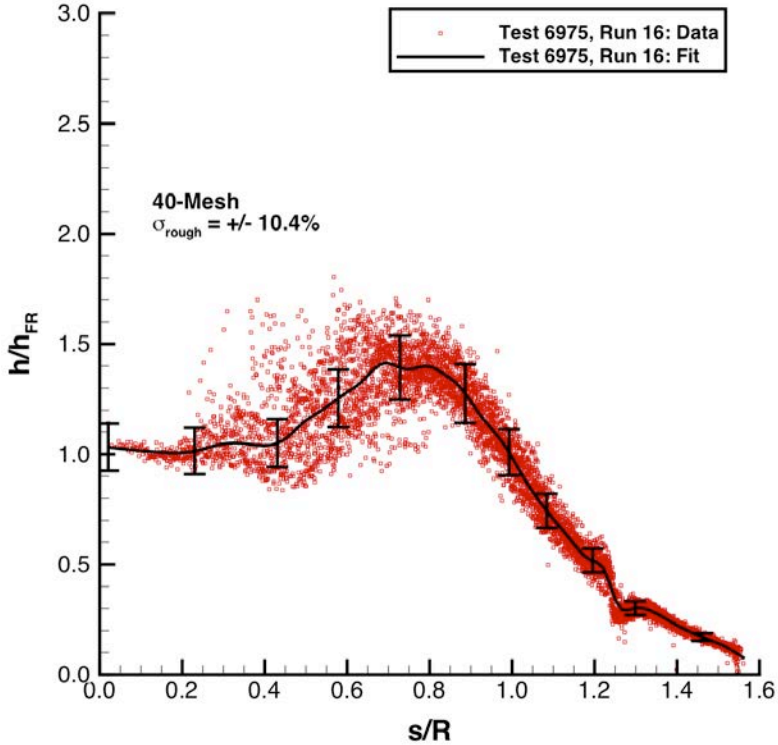

Figure 81. Test 6975, Run 16: Mach 6, $Re_\infty = 3.9\times10^6$/ft, 40-Mesh model, heating data and fit.

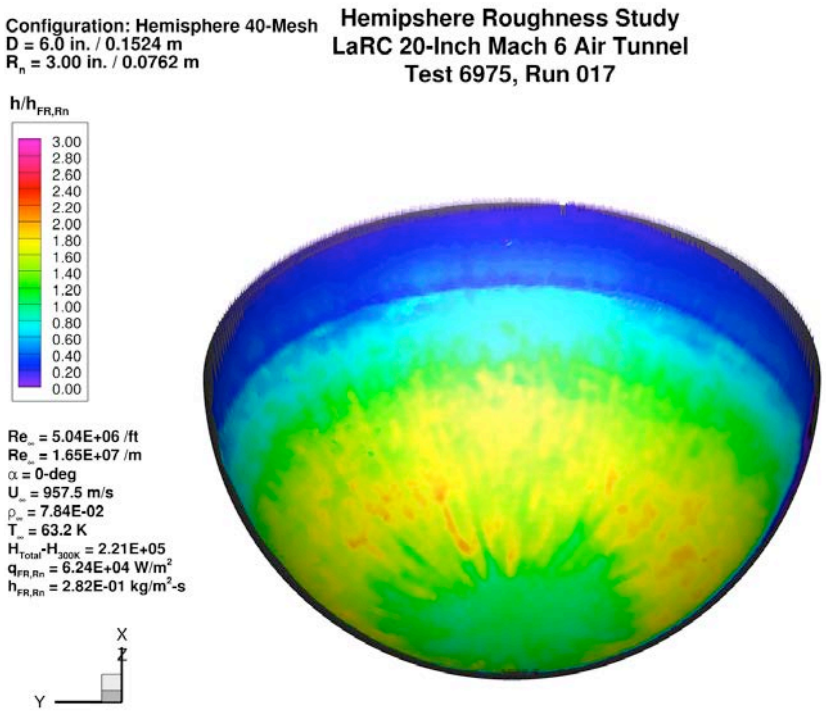

Figure 82. Test 6975, Run 17: Mach 6, $Re_\infty = 5.0\times10^6$/ft, 40-Mesh model, global heating image.

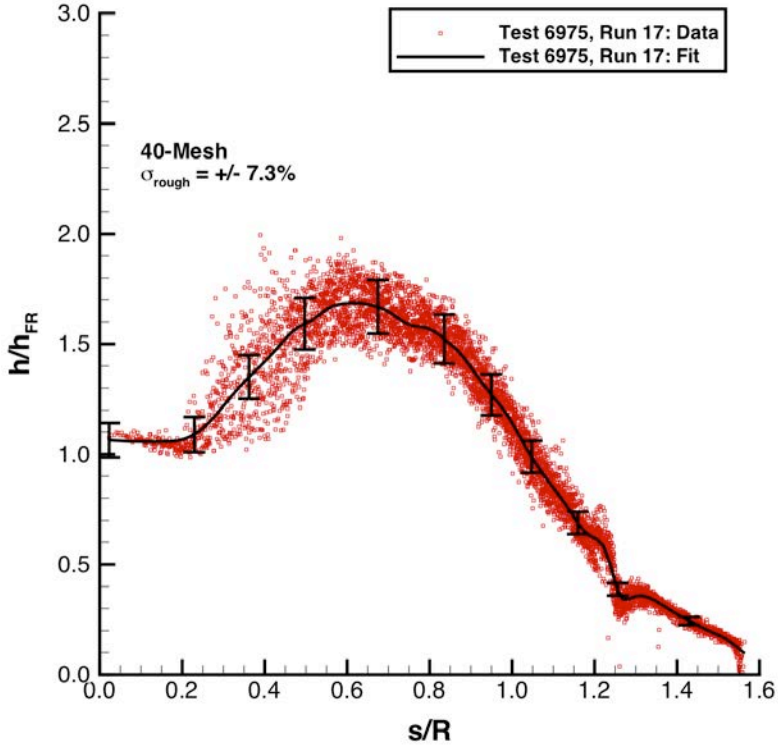

Figure 83. Test 6975, Run 17: Mach 6, $Re_\infty = 5.0\times10^6$/ft, 40-Mesh model, heating data and fit.

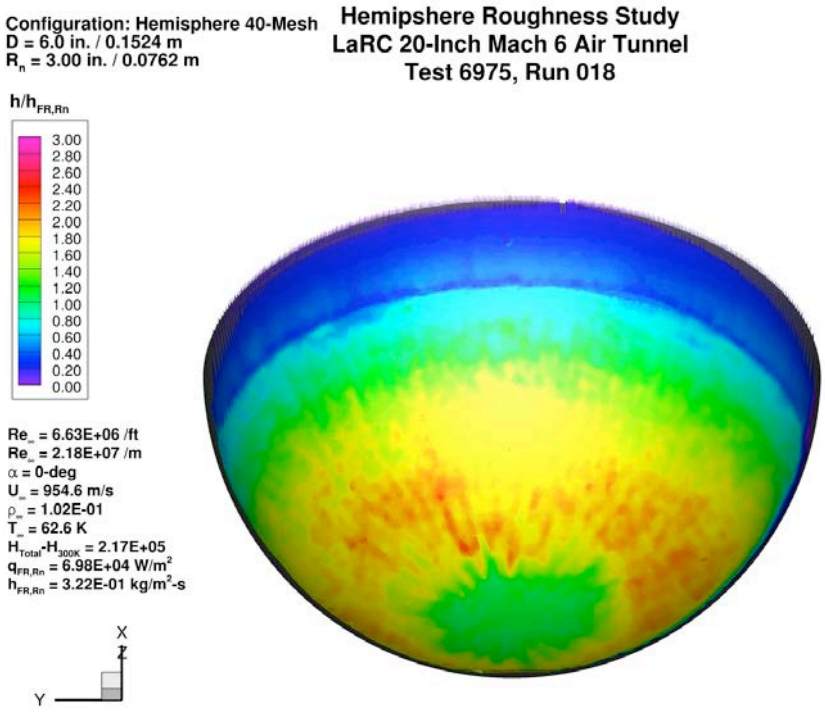

Figure 84. Test 6975, Run 18: Mach 6, $Re_\infty = 6.6\times10^6$/ft, 40-Mesh model, global heating image.

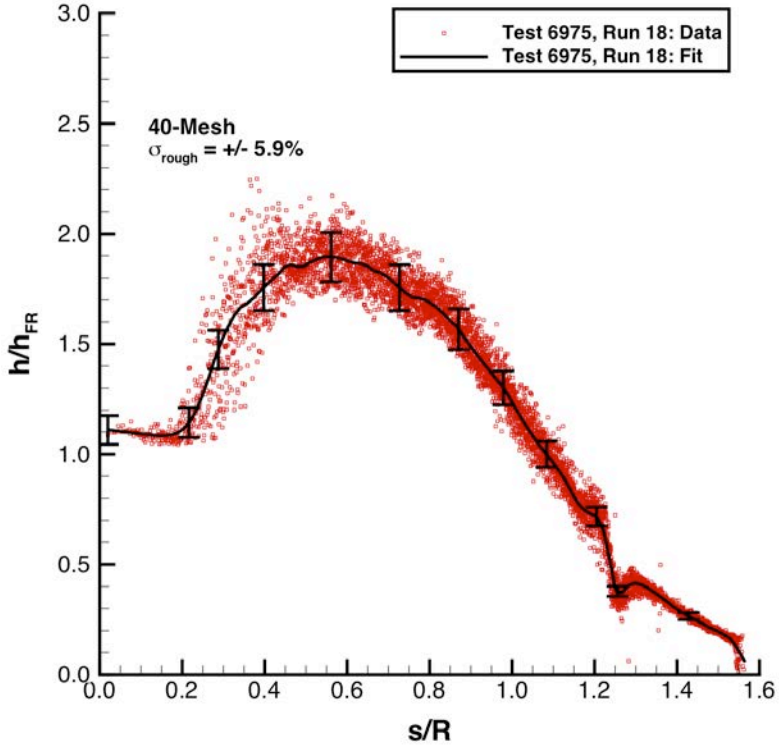

Figure 85. Test 6975, Run 18: Mach 6, $Re_\infty = 6.6\times10^6$/ft, 40-Mesh model, heating data and fit.

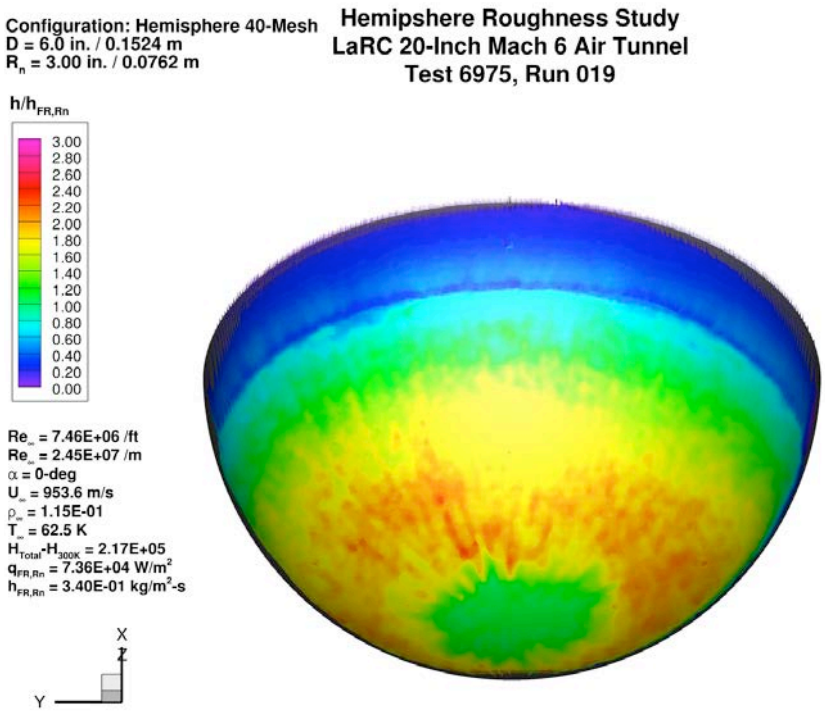

Figure 86. Test 6975, Run 19: Mach 6, $Re_\infty = 7.5\times10^6$/ft, 40-Mesh model, global heating image.

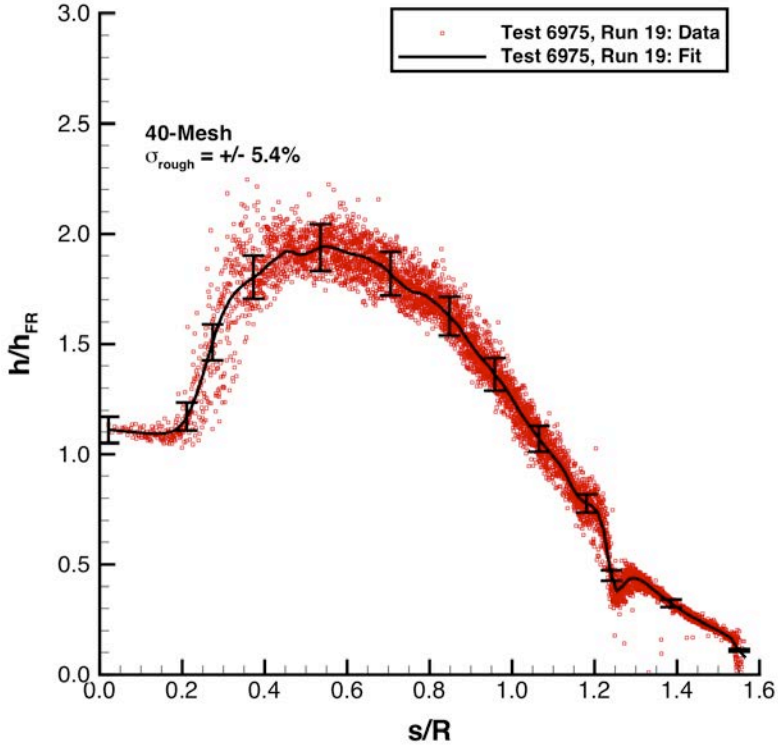

Figure 87. Test 6975, Run 19: Mach 6, $Re_\infty = 7.5\times10^6$/ft, 40-Mesh model, heating data and fit.

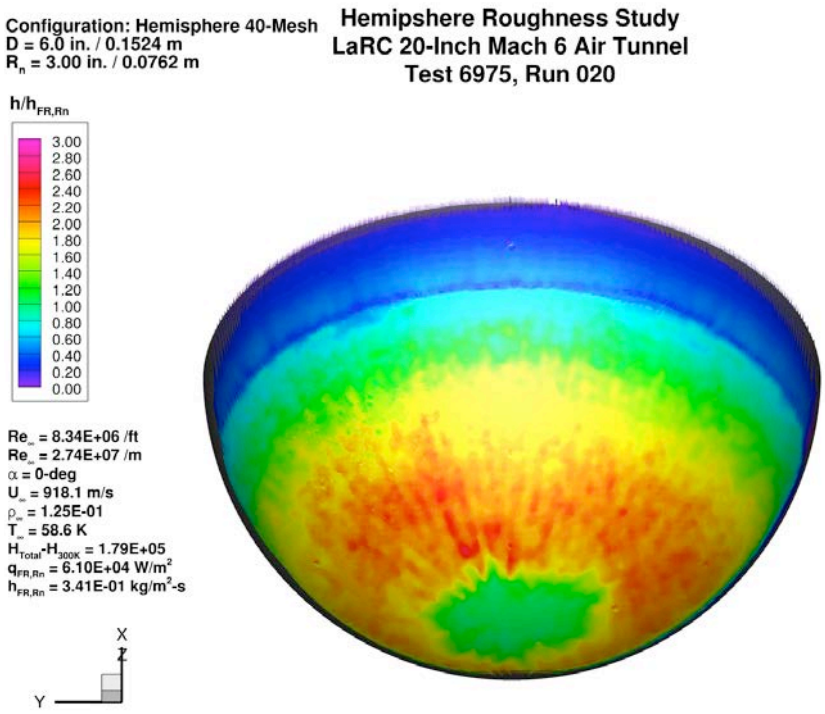

Figure 88. Test 6975, Run 20: Mach 6, $Re_\infty = 8.3\times10^6$/ft, 40-Mesh model, global heating image.

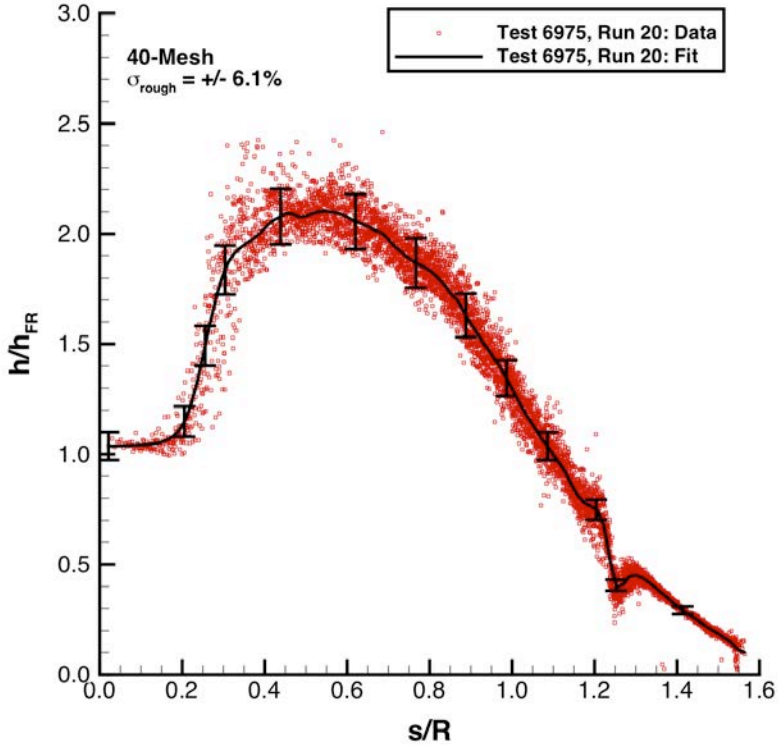

Figure 89. Test 6975, Run 20: Mach 6, $Re_\infty = 8.3\times10^6$/ft, 40-Mesh model, heating data and fit.

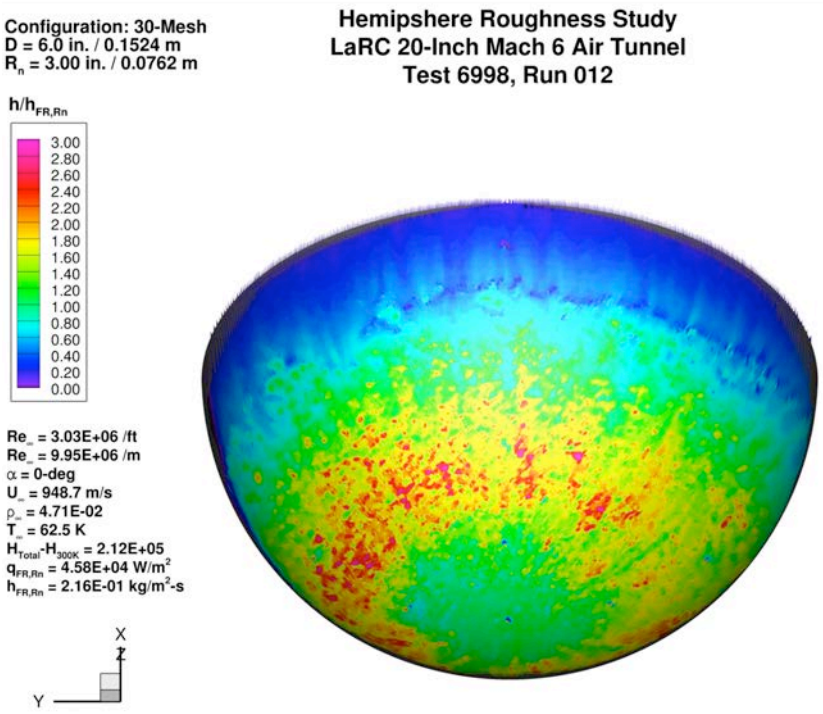

Figure 90. Test 6998, Run 12: Mach 6, $Re_\infty = 3.0\times10^6$/ft, 30-Mesh model, global heating image.

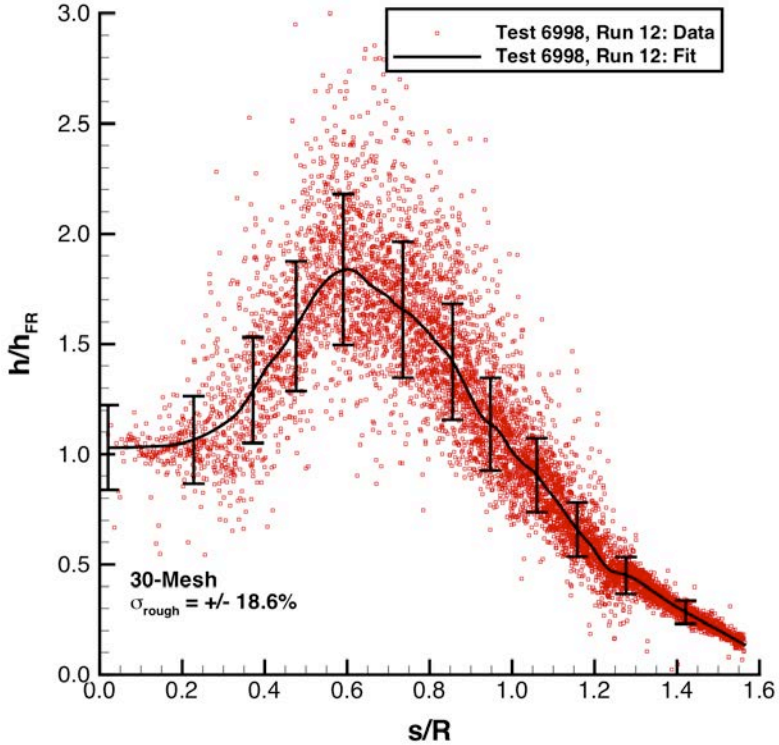

Figure 91. Test 6998, Run 12: Mach 6, $Re_\infty = 3.0\times10^6$/ft, 30-Mesh model, heating data and fit.

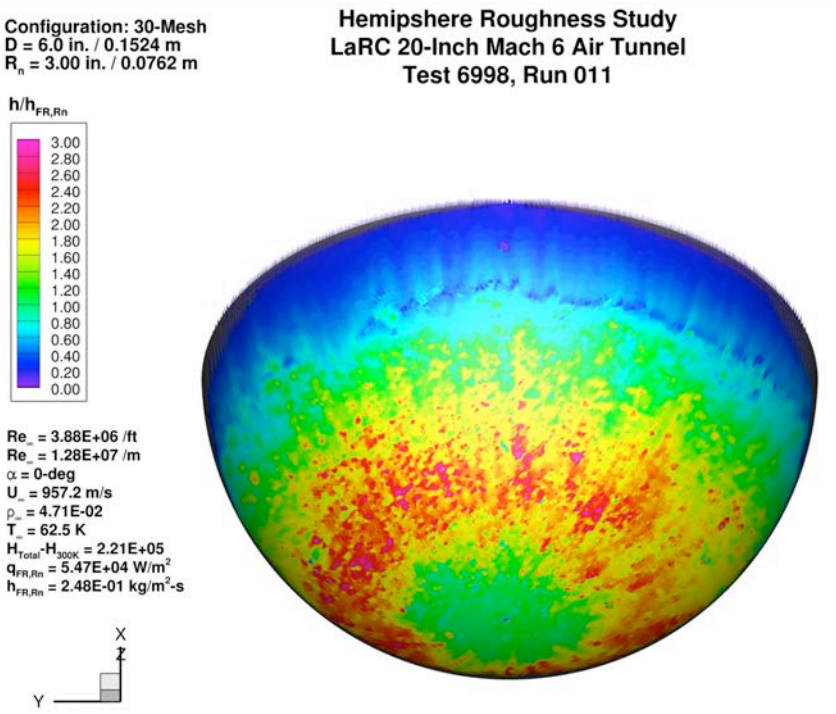

Figure 92. Test 6998, Run 11: Mach 6, $Re_\infty = 3.9\times10^6$/ft, 30-Mesh model, global heating image.

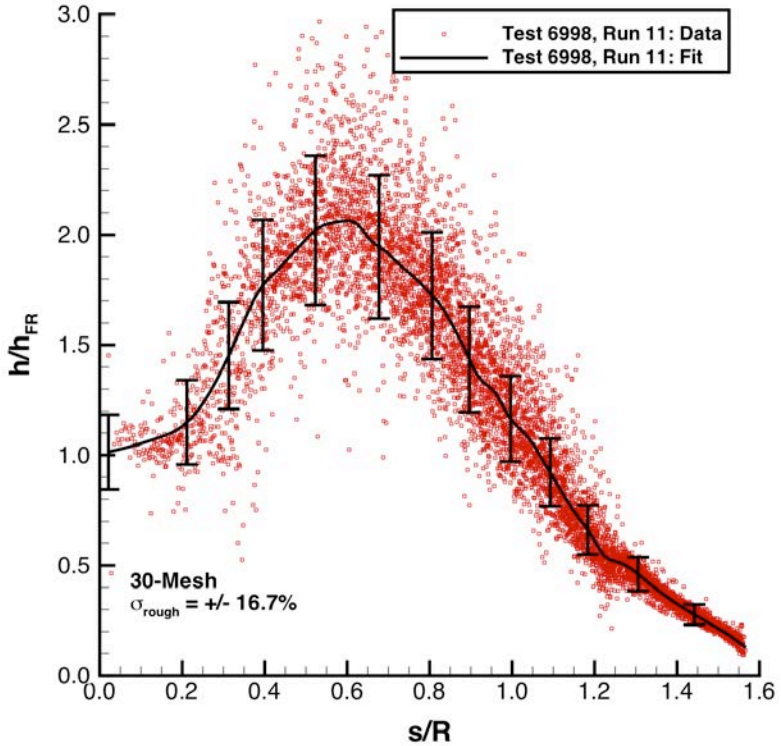

Figure 93. Test 6998, Run 11: Mach 6, $Re_\infty = 3.9\times10^6$/ft, 30-Mesh model, heating data and fit.

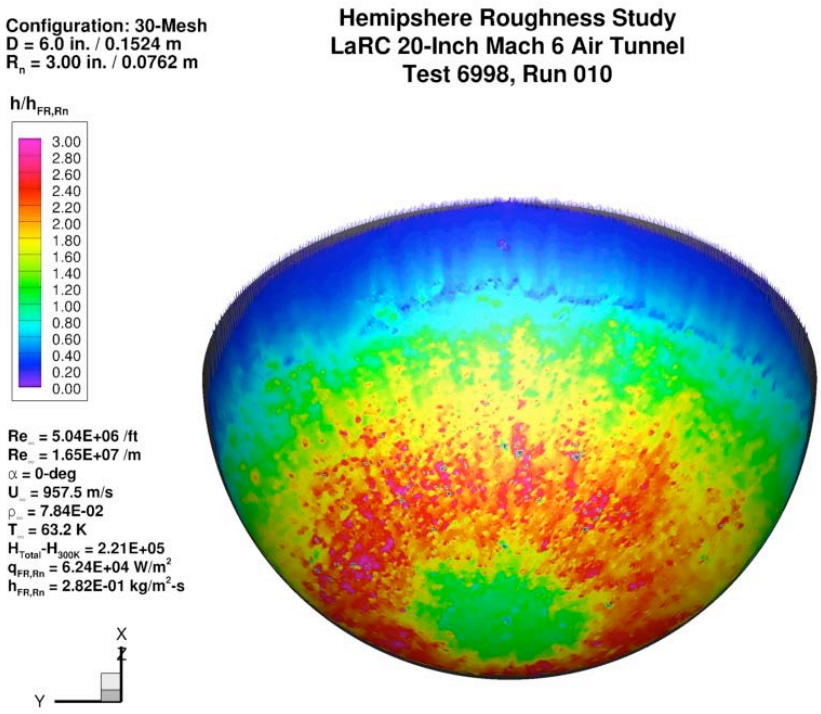

Figure 94. Test 6998, Run 10: Mach 6, $Re_\infty = 5.0\times10^6$/ft, 30-Mesh model, global heating image.

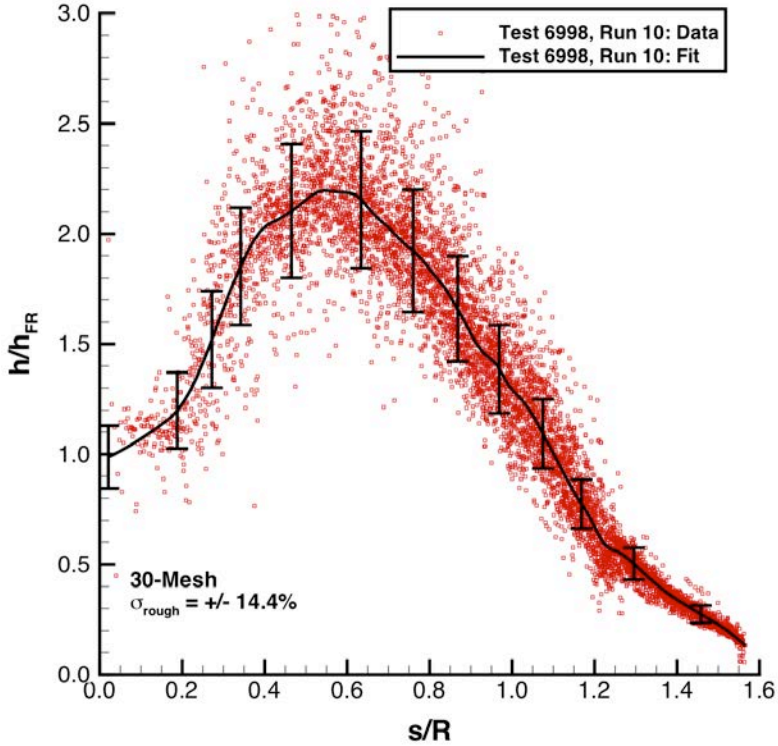

Figure 95. Test 6998, Run 10: Mach 6, $Re_\infty = 5.0\times10^6$/ft, 30-Mesh model, heating data and fit.

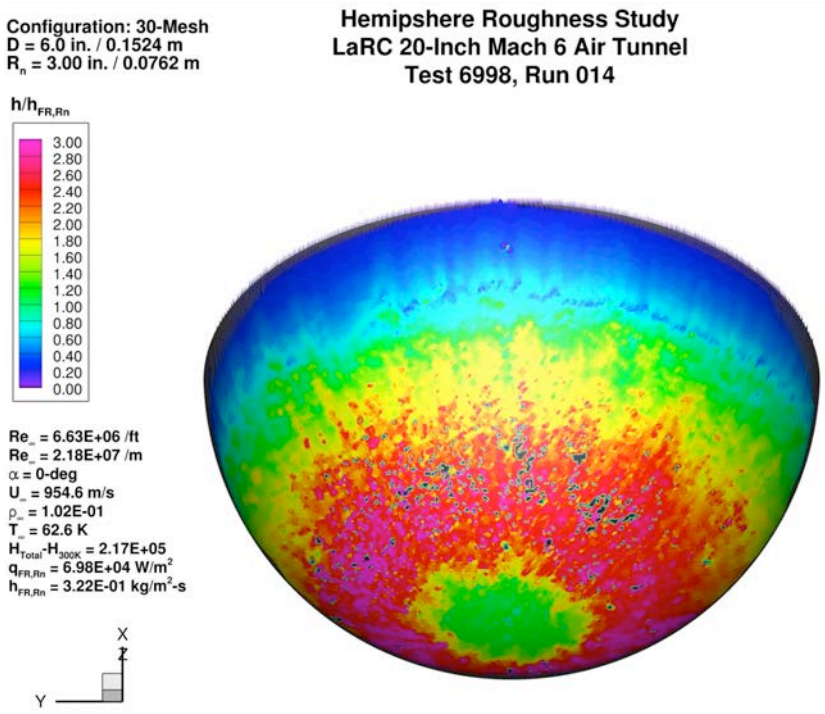

Figure 96. Test 6998, Run 14: Mach 6, $Re_\infty = 6.6\times10^6$/ft, 30-Mesh model, global heating image.

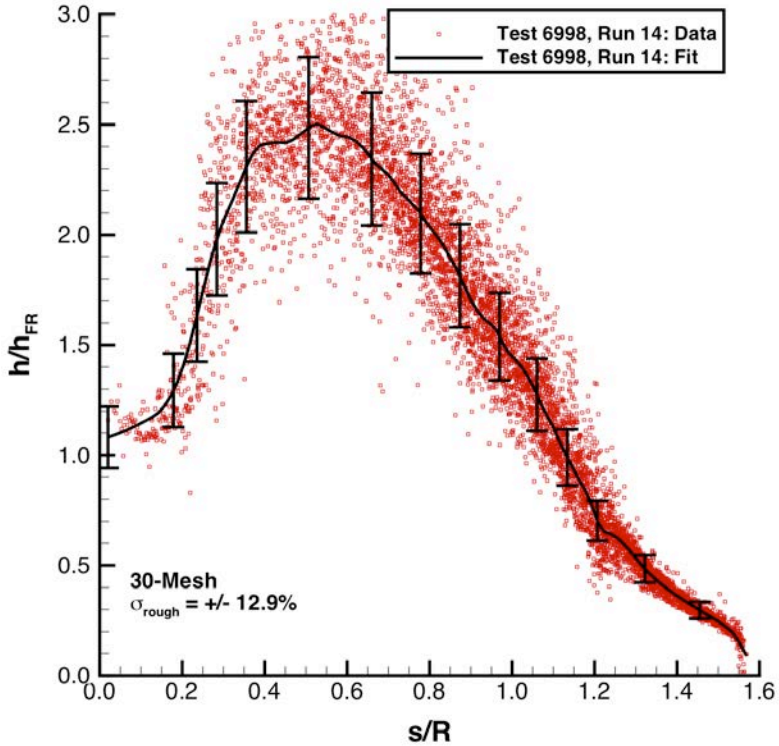

Figure 97. Test 6998, Run 14: Mach 6, $Re_\infty = 6.6\times10^6$/ft, 30-Mesh model, heating data and fit.

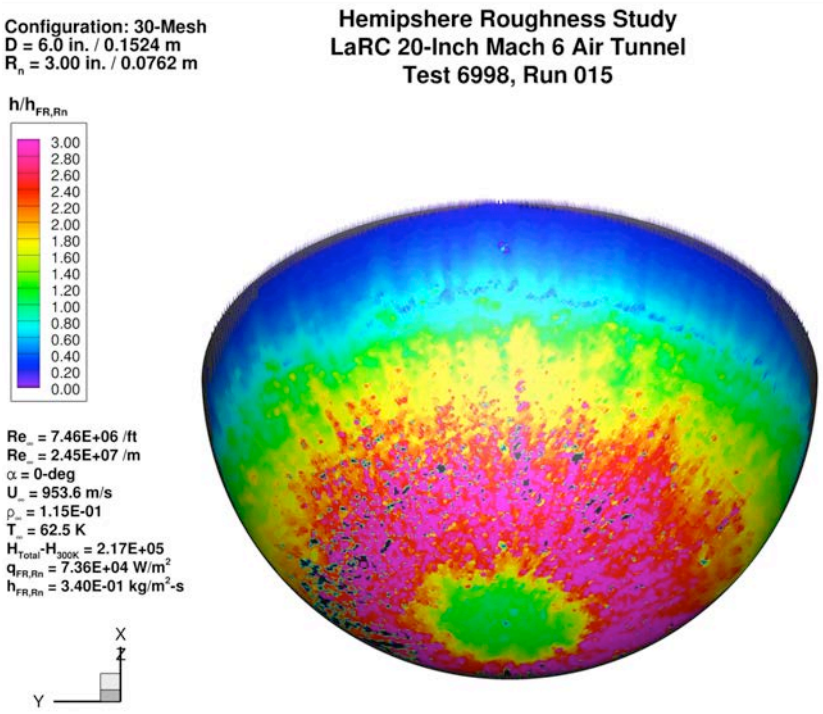

Figure 98. Test 6998, Run 15: Mach 6, $Re_\infty = 7.5\times10^6$/ft, 30-Mesh model, global heating image.

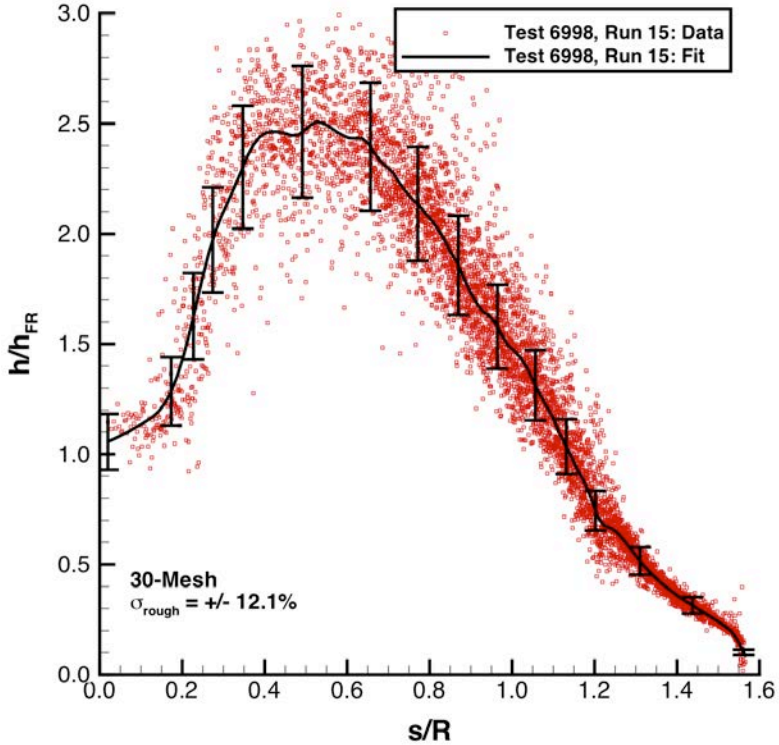

Figure 99. Test 6998, Run 15: Mach 6, $Re_\infty = 7.5\times10^6$/ft, 30-Mesh model, heating data and fit.

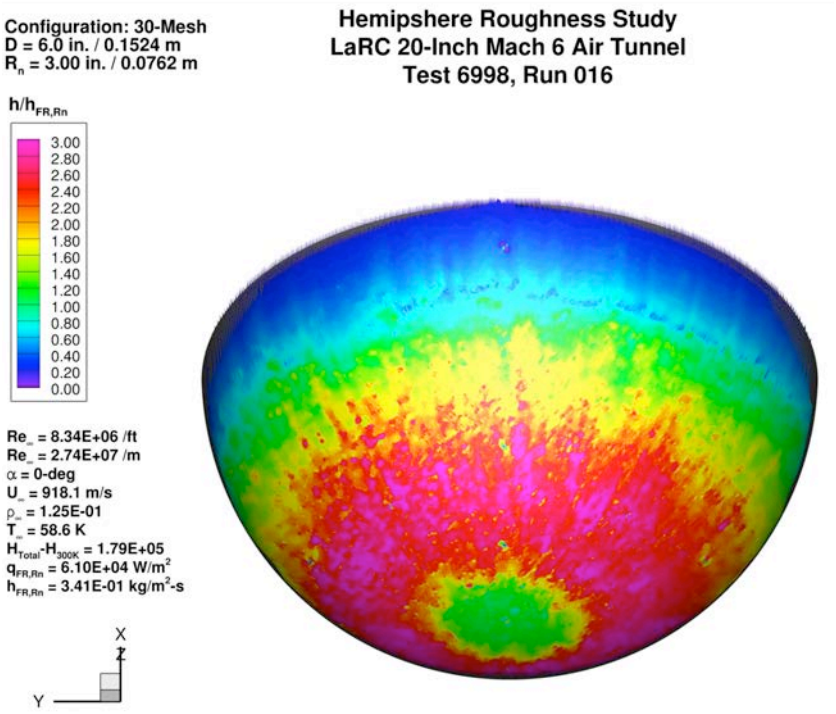

Figure 100. Test 6998, Run 16: Mach 6, $Re_\infty = 8.3\times10^6$/ft, 30-Mesh model, global heating image.

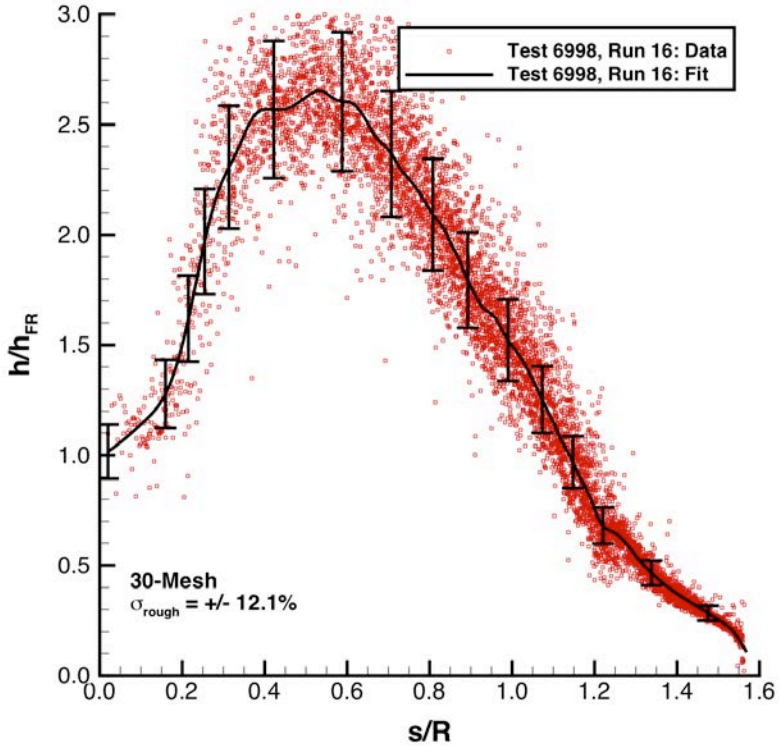

Figure 101. Test 6998, Run 16: Mach 6, $Re_\infty = 8.3\times10^6$/ft, 30-Mesh model, heating data and fit.

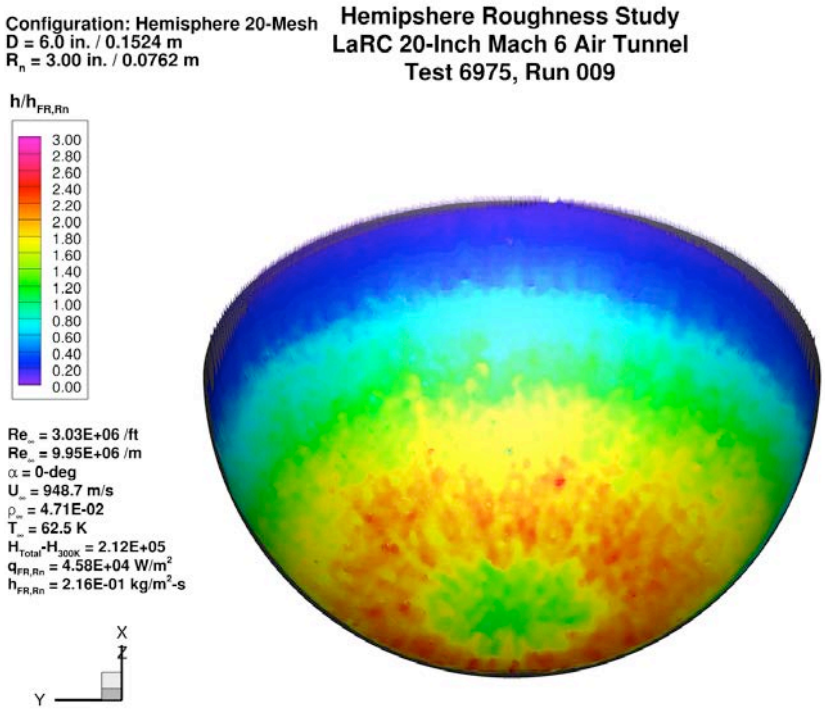

Figure 102. Test 6975, Run 9: Mach 6, $Re_\infty = 3.0\times10^6$/ft, 20-Mesh model, global heating image.

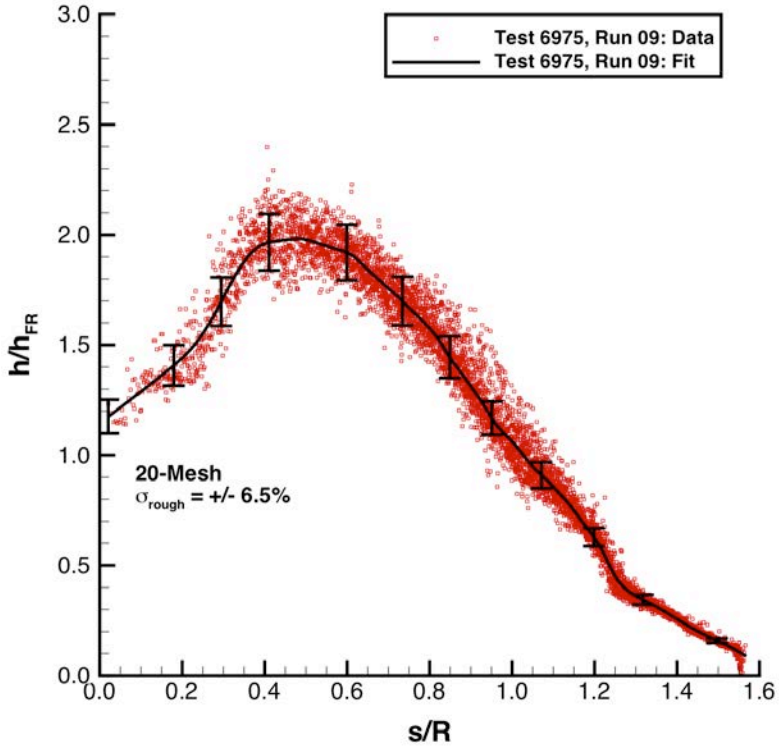

Figure 103. Test 6975, Run 9: Mach 6, $Re_\infty = 3.0\times10^6$/ft, 20-Mesh model, heating data and fit.

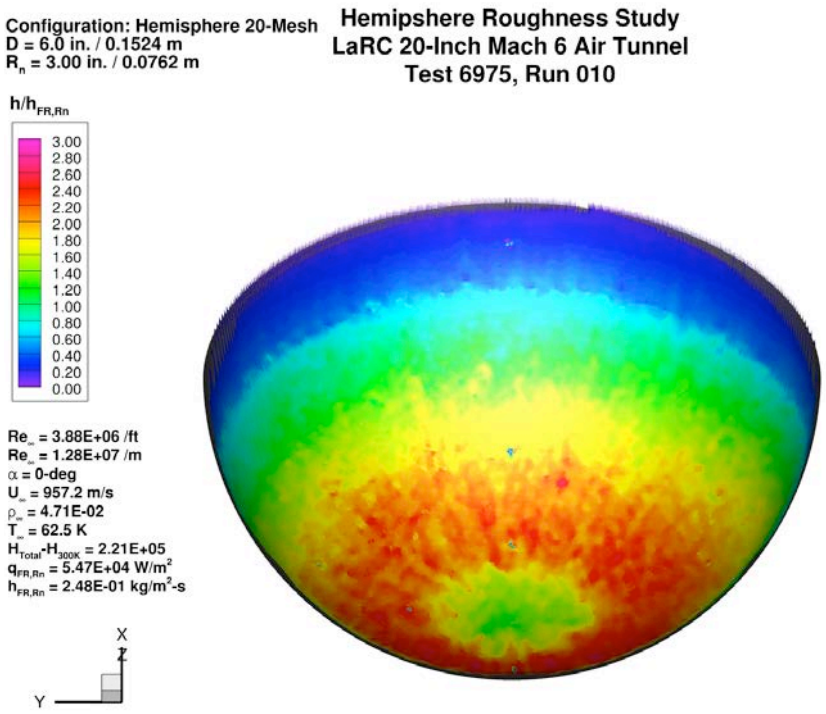

Figure 104. Test 6975, Run 10: Mach 6, $Re_\infty = 3.9\times10^6$/ft, 20-Mesh model, global heating image.

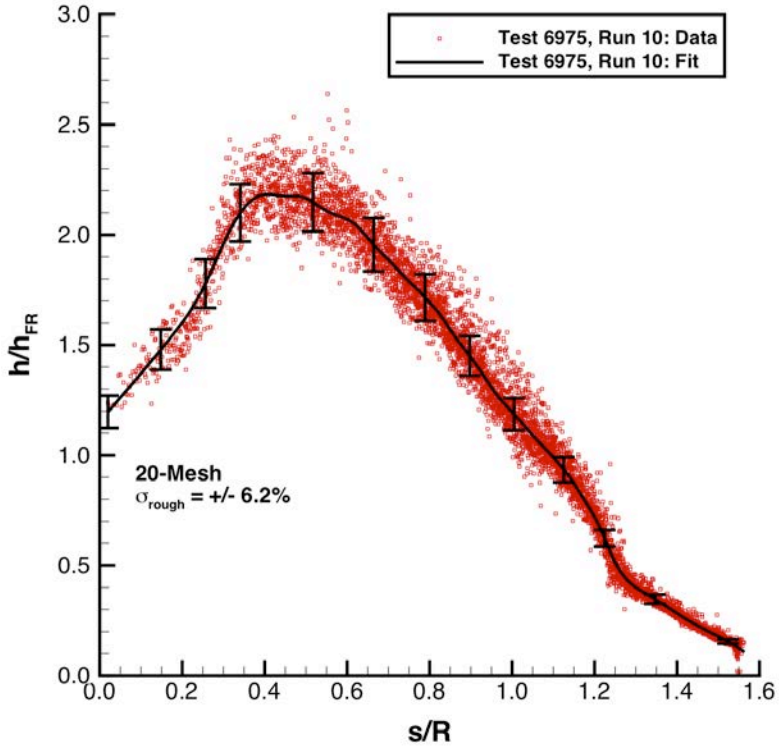

Figure 105. Test 6975, Run 10: Mach 6, $Re_\infty = 3.9\times10^6$/ft, 20-Mesh model, heating data and fit.

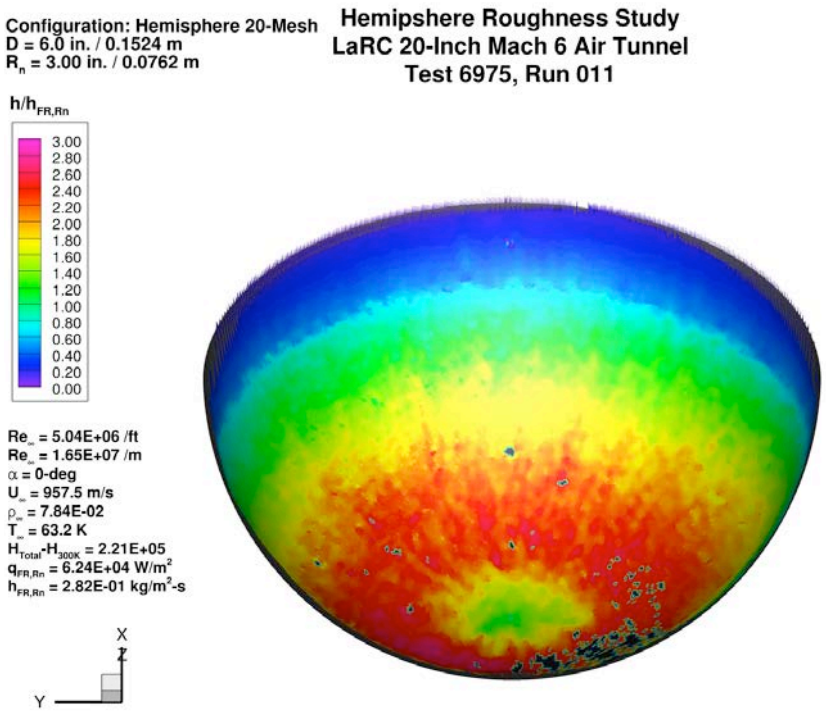

Figure 106. Test 6975, Run 11: Mach 6, $Re_\infty = 5.0\times10^6$/ft, 20-Mesh model, global heating image.

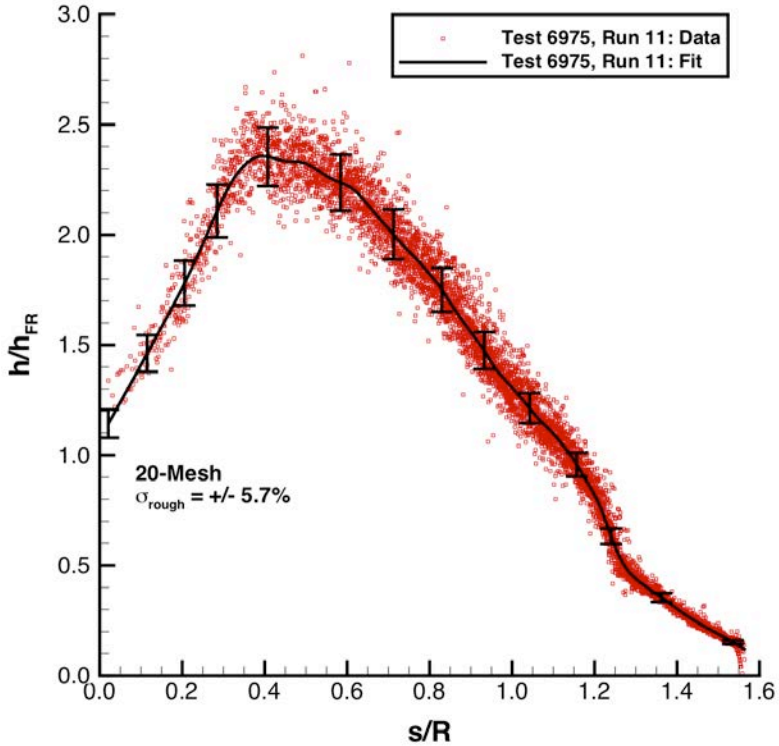

Figure 107. Test 6975, Run 11: Mach 6, $Re_\infty = 5.0\times10^6$/ft, 20-Mesh model, heating data and fit.

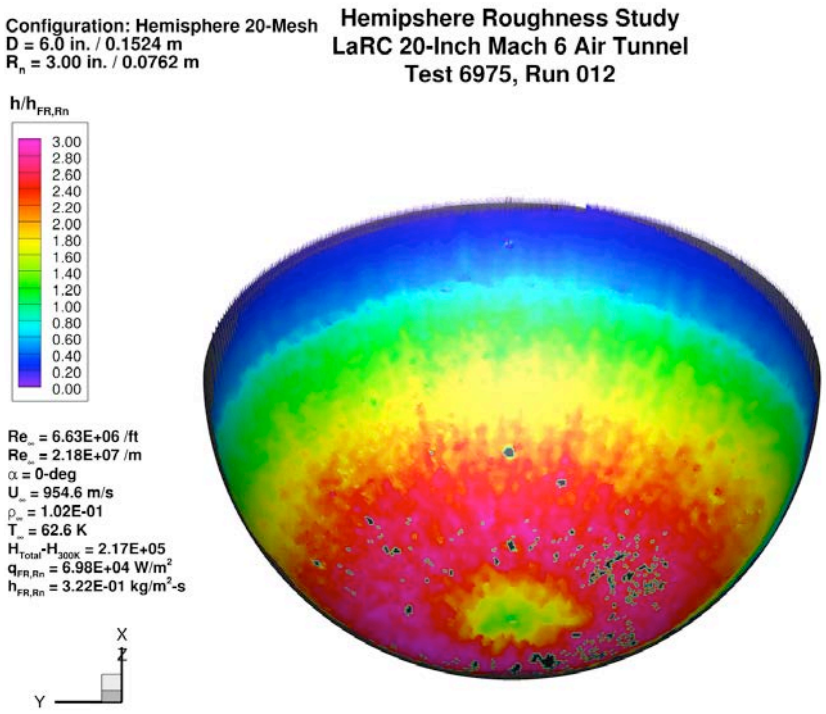

Figure 108. Test 6975, Run 12: Mach 6, $Re_\infty = 6.6\times10^6$/ft, 20-Mesh model, global heating image.

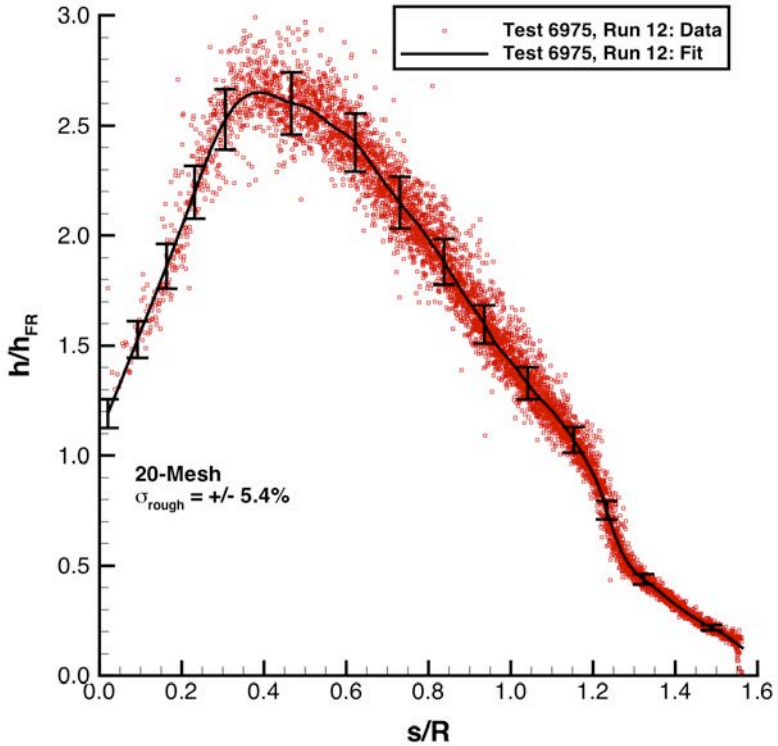

Figure 109. Test 6975, Run 12: Mach 6, $Re_\infty = 6.6\times10^6$/ft, 20-Mesh model, heating data and fit.

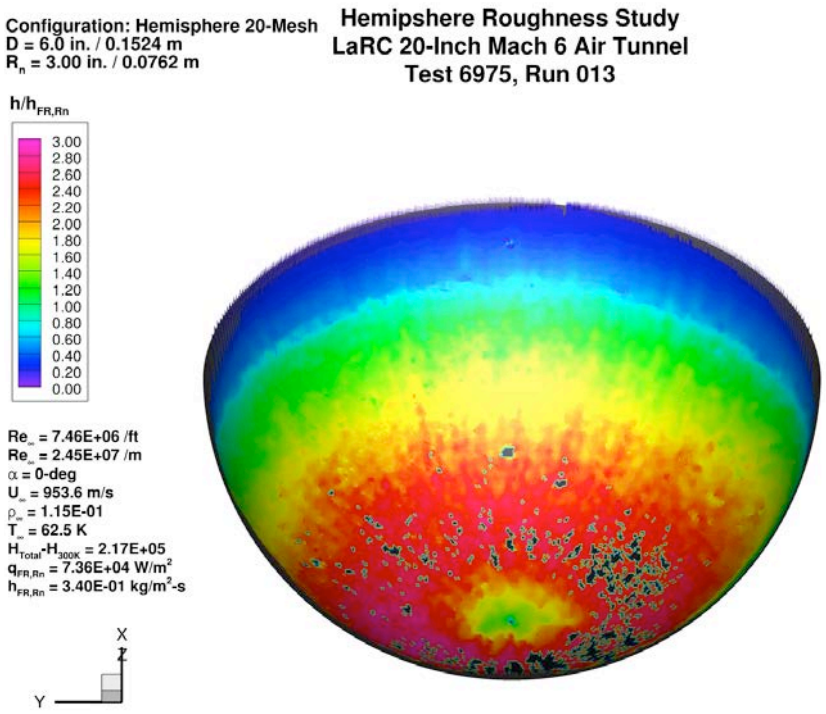

Figure 110. Test 6975, Run 13: Mach 6, $Re_\infty = 7.5\times10^6$/ft, 20-Mesh model, global heating image.

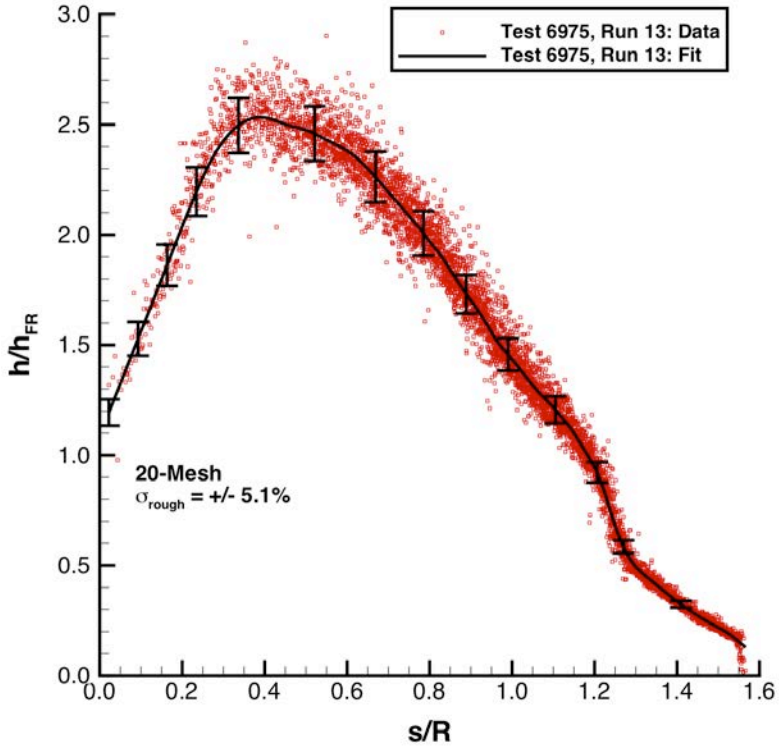

Figure 111. Test 6975, Run 13: Mach 6, $Re_\infty = 7.5\times10^6$/ft, 20-Mesh model, heating data and fit.

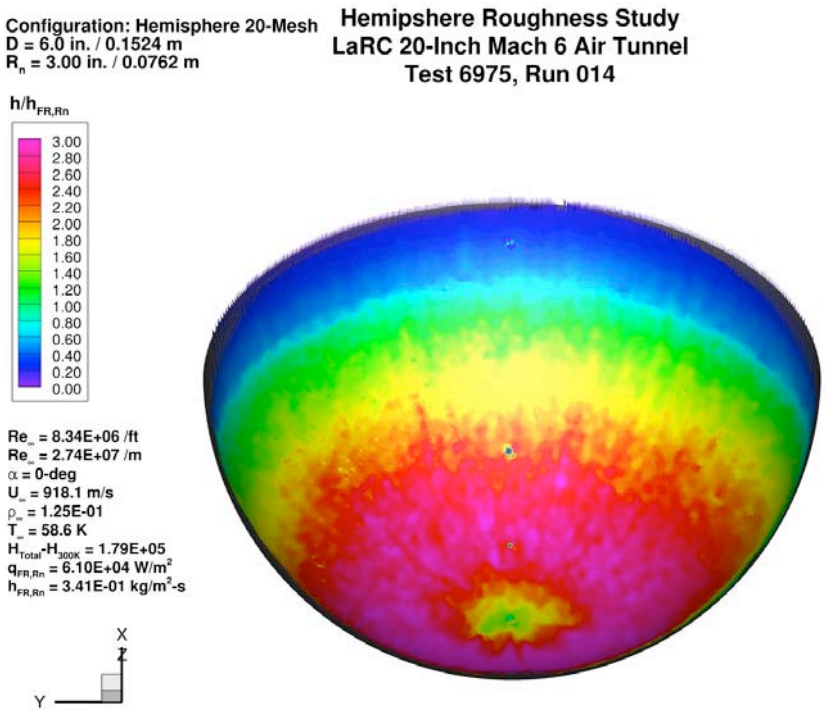

Figure 112. Test 6975, Run 14: Mach 6, $Re_\infty = 8.3\times10^6$/ft, 20-Mesh model, global heating image.

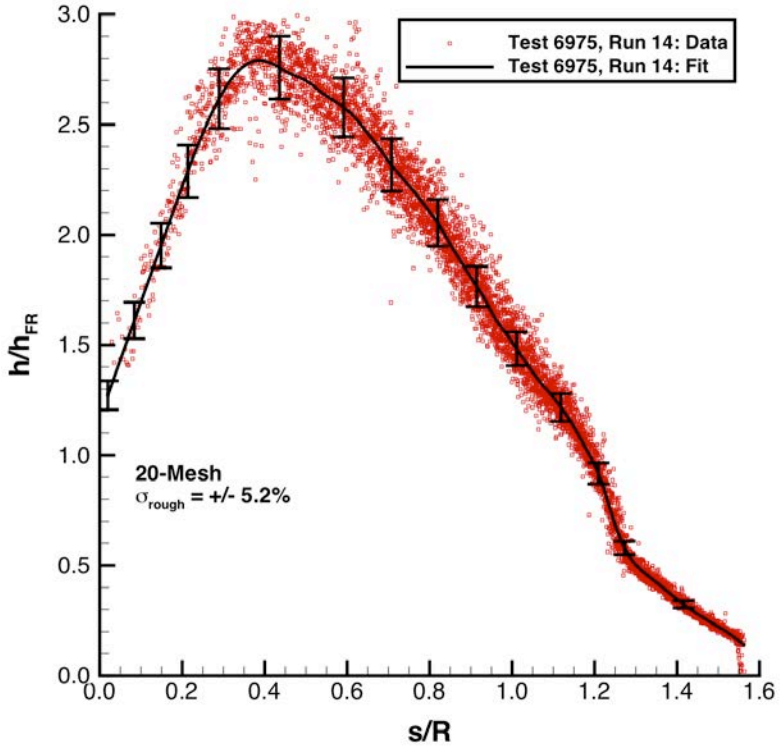

Figure 113. Test 6975, Run 14: Mach 6, $Re_\infty = 8.3\times10^6$/ft, 20-Mesh model, heating data and fit.

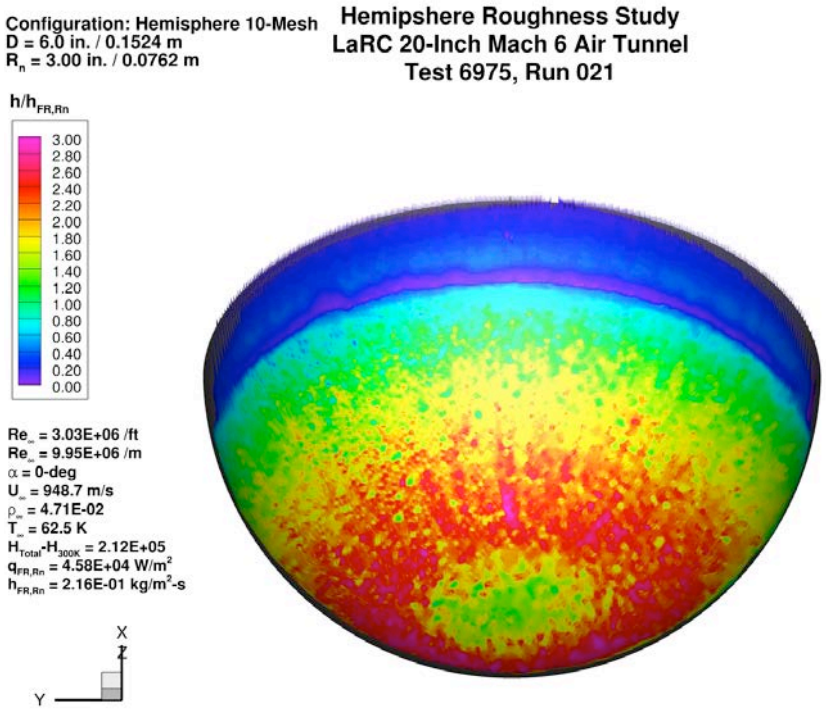

Figure 114. Test 6975, Run 21: Mach 6, $Re_\infty = 3.0\times10^6$/ft, 10-Mesh model, global heating image.

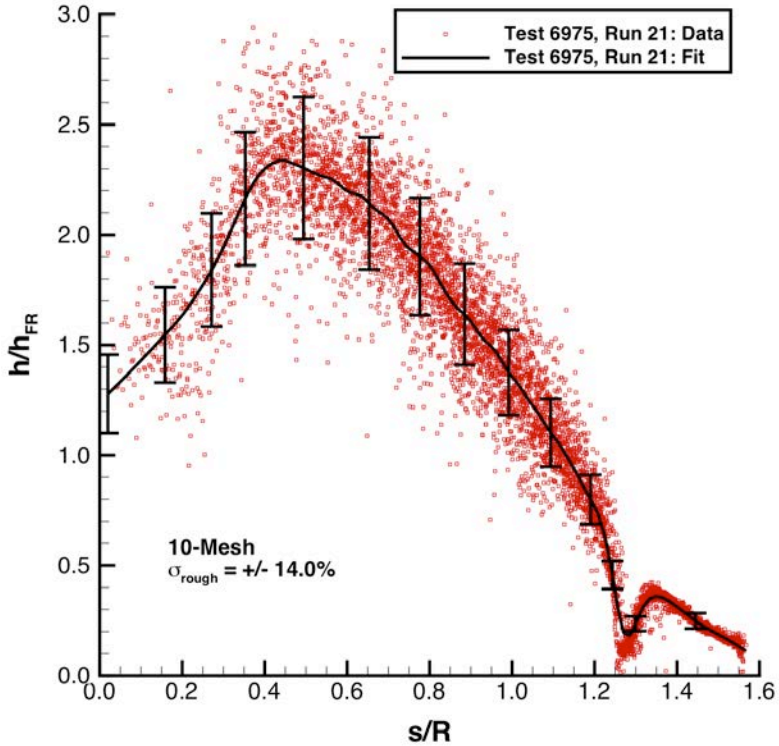

Figure 115. Test 6975, Run 21: Mach 6, $Re_\infty = 3.0\times10^6$/ft, 10-Mesh model, heating data and fit.

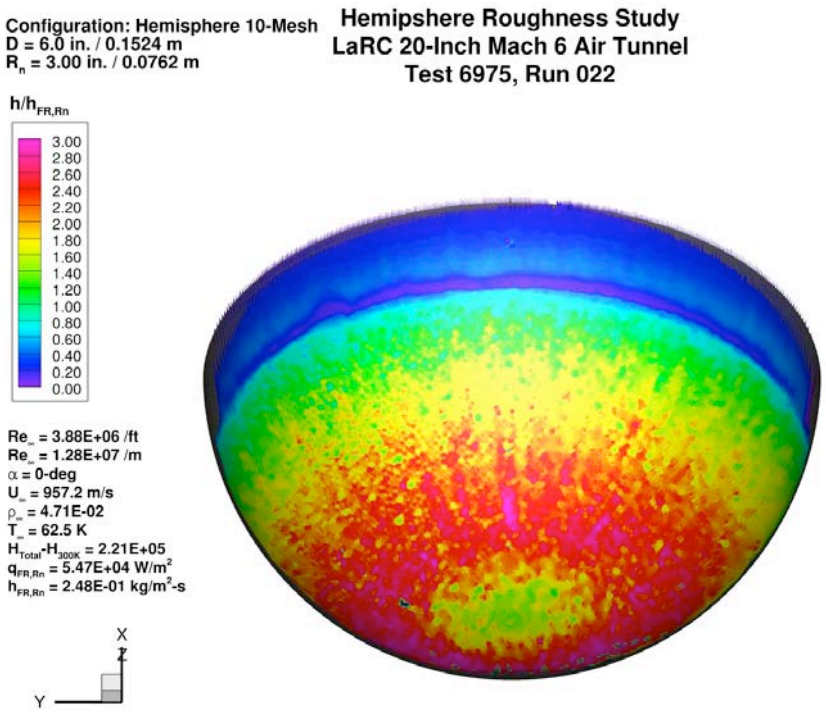

Figure 116. Test 6975, Run 22: Mach 6, $Re_\infty = 3.9\times10^6$/ft, 10-Mesh model, global heating image.

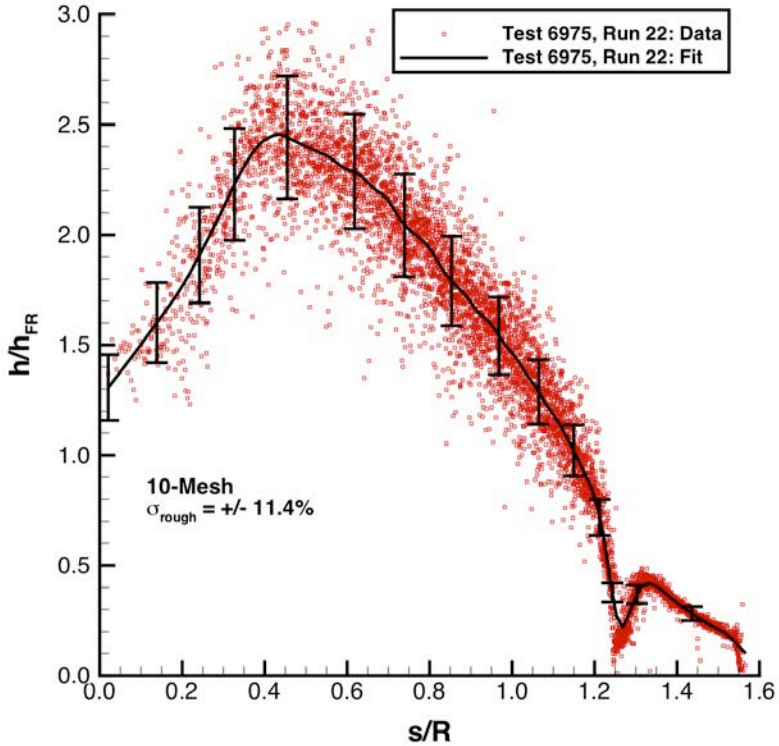

Figure 117. Test 6975, Run 22: Mach 6, $Re_\infty = 3.9\times10^6$/ft, 10-Mesh model, heating data and fit.

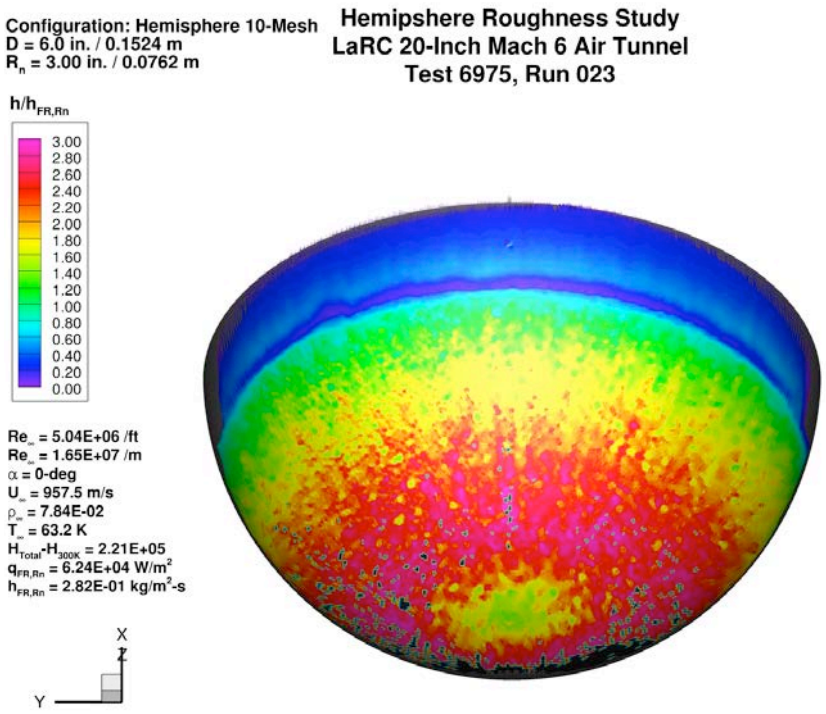

Figure 118. Test 6975, Run 23: Mach 6, $Re_\infty = 5.0\times10^6$/ft, 10-Mesh model, global heating image.

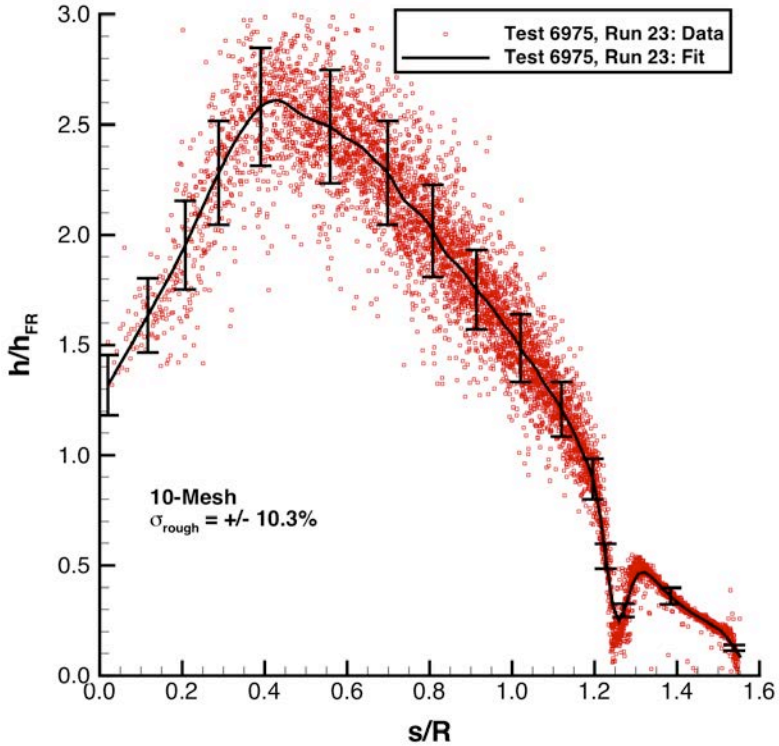

Figure 119. Test 6975, Run 23: Mach 6, $Re_\infty = 5.0\times10^6$/ft, 10-Mesh model, heating data and fit.

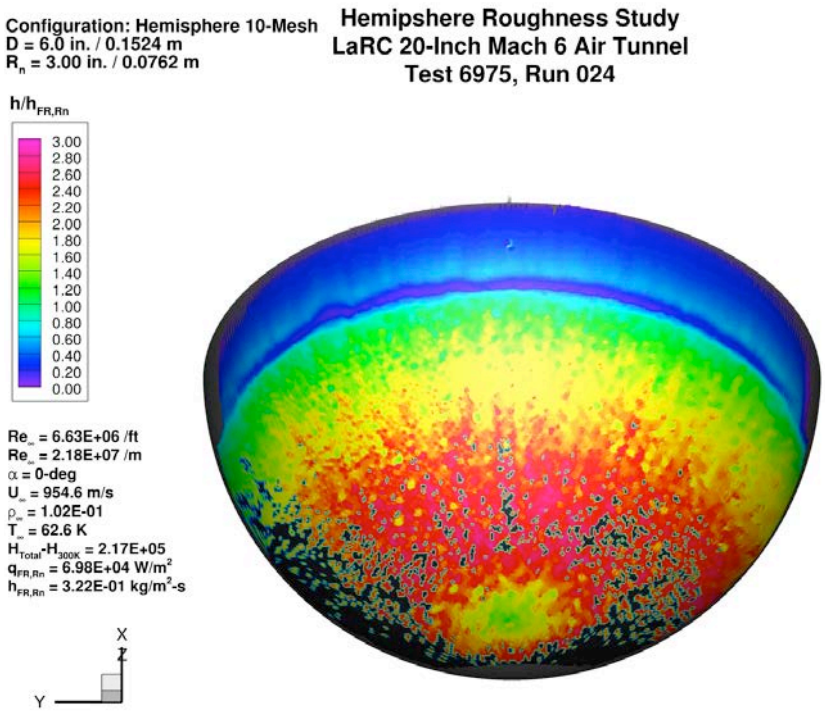

Figure 120. Test 6975, Run 24: Mach 6, $Re_\infty = 6.6\times10^6$/ft, 10-Mesh model, global heating image.

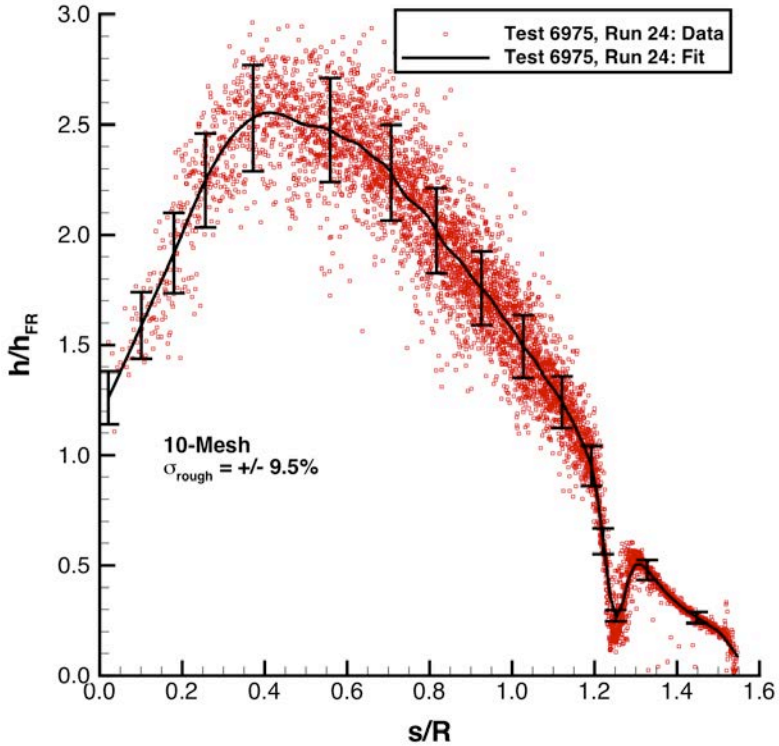

Figure 121. Test 6975, Run 24: Mach 6, $Re_\infty = 6.6\times10^6$/ft, 10-Mesh model, heating data and fit.

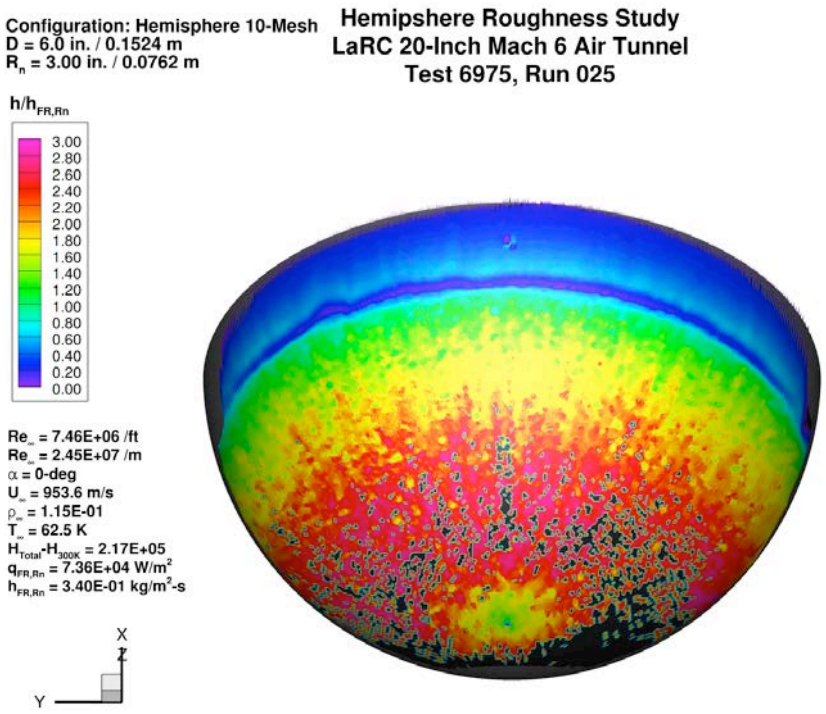

Figure 122. Test 6975, Run 25: Mach 6, $Re_\infty = 7.5\times10^6$/ft, 10-Mesh model, global heating image.

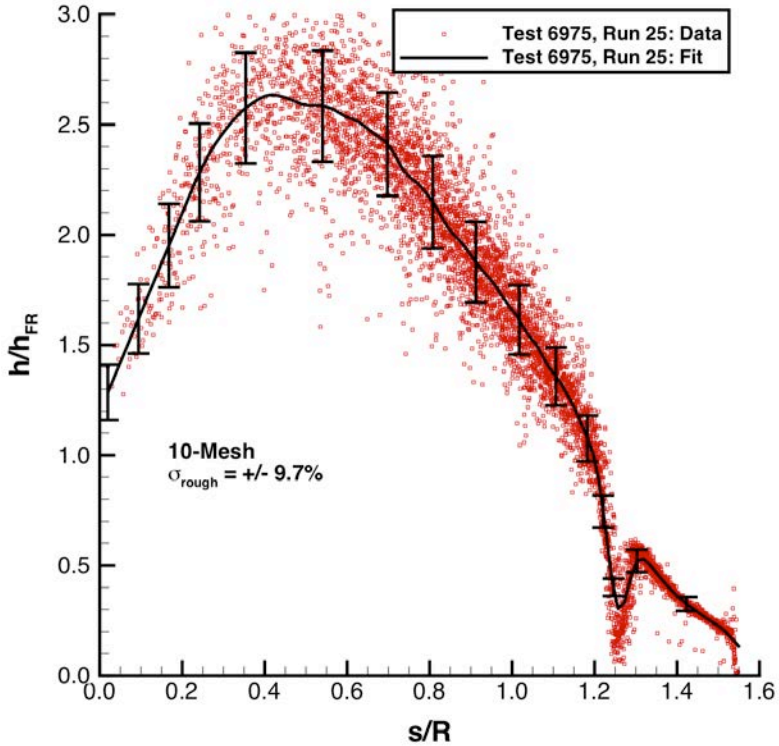

Figure 123. Test 6975, Run 25: Mach 6, $Re_\infty = 7.5\times10^6$/ft, 10-Mesh model, heating data and fit.

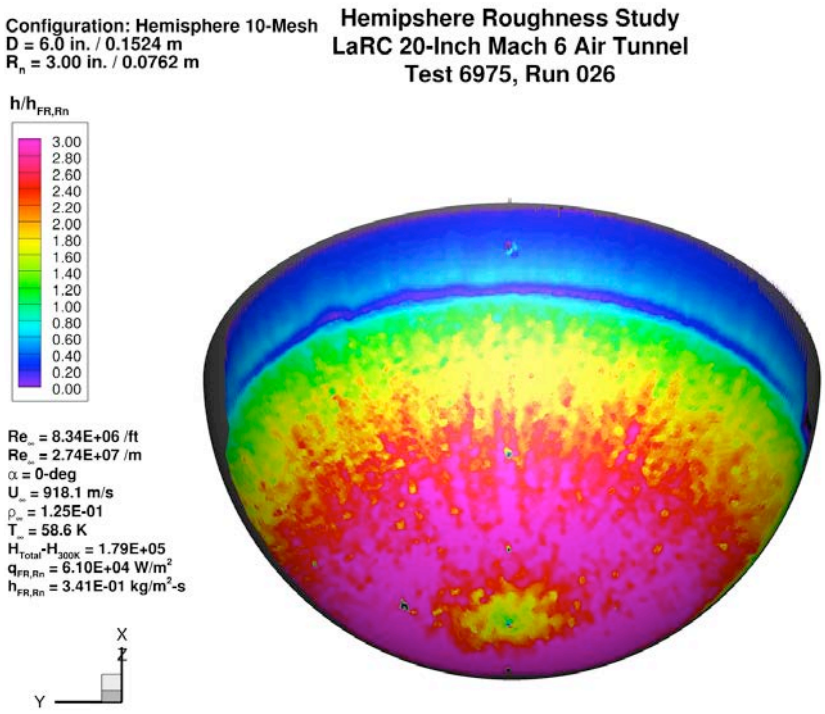

Figure 124. Test 6975, Run 26: Mach 6, $Re_\infty = 8.3\times10^6$/ft, 10-Mesh model, global heating image.

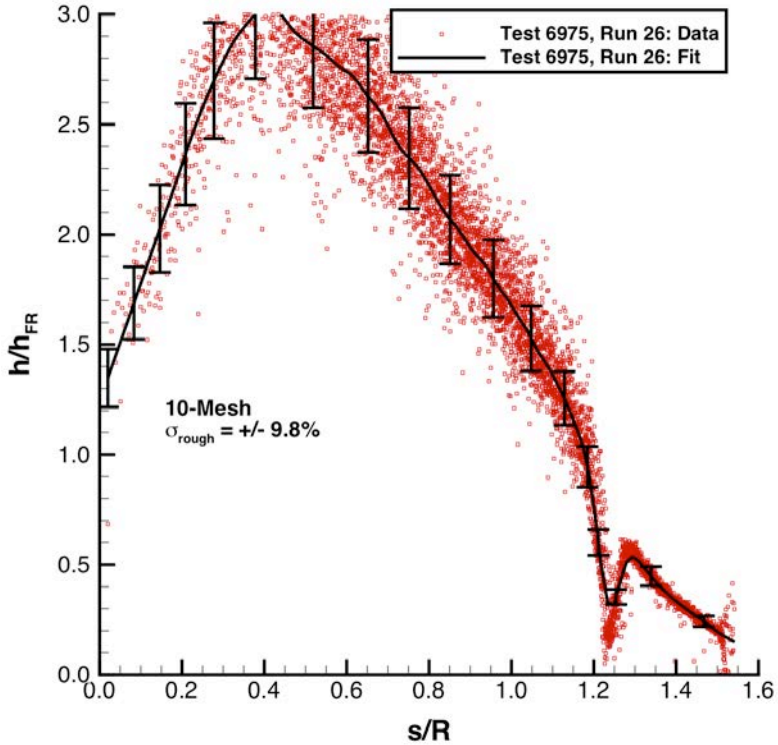

Figure 125. Test 6975, Run 26: Mach 6, $Re_\infty = 8.3\times10^6$/ft, 10-Mesh model, heating data and fit.

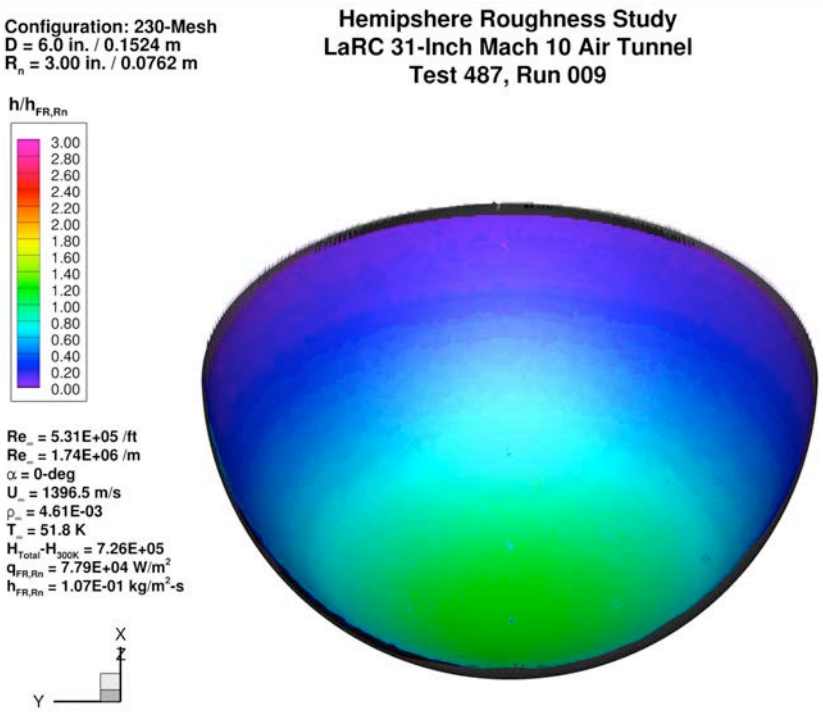

Figure 126. Test 487, Run 09: Mach 10, $Re_\infty = 0.5\times10^6$/ft, 230-Mesh model, global heating image.

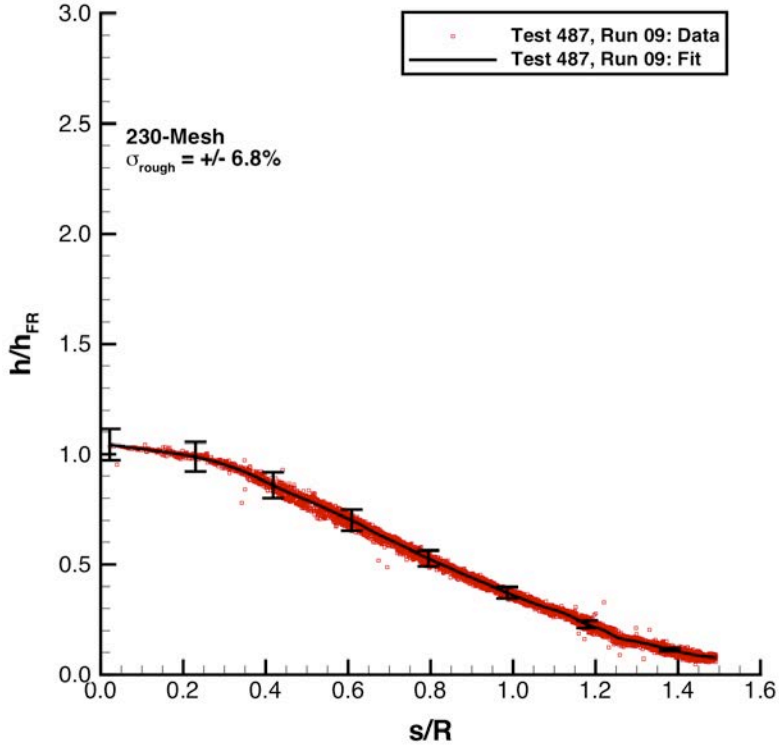

Figure 127. Test 487, Run 09: Mach 10, $Re_\infty = 0.5\times10^6$/ft, 230-Mesh model, heating data and fit.

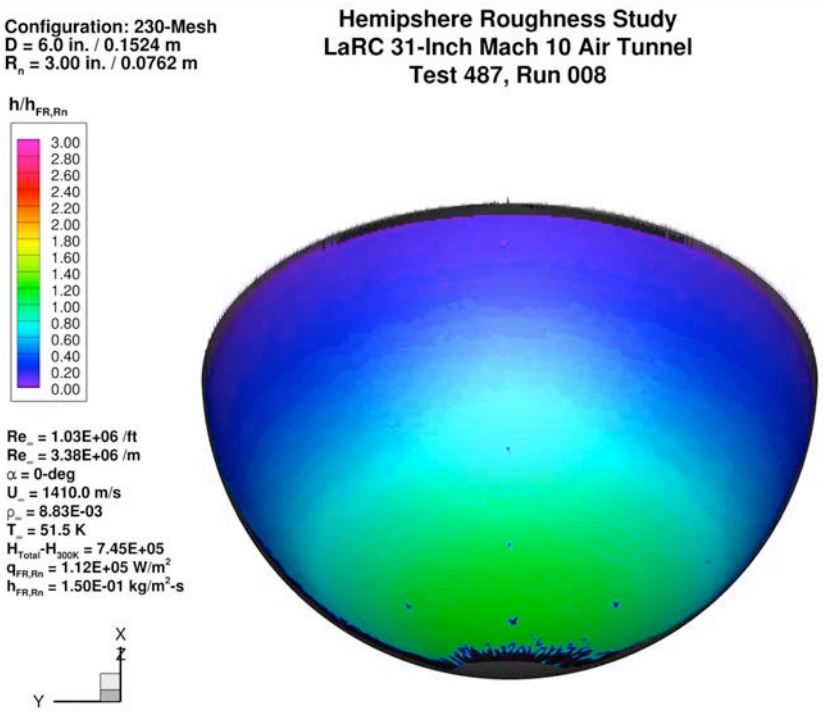

Figure 128. Test 487, Run 08: Mach 10, $Re_\infty = 1.0\times10^6$/ft, 230-Mesh model, global heating image.

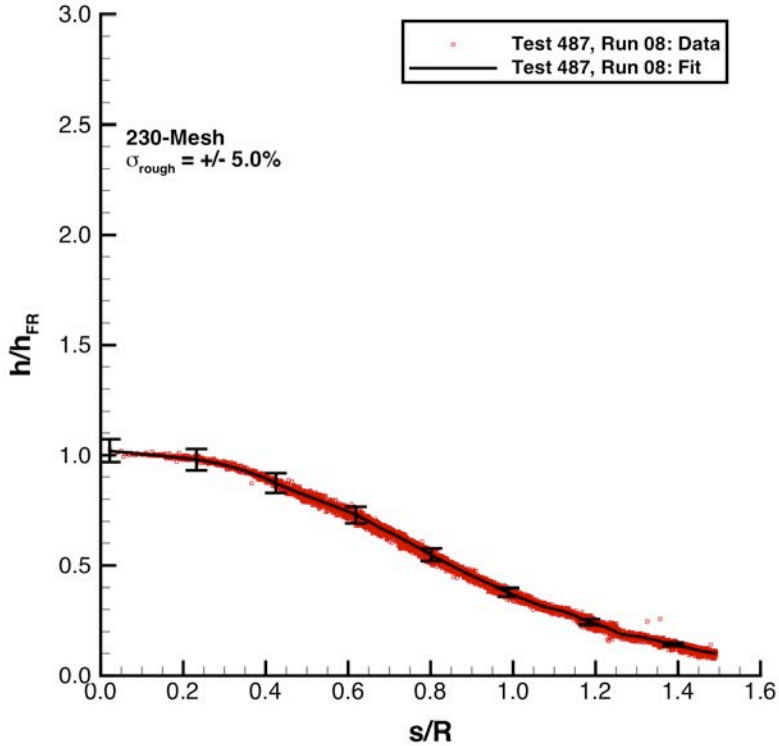

Figure 129. Test 487, Run 08: Mach 10, $Re_\infty = 1.0\times10^6$/ft, 230-Mesh model, heating data and fit.

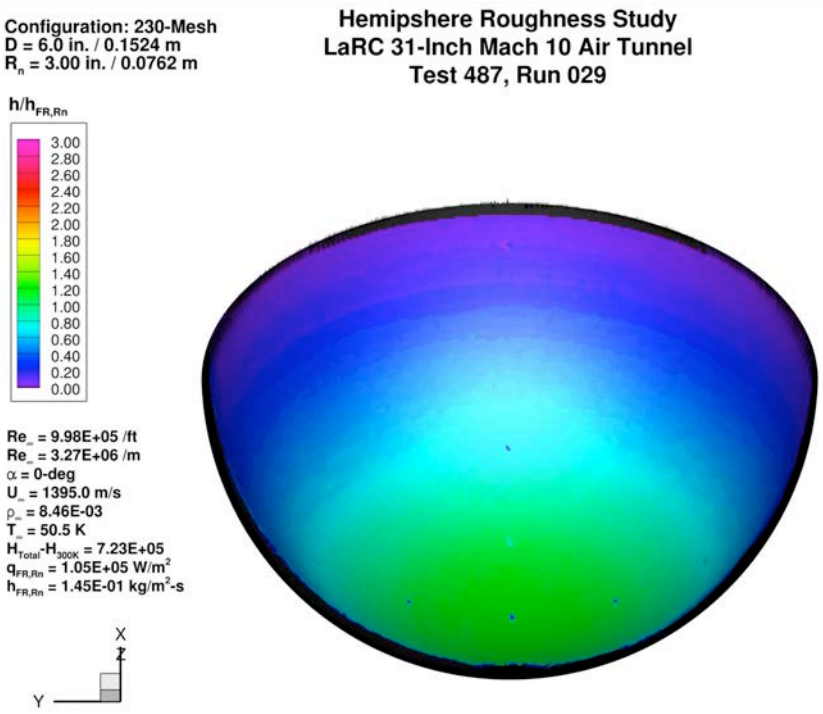

Figure 130. Test 487, Run 29: Mach 10, $Re_\infty = 1.0\times10^6$/ft, 230-Mesh model, global heating image.

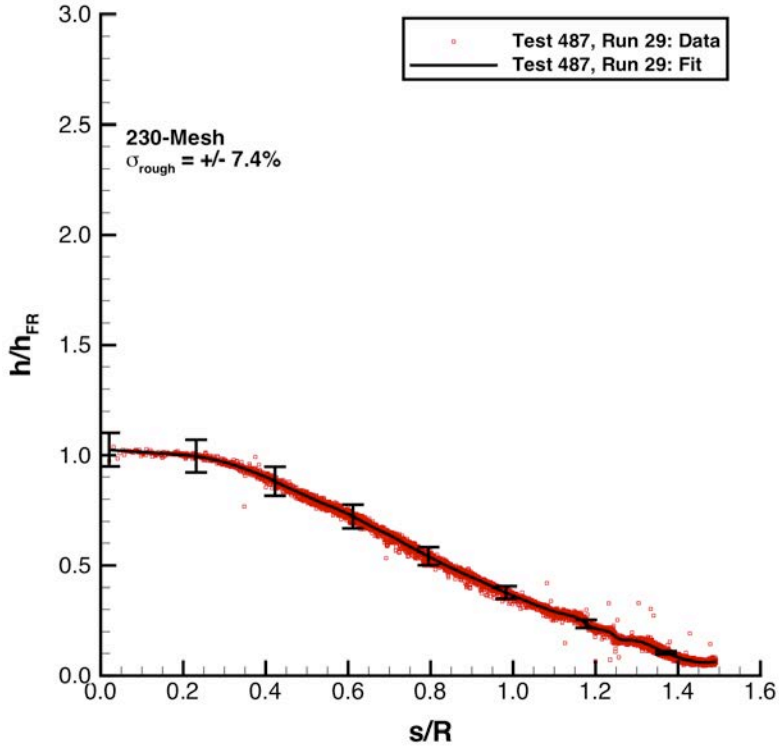

Figure 131. Test 487, Run 29: Mach 10, $Re_\infty = 1.0\times10^6$/ft, 230-Mesh model, heating data and fit.

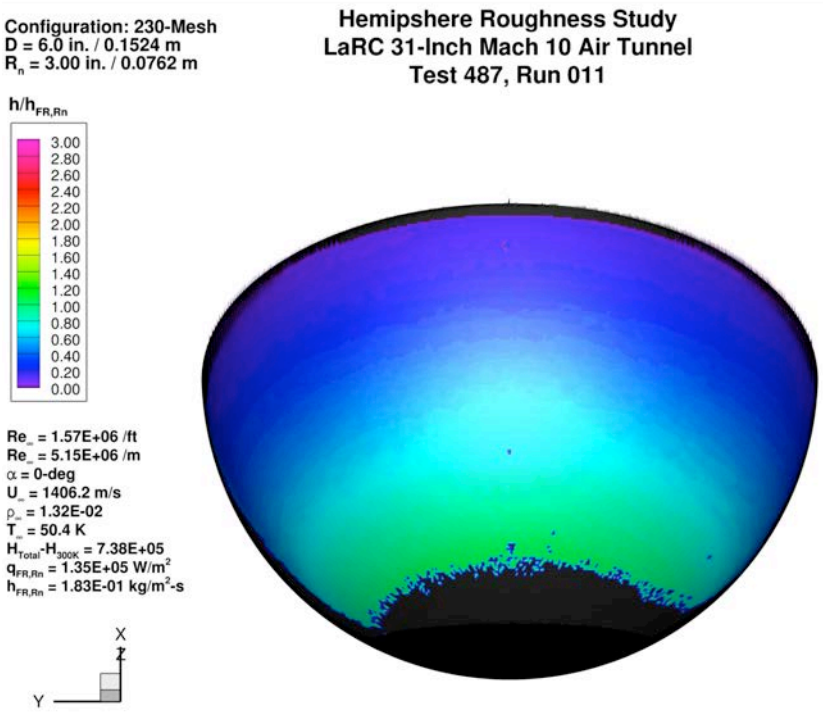

Figure 132. Test 487, Run 11: Mach 10, $Re_\infty = 1.5\times10^6$/ft, 230-Mesh model, global heating image.

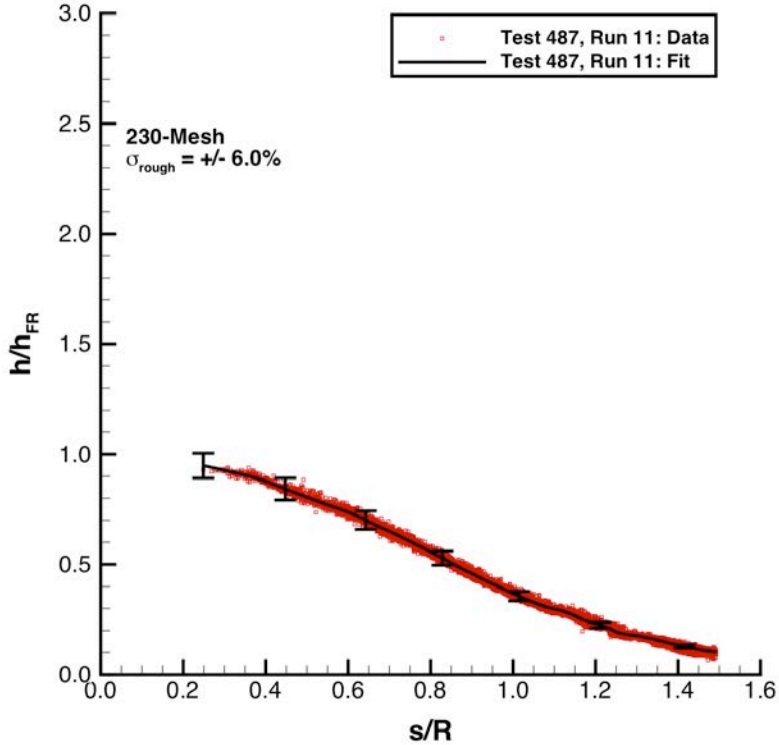

Figure 133. Test 487, Run 11: Mach 10, $Re_\infty = 1.5\times10^6$/ft, 230-Mesh model, heating data and fit.

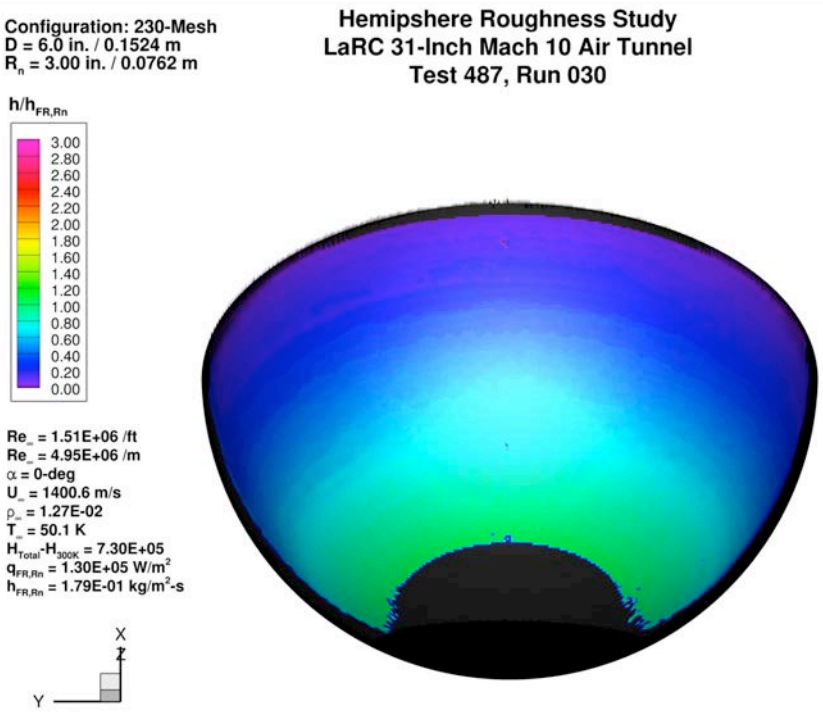

Figure 134. Test 487, Run 30: Mach 10, $Re_\infty = 1.5\times10^6$/ft, 230-Mesh model, global heating image.

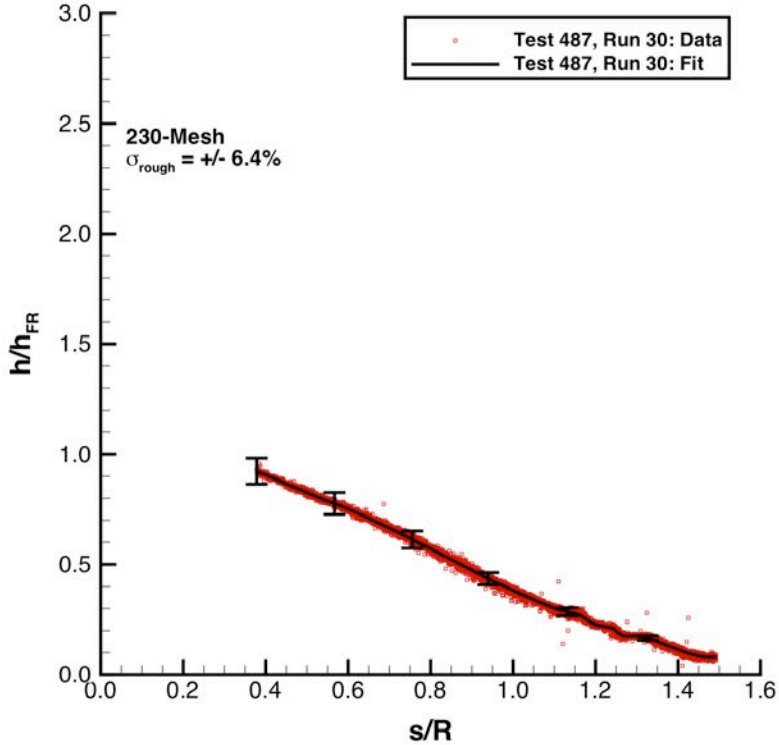

Figure 135. Test 487, Run 30: Mach 10, $Re_\infty = 1.5\times10^6$/ft, 230-Mesh model, heating data and fit.

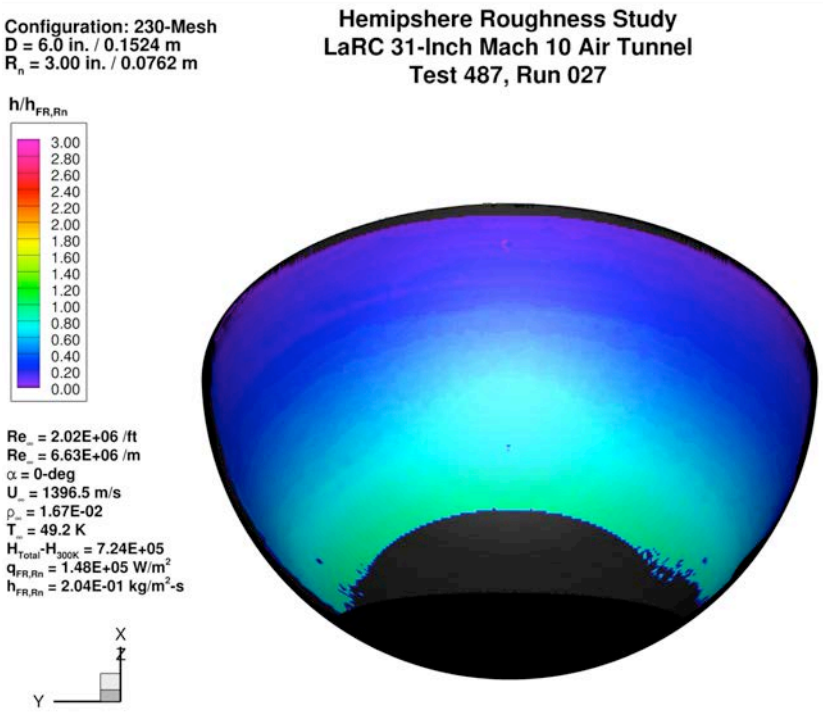

Figure 136. Test 487, Run 27: Mach 10, $Re_\infty = 2.0\times10^6$/ft, 230-Mesh model, global heating image.

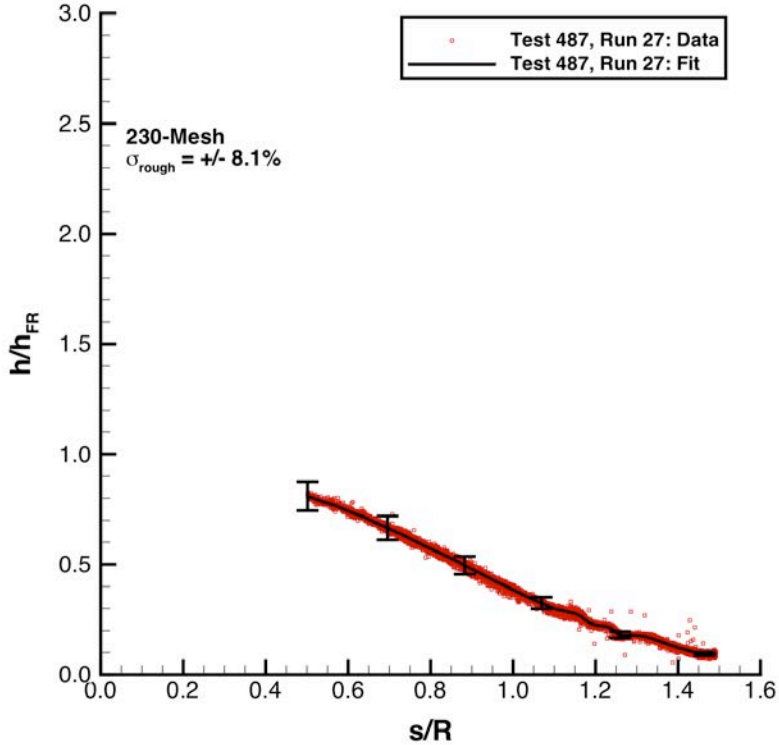

Figure 137. Test 487, Run 27: Mach 10, $Re_\infty = 2.0\times10^6$/ft, 230-Mesh model, heating data and fit.

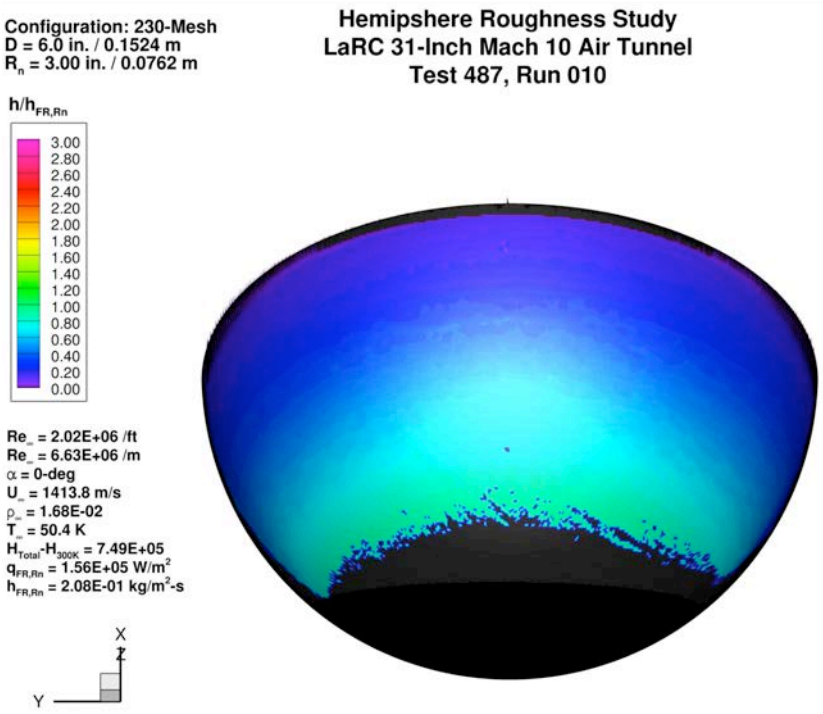

Figure 138. Test 487, Run 10: Mach 10, $Re_\infty = 2.0\times10^6$/ft, 230-Mesh model, global heating image.

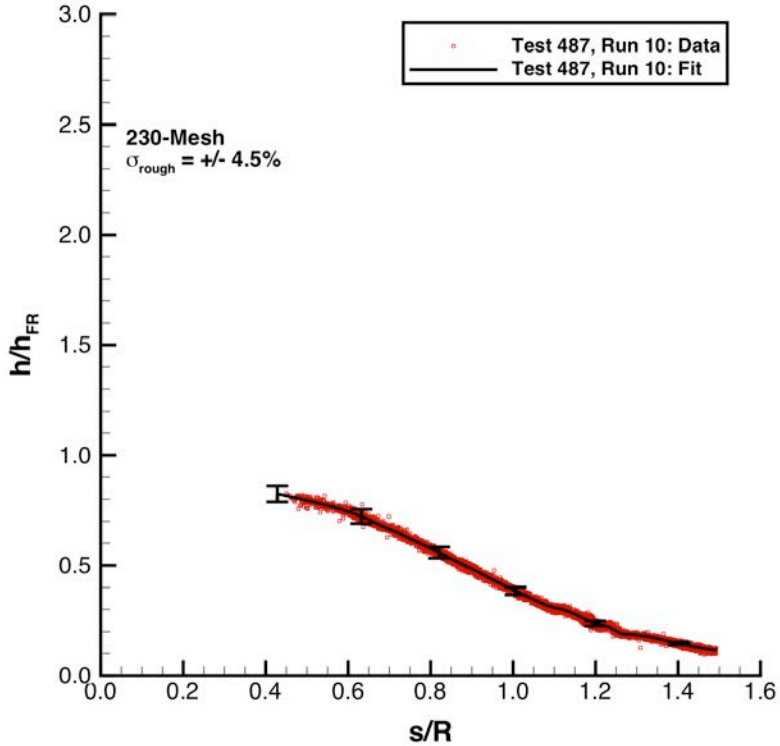

Figure 139. Test 487, Run 10: Mach 10, $Re_\infty = 2.0\times10^6$/ft, 230-Mesh model, heating data and fit.

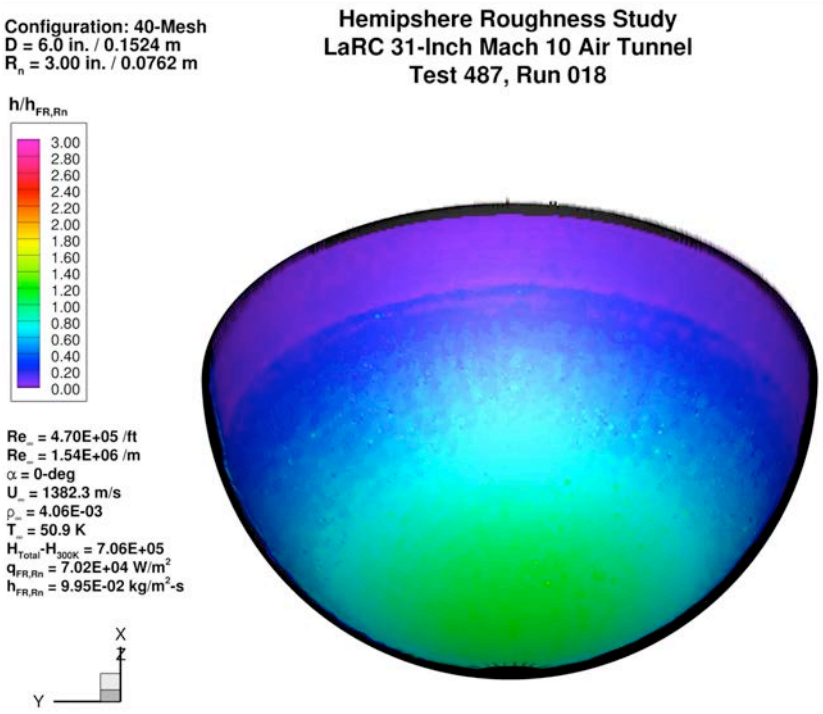

Figure 140. Test 487, Run 18: Mach 10, $Re_\infty = 0.5\times10^6$/ft, 40-Mesh model, global heating image.

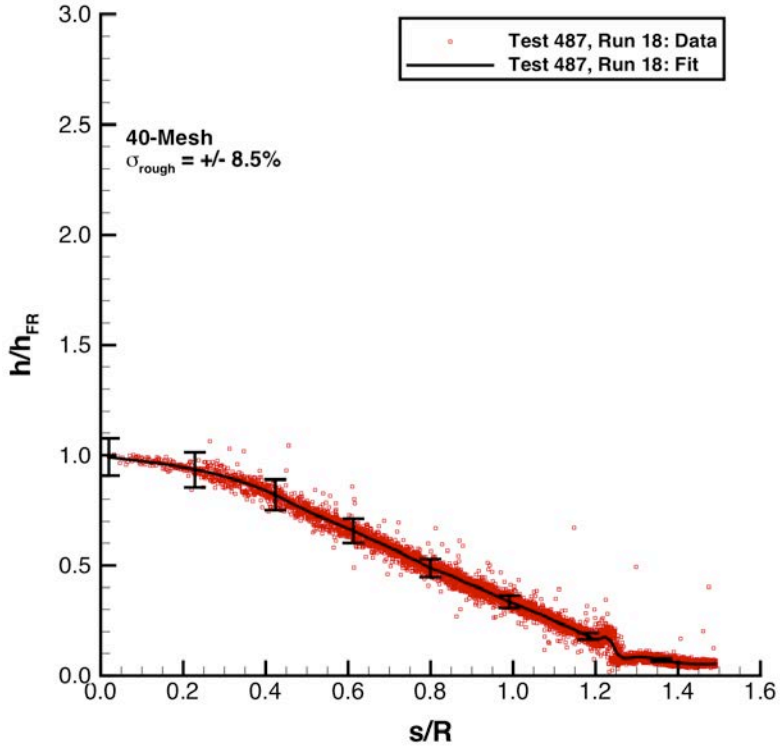

Figure 141. Test 487, Run 18, Mach 10, $Re_\infty = 0.5\times10^6$/ft, 40-Mesh model, heating data and fit.

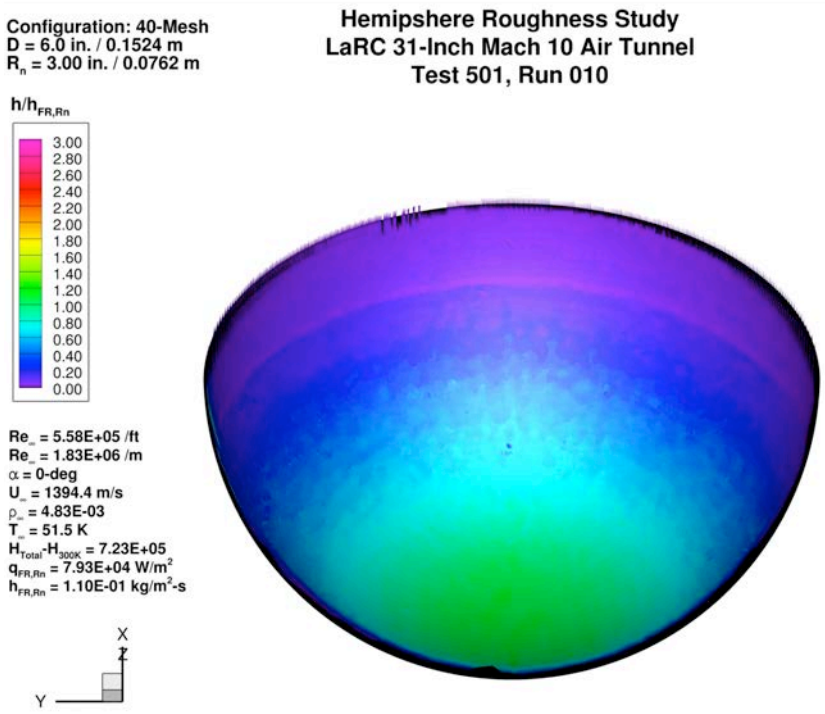

Figure 142. Test 501, Run 10: Mach 10, $Re_\infty = 0.5\times10^6$/ft, 40-Mesh model, global heating image.

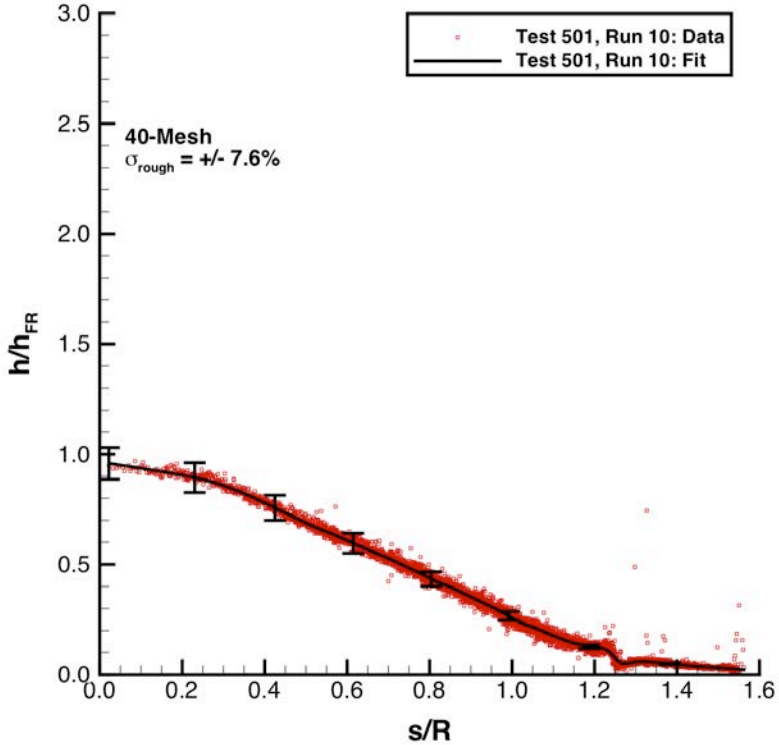

Figure 143. Test 501, Run 10: Mach 10, $Re_\infty = 0.5\times10^6$/ft, 40-Mesh model, heating data and fit.

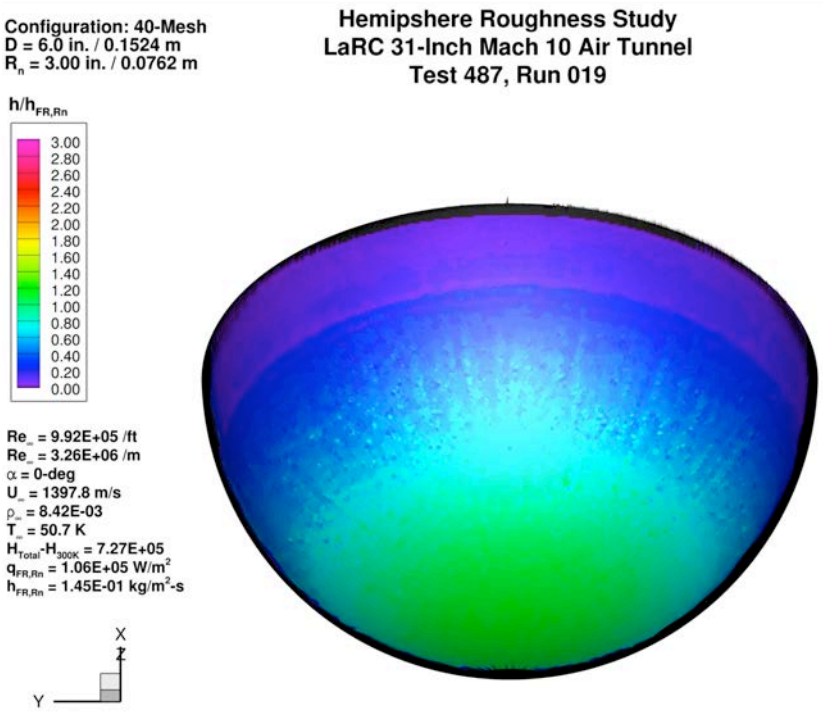

Figure 144. Test 487, Run 19: Mach 10, $Re_\infty = 1.0\times10^6$/ft, 40-Mesh model, global heating image.

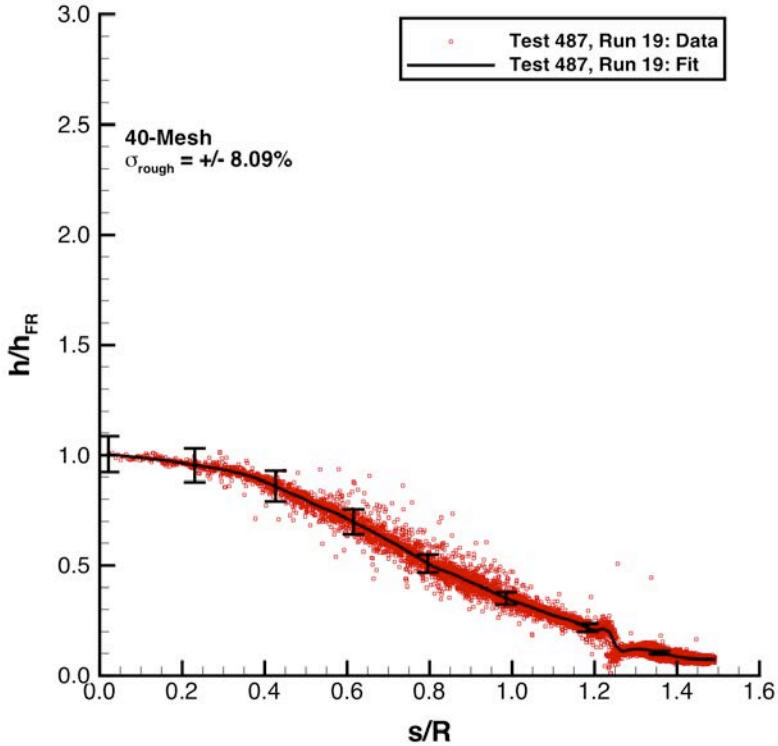

Figure 145. Test 487, Run 19: Mach 10, $Re_\infty = 1.0\times10^6$/ft, 40-Mesh model, heating data and fit.

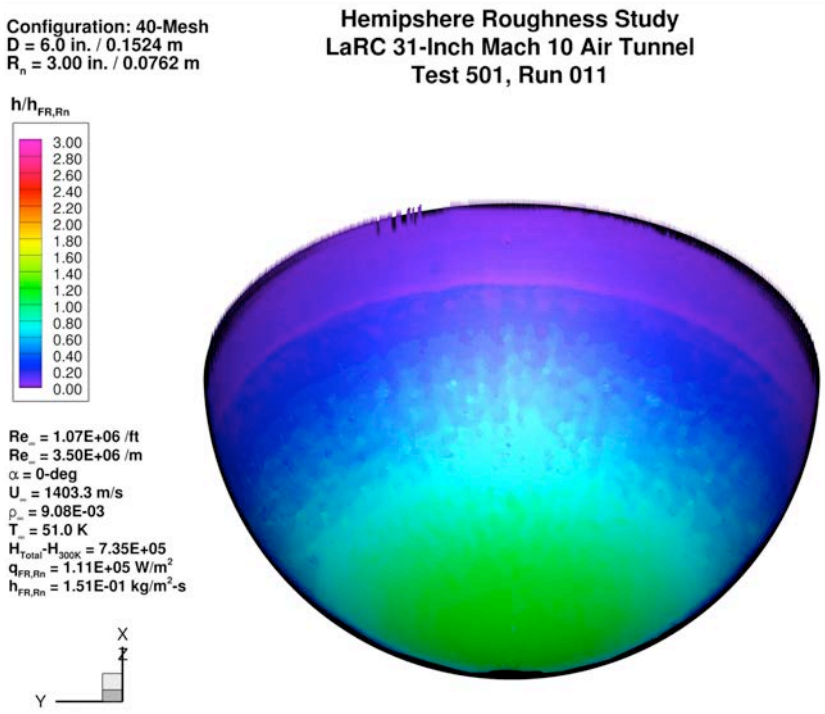

Figure 146. Test 501, Run 11: Mach 10, $Re_\infty = 1.0\times10^6$/ft, 40-Mesh model, global heating image.

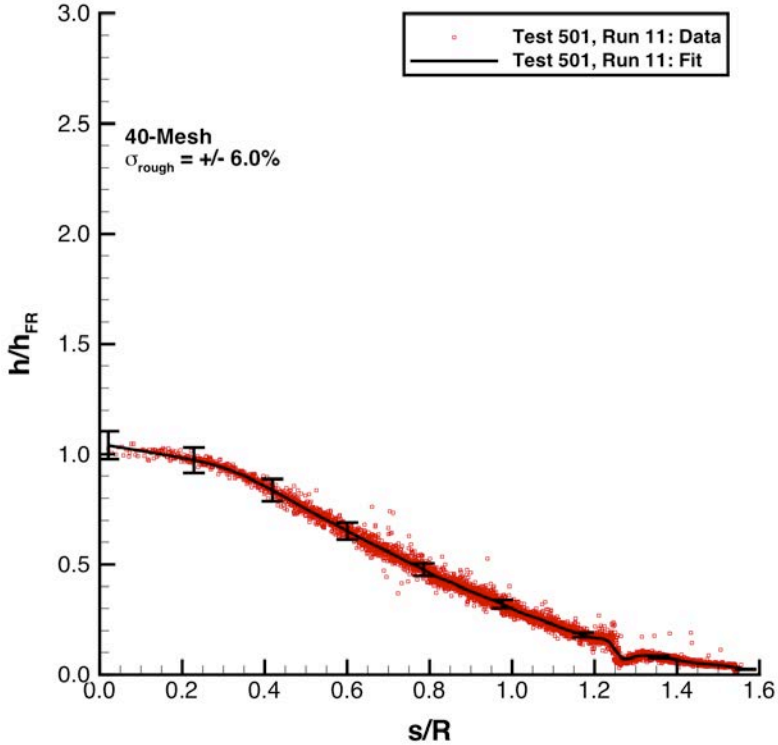

Figure 147. Test 501, Run 11: Mach 10, $Re_\infty = 1.0\times10^6$/ft, 40-Mesh model, heating data and fit.

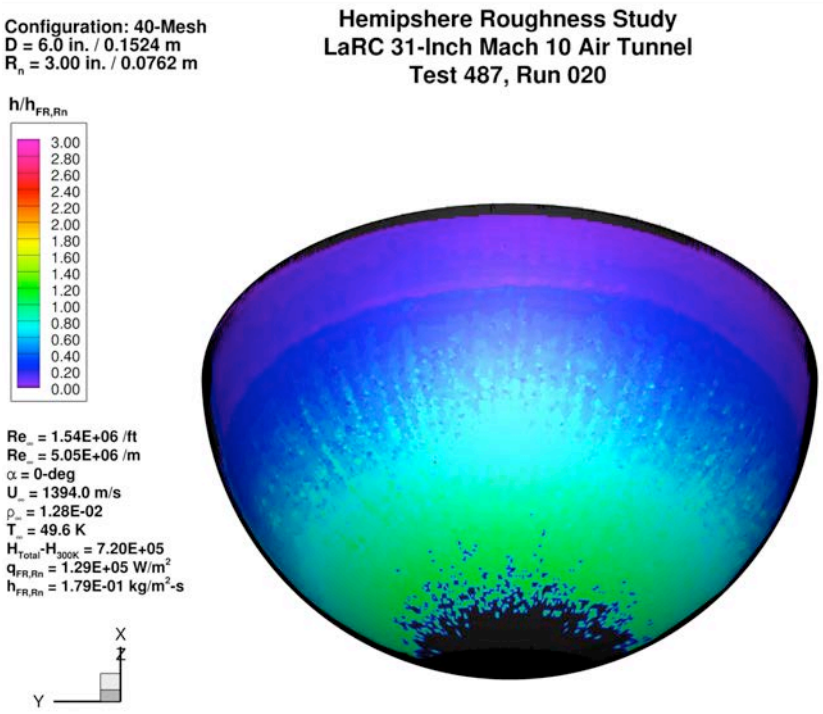

Figure 148. Test 487, Run 20: Mach 10, $Re_\infty = 1.5\times10^6$/ft, 40-Mesh model, global heating image.

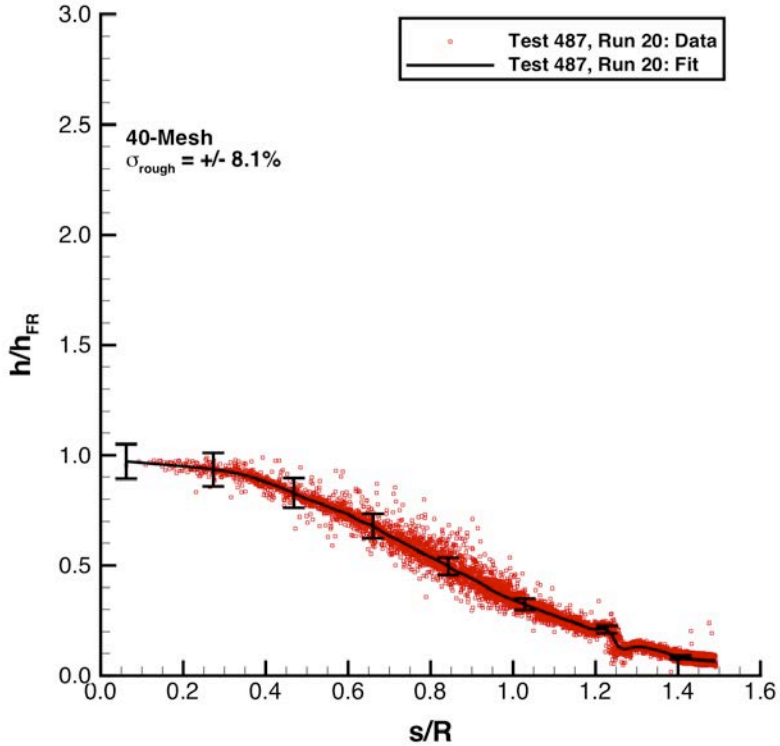

Figure 149. Test 487, Run 20: Mach 10, $Re_\infty = 1.5\times10^6$/ft, 40-Mesh model, heating data and fit.

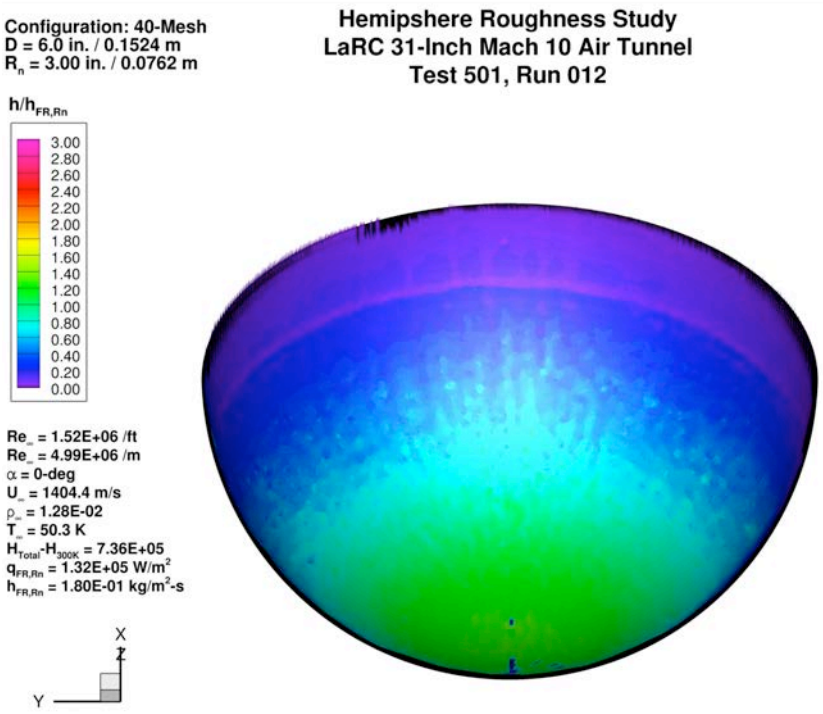

Figure 150. Test 501, Run 12: Mach 10, $Re_\infty = 1.5\times10^6$/ft, 140-Mesh model, global heating image.

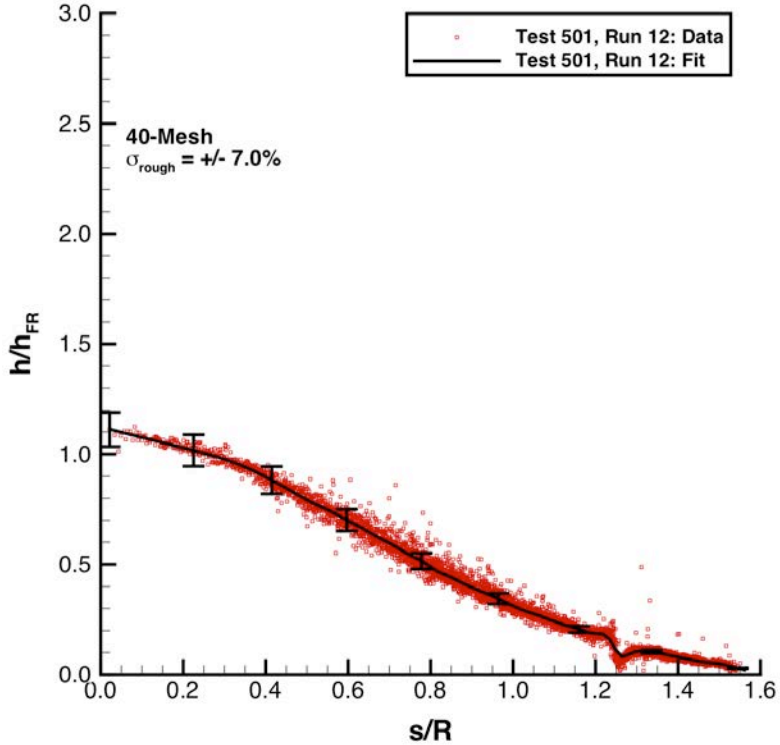

Figure 151. Test 501, Run 12: Mach 10, $Re_\infty = 1.5\times10^6$/ft, 140-Mesh model, heating data and fit.

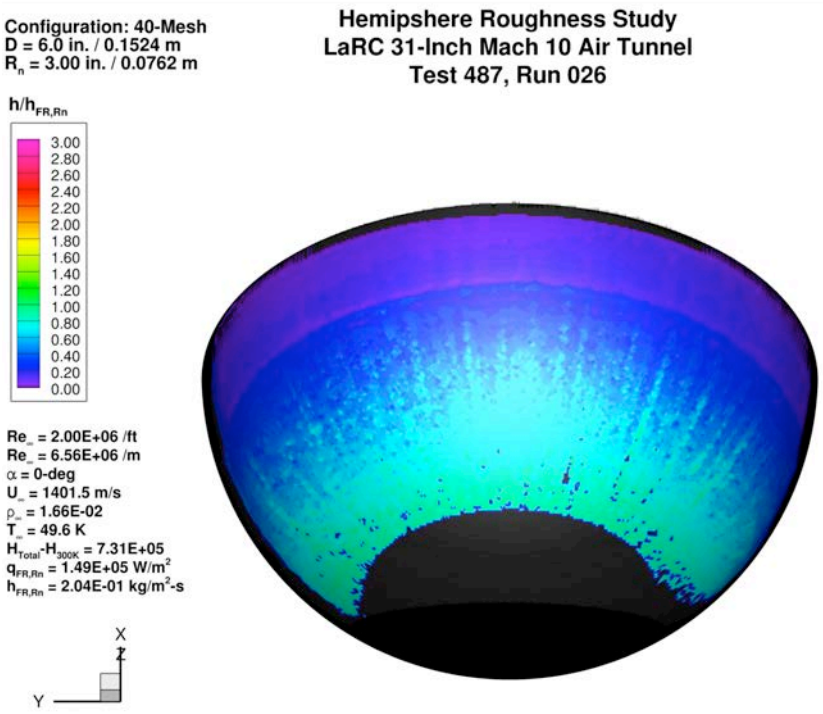

Figure 152. Test 487, Run 26: Mach 10, $Re_\infty = 2.0\times10^6$/ft, 40-Mesh model, global heating image.

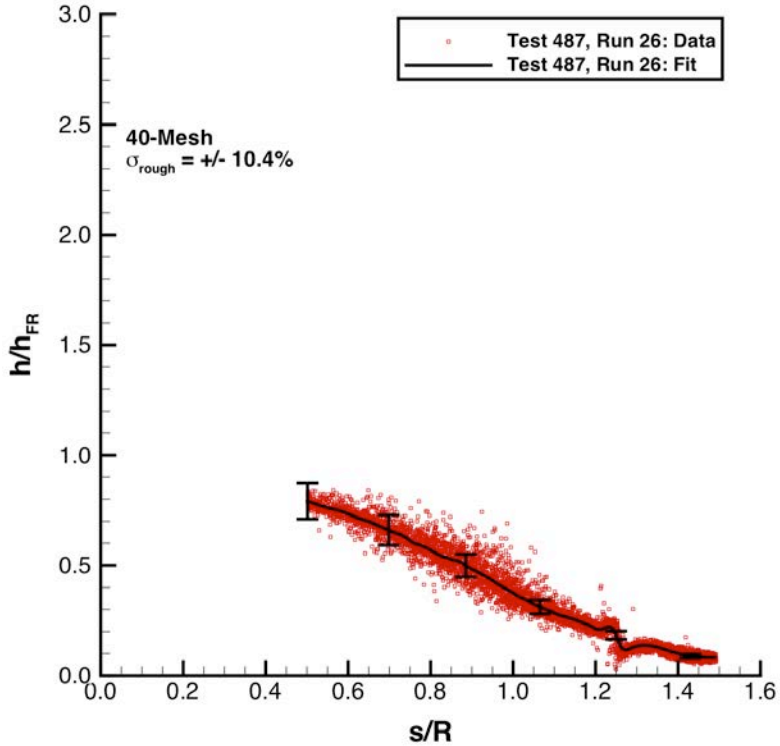

Figure 153. Test 487, Run 26: Mach 10, $Re_\infty = 2.0\times10^6$/ft, 40-Mesh model, heating data and fit.

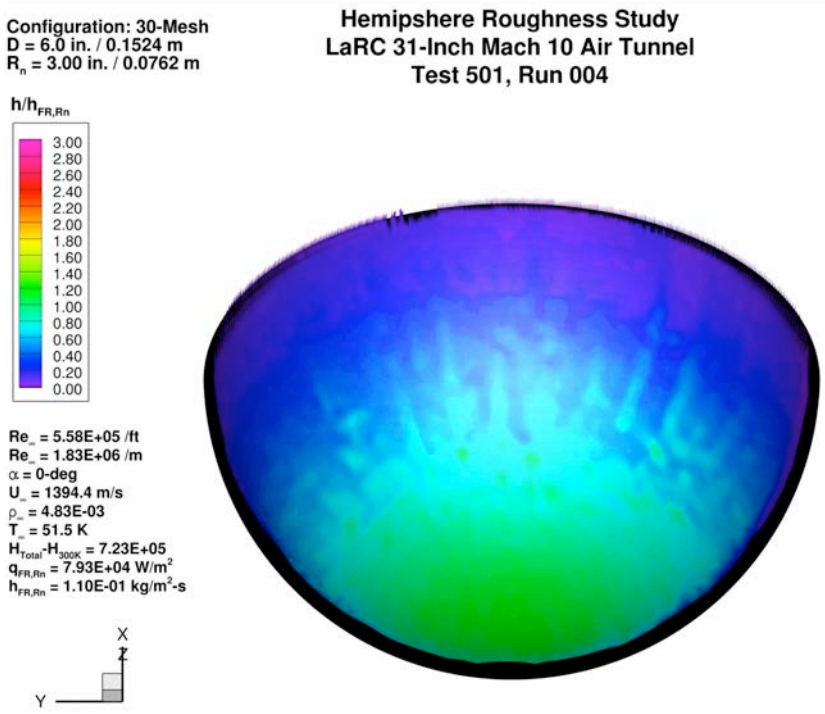

Figure 154. Test 501, Run 04: Mach 10, $Re_\infty = 0.5\times10^6$/ft, 30-Mesh model, global heating image.

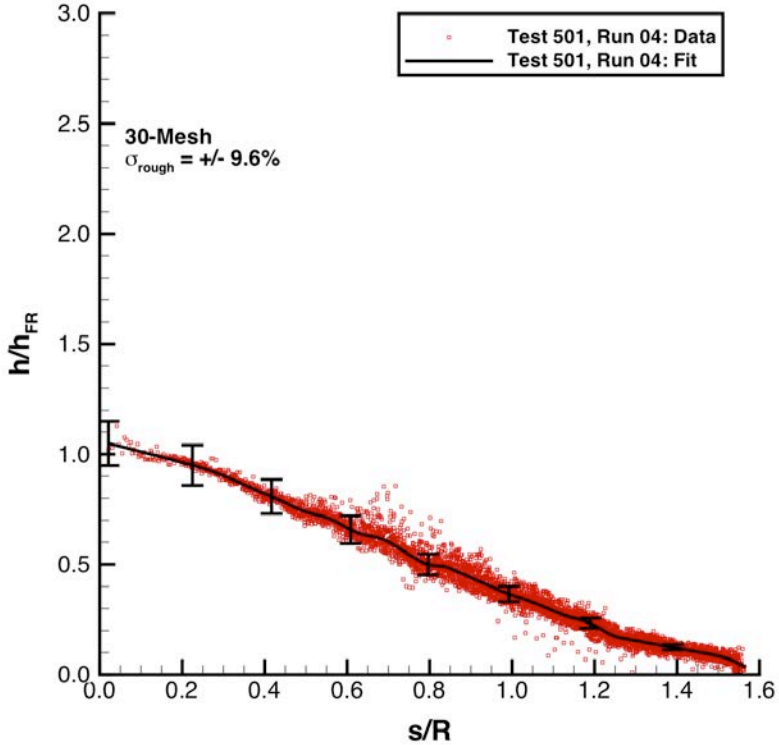

Figure 155. Test 501, Run 04: Mach 10, $Re_\infty = 0.5\times10^6$/ft, 30-Mesh model, heating data and fit.

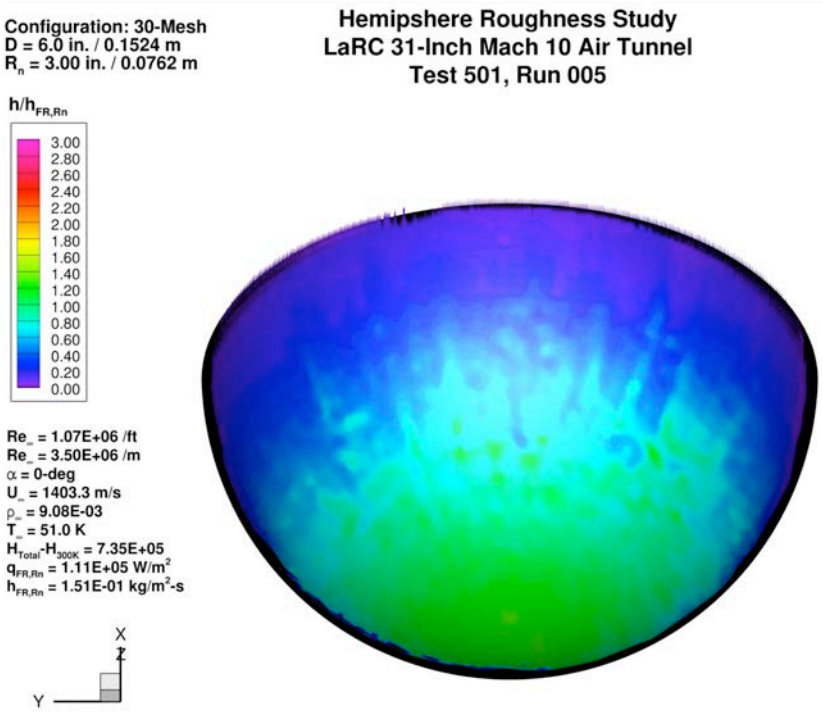

Figure 156. Test 501, Run 05: Mach 10, $Re_\infty = 1.0\times10^6$/ft, 30-Mesh model, global heating image.

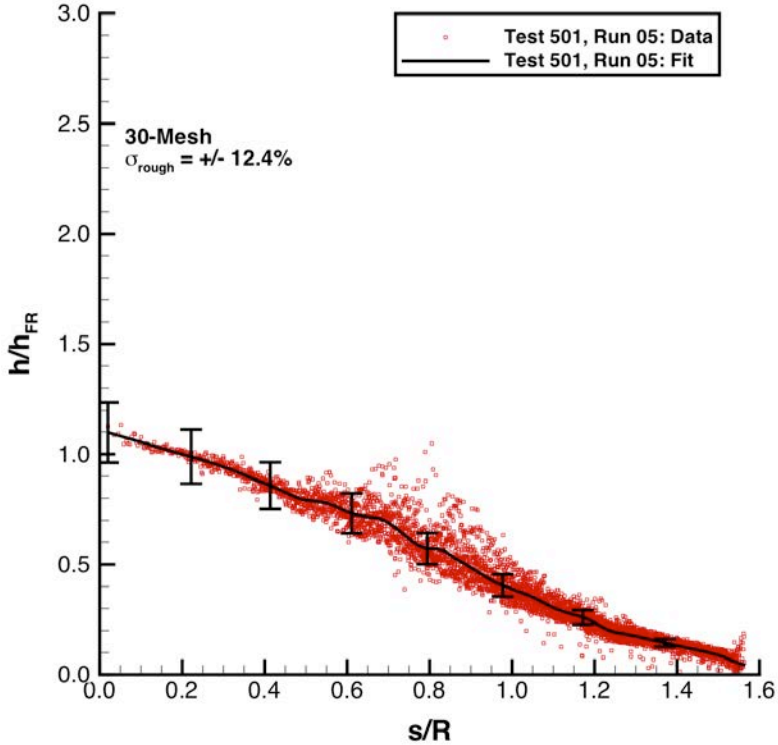

Figure 157. Test 501, Run 05: Mach 10, $Re_\infty = 1.0\times10^6$/ft, 30-Mesh model, heating data and fit.

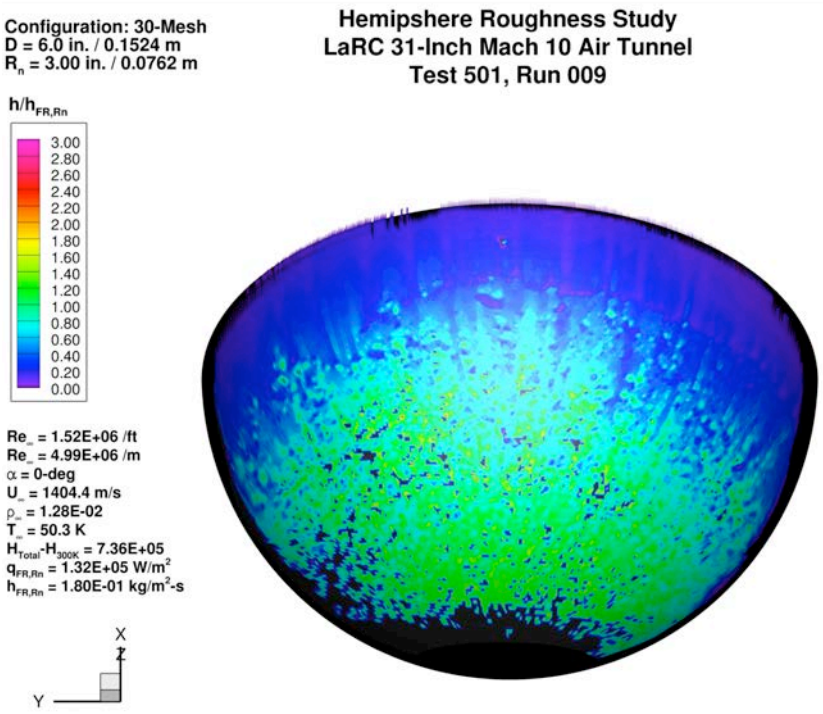

Figure 158. Test 501, Run 09: Mach 10, $Re_\infty = 1.5\times10^6$/ft, 30-Mesh model, global heating image.

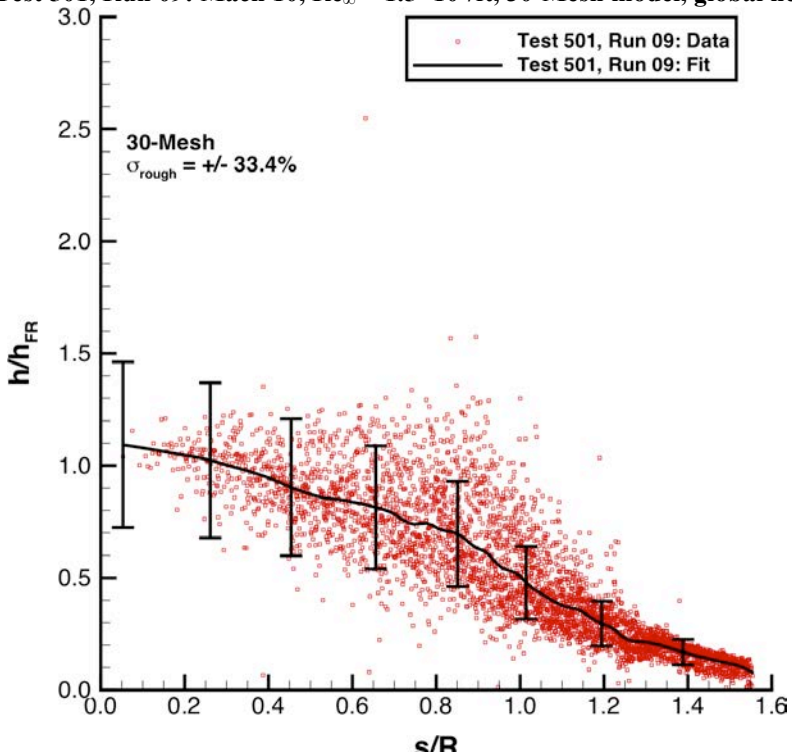

Figure 159. Test 501, Run 09: Mach 10, $Re_\infty = 1.5\times10^6$/ft, 30-Mesh model, heating data and fit.

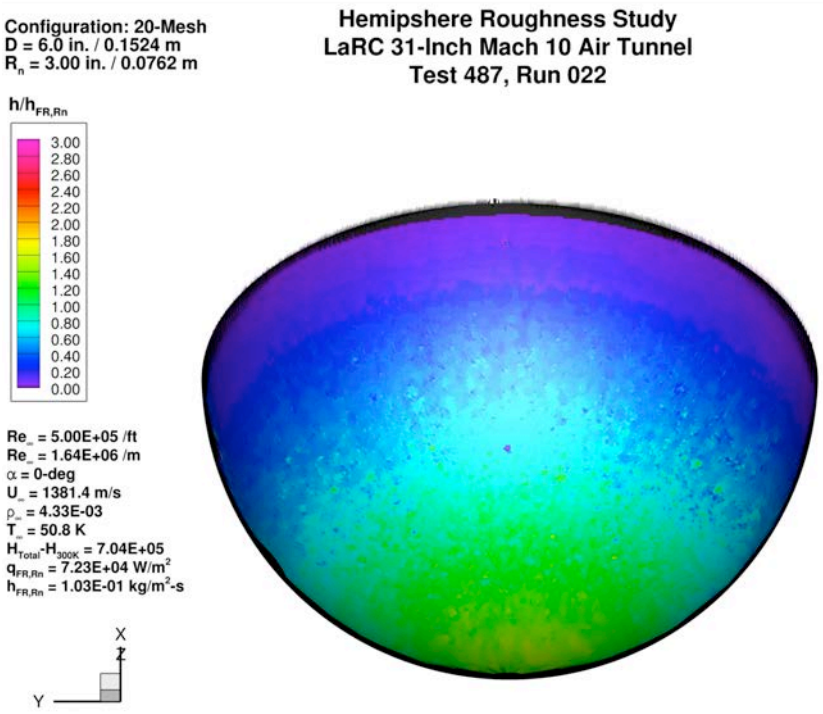

Figure 160. Test 487, Run 22: Mach 10, $Re_\infty = 0.5\times10^6$/ft, 20-Mesh model, global heating image.

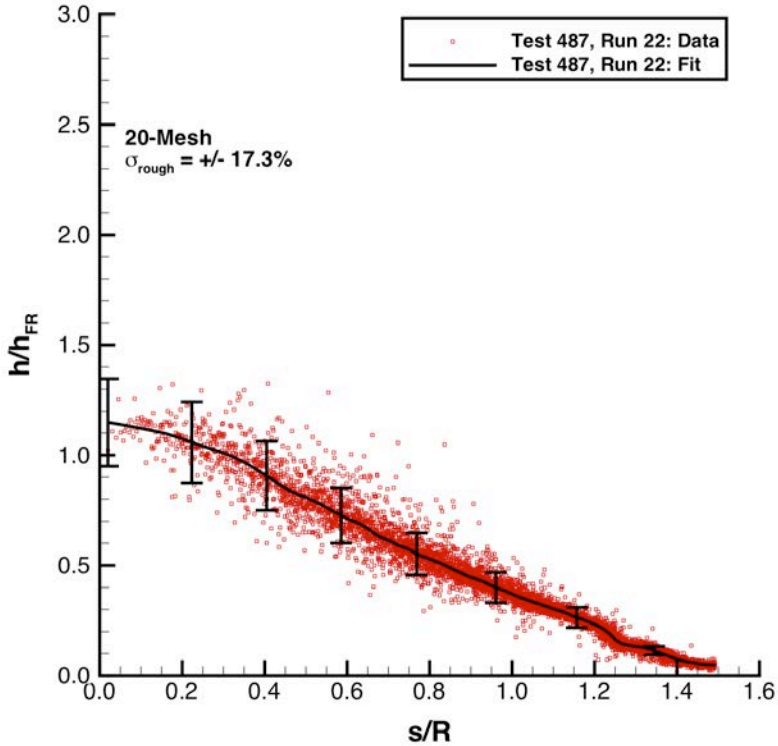

Figure 161. Test 487, Run 22: Mach 10, $Re_\infty = 0.5\times10^6$/ft, 20-Mesh model, heating data and fit.

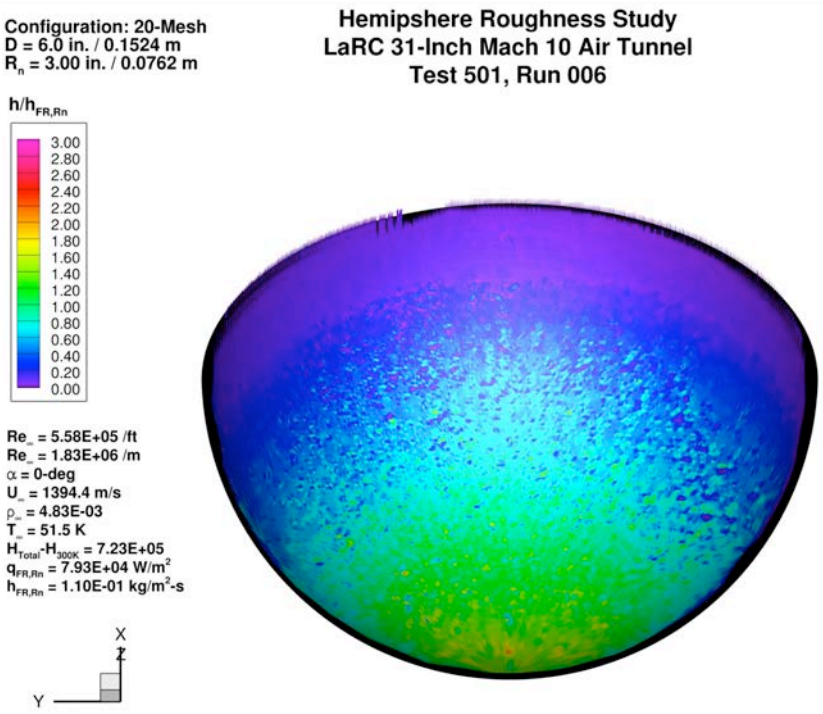

Figure 162. Test 501, Run 06: Mach 10, $Re_\infty = 0.5\times10^6$/ft, 20-Mesh model, global heating image.

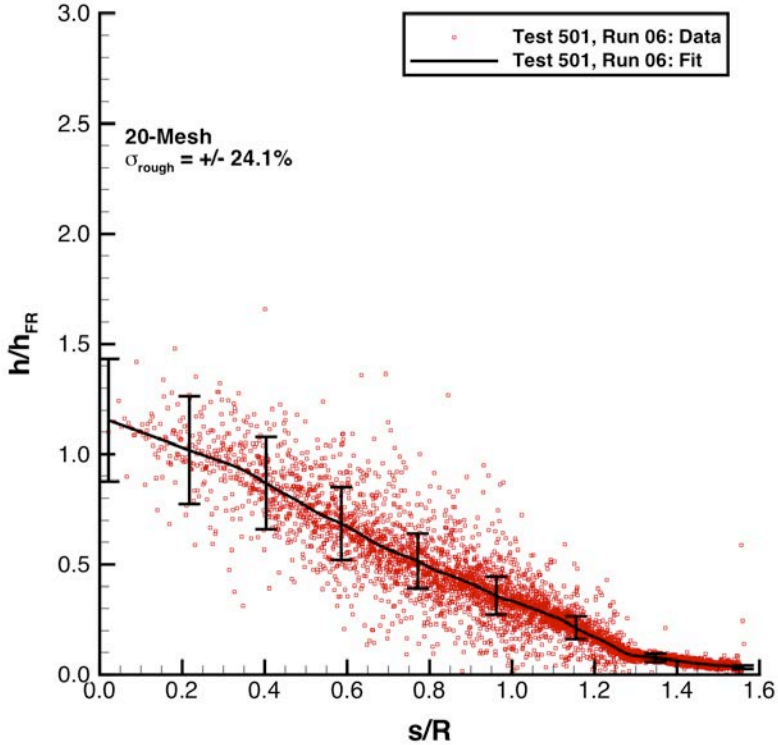

Figure 163. Test 501, Run 06: Mach 10, $Re_\infty = 0.50\times10^6$/ft, 20-Mesh model, heating data and fit.

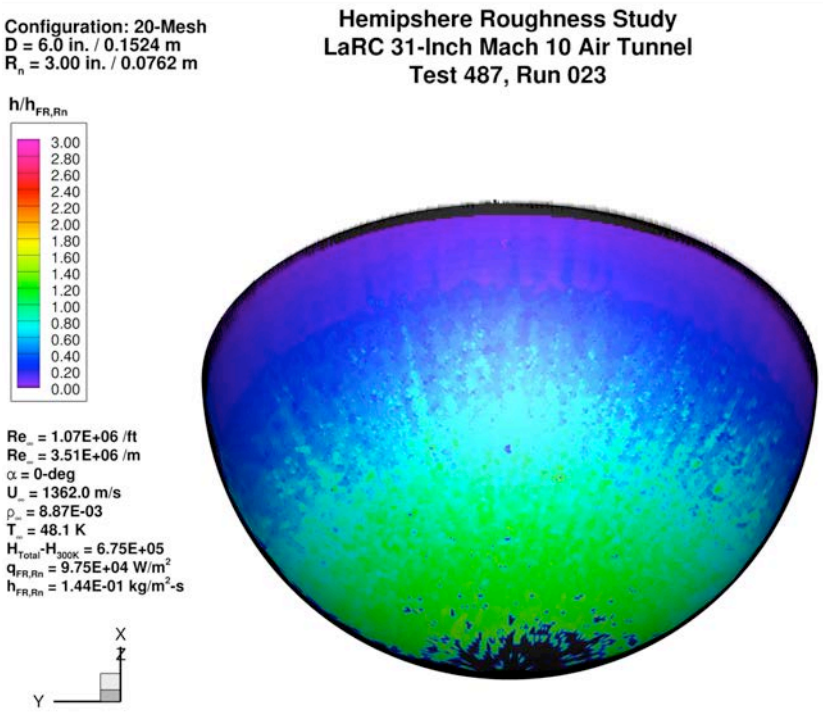

Figure 164. Test 487, Run 23: Mach 10, $Re_\infty = 1.0\times10^6$/ft, 20-Mesh model, global heating image.

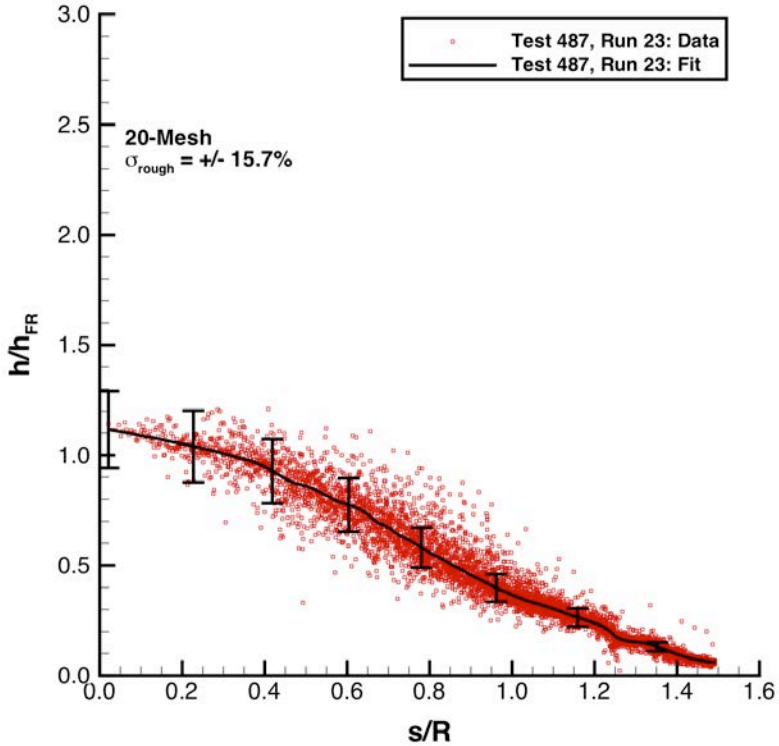

Figure 165. Test 487, Run 23: Mach 10, $Re_\infty = 1.0\times10^6$/ft, 20-Mesh model, heating data and fit.

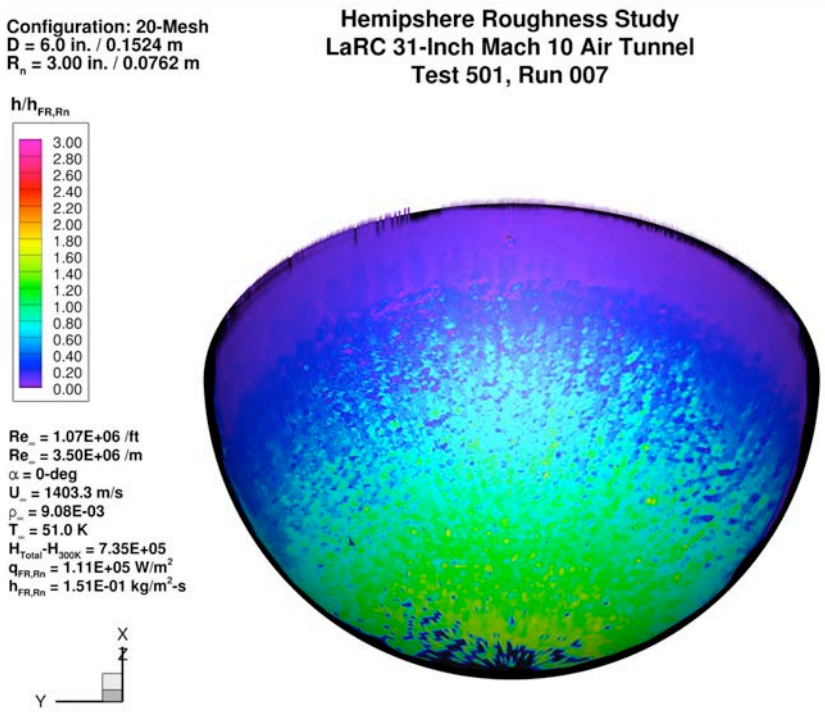

Figure 166. Test 501, Run 07: Mach 10, $Re_\infty = 1.0\times10^6$/ft, 20-Mesh model, global heating image.

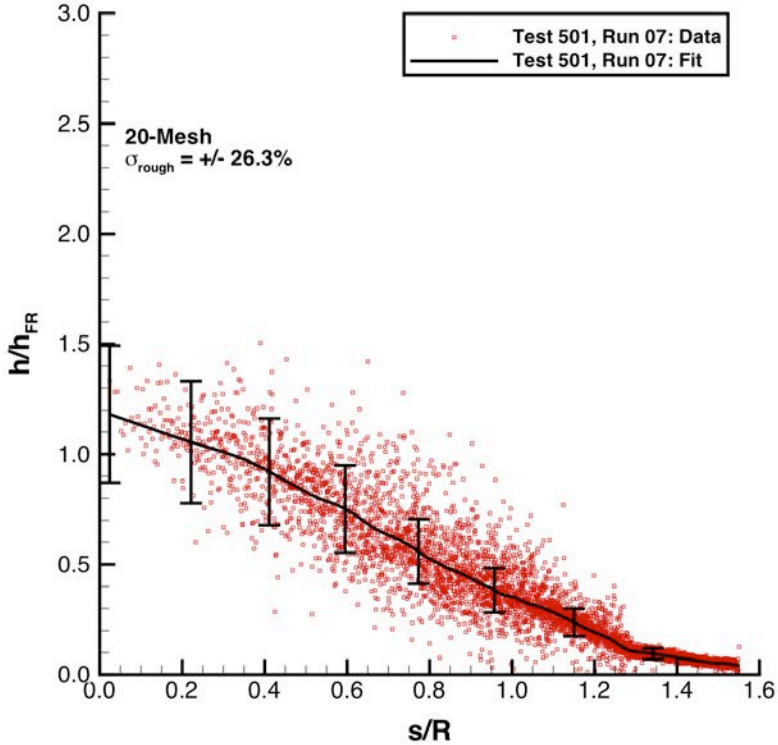

Figure 167. Test 501, Run 07: Mach 10, $Re_\infty = 1.0\times10^6$/ft, 20-Mesh model, heating data and fit.

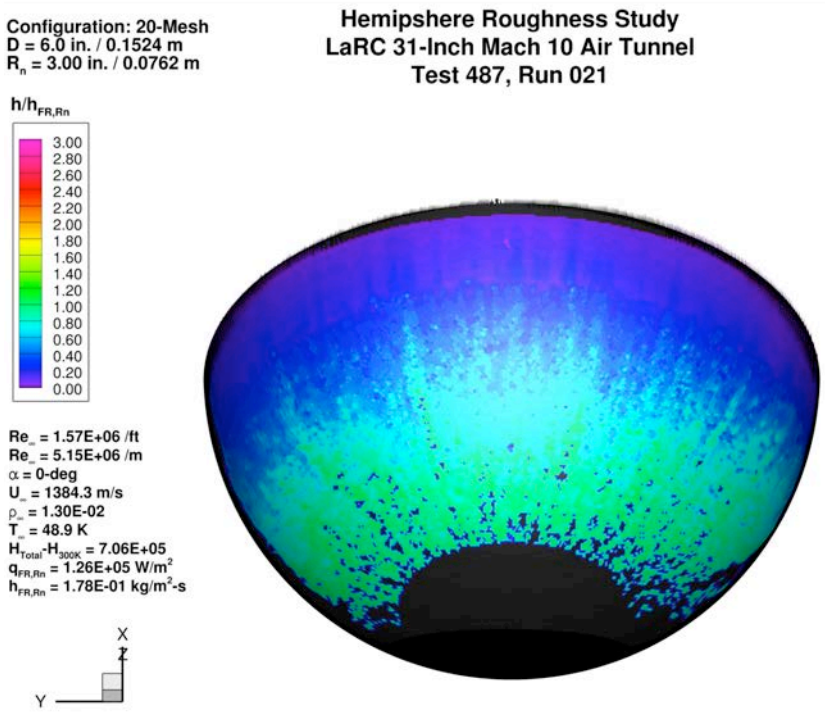

Figure 168. Test 487, Run 21: Mach 10, $Re_\infty = 1.5\times10^6$/ft, 20-Mesh model, global heating image.

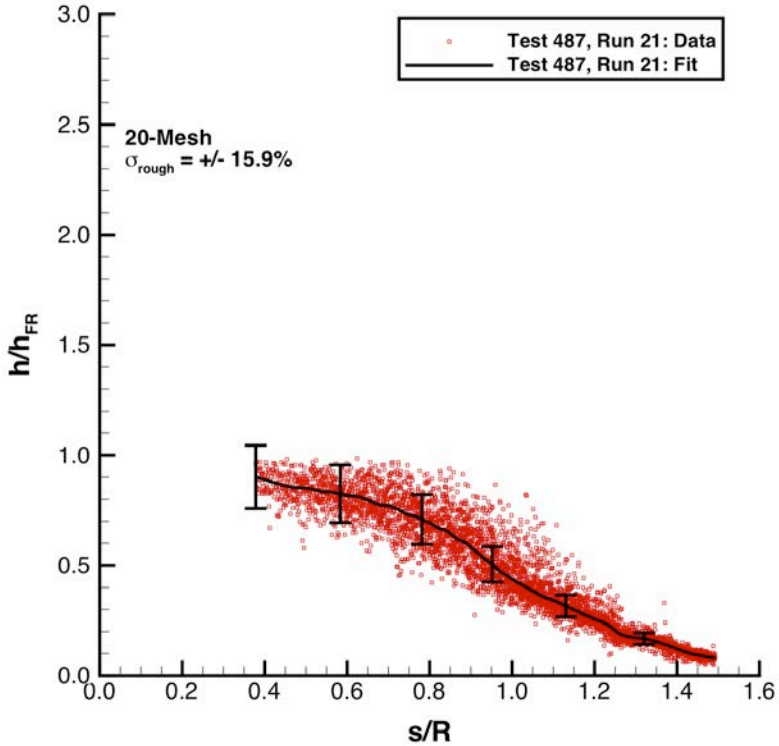

Figure 169. Test 487, Run 21: Mach 10, $Re_\infty = 1.5\times10^6$/ft, 20-Mesh model, heating data and fit.

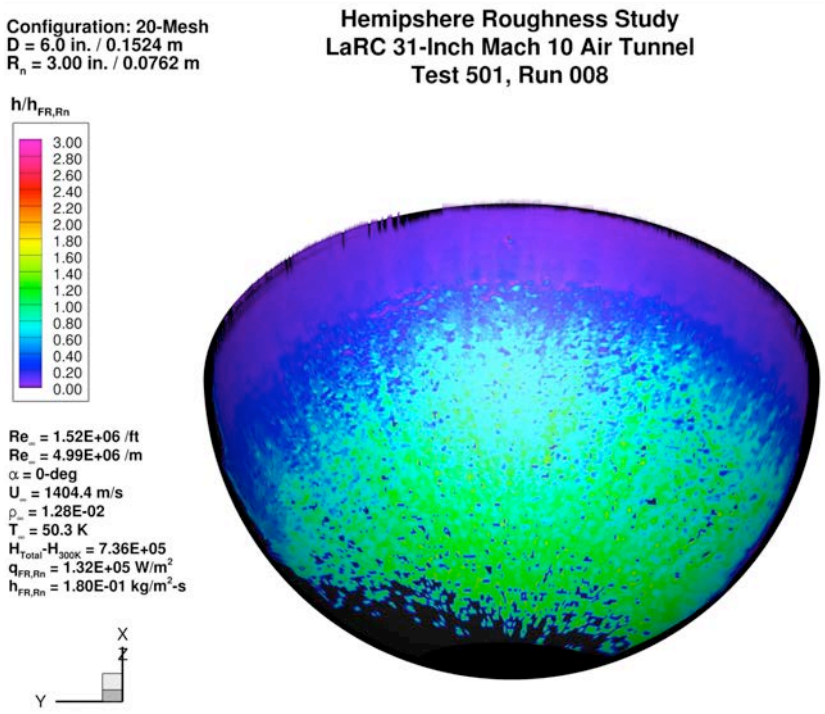

Figure 170. Test 501, Run 08: Mach 10, $Re_\infty = 1.5\times10^6$/ft, 20-Mesh model, global heating image.

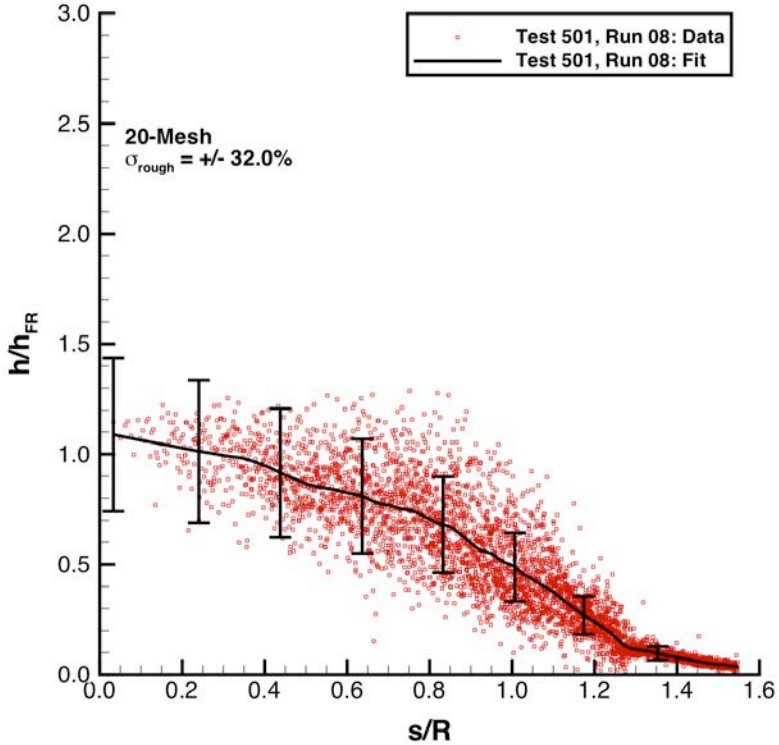

Figure 171. Test 501, Run 08: Mach 10, $Re_\infty = 1.5\times10^6$/ft, 20-Mesh model, heating data and fit.

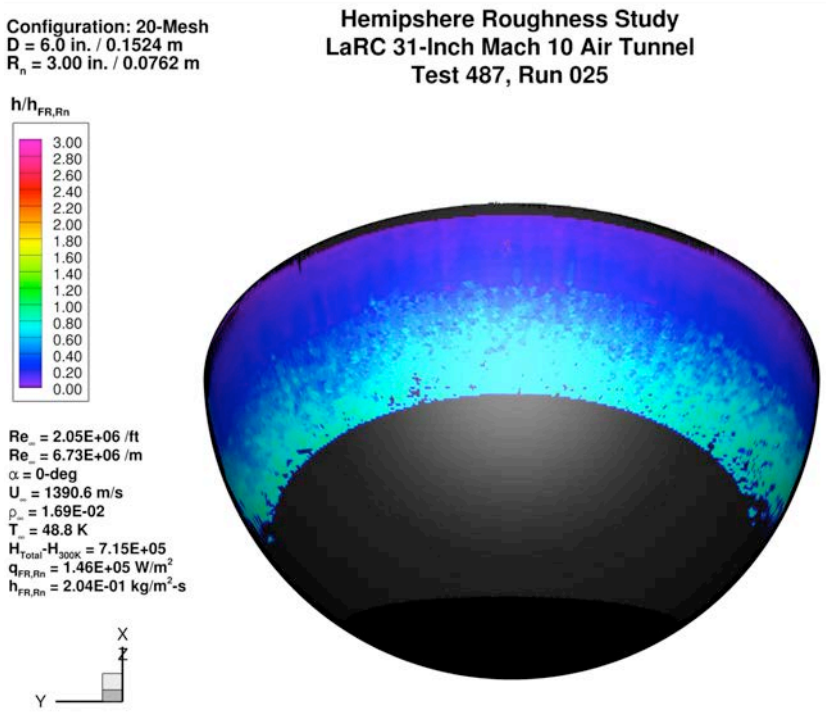

Figure 172. Test 487, Run 25: Mach 10, $Re_\infty = 2.0\times10^6$/ft, 20-Mesh model, global heating image.

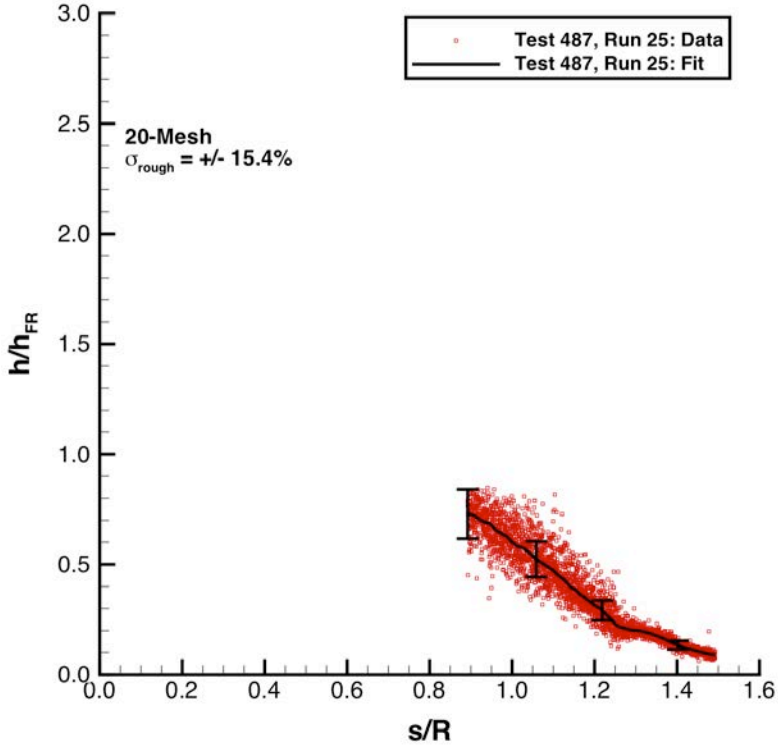

Figure 173. Test 487, Run 25: Mach 10, $Re_\infty = 2.0\times10^6$/ft, 20-Mesh model, heating data and fit.

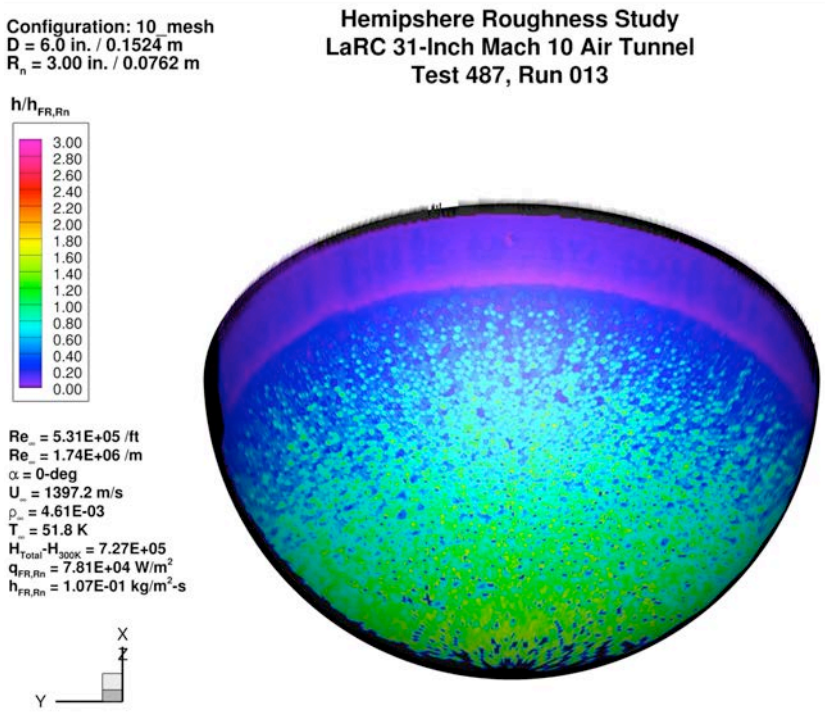

Figure 174. Test 487, Run 13: Mach 10, $Re_\infty = 0.5\times10^6$/ft, 10-Mesh model, global heating image.

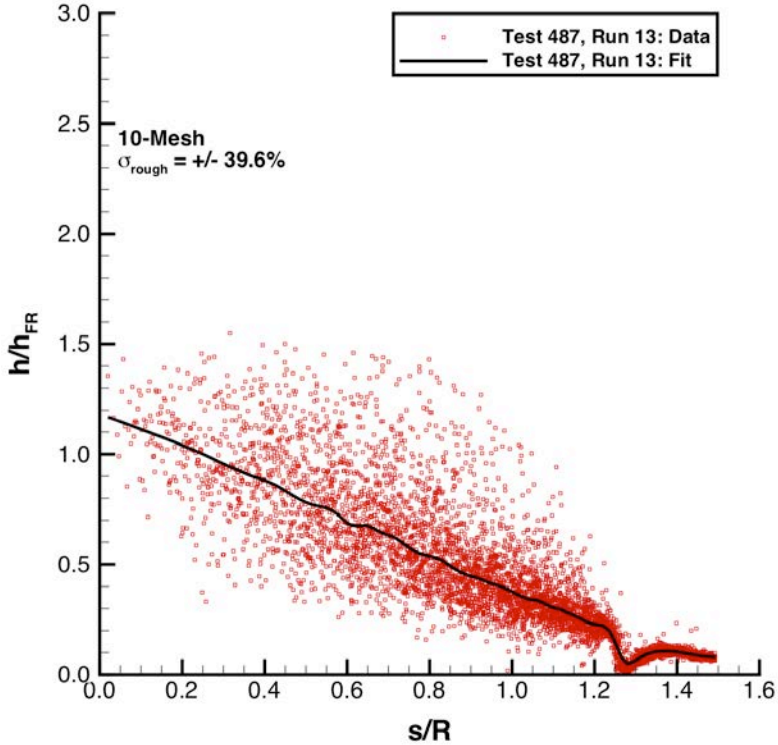

Figure 175. Test 487, Run 13: Mach 10, $Re_\infty = 0.5\times10^6$/ft, 10-Mesh model, heating data and fit.

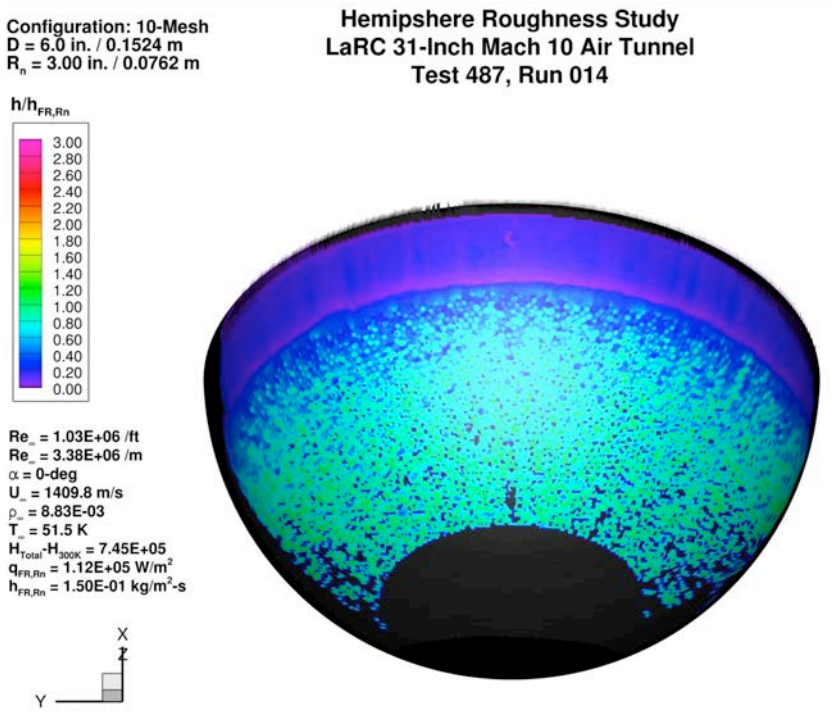

Figure 176. Test 487, Run 14: Mach 10, $Re_\infty = 1.0\times10^6$/ft, 10-Mesh model, global heating image.

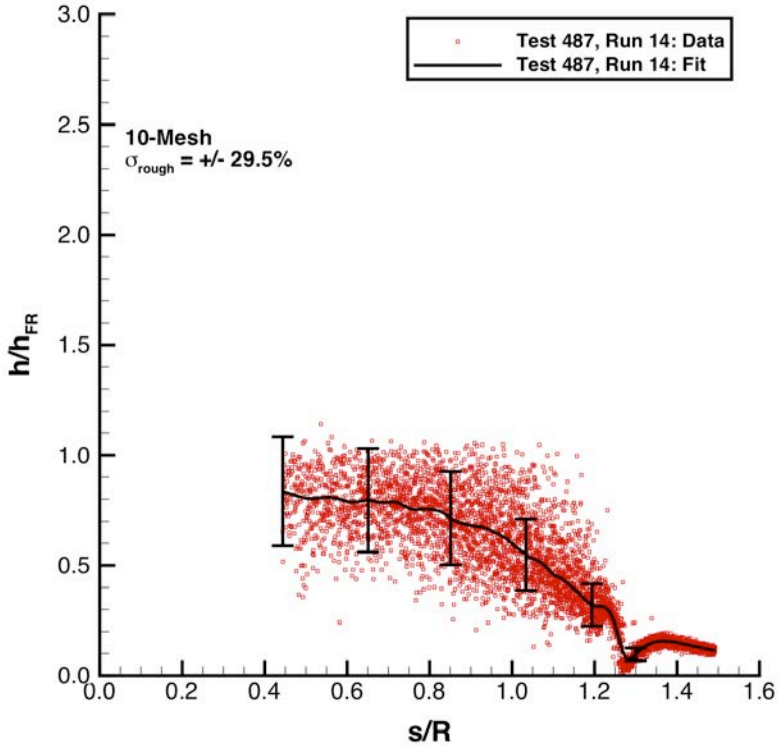

Figure 177. Test 487, Run 14: Mach 10, $Re_\infty = 1.0\times10^6$/ft, 10-Mesh model, heating data and fit.

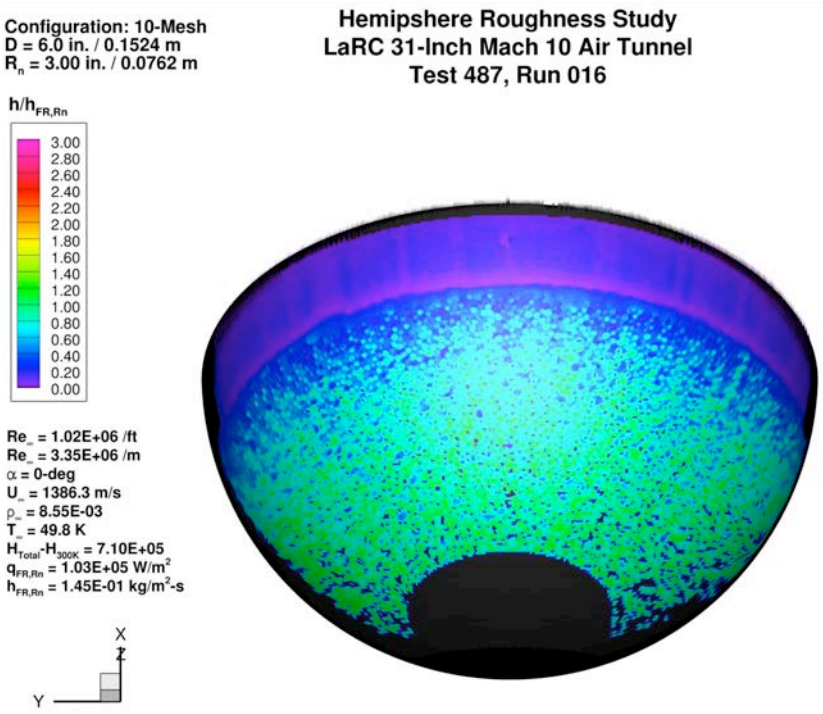

Figure 178. Test 487, Run 16: Mach 10, $Re_\infty = 1.0\times10^6$/ft, 10-Mesh model, global heating image.

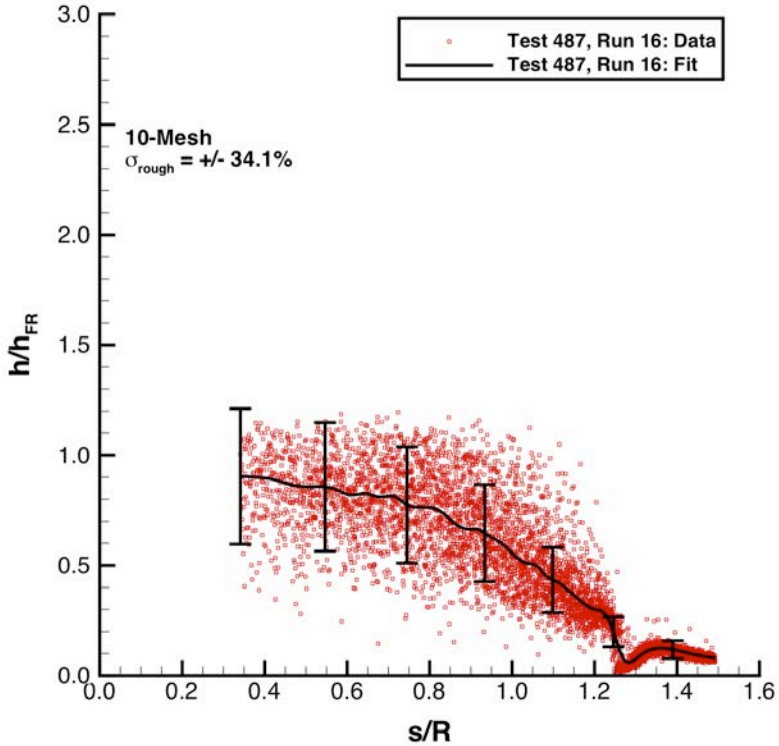

Figure 179. Test 487, Run 16: Mach 10, $Re_\infty = 1.0\times10^6$/ft, 10-Mesh model, heating data and fit.

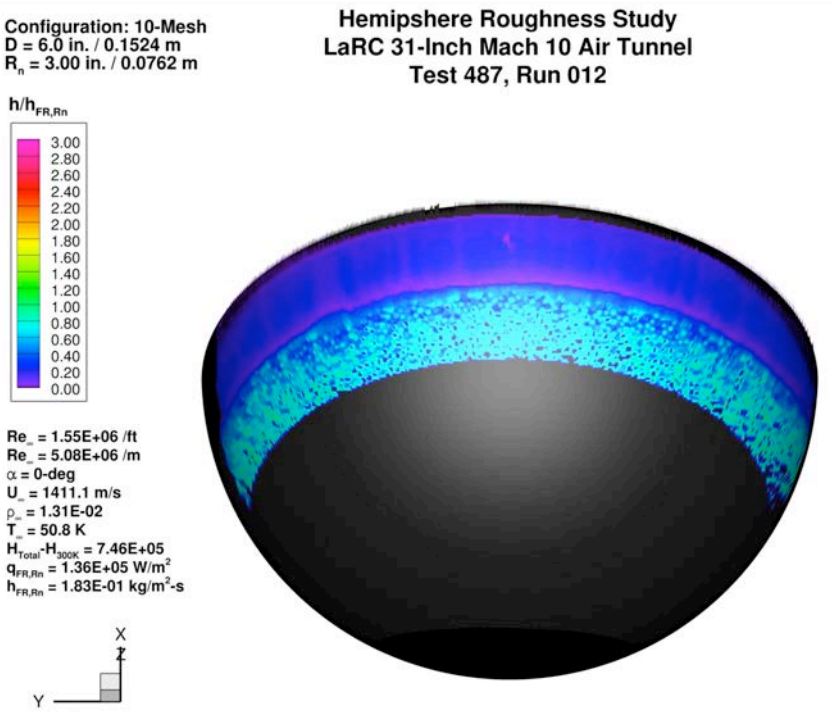

Figure 180. Test 487, Run 12: Mach 10, $Re_\infty = 1.5\times10^6$/ft, 10-Mesh model, global heating image.

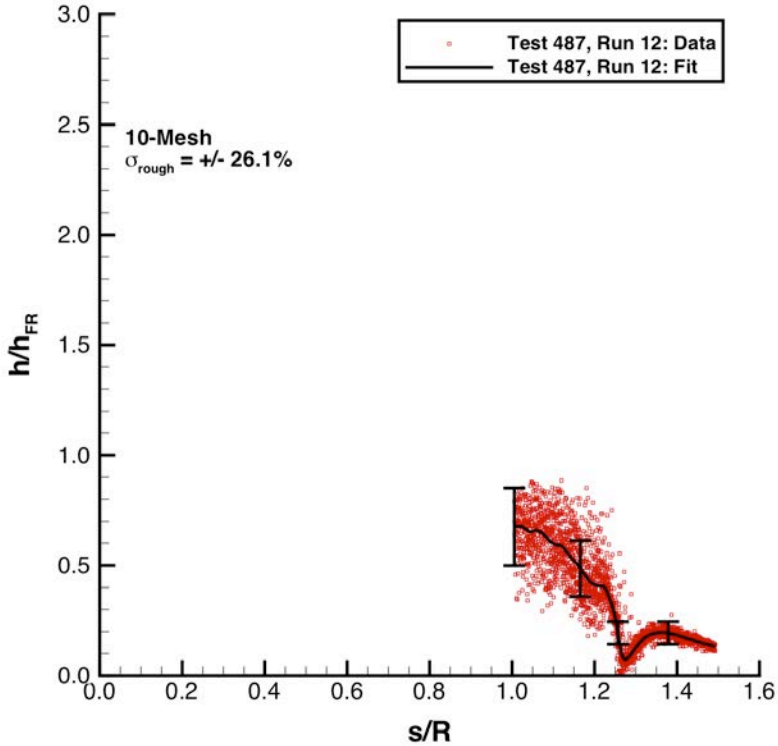

Figure 181. Test 487, Run 12: Mach 10, $Re_\infty = 1.5\times10^6$/ft, 10-Mesh model, heating data and fit.

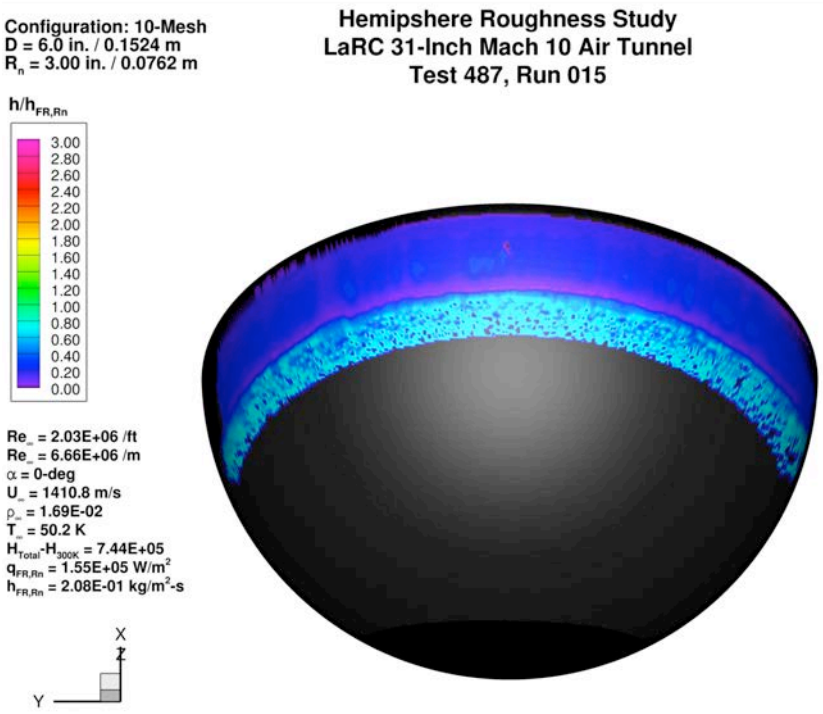

Figure 182. Test 487, Run 15: Mach 10, $Re_\infty = 2.0\times10^6$/ft, 10-Mesh model, global heating image.

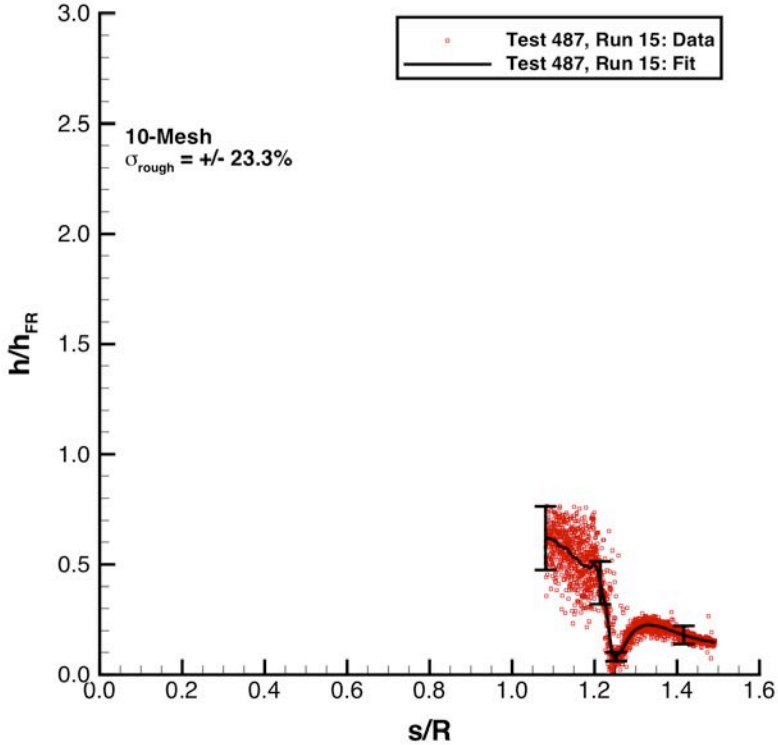

Figure 183. Test 487, Run 15: Mach 10, $Re_\infty = 2.0\times10^6$/ft, 10-Mesh model, heating data and fit.

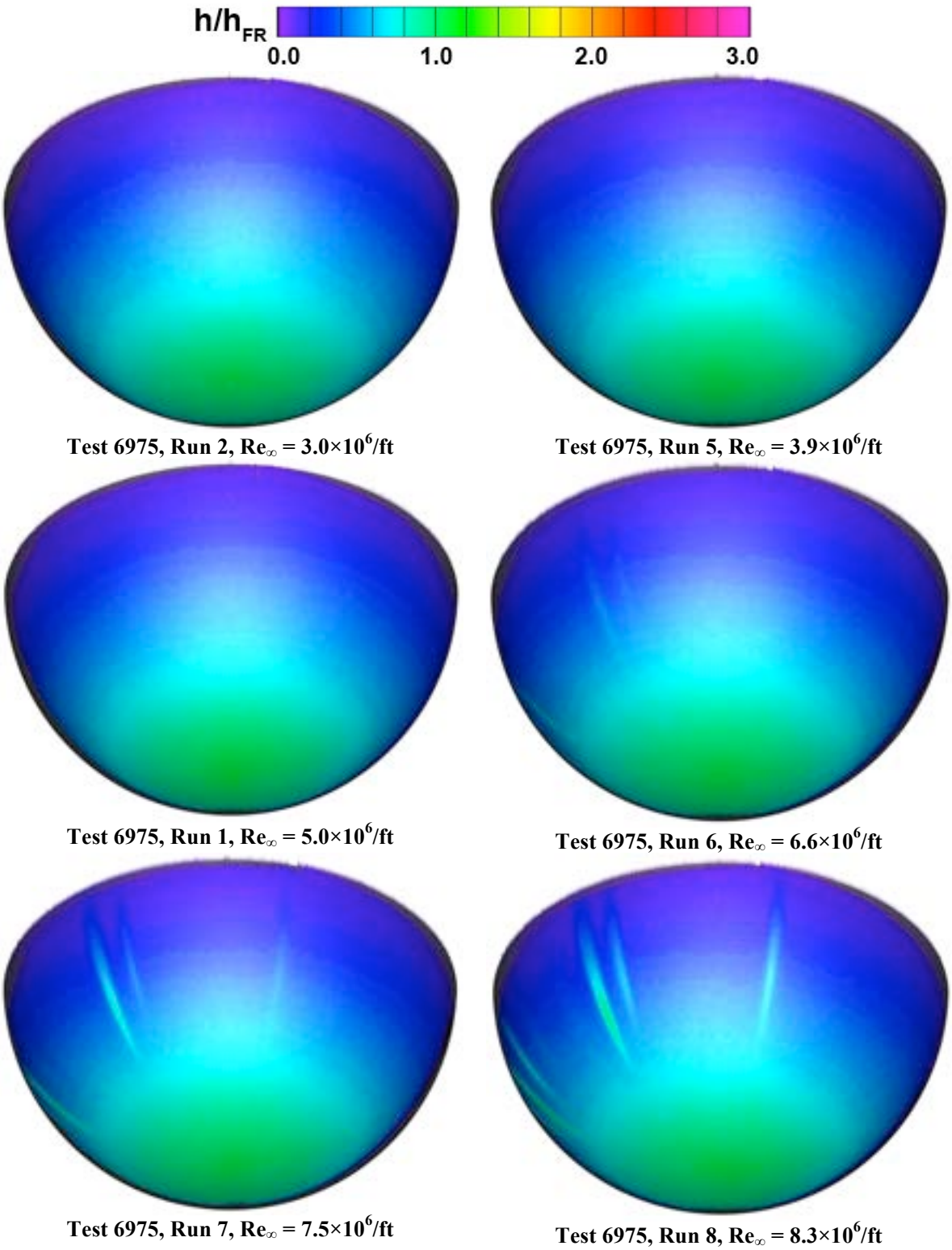

Test 6975, Run 2, $Re_\infty = 3.0\times10^6$/ft

Test 6975, Run 5, $Re_\infty = 3.9\times10^6$/ft

Test 6975, Run 1, $Re_\infty = 5.0\times10^6$/ft

Test 6975, Run 6, $Re_\infty = 6.6\times10^6$/ft

Test 6975, Run 7, $Re_\infty = 7.5\times10^6$/ft

Test 6975, Run 8, $Re_\infty = 8.3\times10^6$/ft

Figure 184. Reynolds Number effects at Mach 6, smooth model.

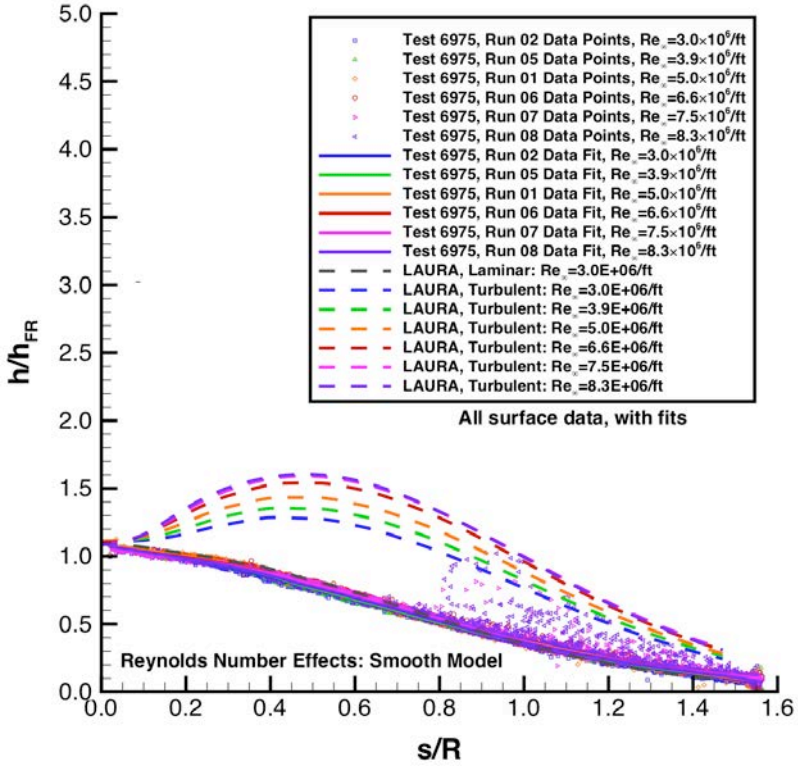

Figure 185. Reynolds Number effects at Mach 6, smooth model, data and fits.

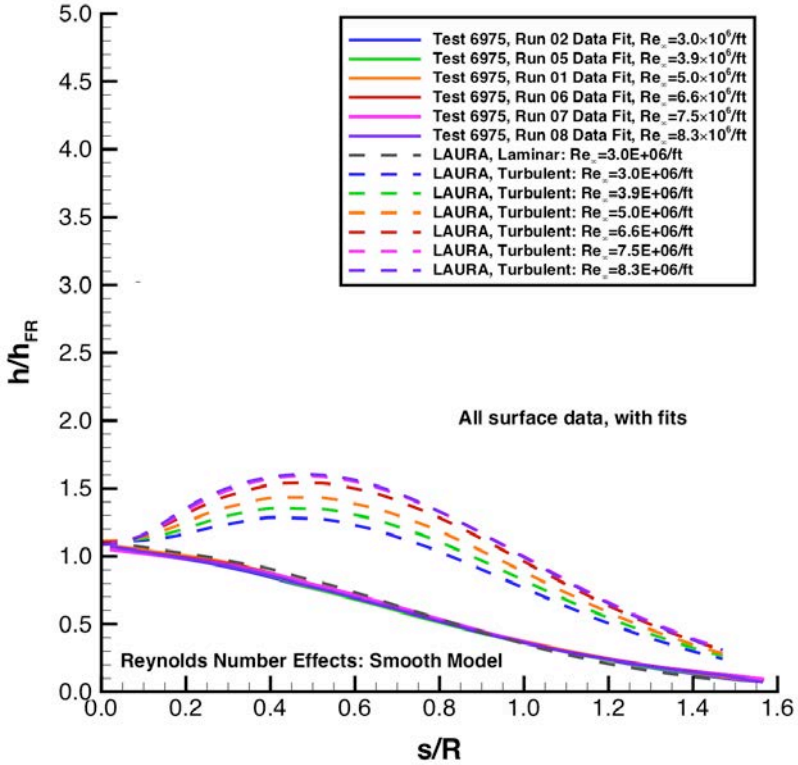

Figure 186. Reynolds Number effects at Mach 6, smooth model, fits only.

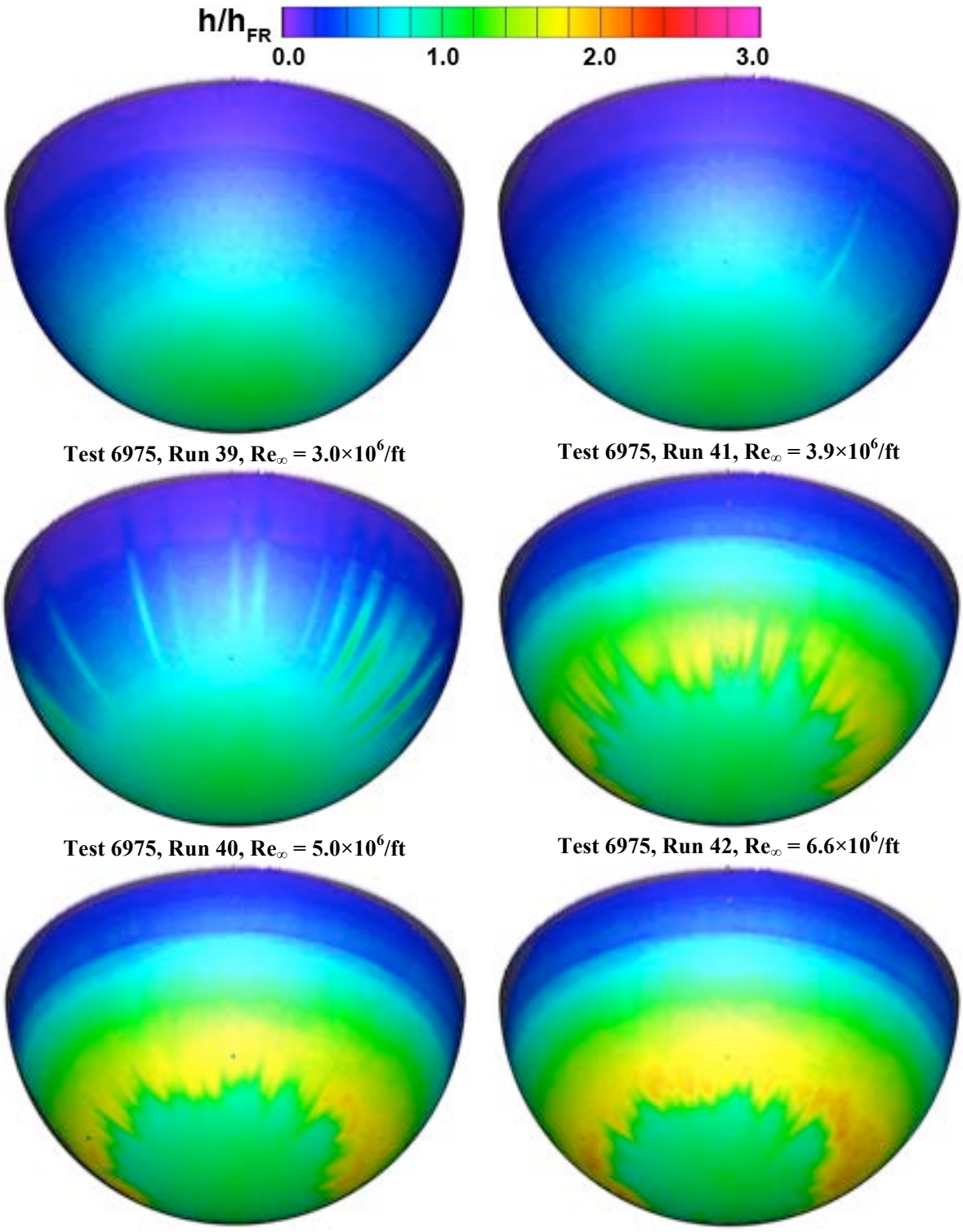

Test 6975, Run 39, $Re_\infty = 3.0\times10^6$/ft

Test 6975, Run 41, $Re_\infty = 3.9\times10^6$/ft

Test 6975, Run 40, $Re_\infty = 5.0\times10^6$/ft

Test 6975, Run 42, $Re_\infty = 6.6\times10^6$/ft

Test 6975, Run 43, $Re_\infty = 7.5\times10^6$/ft

Test 6975, Run 44, $Re_\infty = 8.3\times10^6$/ft

Figure 187. Reynolds Number effects at Mach 6, 230-Mesh model.

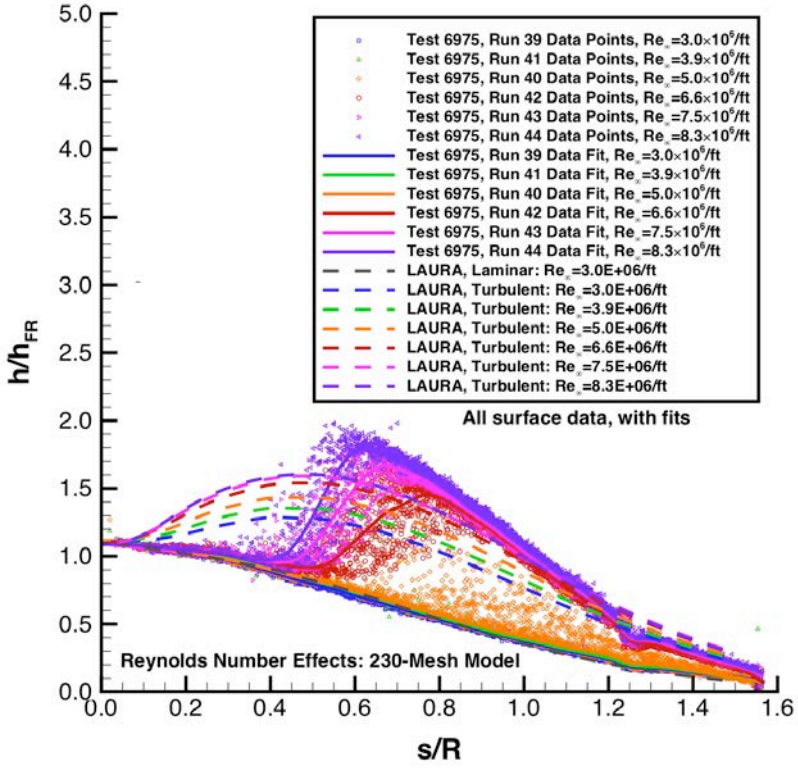

Figure 188. Reynolds Number effects at Mach 6, 230-Mesh model, data and fits.

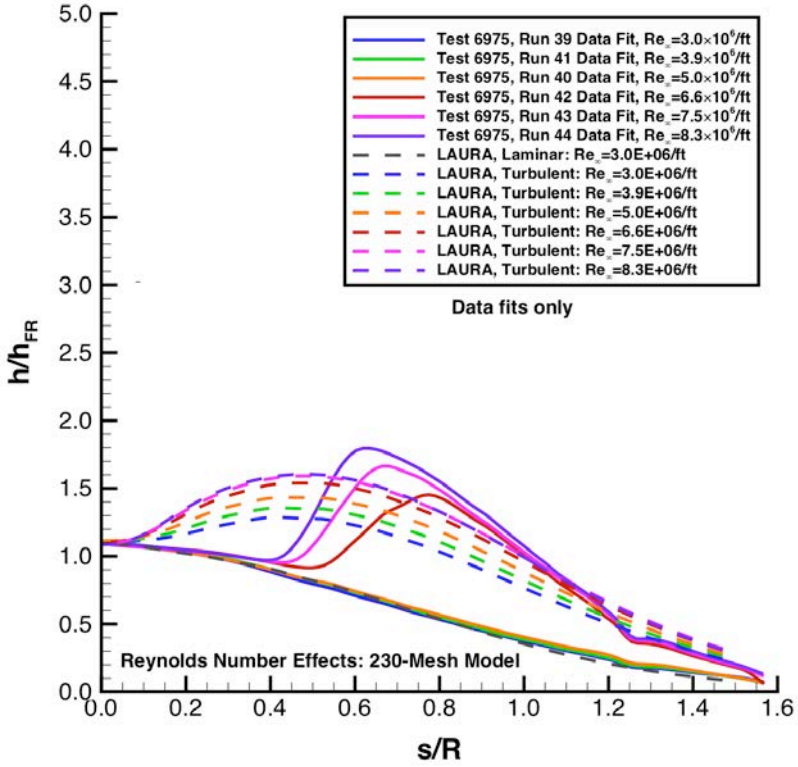

Figure 189. Reynolds Number effects at Mach 6, 230-Mesh model, fits only.

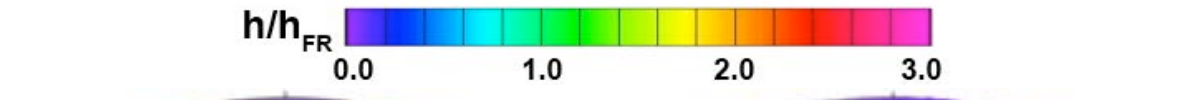

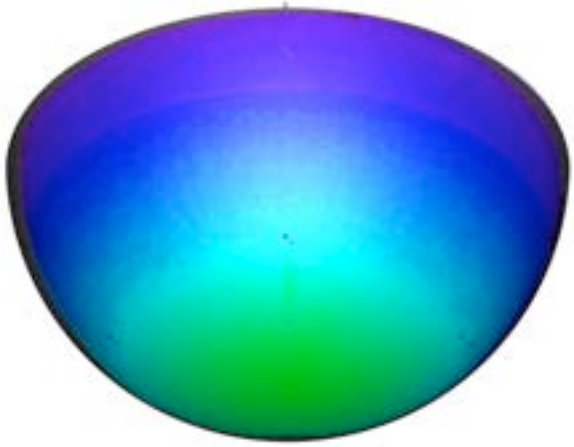

Test 6975, Run 27, $Re_\infty = 3.0\times10^6$/ft

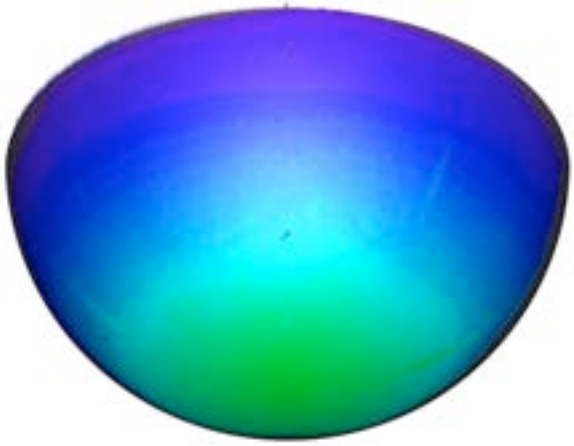

Test 6975, Run 28, $Re_\infty = 3.9\times10^6$/ft

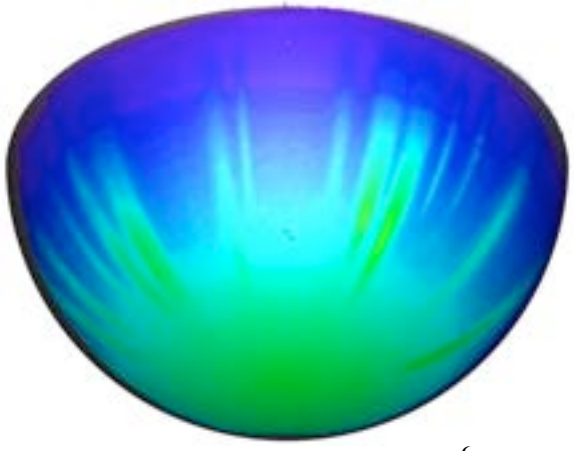

Test 6975, Run 29, $Re_\infty = 5.0\times10^6$/ft

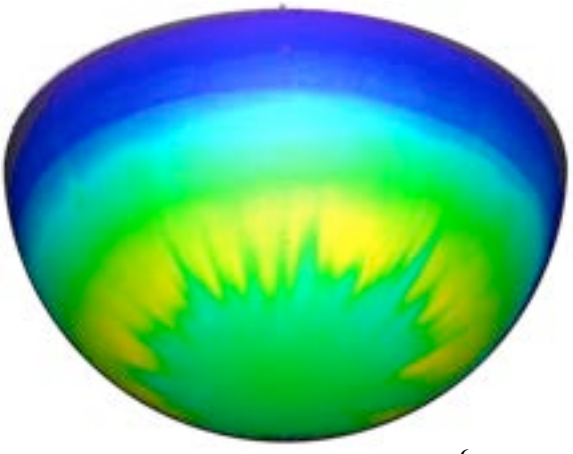

Test 6975, Run 30, $Re_\infty = 6.6\times10^6$/ft

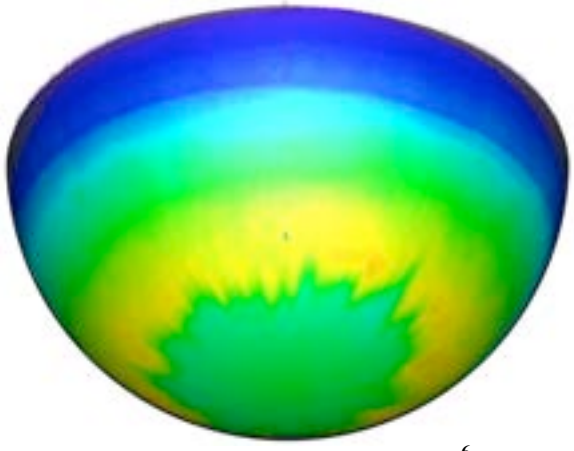

Test 6975, Run 31, $Re_\infty = 7.5\times10^6$/ft

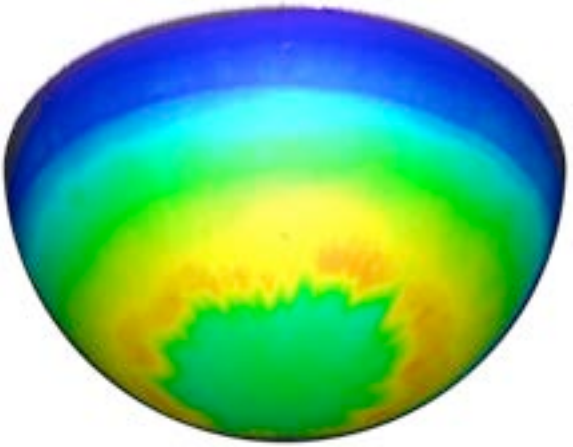

Test 6975, Run 32, $Re_\infty = 8.3\times10^6$/ft

Figure 190. Reynolds Number effects at Mach 6, 140-Mesh Model

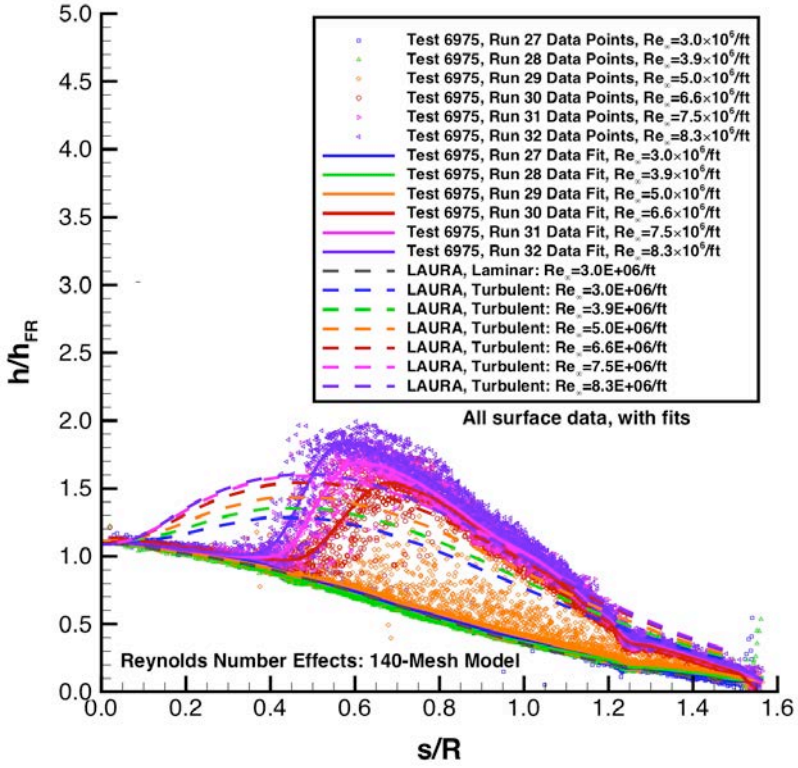

Figure 191. Reynolds Number effects at Mach 6, 140-Mesh model, data and fits.

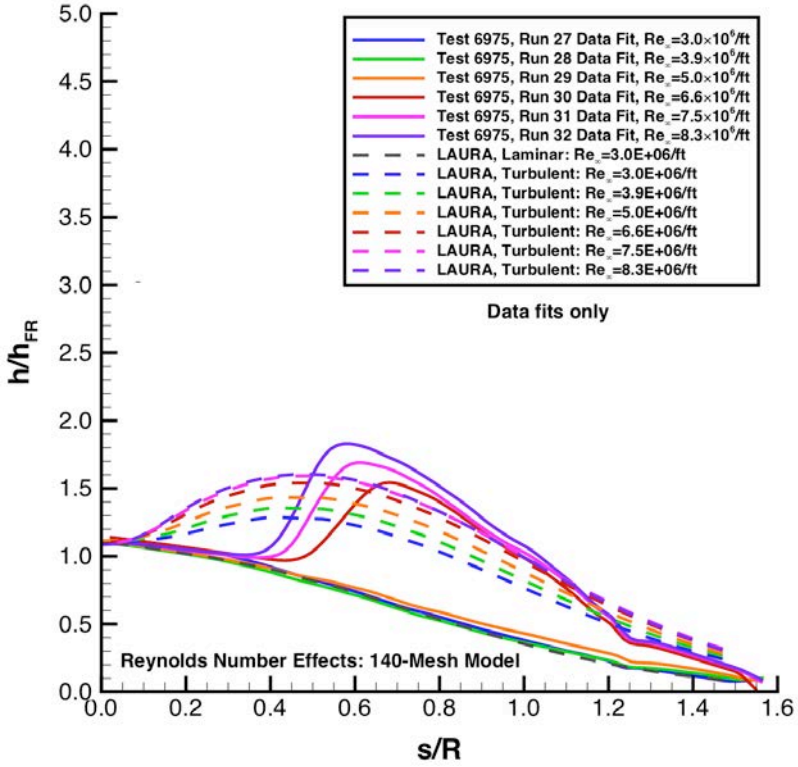

Figure 192. Reynolds Number effects at Mach 6, 140-Mesh model, fits only.

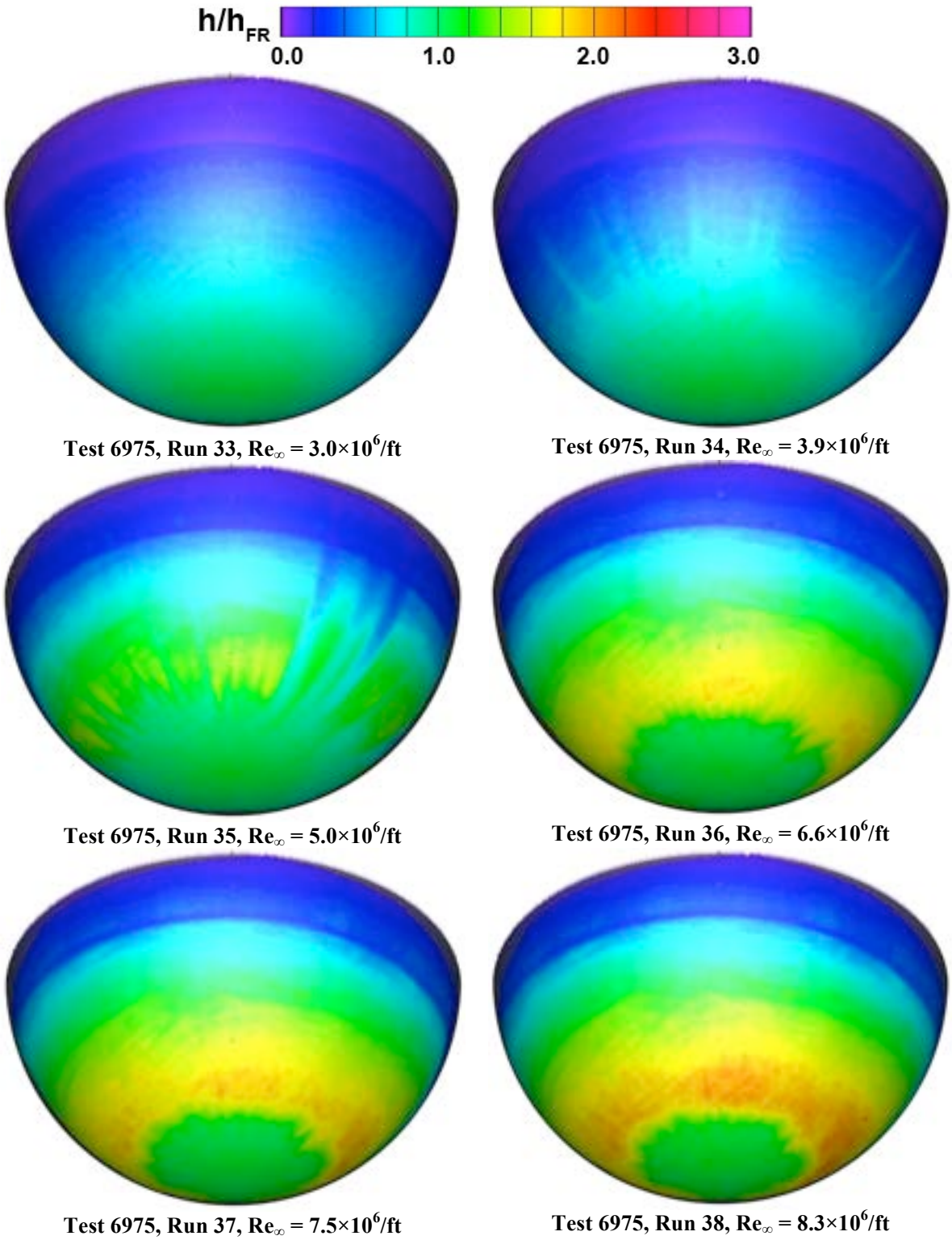

Test 6975, Run 33, $Re_\infty = 3.0\times10^6$/ft

Test 6975, Run 34, $Re_\infty = 3.9\times10^6$/ft

Test 6975, Run 35, $Re_\infty = 5.0\times10^6$/ft

Test 6975, Run 36, $Re_\infty = 6.6\times10^6$/ft

Test 6975, Run 37, $Re_\infty = 7.5\times10^6$/ft

Test 6975, Run 38, $Re_\infty = 8.3\times10^6$/ft

Figure 193. Reynolds Number effects at Mach 6, 80-Mesh Model

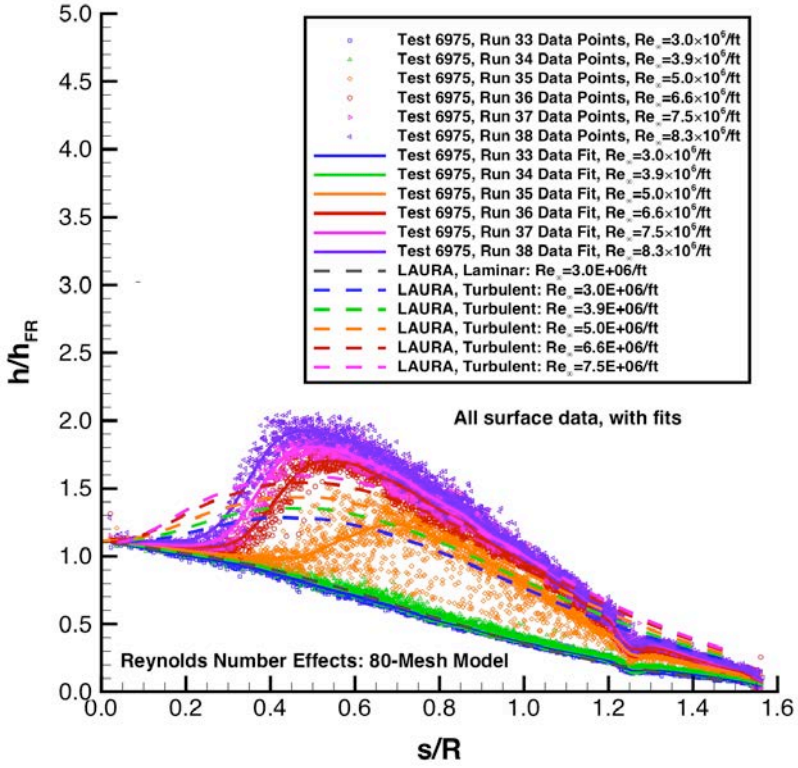

Figure 194. Reynolds Number effects at Mach 6, 80-Mesh model, data and fits.

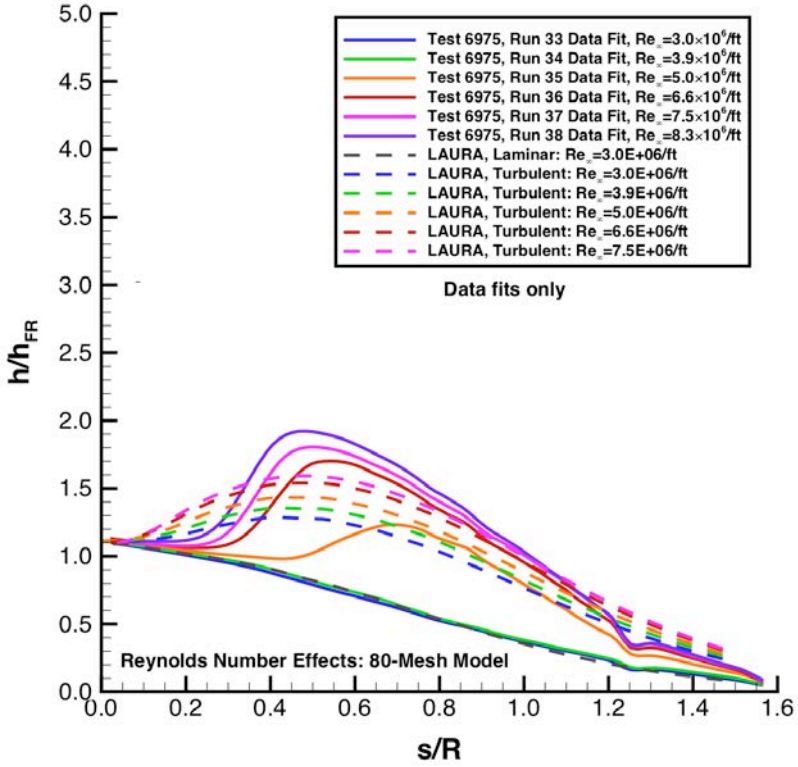

Figure 195. Reynolds Number effects at Mach 6, 80-Mesh model, fits only.

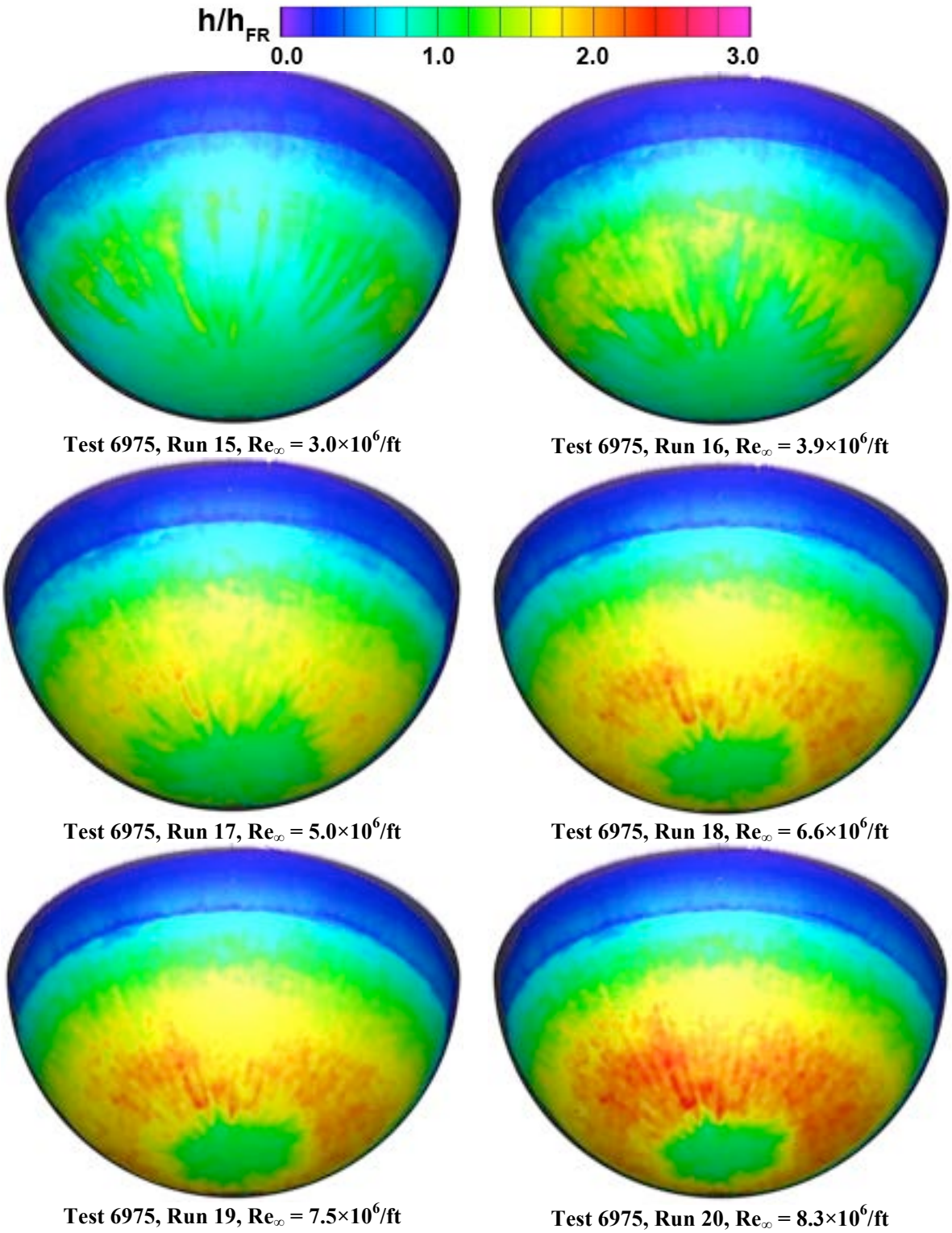

Test 6975, Run 15, $Re_\infty = 3.0\times10^6$/ft

Test 6975, Run 16, $Re_\infty = 3.9\times10^6$/ft

Test 6975, Run 17, $Re_\infty = 5.0\times10^6$/ft

Test 6975, Run 18, $Re_\infty = 6.6\times10^6$/ft

Test 6975, Run 19, $Re_\infty = 7.5\times10^6$/ft

Test 6975, Run 20, $Re_\infty = 8.3\times10^6$/ft

Figure 196. Reynolds Number effects at Mach 6, 40-Mesh Model

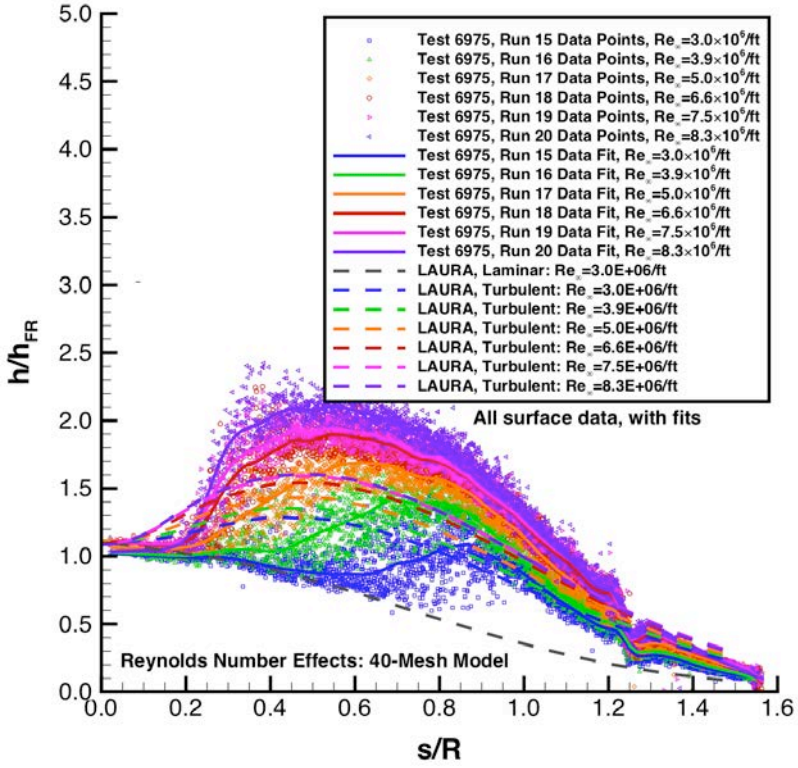

Figure 197. Reynolds Number effects at Mach 6, 40-Mesh model, data and fits.

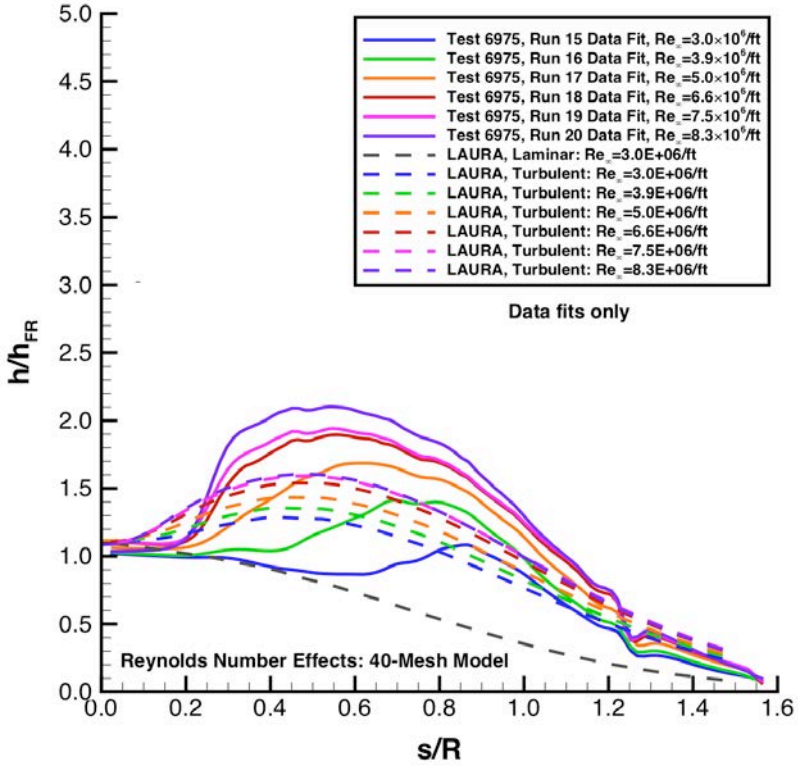

Figure 198. Reynolds Number effects at Mach 6, 40-Mesh model, fits only.

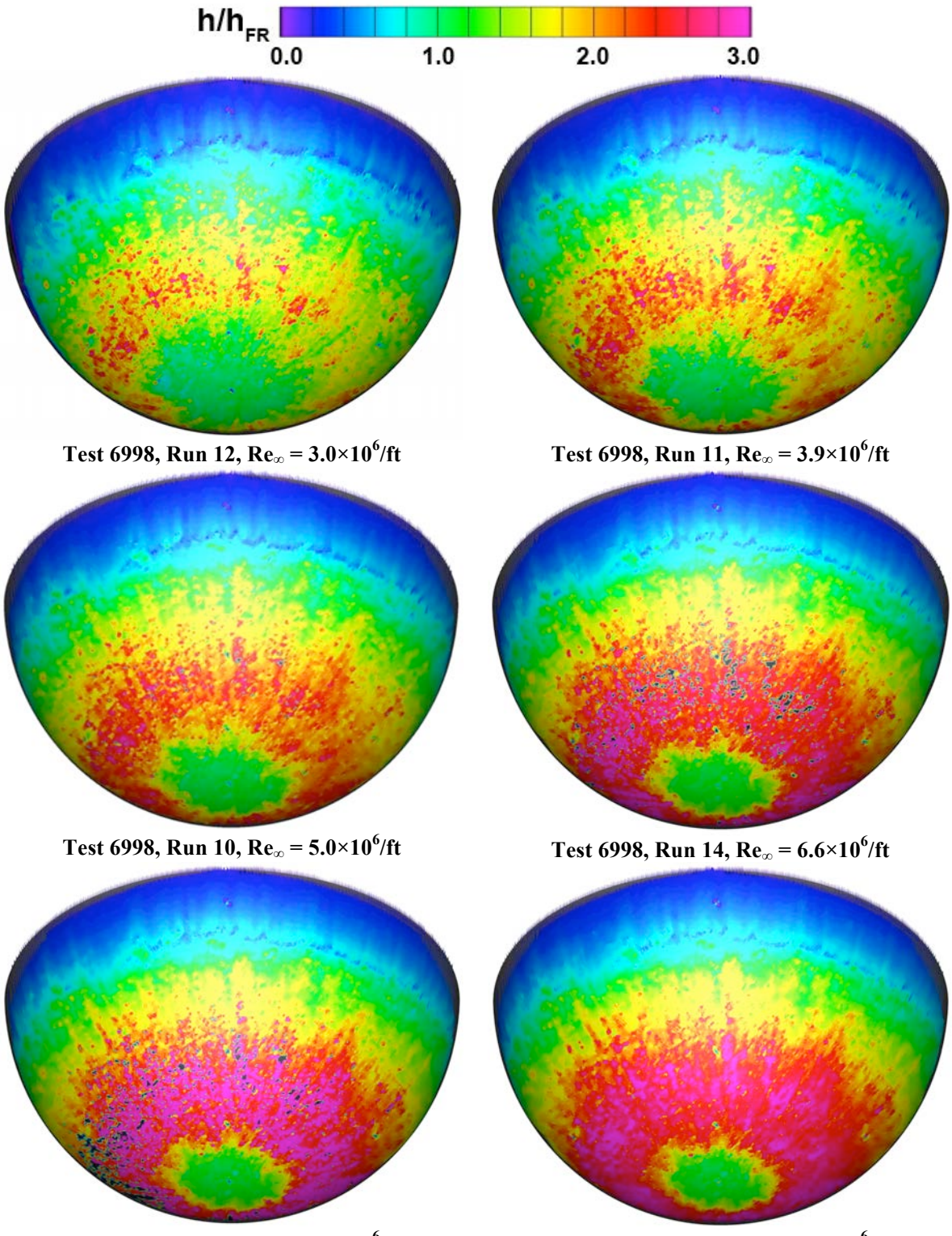

Test 6998, Run 12, $Re_\infty = 3.0\times10^6$/ft **Test 6998, Run 11, $Re_\infty = 3.9\times10^6$/ft**

Test 6998, Run 10, $Re_\infty = 5.0\times10^6$/ft **Test 6998, Run 14, $Re_\infty = 6.6\times10^6$/ft**

Test 6998, Run 15, $Re_\infty = 7.5\times10^6$/ft **Test 6998, Run 16, $Re_\infty = 8.3\times10^6$/ft**

Figure 199. Reynolds Number effects at Mach 6, 30-Mesh Model

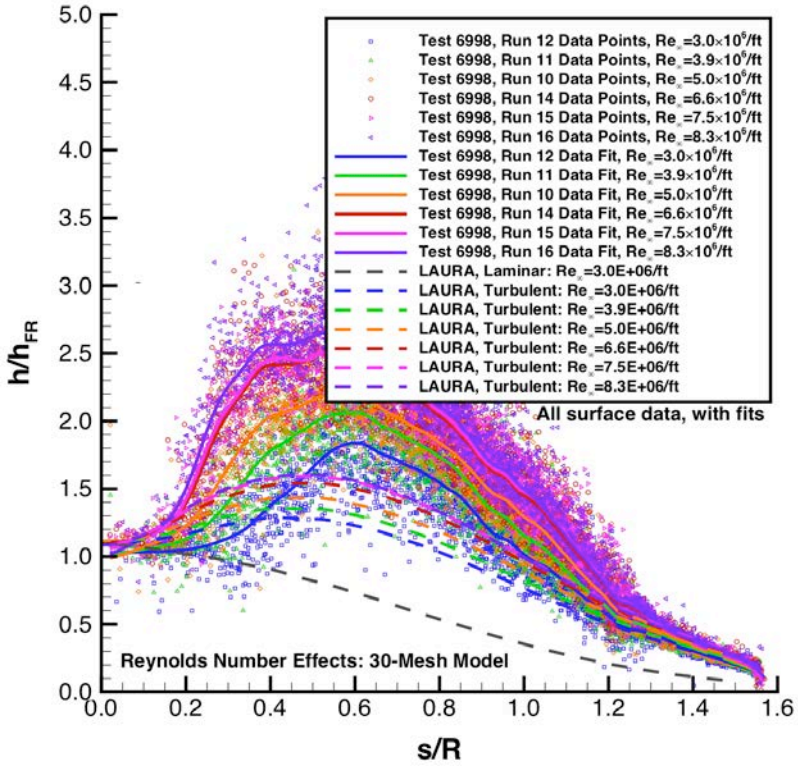

Figure 200. Reynolds Number effects at Mach 6, 30-Mesh model, data and fits.

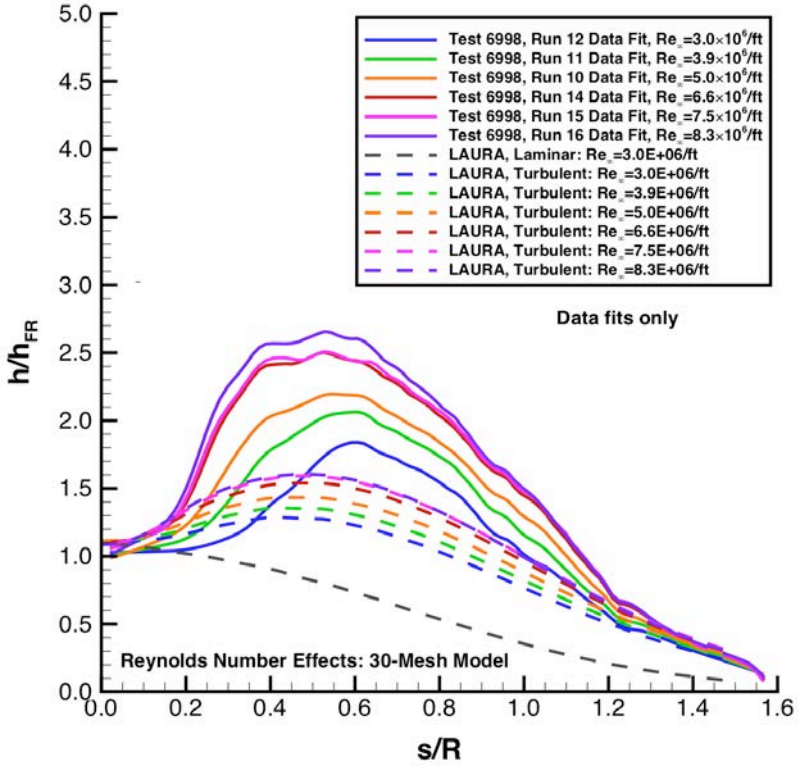

Figure 201. Reynolds Number effects at Mach 6, 30-Mesh model, fits only.

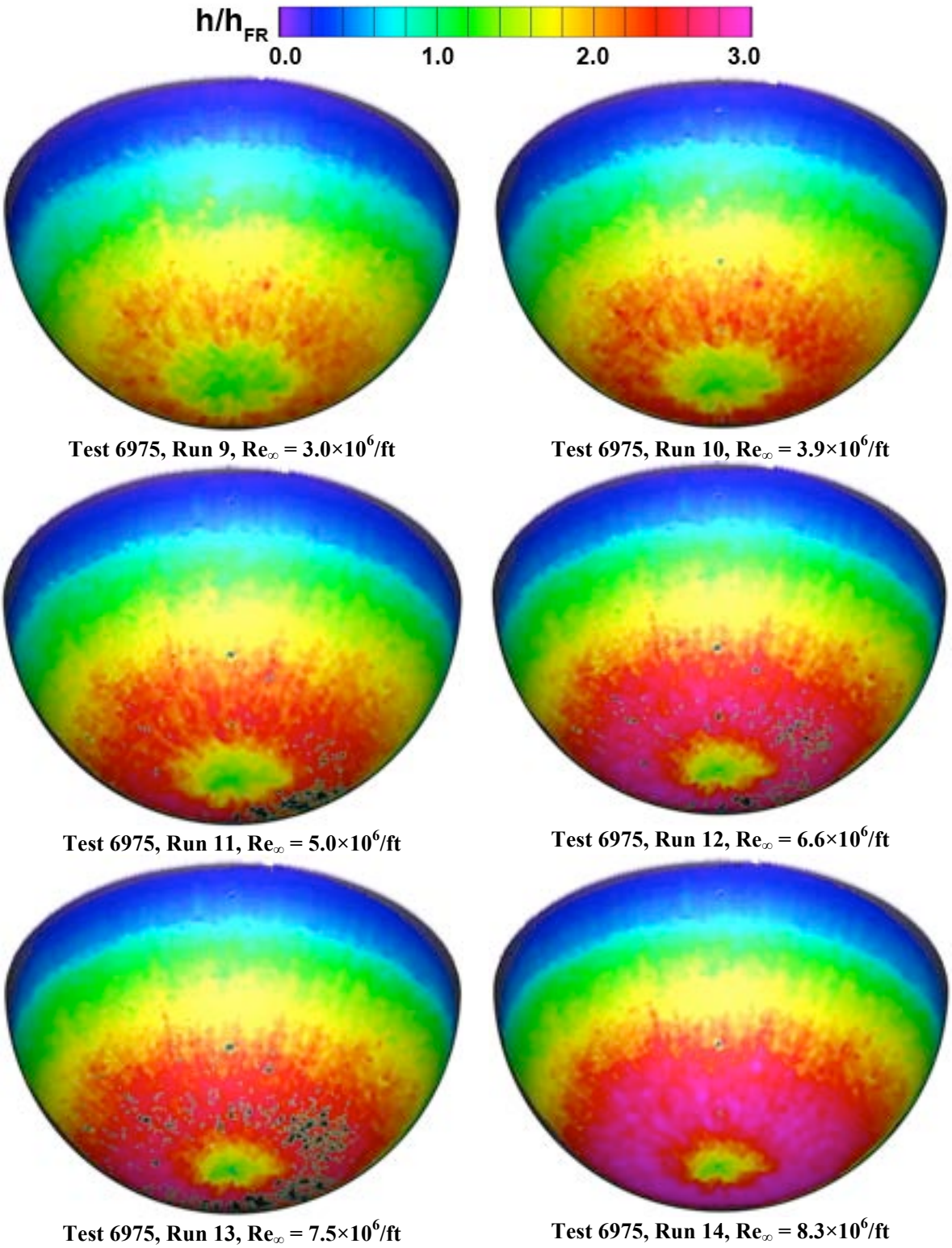

Test 6975, Run 9, $Re_\infty = 3.0\times10^6$/ft

Test 6975, Run 10, $Re_\infty = 3.9\times10^6$/ft

Test 6975, Run 11, $Re_\infty = 5.0\times10^6$/ft

Test 6975, Run 12, $Re_\infty = 6.6\times10^6$/ft

Test 6975, Run 13, $Re_\infty = 7.5\times10^6$/ft

Test 6975, Run 14, $Re_\infty = 8.3\times10^6$/ft

Figure 202. Reynolds Number effects at Mach 6, 20-Mesh Model

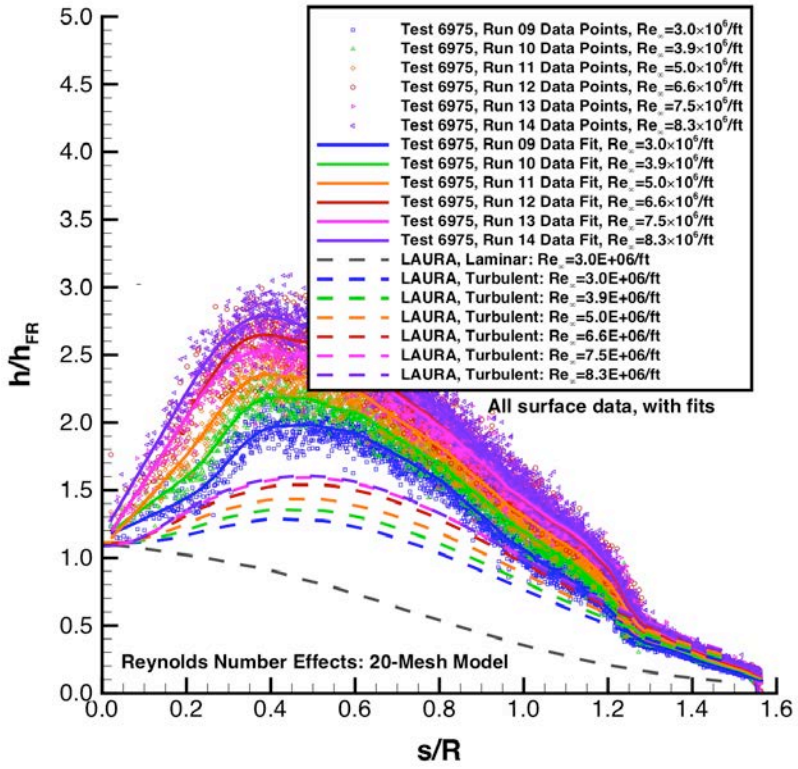

Figure 203. Reynolds Number effects at Mach 6, 20-Mesh model, data and fits.

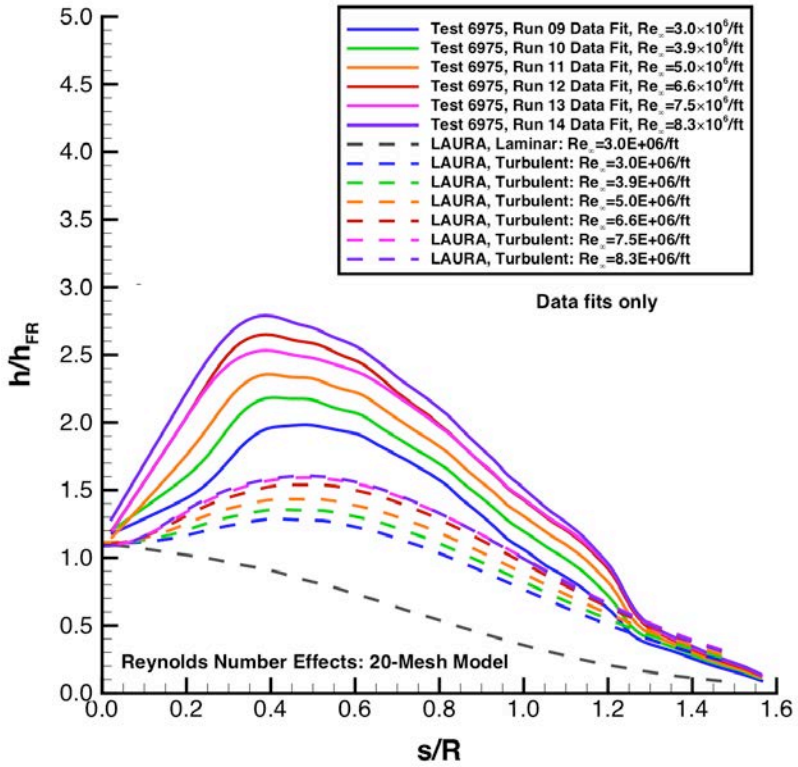

Figure 204. Reynolds Number effects at Mach 6, 20-Mesh model, fits only.

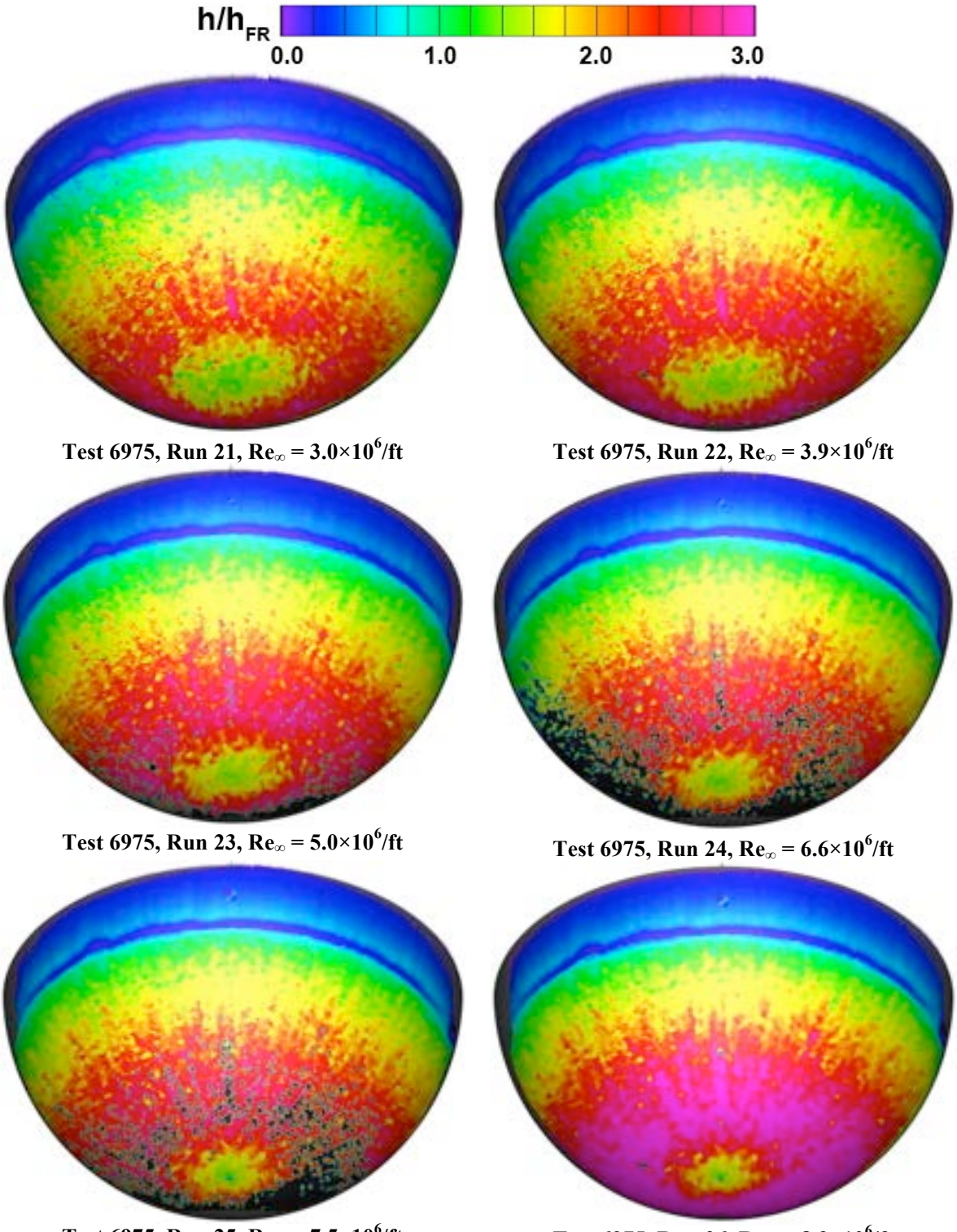

Test 6975, Run 21, $Re_\infty = 3.0\times10^6$/ft

Test 6975, Run 22, $Re_\infty = 3.9\times10^6$/ft

Test 6975, Run 23, $Re_\infty = 5.0\times10^6$/ft

Test 6975, Run 24, $Re_\infty = 6.6\times10^6$/ft

Test 6975, Run 25, $Re_\infty = 7.5\times10^6$/ft

Test 6975, Run 26, $Re_\infty = 8.3\times10^6$/ft

Figure 205. Reynolds Number effects at Mach 6, 10-Mesh Model

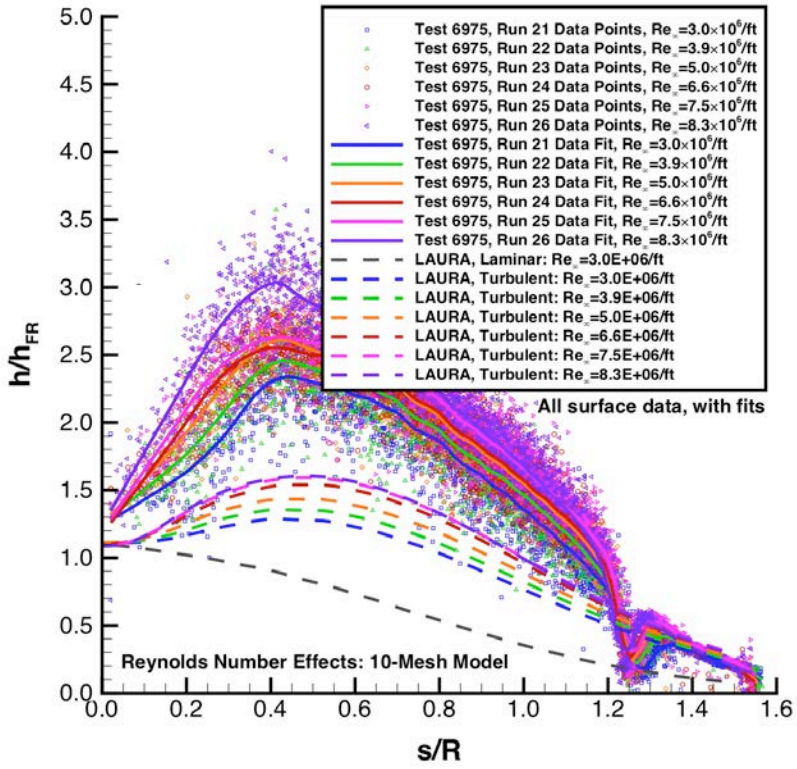

Figure 206. Reynolds Number effects at Mach 6, 10-Mesh model, data and fits.

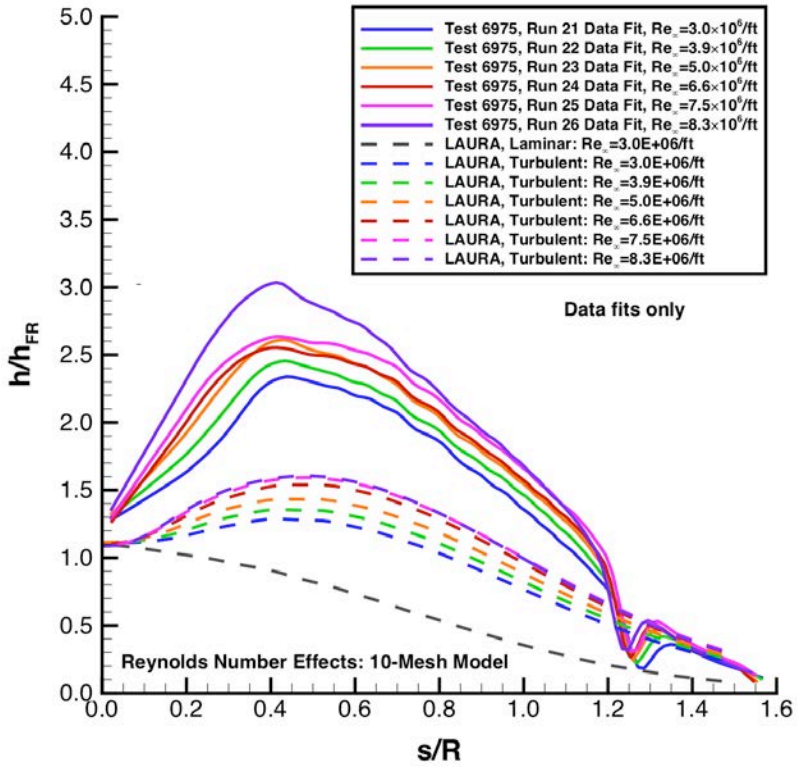

Figure 207. Reynolds Number effects at Mach 6, 10-Mesh model, fits only.

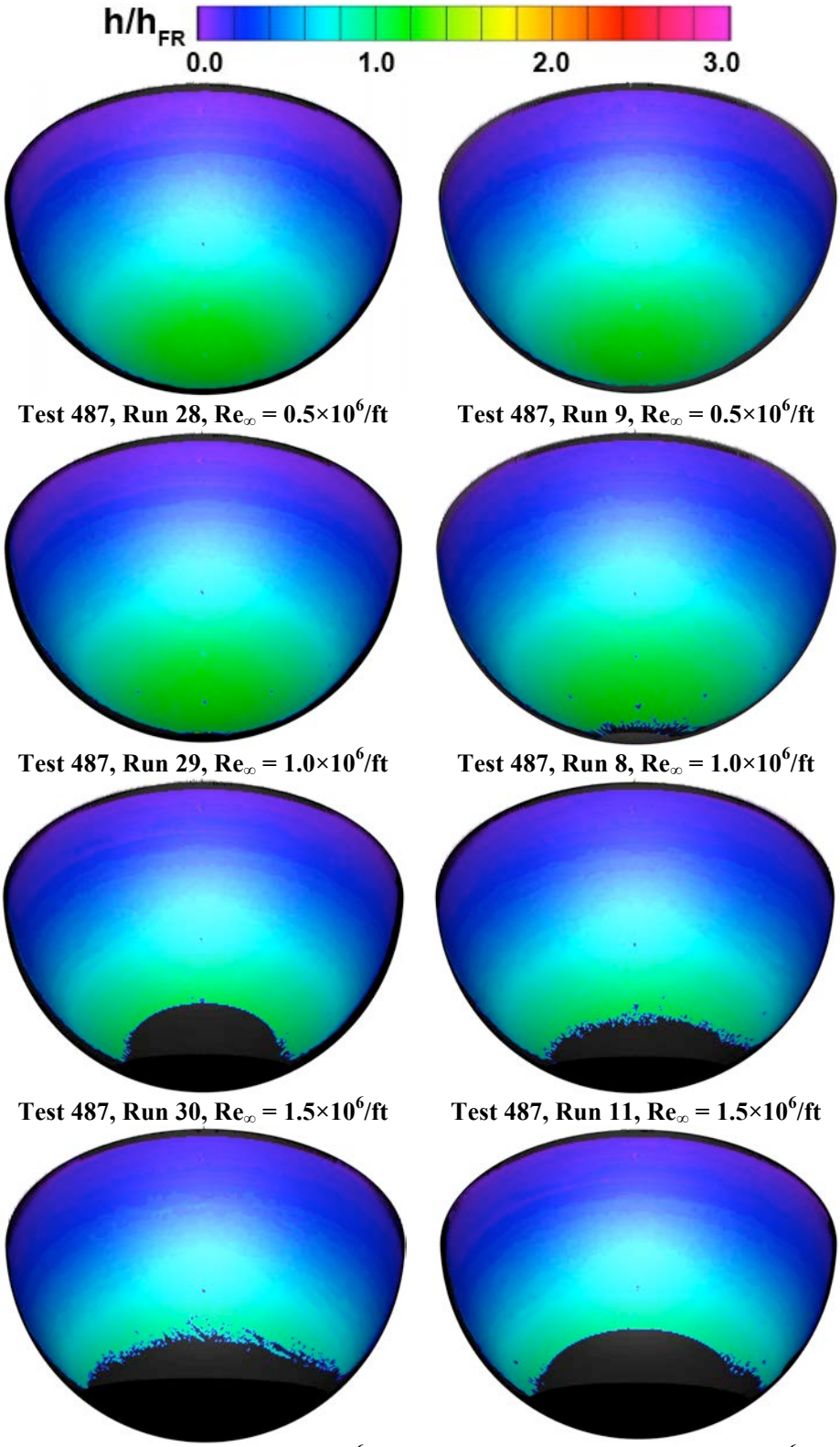

Test 487, Run 28, $Re_\infty = 0.5\times10^6$/ft

Test 487, Run 9, $Re_\infty = 0.5\times10^6$/ft

Test 487, Run 29, $Re_\infty = 1.0\times10^6$/ft

Test 487, Run 8, $Re_\infty = 1.0\times10^6$/ft

Test 487, Run 30, $Re_\infty = 1.5\times10^6$/ft

Test 487, Run 11, $Re_\infty = 1.5\times10^6$/ft

Test 487, Run 10, $Re_\infty = 2.0\times10^6$/ft

Test 487, Run 27, $Re_\infty = 2.0\times10^6$/ft

Figure 208. Reynolds Number effects at Mach 10, 230-Mesh Model

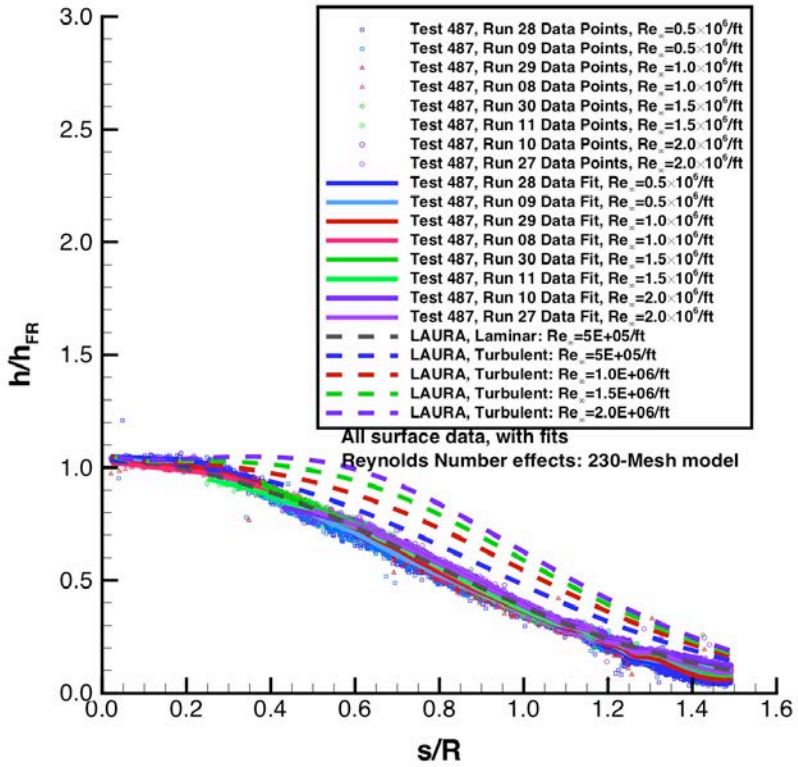

Figure 209. Reynolds Number effects at Mach 10, 230-Mesh model, data and fits.

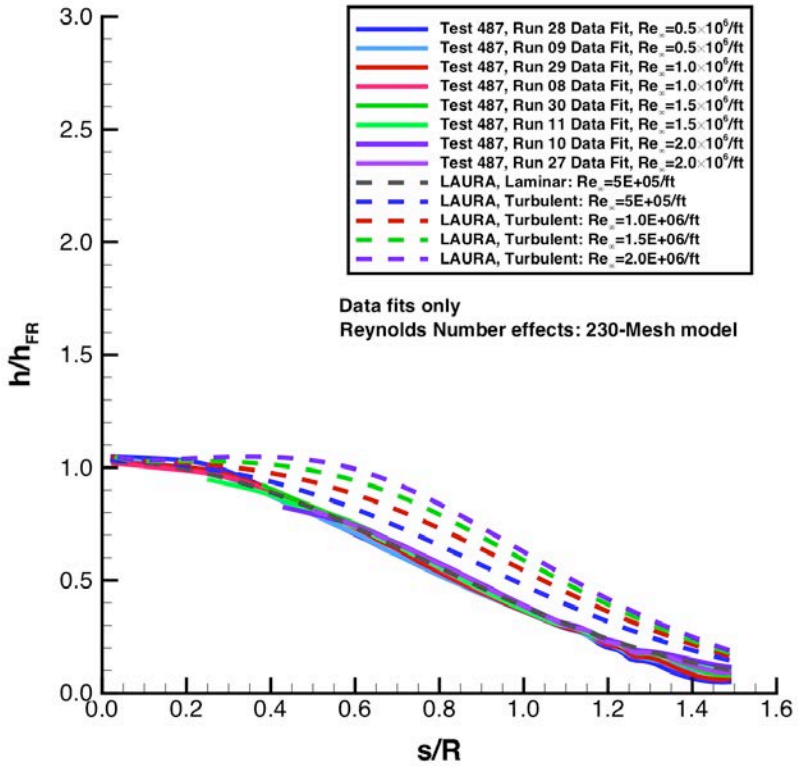

Figure 210. Reynolds Number effects at Mach 10, 230-Mesh model, fits only.

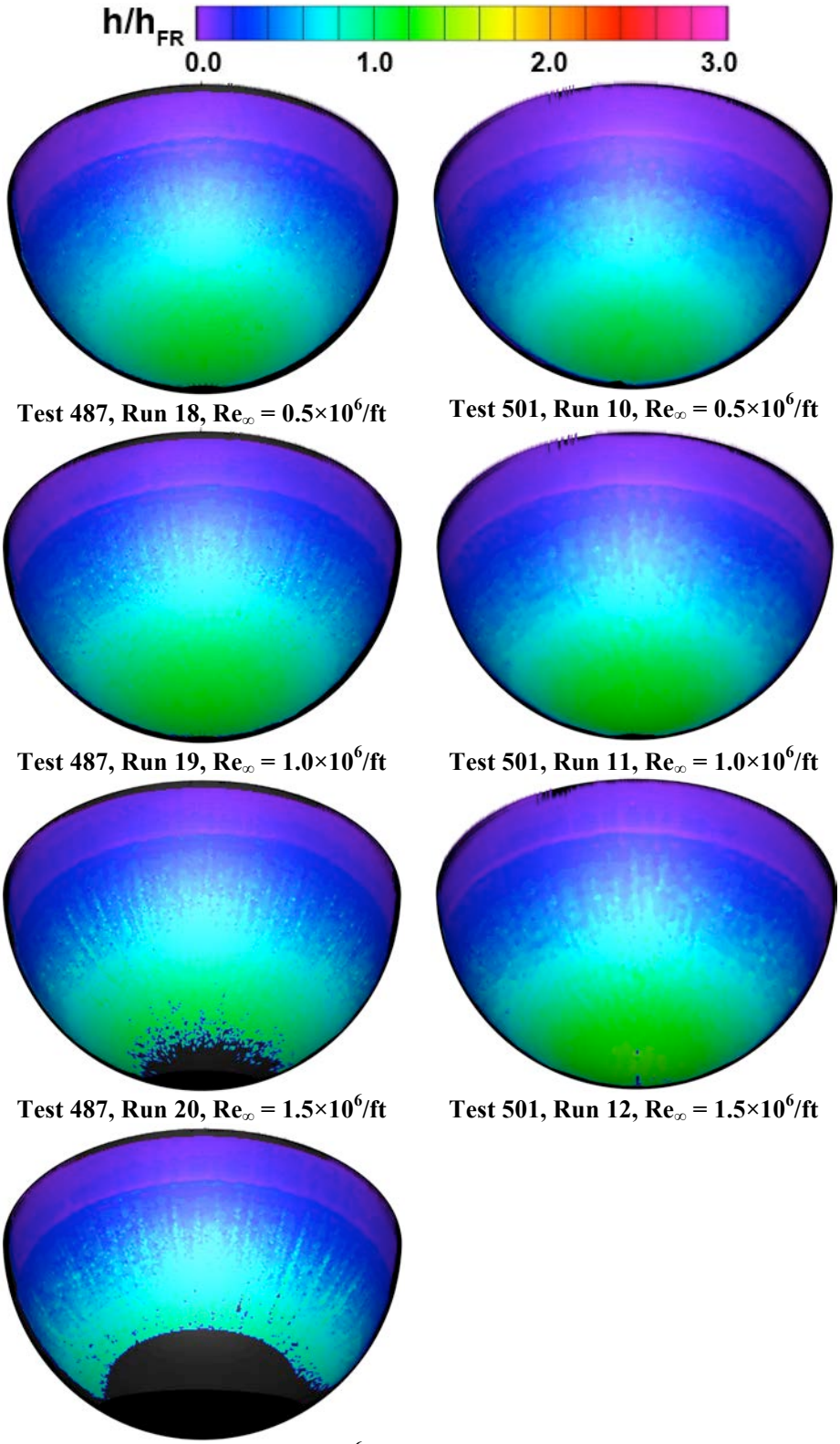

Test 487, Run 18, $Re_\infty = 0.5\times10^6$/ft

Test 501, Run 10, $Re_\infty = 0.5\times10^6$/ft

Test 487, Run 19, $Re_\infty = 1.0\times10^6$/ft

Test 501, Run 11, $Re_\infty = 1.0\times10^6$/ft

Test 487, Run 20, $Re_\infty = 1.5\times10^6$/ft

Test 501, Run 12, $Re_\infty = 1.5\times10^6$/ft

Test 487, Run 26, $Re_\infty = 2.0\times10^6$/ft

Figure 211. Reynolds Number effects at Mach 10, 40-Mesh Model

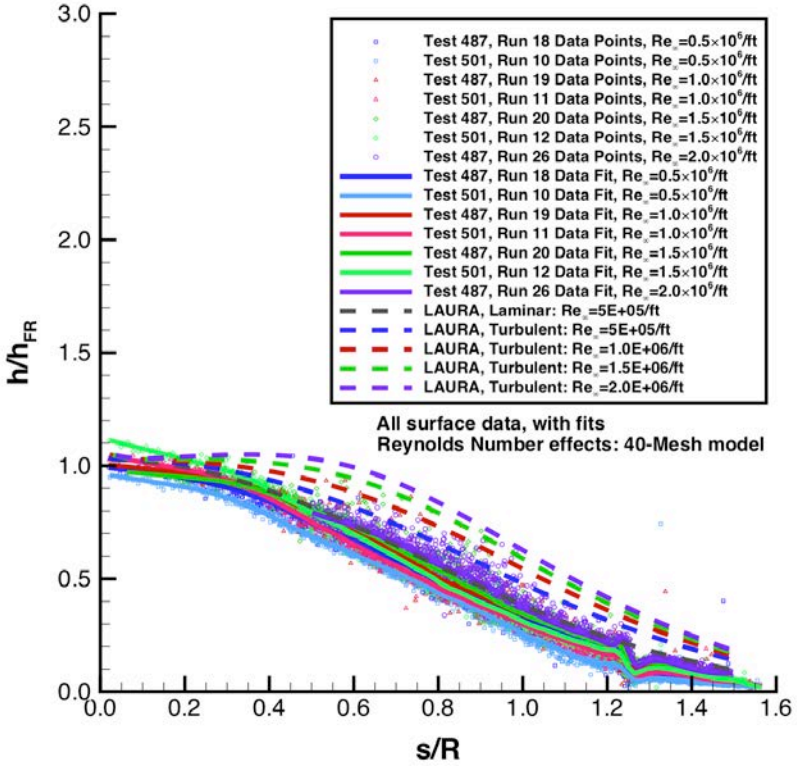

Figure 212. Reynolds Number effects at Mach 10, 40-Mesh model, data and fits.

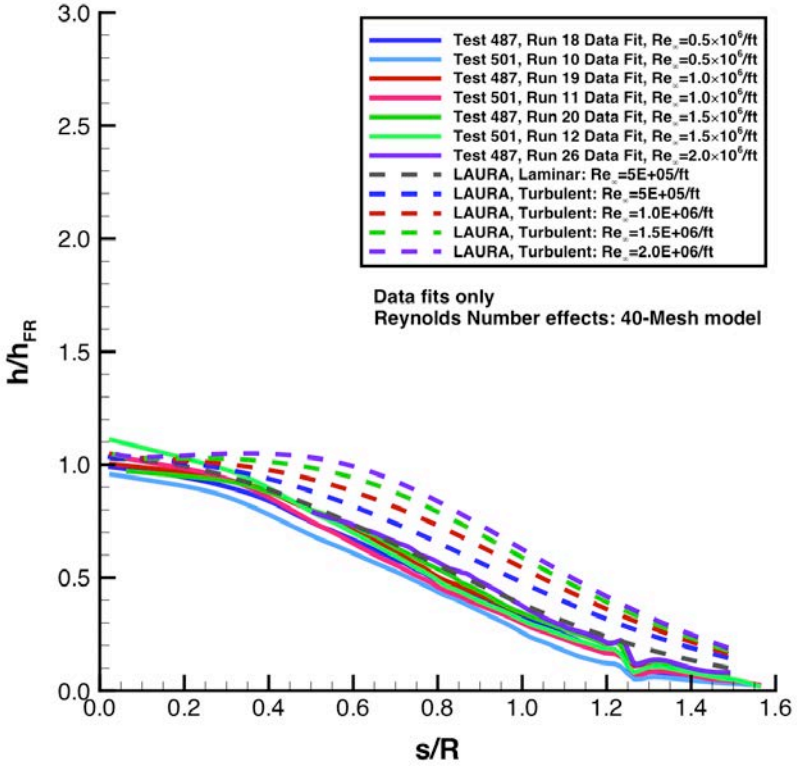

Figure 213. Reynolds Number effects at Mach 10, 40-Mesh model, fits only.

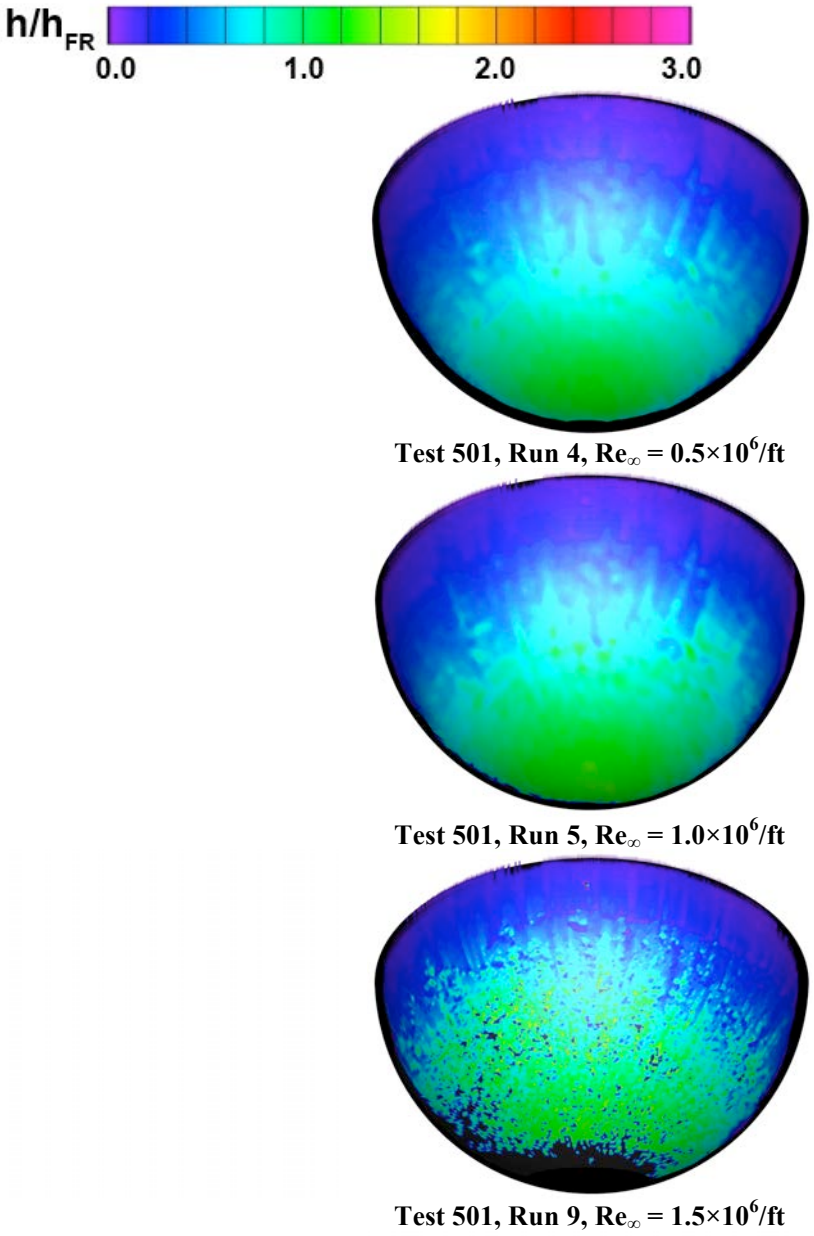

Figure 214. Reynolds Number effects at Mach 10, 30-Mesh model

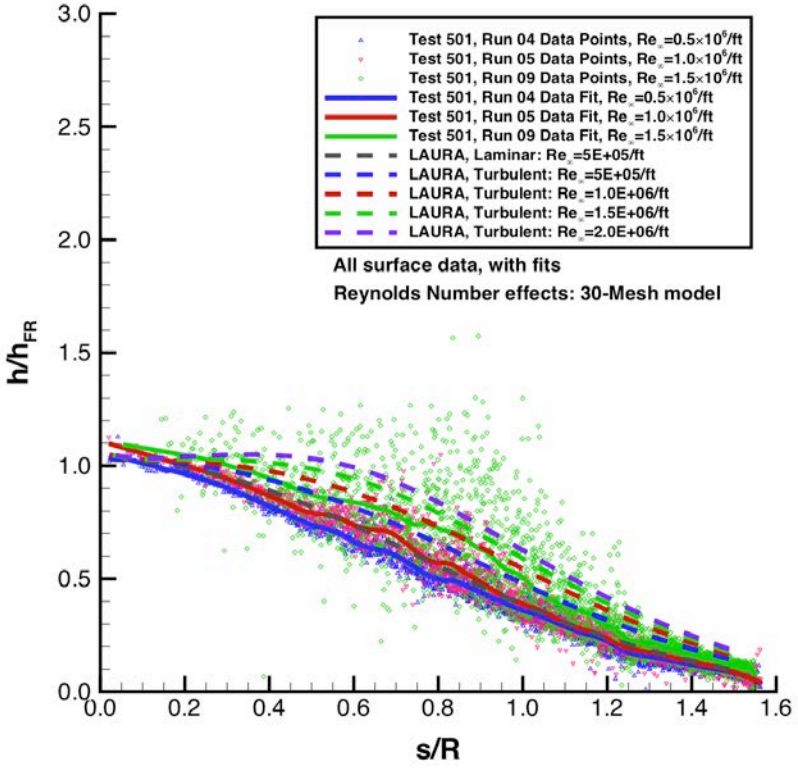

Figure 215. Reynolds Number effects at Mach 10, 30-Mesh model, data and fits.

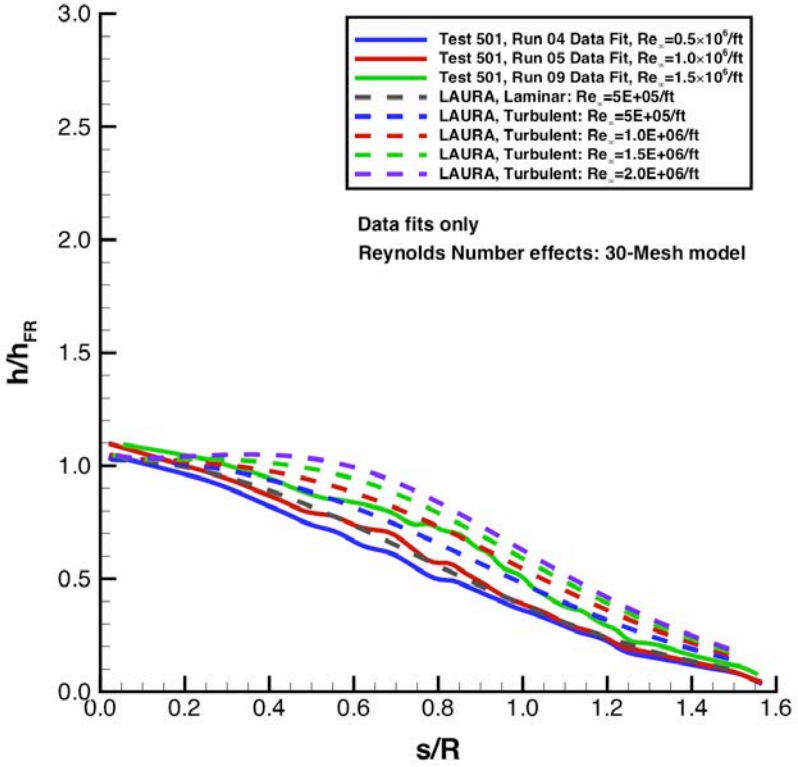

Figure 216. Reynolds Number effects at Mach 10, 30-Mesh model, fits only.

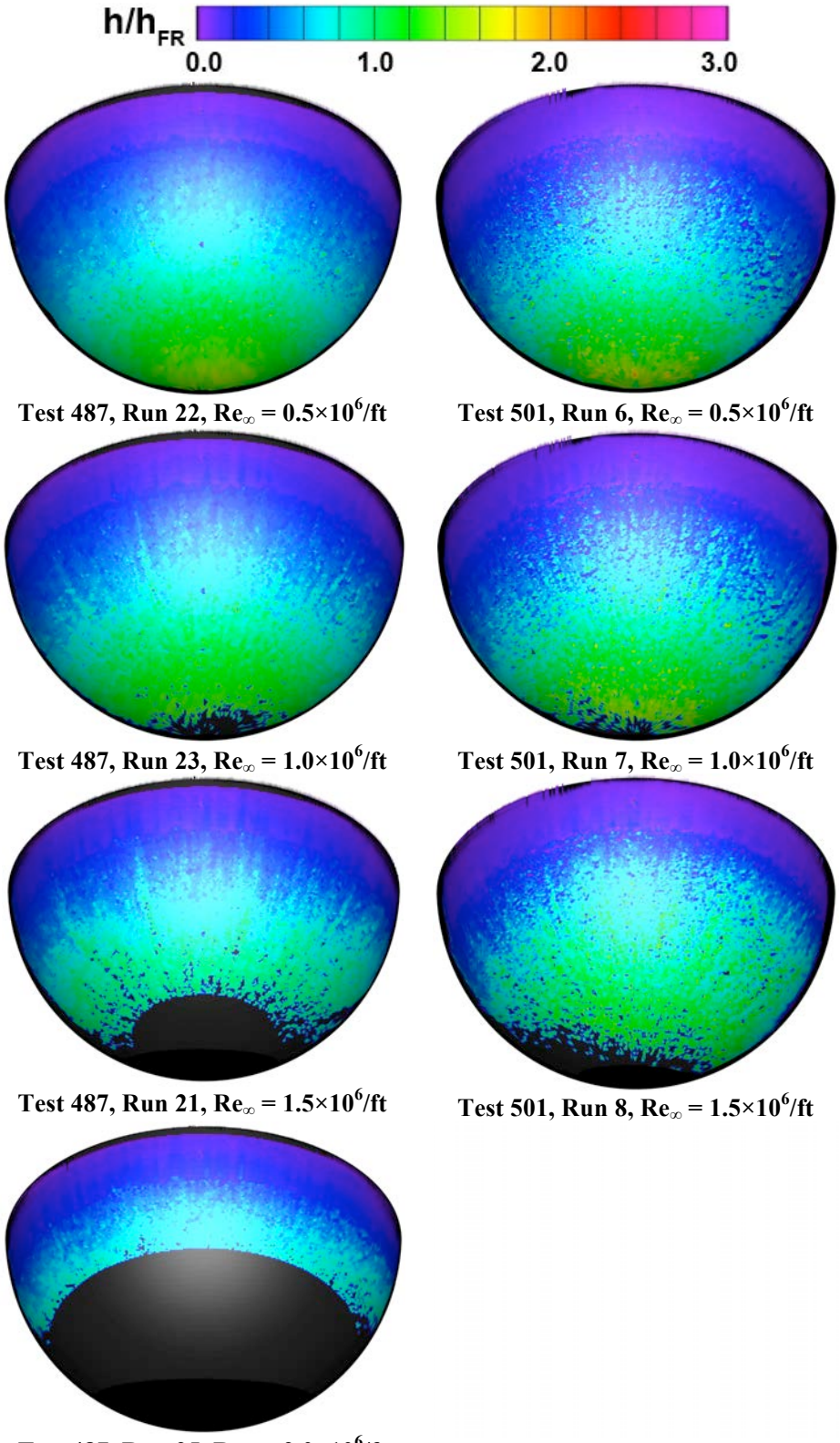

Test 487, Run 22, $Re_\infty = 0.5\times10^6$/ft

Test 501, Run 6, $Re_\infty = 0.5\times10^6$/ft

Test 487, Run 23, $Re_\infty = 1.0\times10^6$/ft

Test 501, Run 7, $Re_\infty = 1.0\times10^6$/ft

Test 487, Run 21, $Re_\infty = 1.5\times10^6$/ft

Test 501, Run 8, $Re_\infty = 1.5\times10^6$/ft

Test 487, Run 25, $Re_\infty = 2.0\times10^6$/ft

Figure 217. Reynolds Number effects at Mach 10, 20-Mesh model

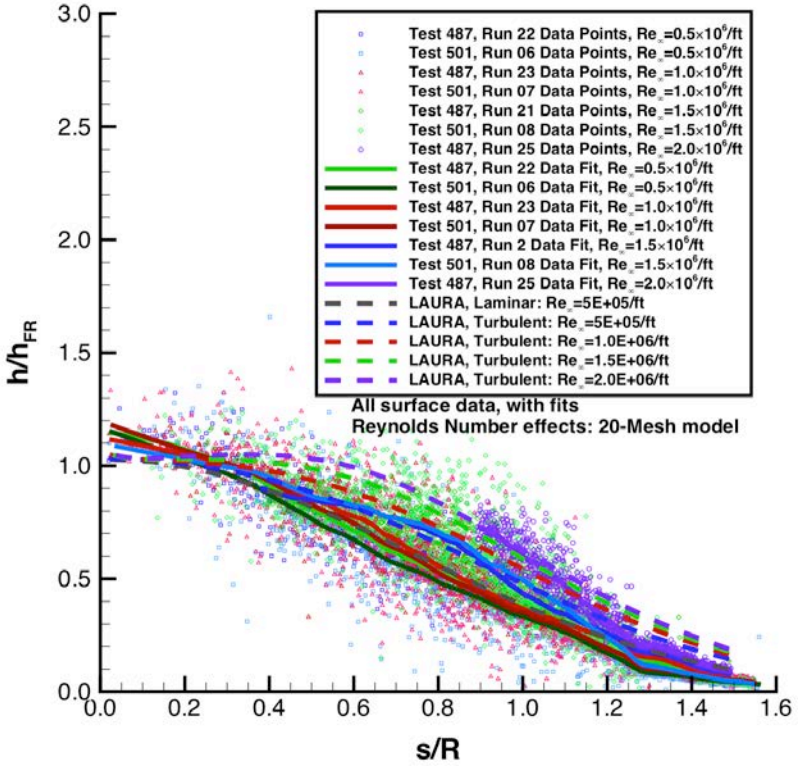

Figure 218. Reynolds Number effects at Mach 10, 20-Mesh model, data and fits.

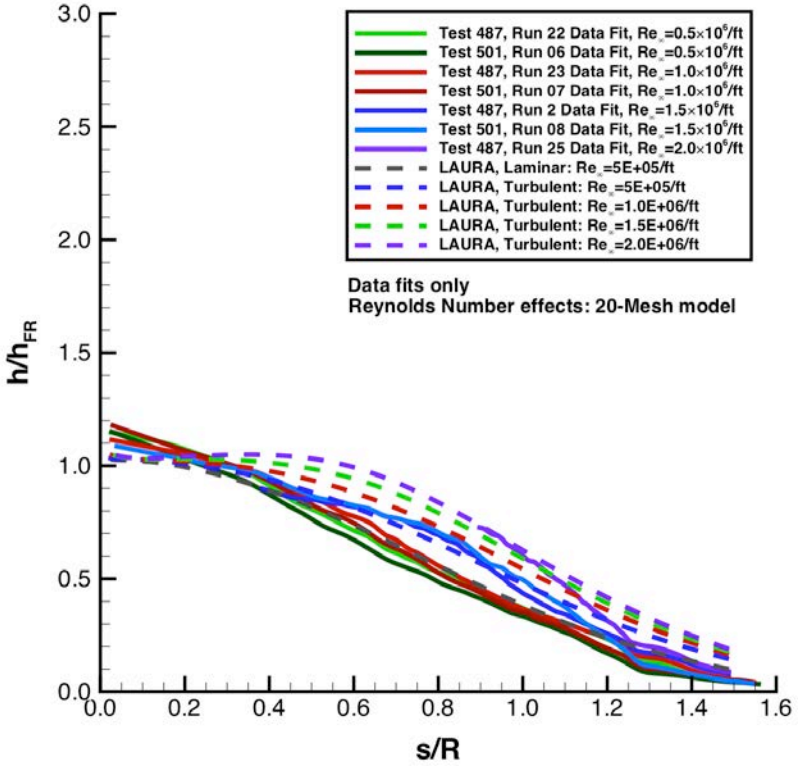

Figure 219. Reynolds Number effects at Mach 10, 20-Mesh model, fits only.

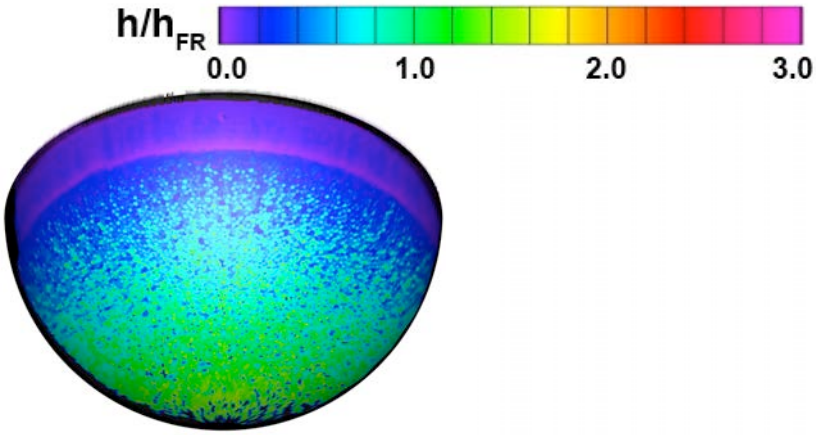

Test 487, Run 13, $Re_\infty = 0.5\times10^6$/ft

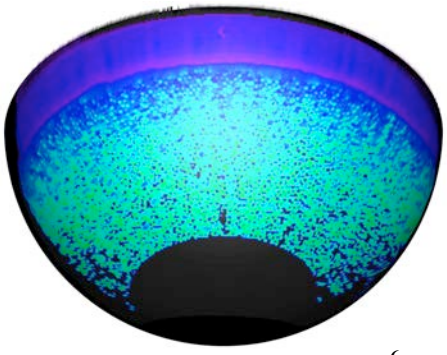

Test 487, Run 14, $Re_\infty = 1.0\times10^6$/ft

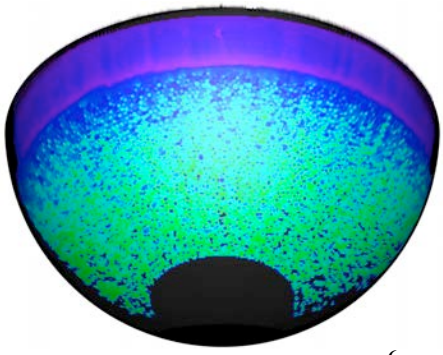

Test 487, Run 16, $Re_\infty = 1.0\times10^6$/ft

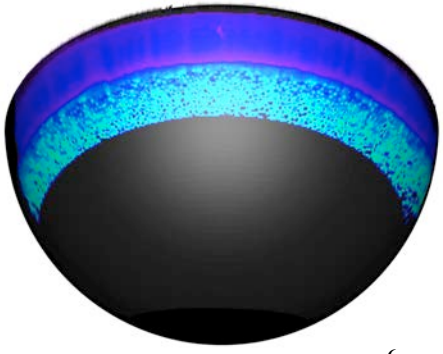

Test 487, Run 12, $Re_\infty = 1.5\times10^6$/ft

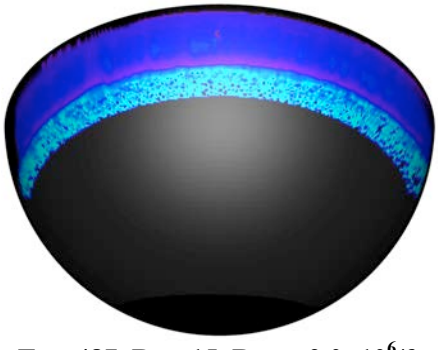

Test 487, Run 15, $Re_\infty = 2.0\times10^6$/ft

Figure 220. Reynolds Number effects at Mach 10, 10-Mesh model

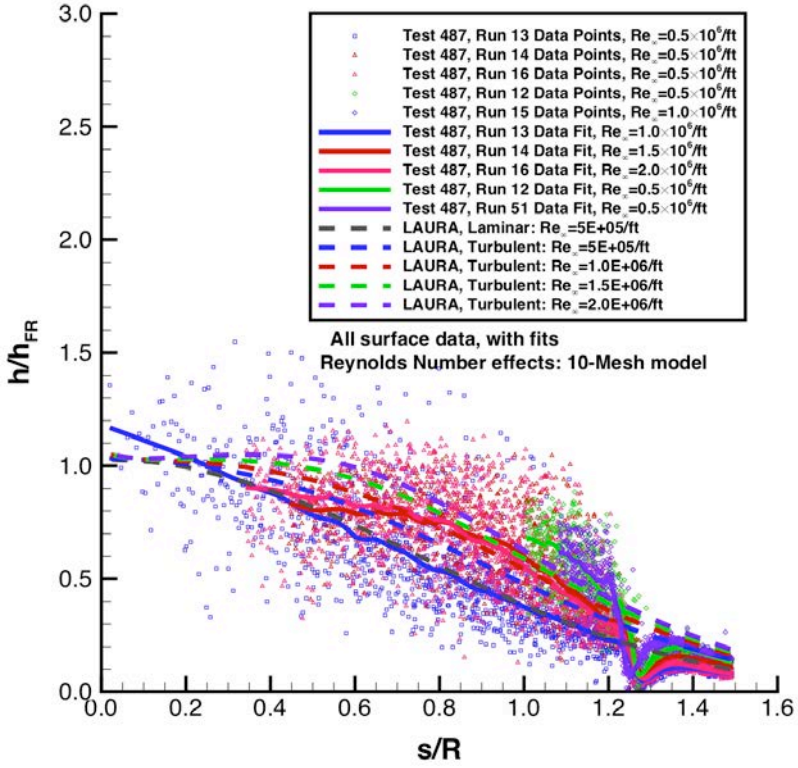

Figure 221. Reynolds Number effects at Mach 10, 10-Mesh model, data and fits.

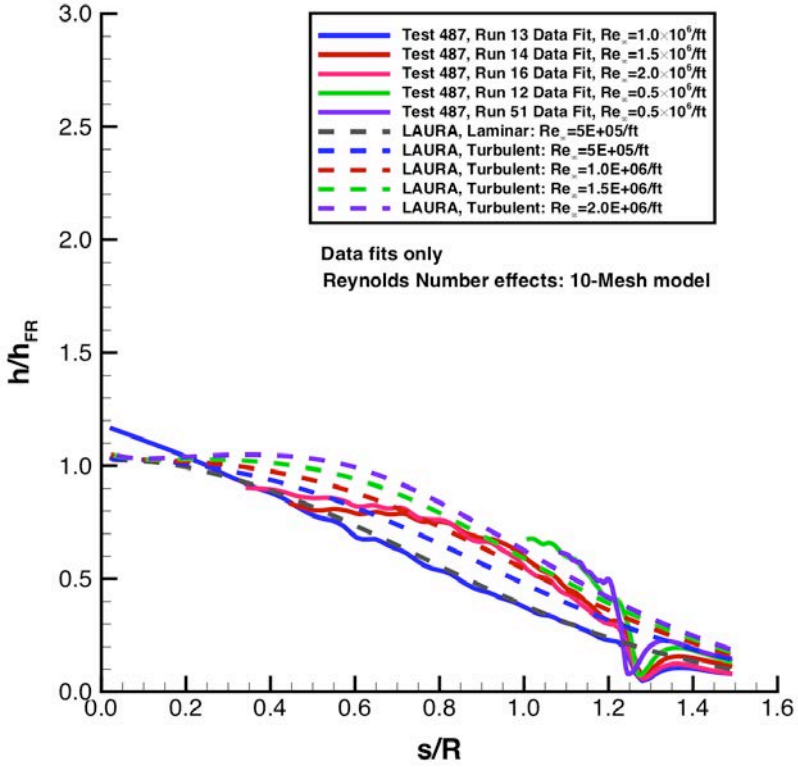

Figure 222. Reynolds Number effects at Mach 10, 10-Mesh model, fits only.

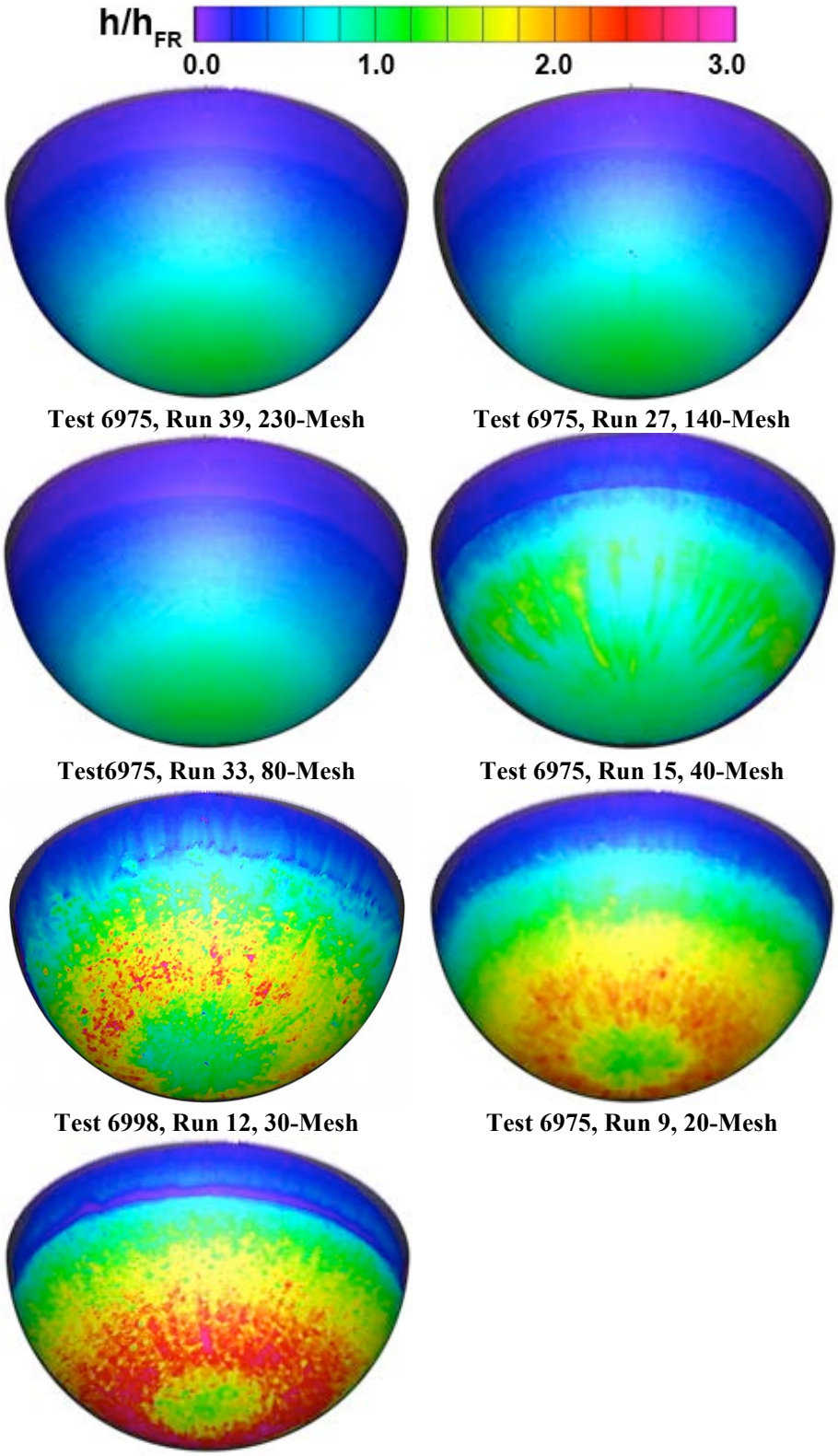

Figure 223. Roughness effects at Mach 6, $Re_\infty = 3.0\times10^6$/ft

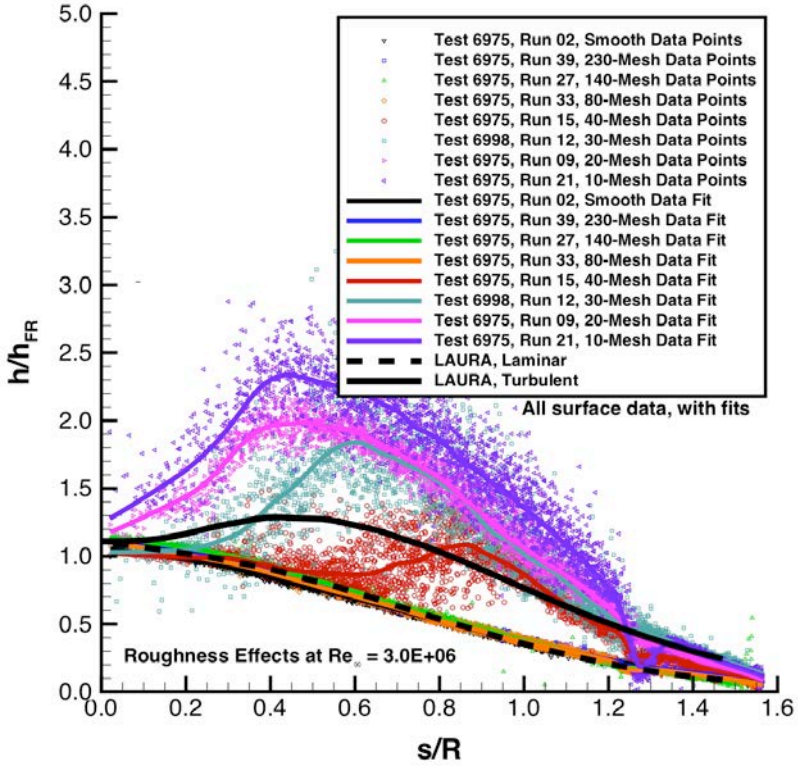

Figure 224. Roughness effects at Mach 6, $Re_\infty = 3.0\times10^6$/ft, data and fits

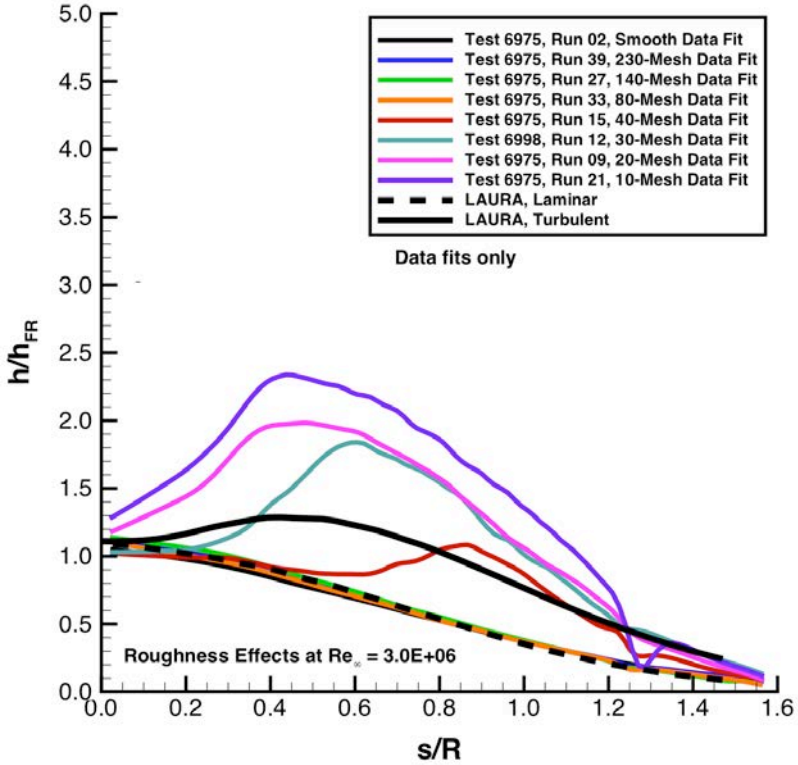

Figure 225. Roughness effects at Mach 6, $Re_\infty = 3.0\times10^6$/ft, fits only.

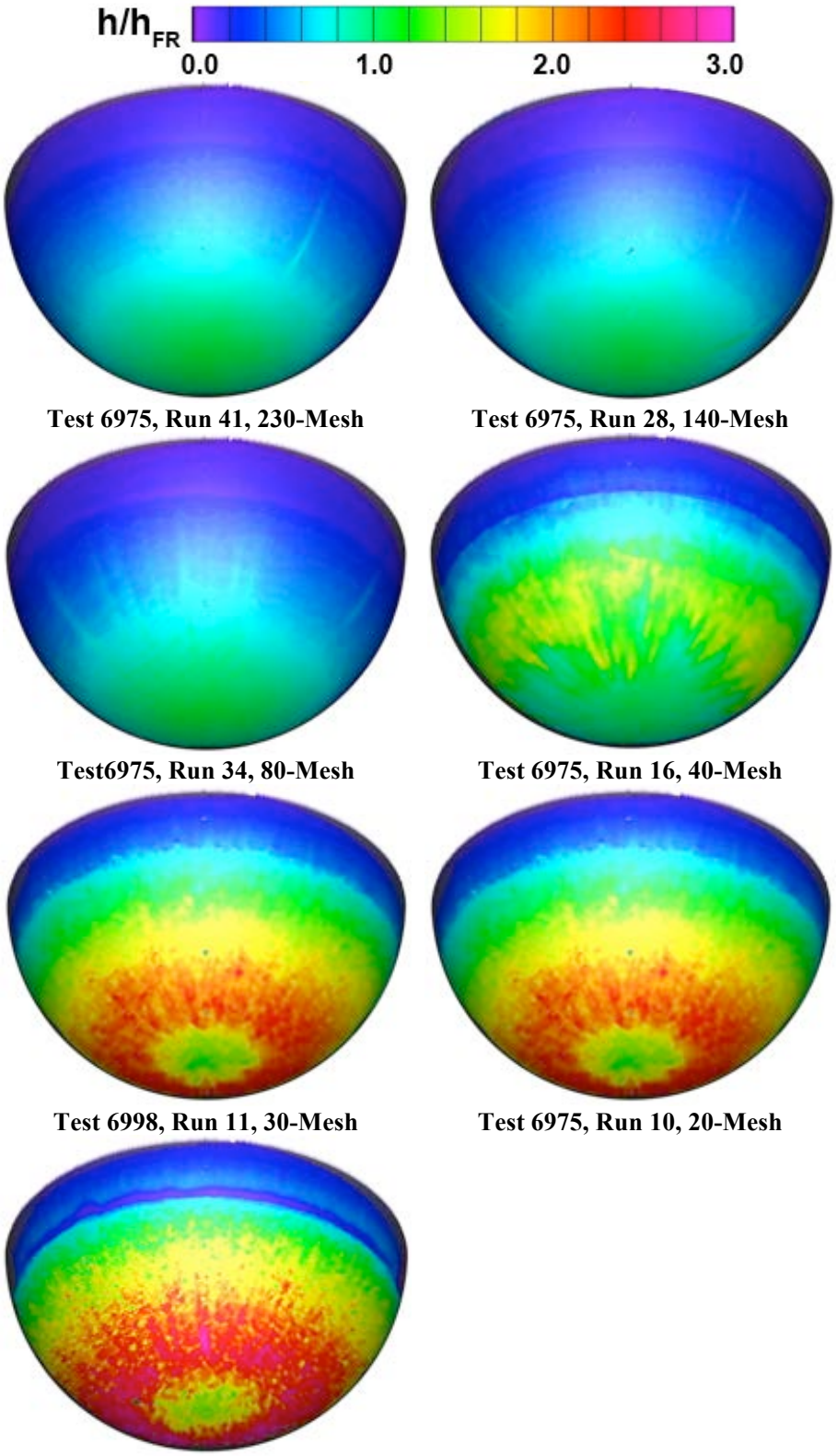

Figure 226. Roughness effects at Mach 6, $Re_\infty = 3.9\times10^6$/ft.

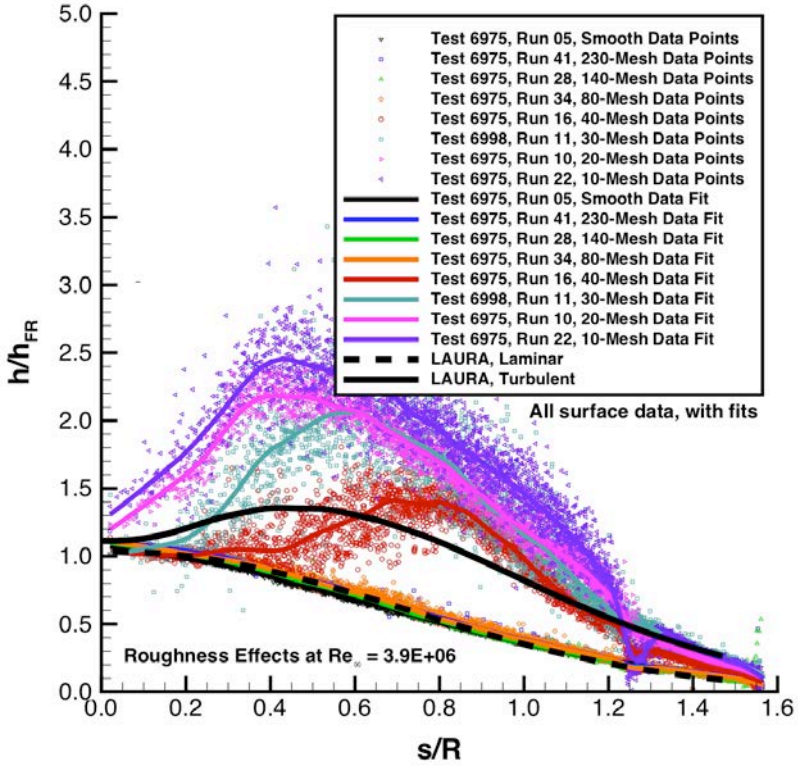

Figure 227. Roughness effects at Mach 6, $Re_\infty = 3.9\times10^6$/ft, data and fits.

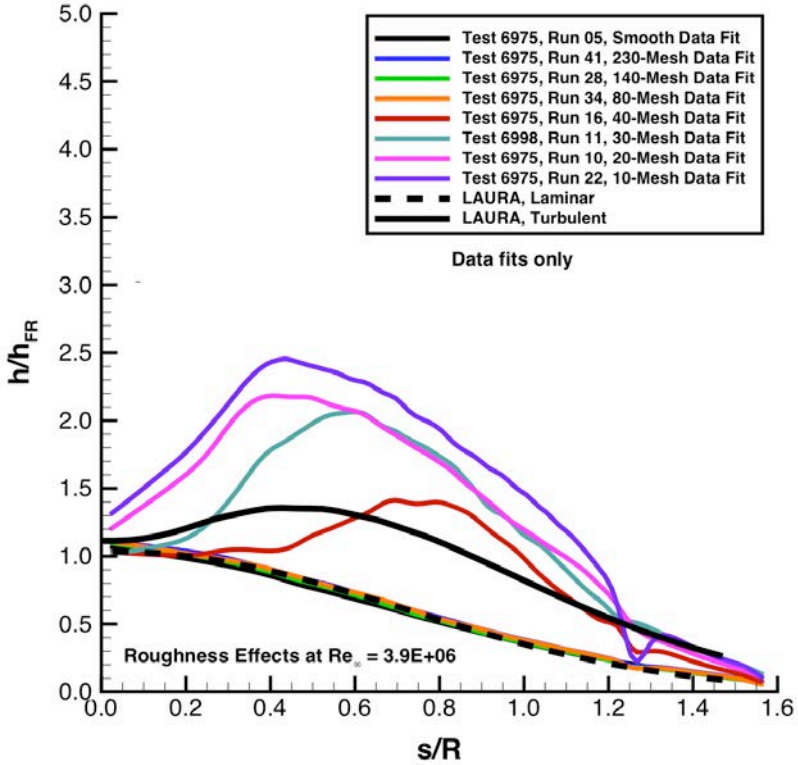

Figure 228. Roughness effects at Mach 6, $Re_\infty = 3.9\times10^6$/ft, fits only.

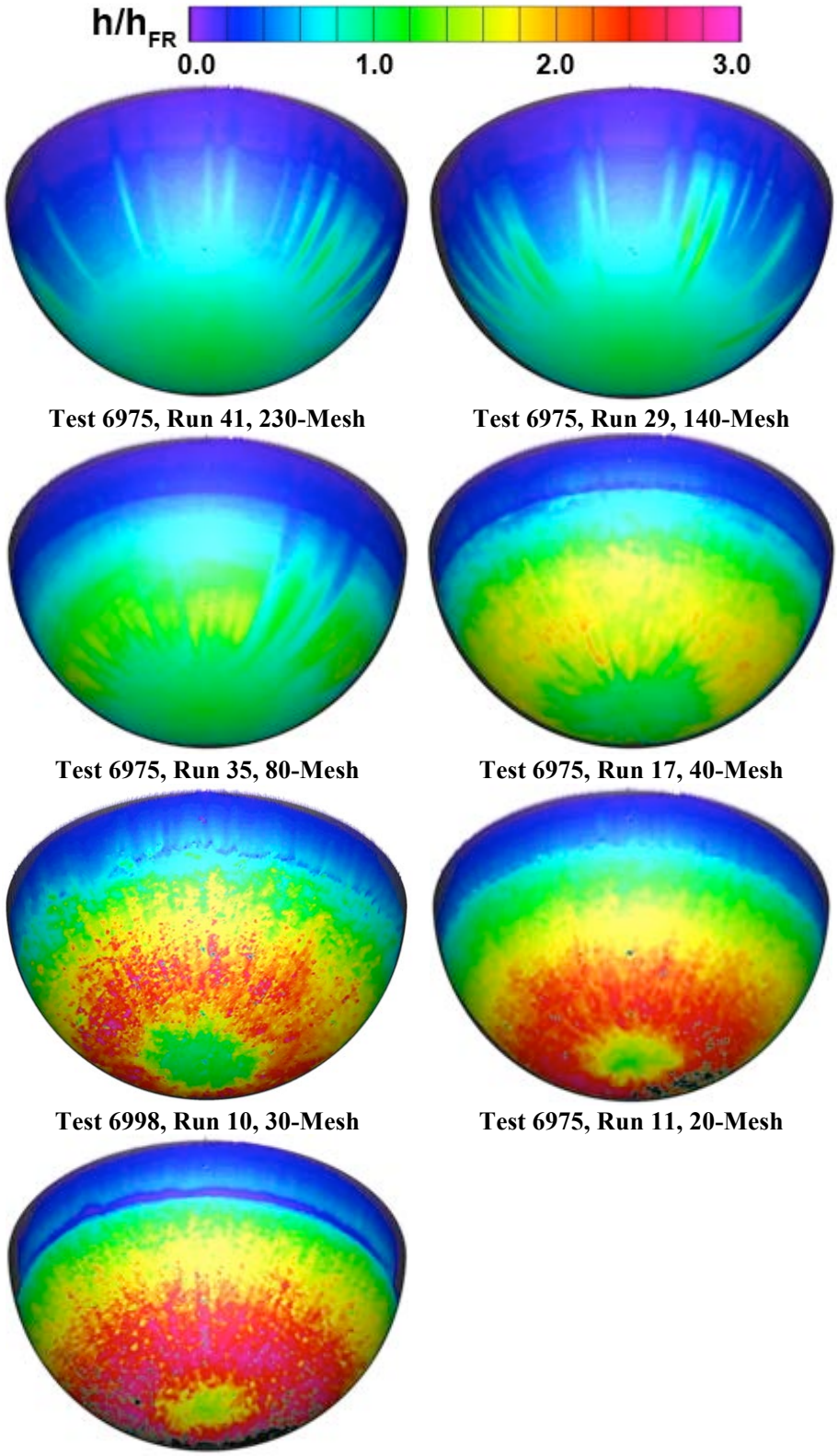

Test 6975, Run 41, 230-Mesh

Test 6975, Run 29, 140-Mesh

Test 6975, Run 35, 80-Mesh

Test 6975, Run 17, 40-Mesh

Test 6998, Run 10, 30-Mesh

Test 6975, Run 11, 20-Mesh

Test 6975, Run 23, 10-Mesh

Figure 229. Roughness effects at Mach 6, $Re_\infty = 5.0\times10^6$/ft.

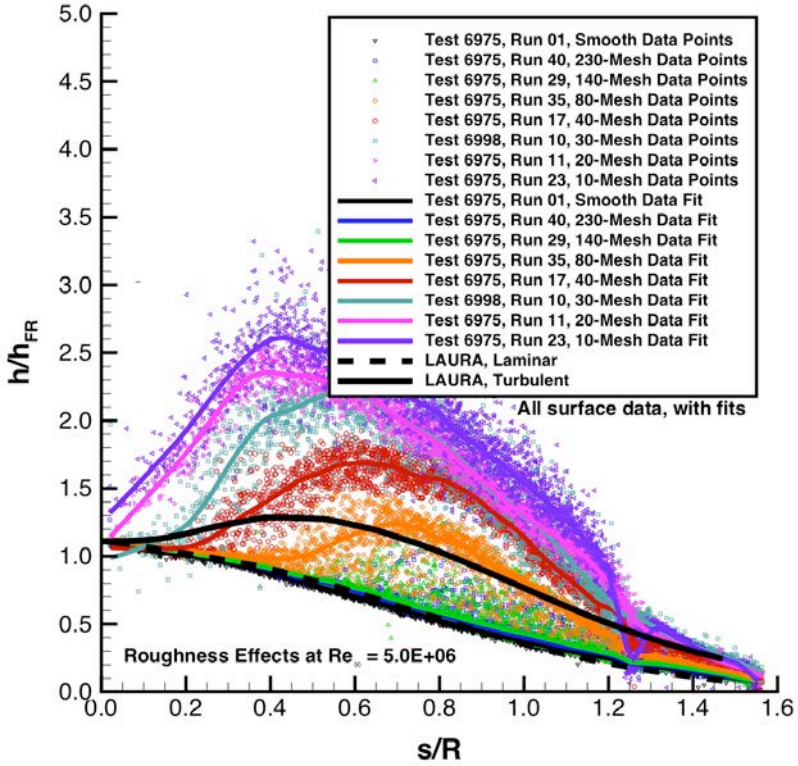

Figure 230. Roughness effects at Mach 6, $Re_\infty = 5.0\times10^6$/ft, data and fits.

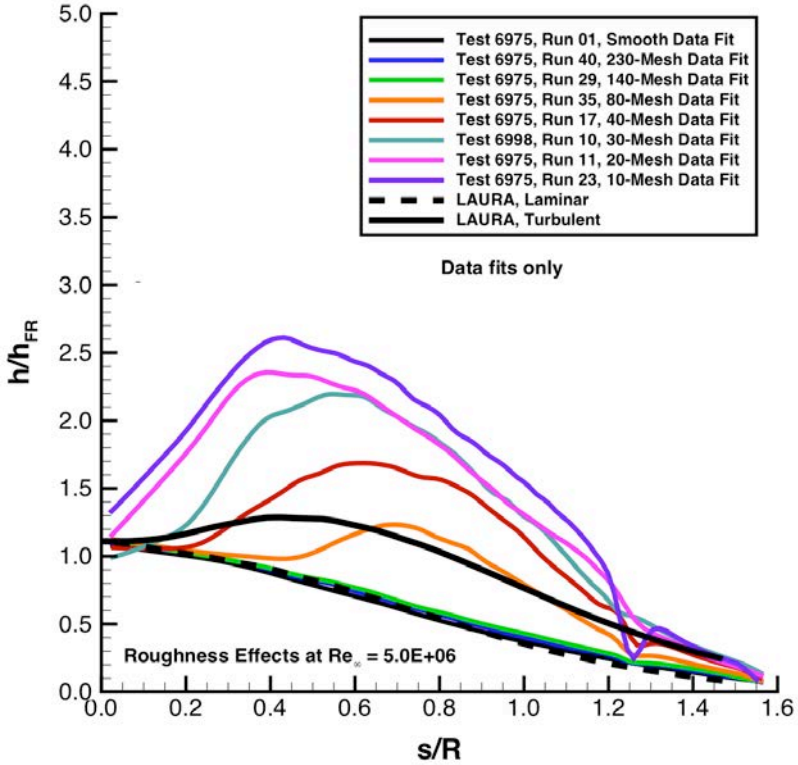

Figure 231. Roughness effects at Mach 6, $Re_\infty = 5.0\times10^6$/ft, fits only.

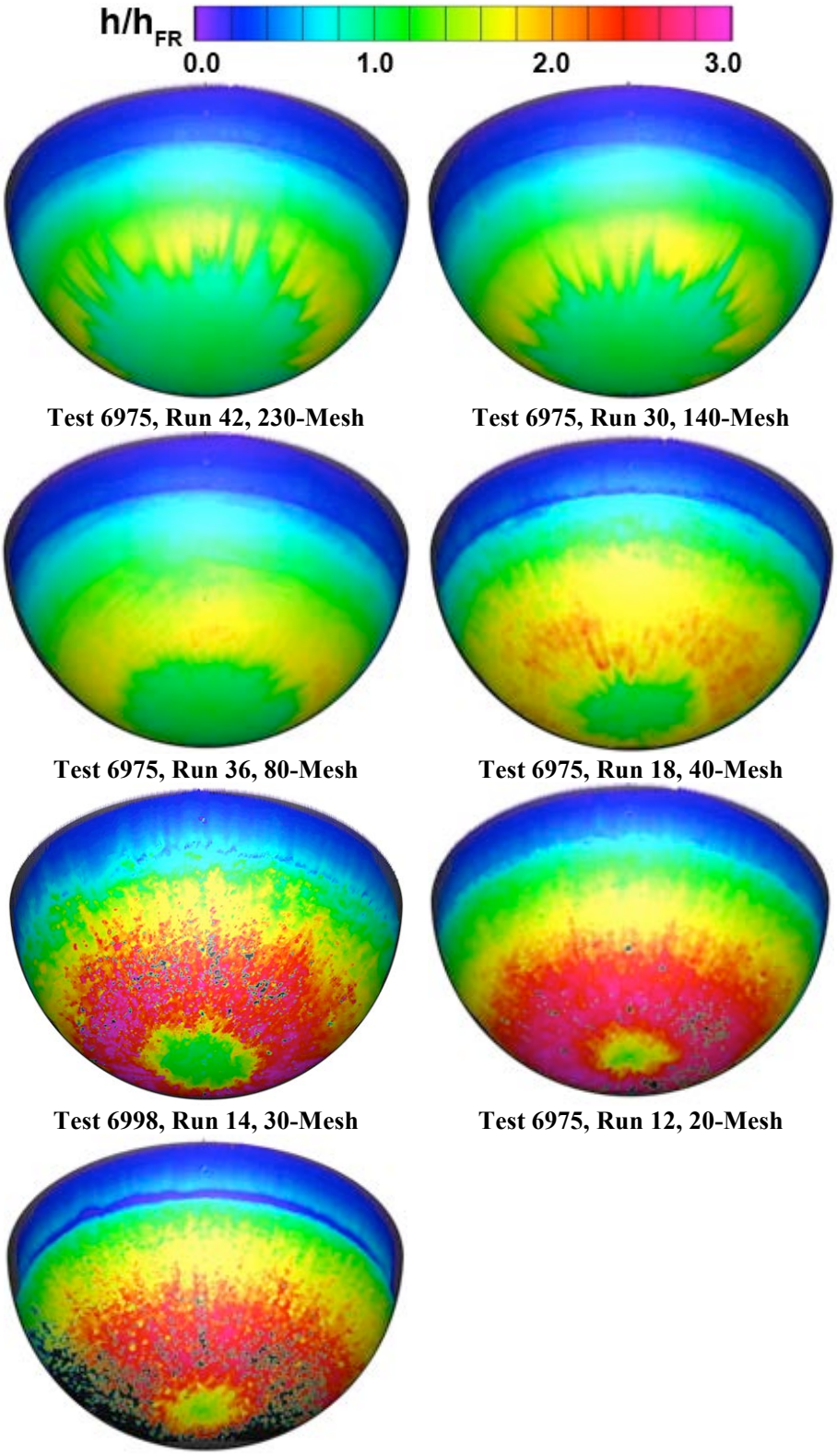

Test 6975, Run 42, 230-Mesh

Test 6975, Run 30, 140-Mesh

Test 6975, Run 36, 80-Mesh

Test 6975, Run 18, 40-Mesh

Test 6998, Run 14, 30-Mesh

Test 6975, Run 12, 20-Mesh

Test 6975, Run 24, 10-Mesh

Figure 232. Roughness effects at Mach 6, $Re_\infty = 6.6\times10^6$/ft.

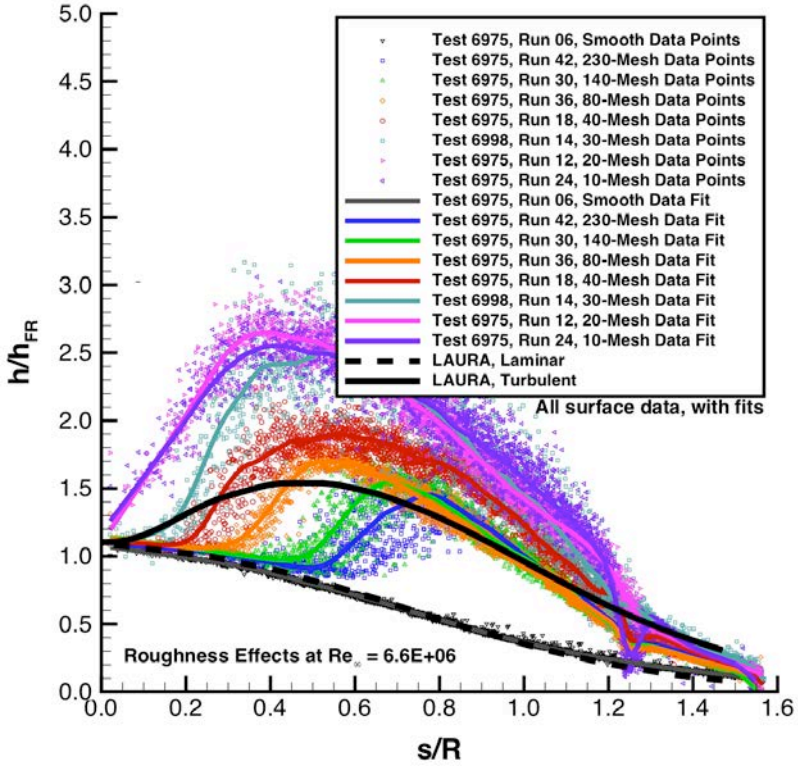

Figure 233. Roughness effects at Mach 6, $Re_\infty = 6.6\times10^6$/ft, data and fits.

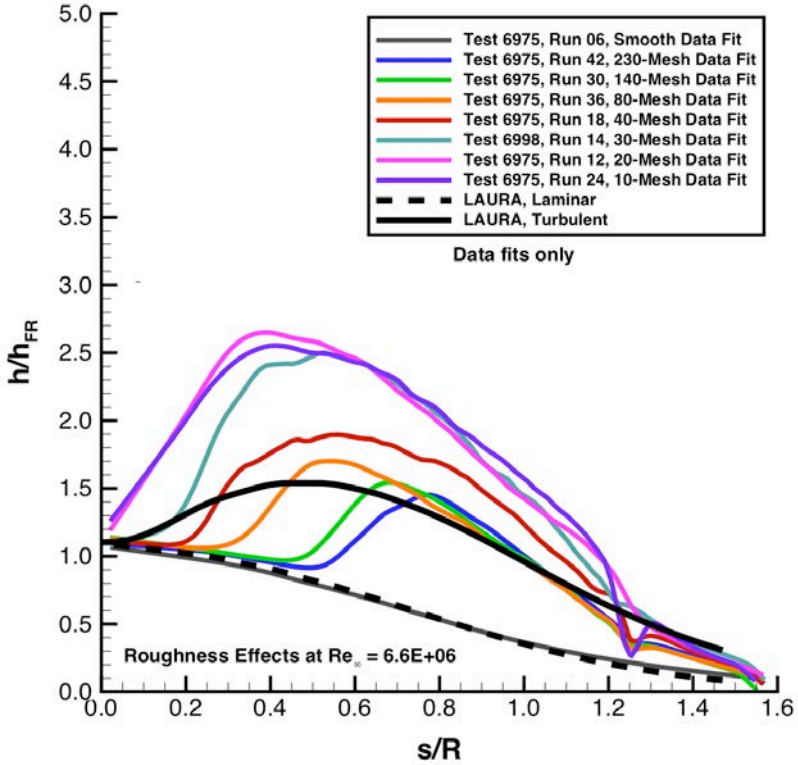

Figure 234. Roughness effects at Mach 6, $Re_\infty = 6.6\times10^6$/ft, fits only.

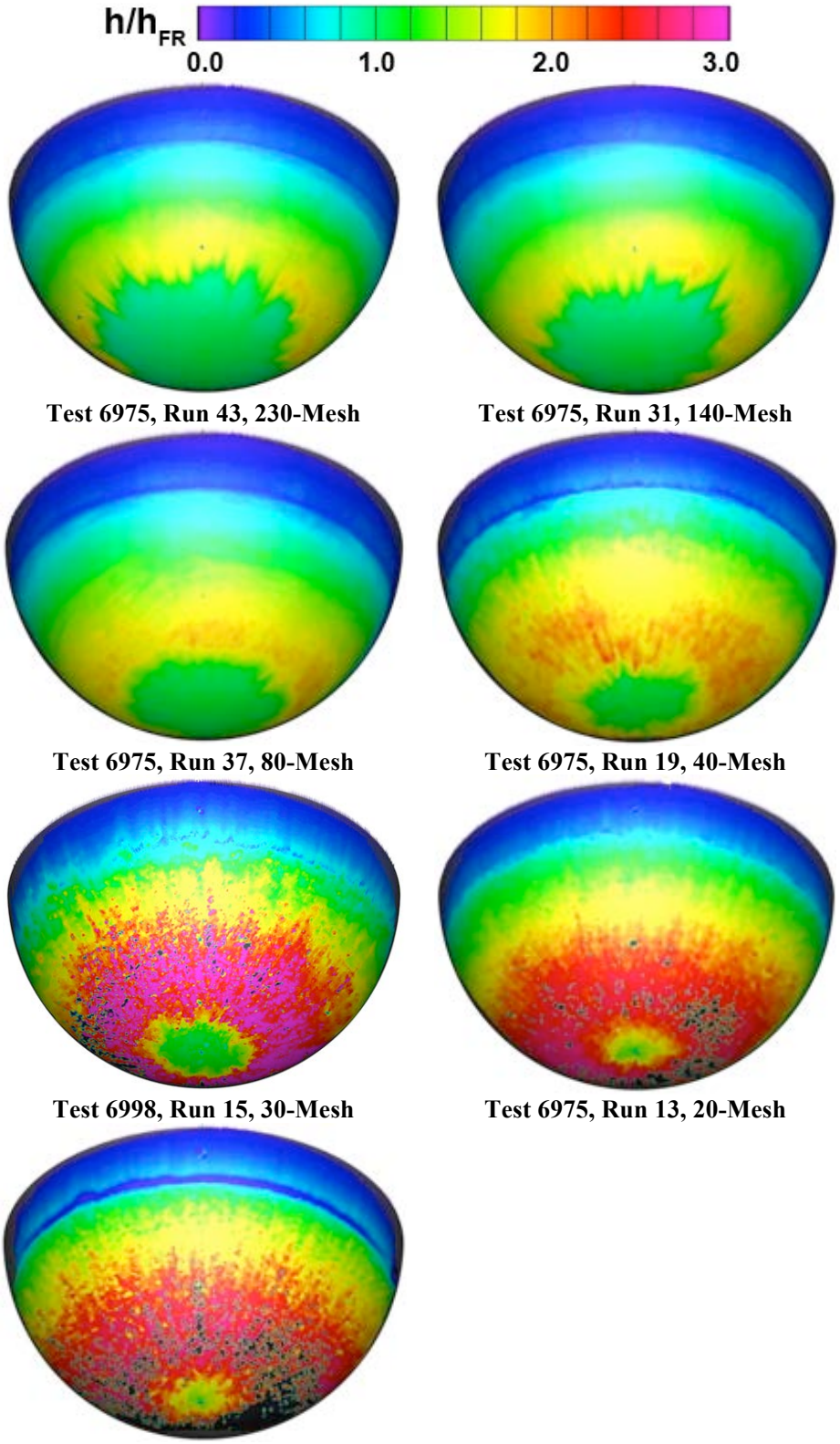

Test 6975, Run 43, 230-Mesh

Test 6975, Run 31, 140-Mesh

Test 6975, Run 37, 80-Mesh

Test 6975, Run 19, 40-Mesh

Test 6998, Run 15, 30-Mesh

Test 6975, Run 13, 20-Mesh

Test 6975, Run 25, 10-Mesh

Figure 235. Roughness effects at Mach 6, $Re_\infty = 7.5\times10^6$/ft.

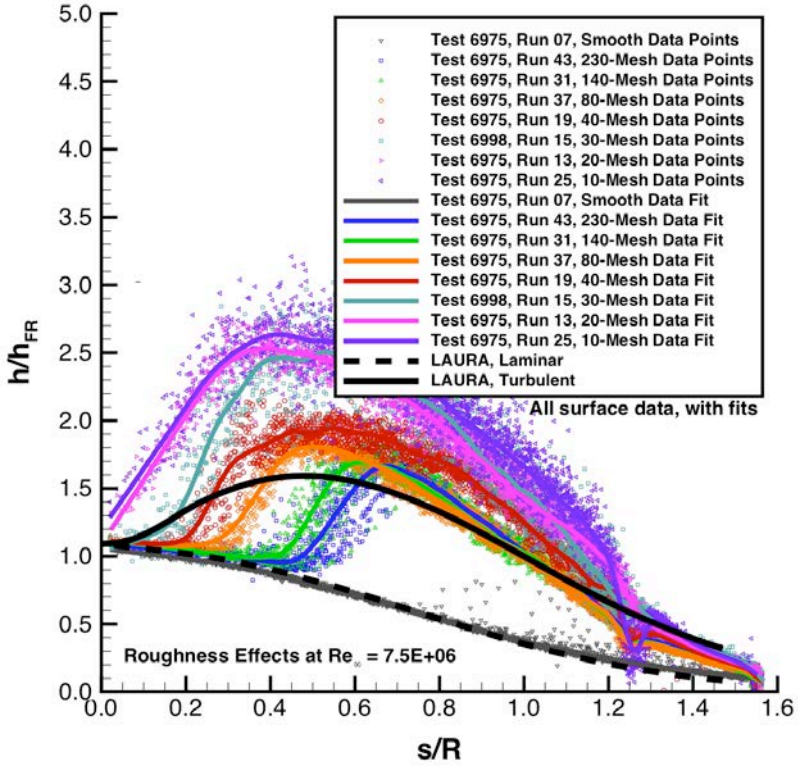

Figure 236. Roughness effects at Mach 6, $Re_\infty = 7.5\times10^6$/ft, data and fits.

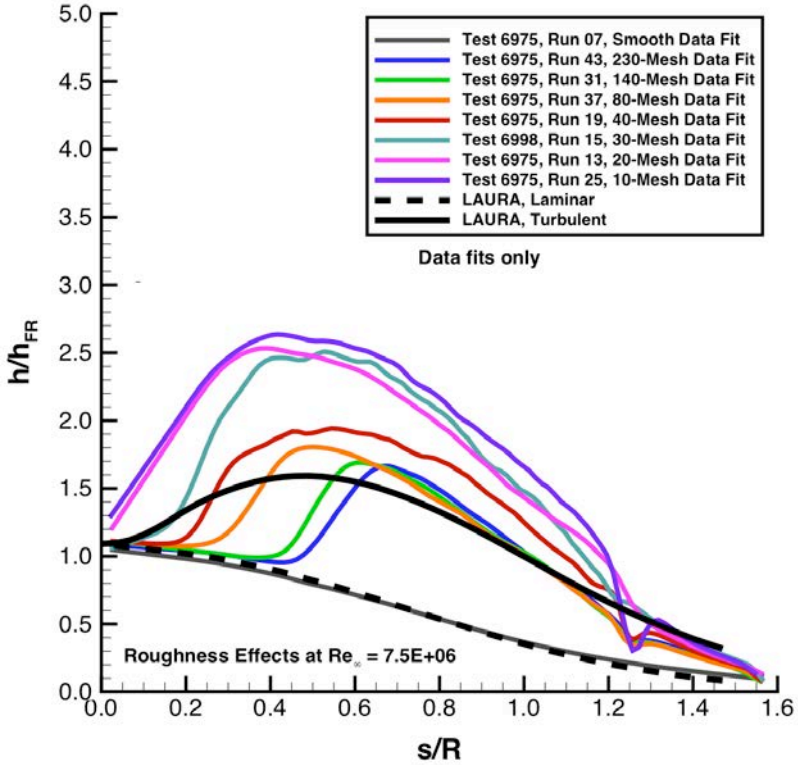

Figure 237. Roughness effects at Mach 6, $Re_\infty = 7.5\times10^6$/ft, fits only.

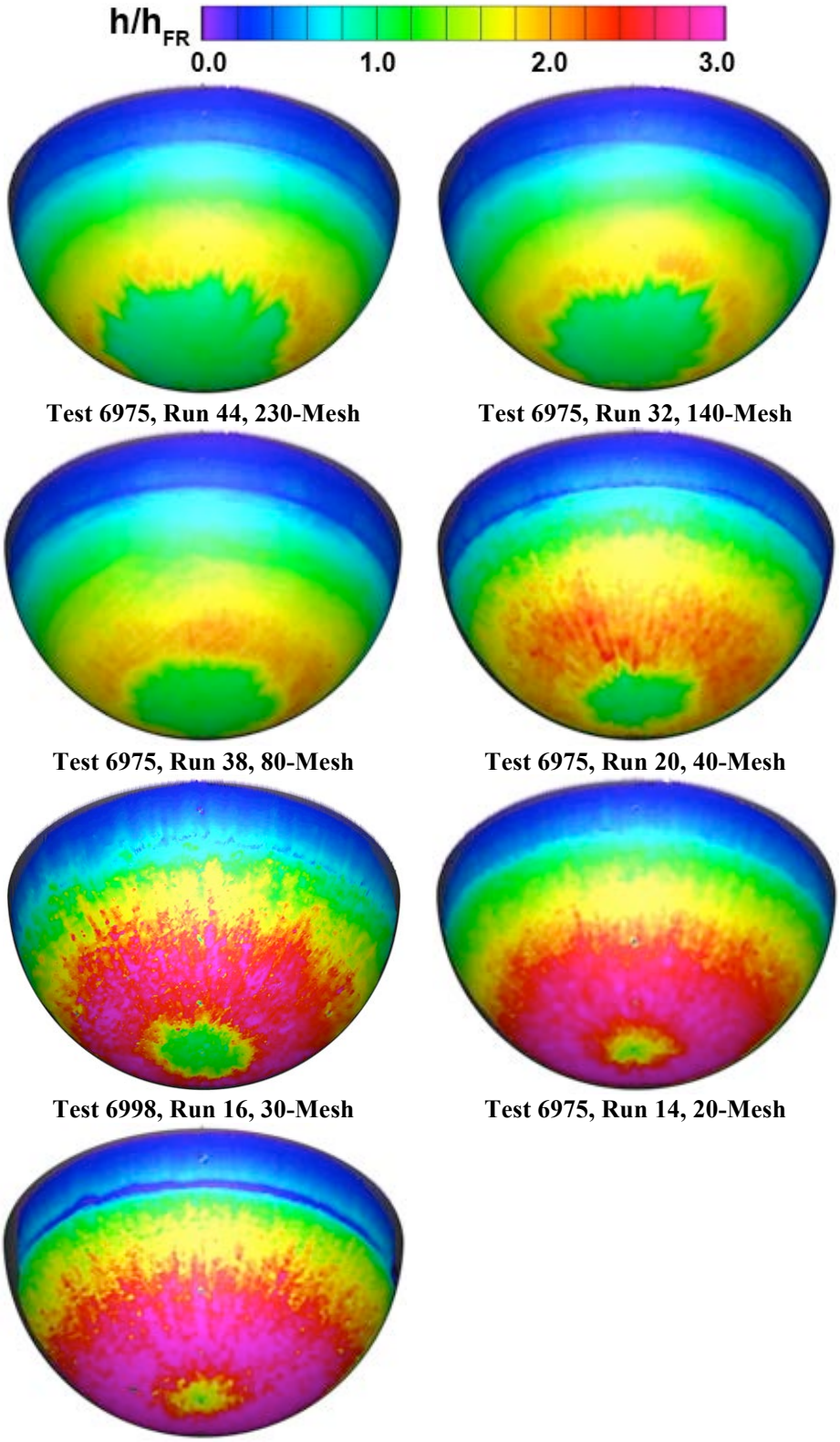

Test 6975, Run 44, 230-Mesh

Test 6975, Run 32, 140-Mesh

Test 6975, Run 38, 80-Mesh

Test 6975, Run 20, 40-Mesh

Test 6998, Run 16, 30-Mesh

Test 6975, Run 14, 20-Mesh

Test 6975, Run 26, 10-Mesh

Figure 238. Roughness effects at Mach 6, $Re_\infty = 8.4\times10^6$/ft.

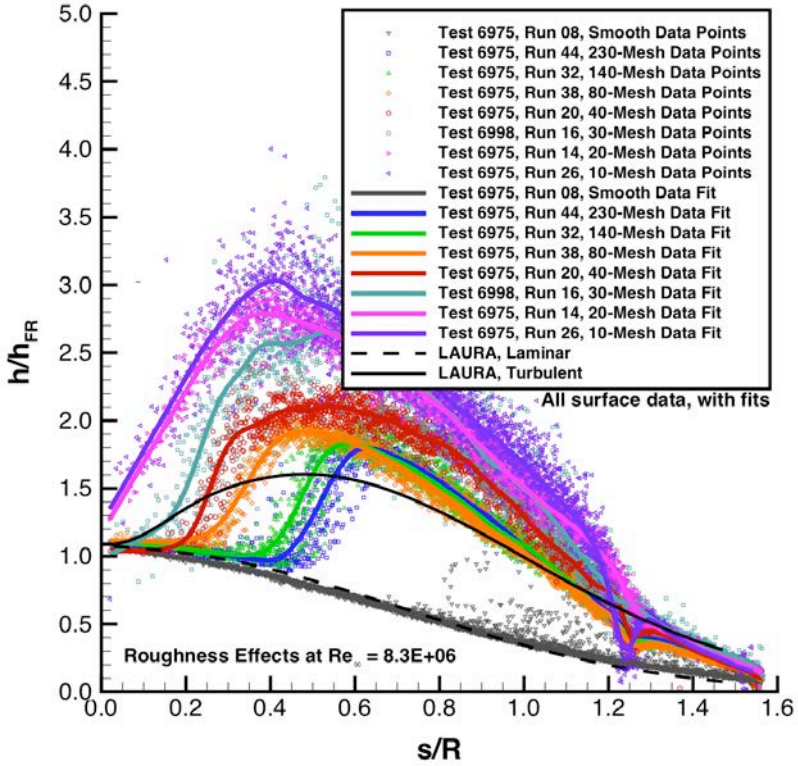

Figure 239. Roughness effects at Mach 6, $Re_\infty = 8.4\times10^6$/ft, data and fits.

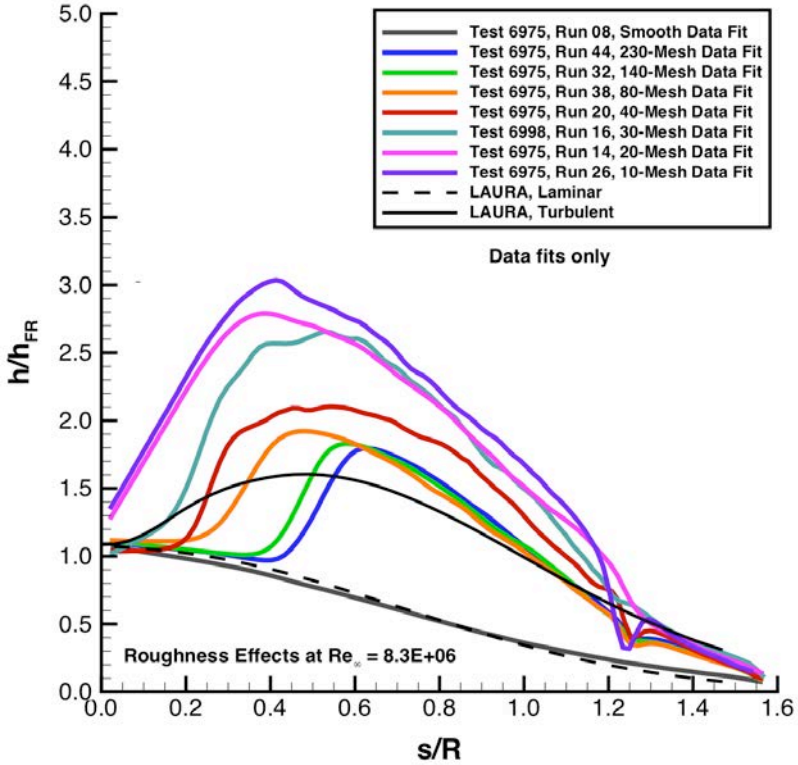

Figure 240. Roughness effects at Mach 6, $Re_\infty = 8.4\times10^6$/ft, fits only.

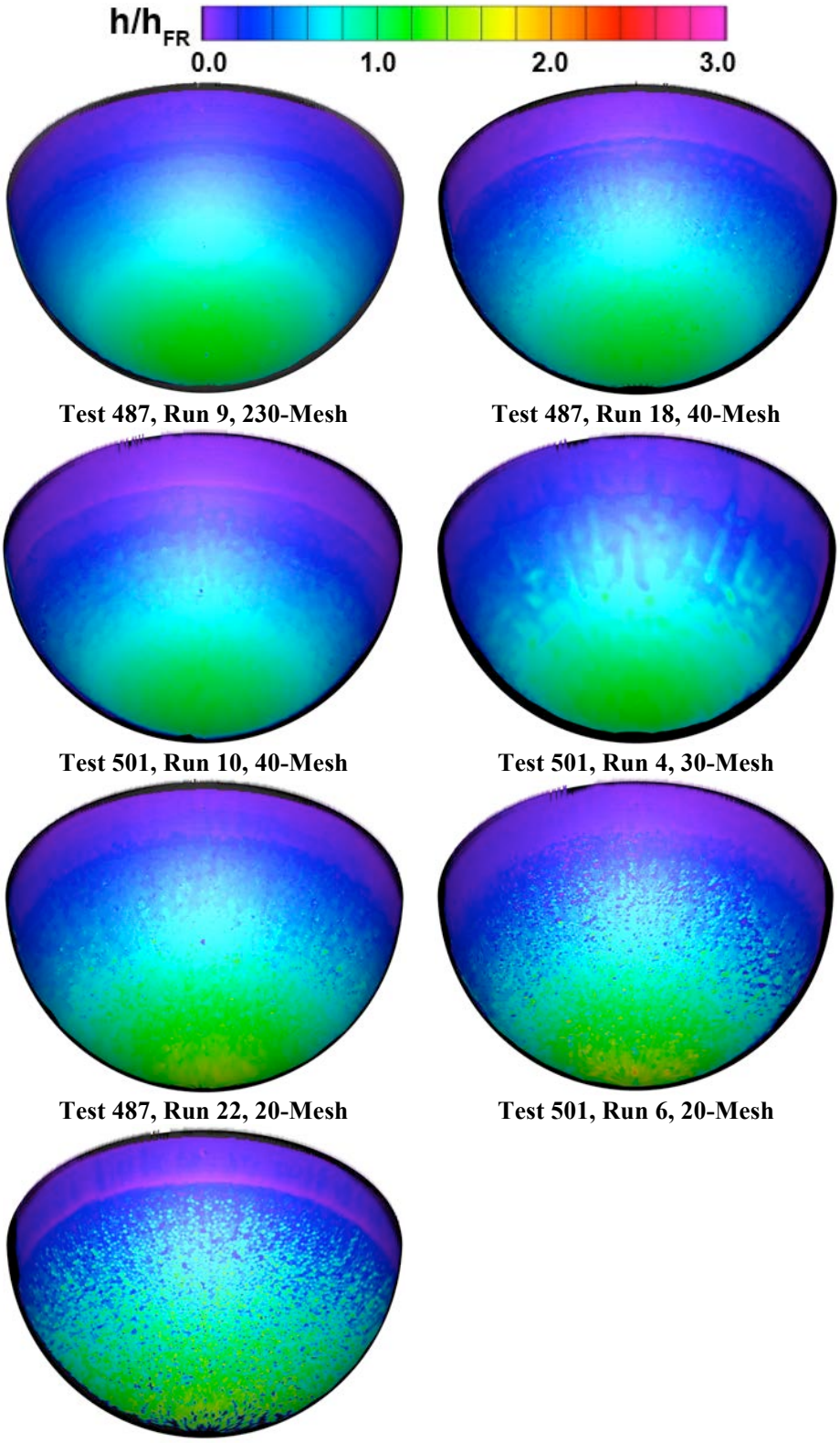

Test 487, Run 9, 230-Mesh

Test 487, Run 18, 40-Mesh

Test 501, Run 10, 40-Mesh

Test 501, Run 4, 30-Mesh

Test 487, Run 22, 20-Mesh

Test 501, Run 6, 20-Mesh

Test 487, Run 13, 10-Mesh

Figure 241. Roughness effects at Mach 10, $Re_\infty = 0.5\times10^6$/ft.

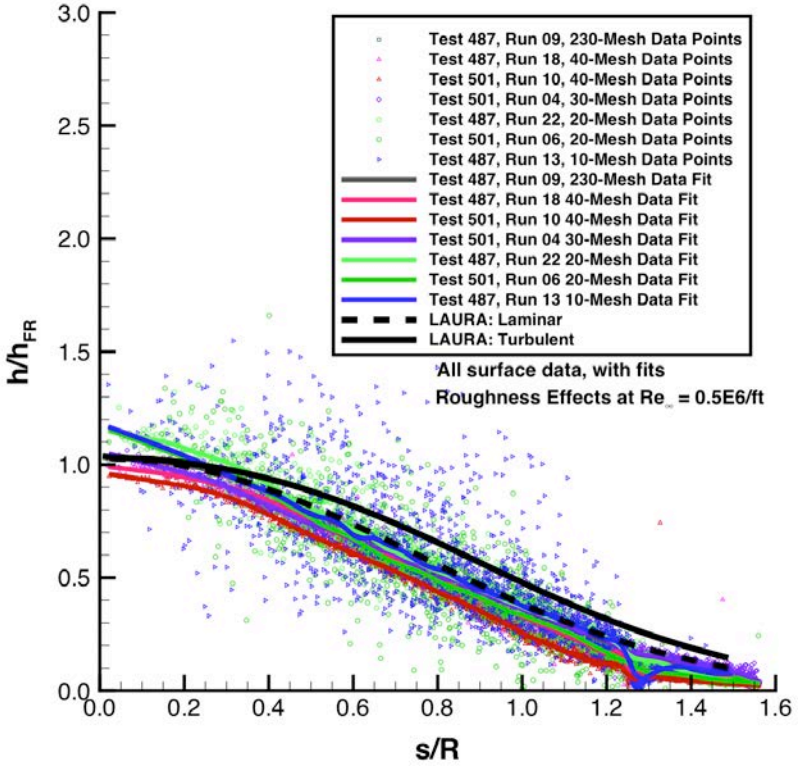

Figure 242. Roughness effects at Mach 10, $Re_\infty = 0.5\times10^6$/ft, data and fits.

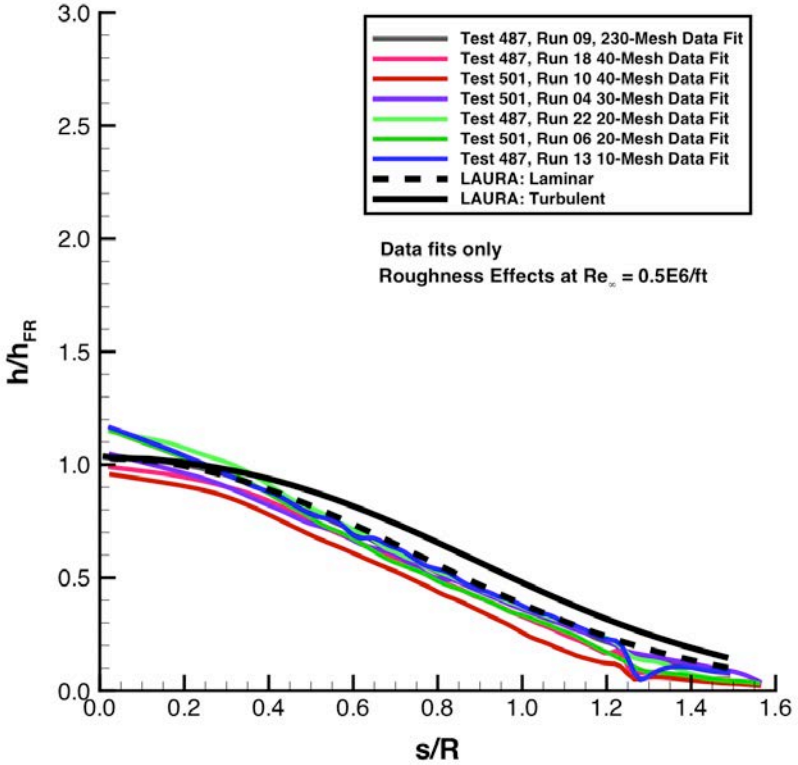

Figure 243. Roughness effects at Mach 10, $Re_\infty = 0.5\times10^6$/ft, fits only.

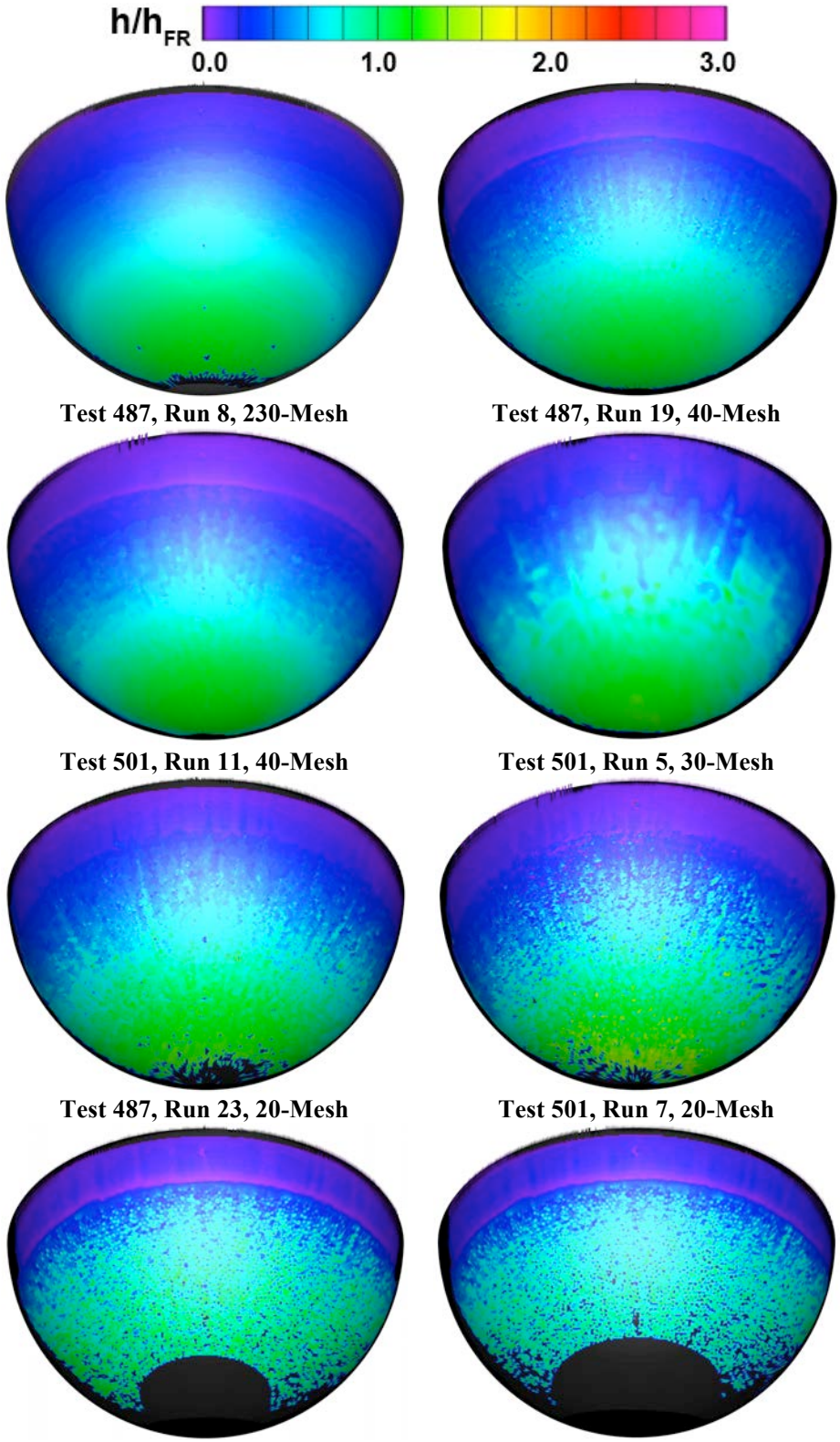

Test 487, Run 8, 230-Mesh | Test 487, Run 19, 40-Mesh

Test 501, Run 11, 40-Mesh | Test 501, Run 5, 30-Mesh

Test 487, Run 23, 20-Mesh | Test 501, Run 7, 20-Mesh

Test 487, Run 16, 10-Mesh | Test 487, Run 14, 10-Mesh

Figure 244. Roughness effects at Mach 10, $Re_\infty = 1.0\times10^6$/ft.

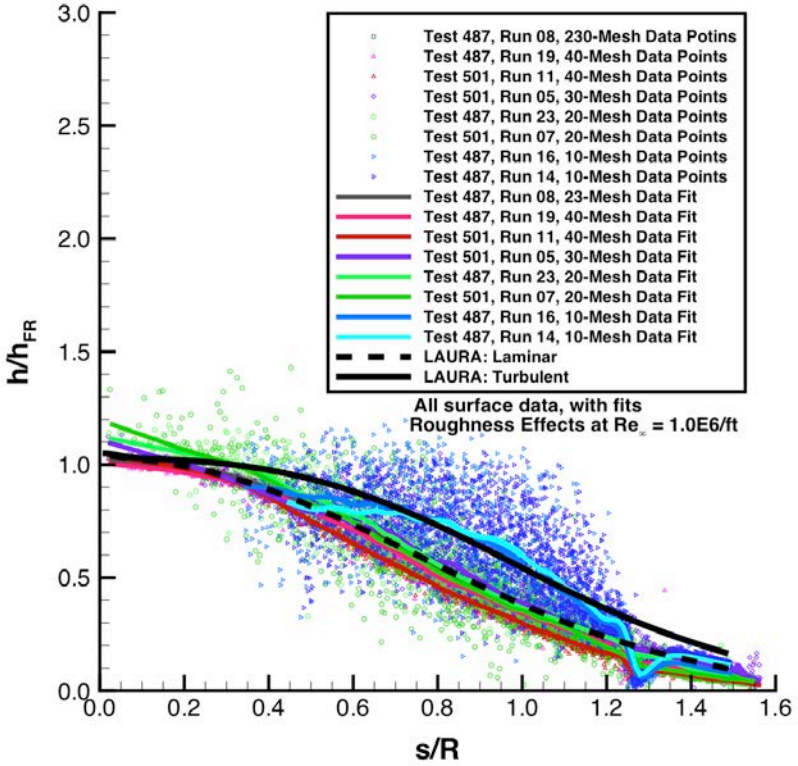

Figure 245. Roughness effects at Mach 10, $Re_\infty = 1.0\times10^6$/ft, data and fits.

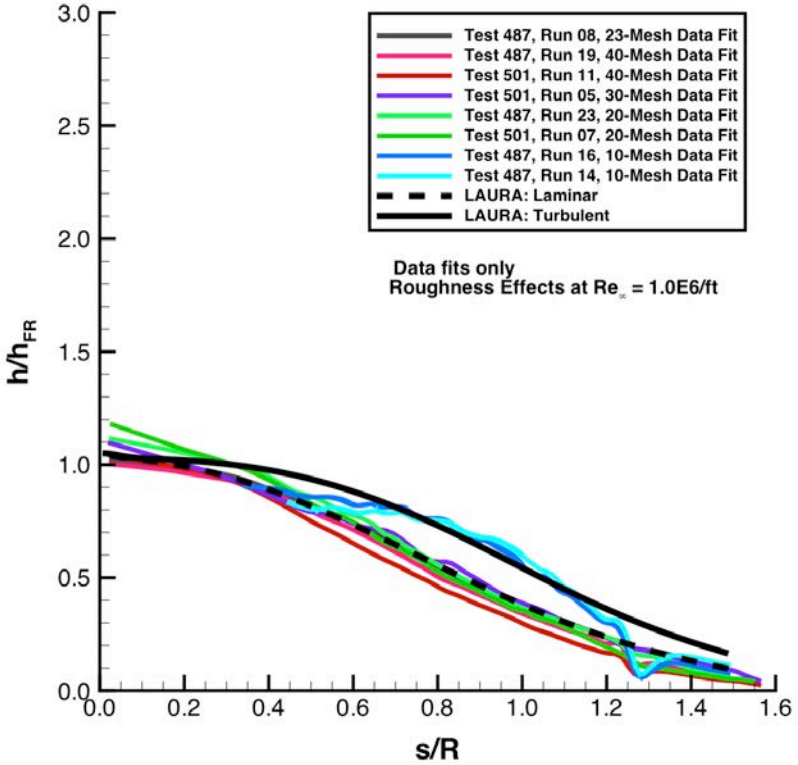

Figure 246. Roughness effects at Mach 10, $Re_\infty = 1.0\times10^6$/ft, fits only.

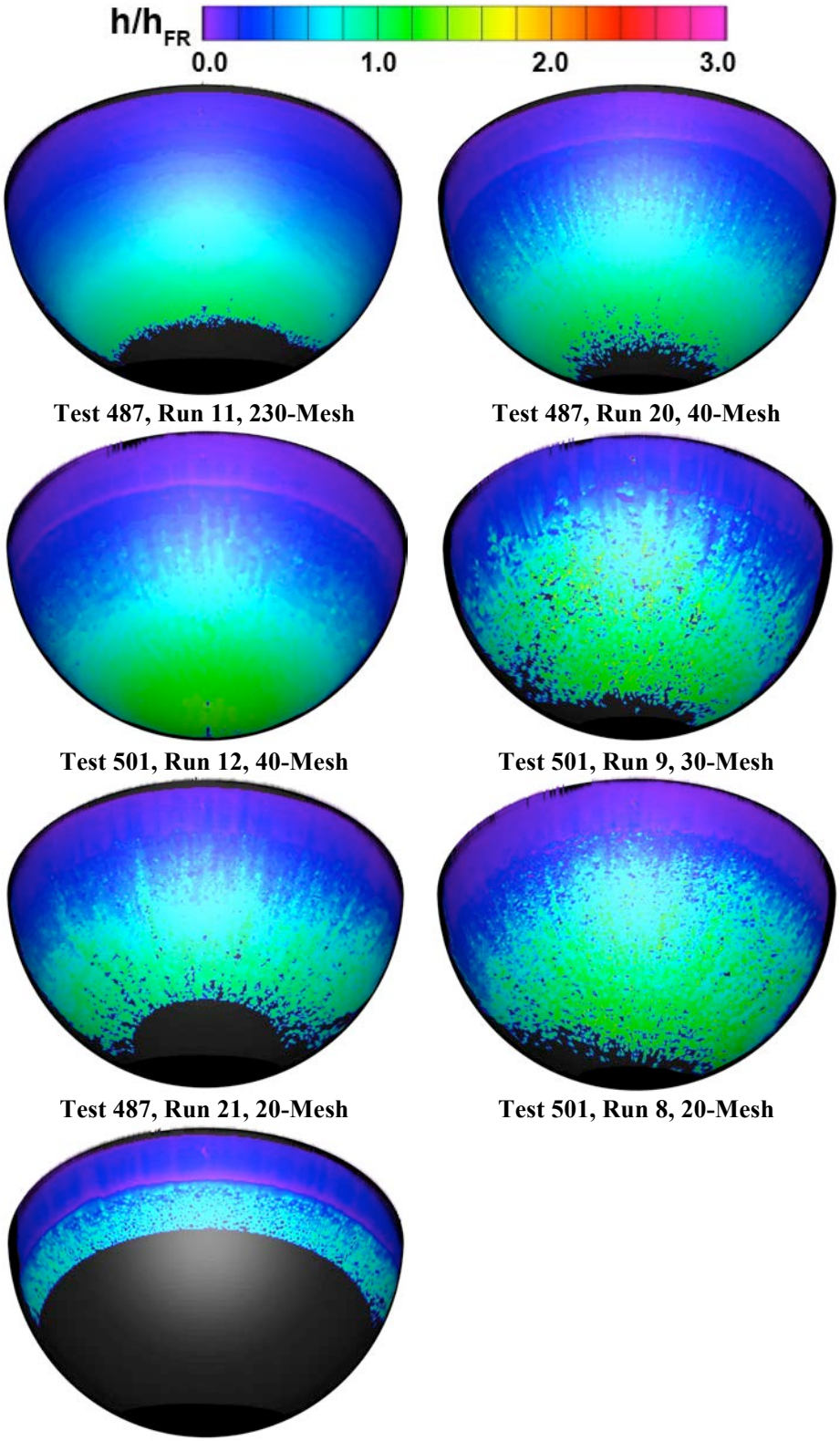

Figure 247. Roughness effects at Mach 10, $Re_\infty = 1.5\times10^6$/ft.

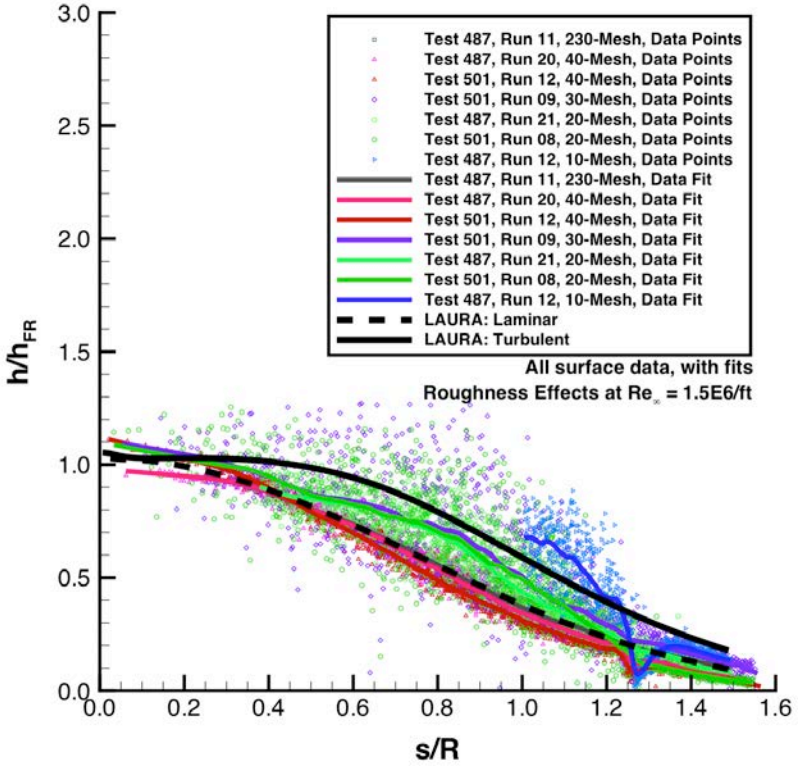

Figure 248. Roughness effects at Mach 10, $Re_\infty = 1.5\times10^6$/ft, data and fits.

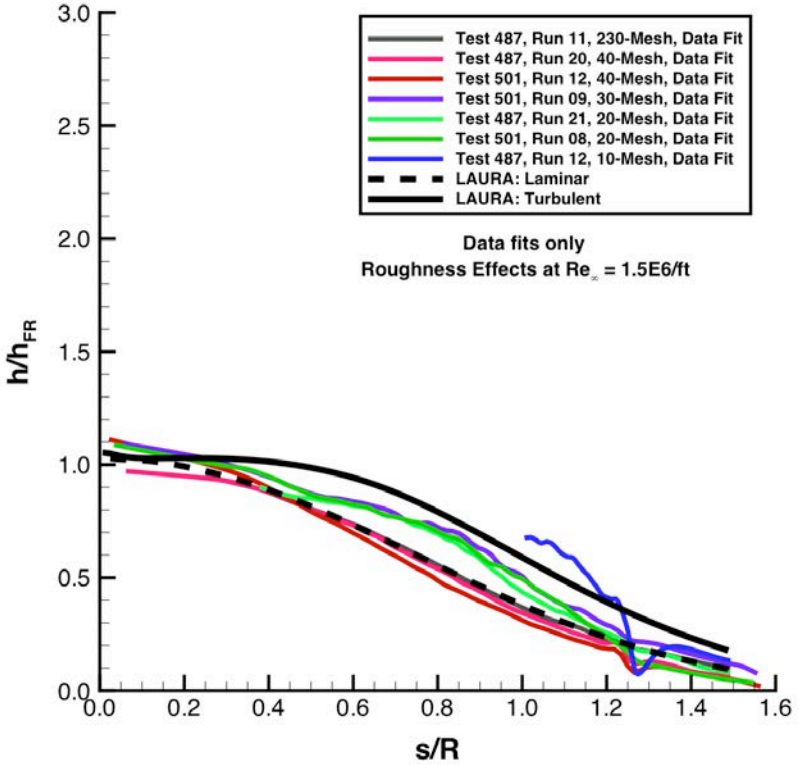

Figure 249. Roughness effects at Mach 10, $Re_\infty = 1.5\times10^6$/ft, fits only.

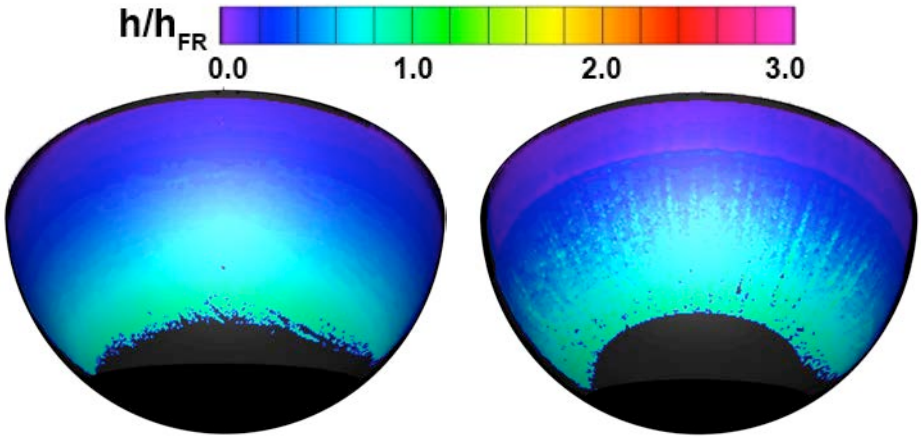

Test 487, Run 10, 230-Mesh

Test 487, Run 26, 40-Mesh

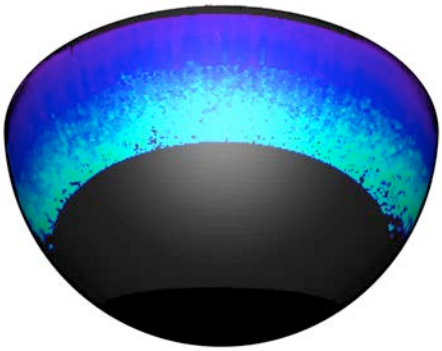

Test 487, Run 25, 20-Mesh

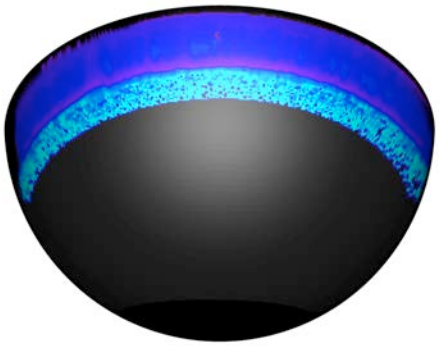

Test 487, Run 15, 10-Mesh

Figure 250. Roughness effects at Mach 10, $Re_\infty = 2.0\times10^6$/ft.

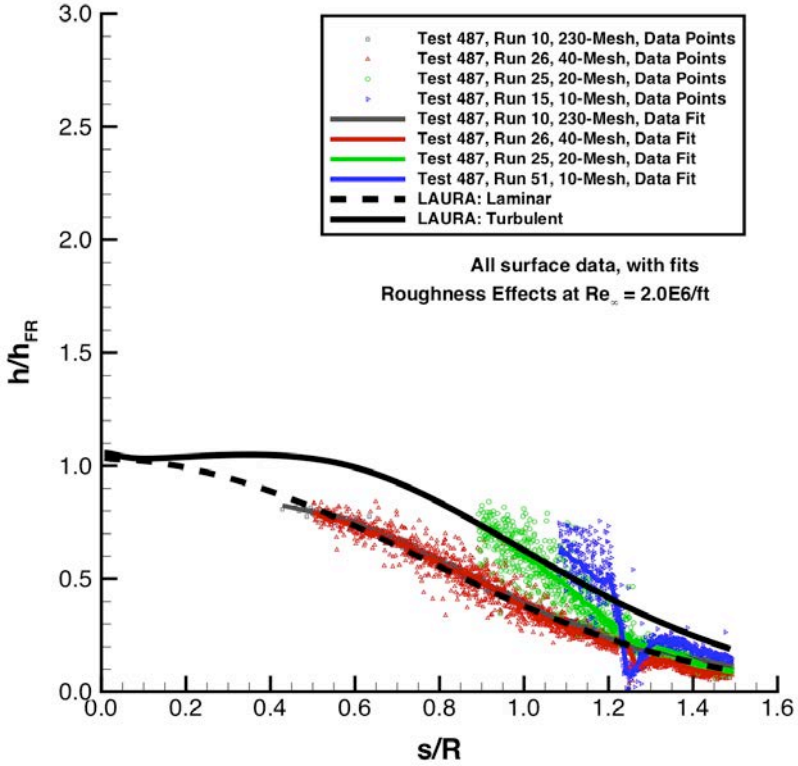

Figure 251. Roughness effects at Mach 10, $Re_\infty = 2.0\times10^6$/ft, data and fits.

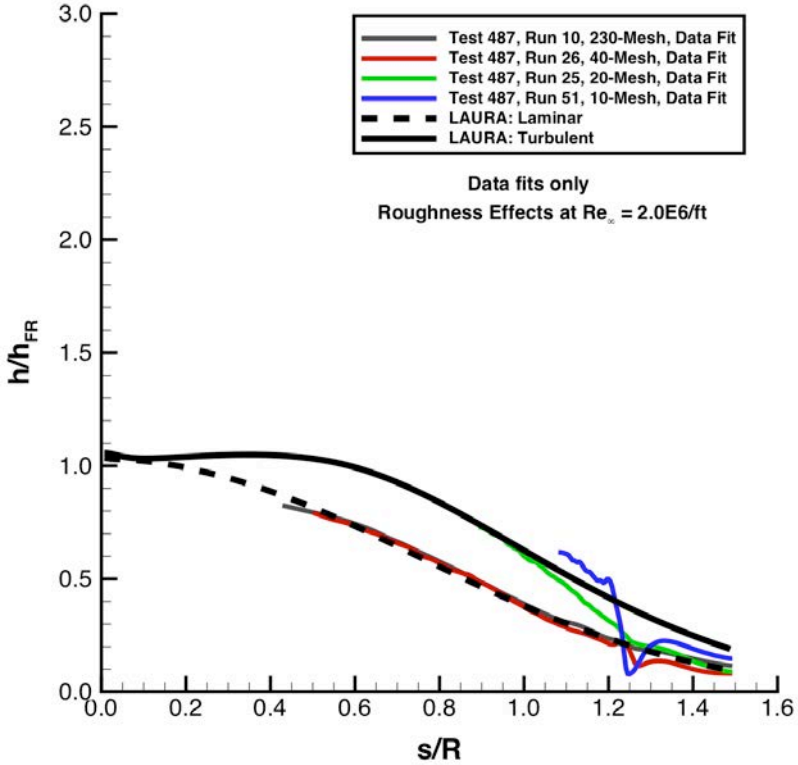

Figure 252. Roughness effects at Mach 10, $Re_\infty = 2.0\times10^6$/ft, fits only.

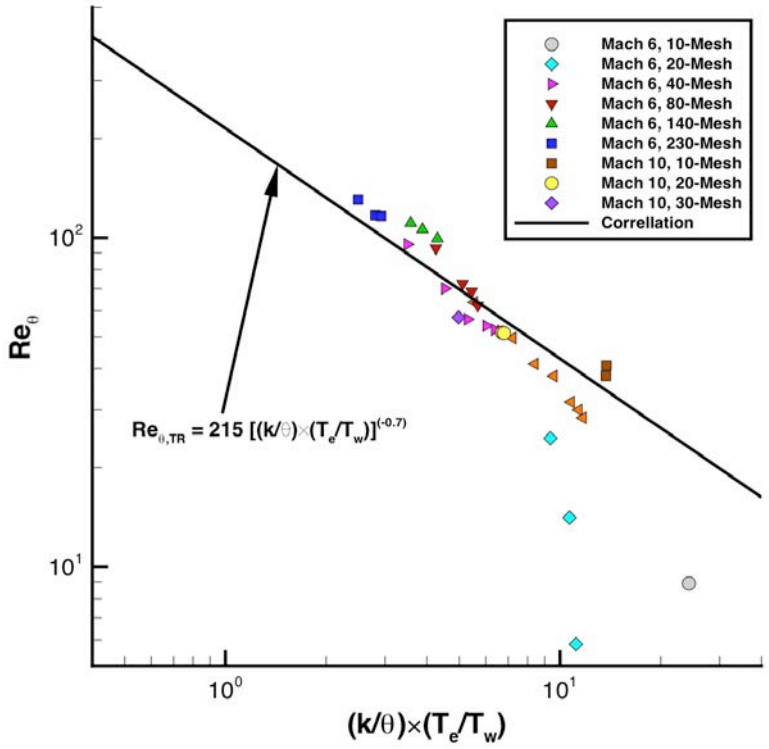

Figure 253. Wind tunnel transition onset correlation.

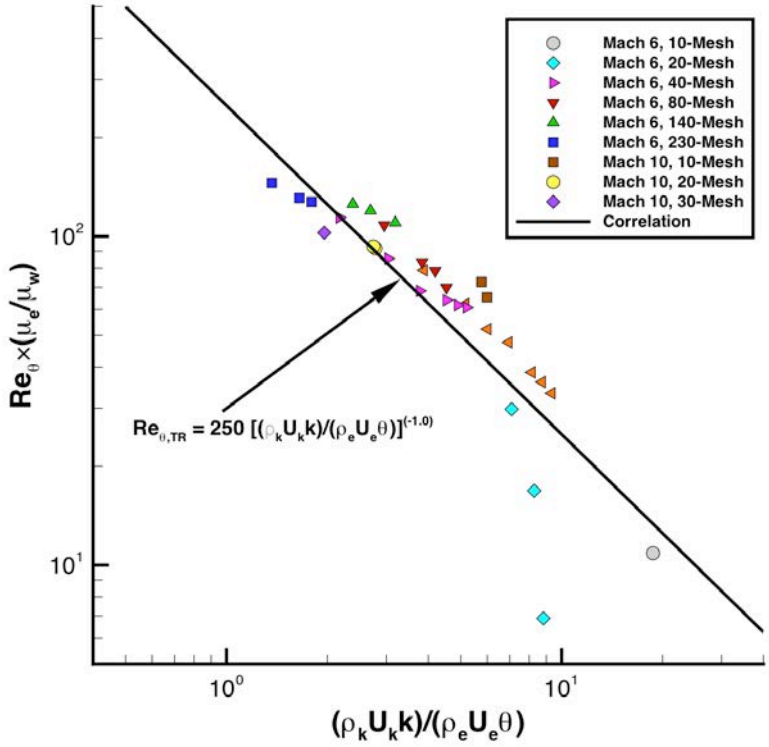

Figure 254. Ballistics range transition onset correlation.

REPORT DOCUMENTATION PAGE

Form Approved
OMB No. 0704-0188

1. REPORT DATE *(DD-MM-YYYY)*
01-05-2017

2. REPORT TYPE
Technical Memorandum

3. DATES COVERED *(From - To)*

4. TITLE AND SUBTITLE
Experimental Investigation of Roughness Effects on Transition Onset and Turbulent Heating Augmentation on a Hemisphere at Mach 6 and Mach 10

5a. CONTRACT NUMBER

5b. GRANT NUMBER

5c. PROGRAM ELEMENT NUMBER

6. AUTHOR(S)
Hollis, Brian R.

5d. PROJECT NUMBER

5e. TASK NUMBER

5f. WORK UNIT NUMBER
470883.04.07.01.03

7. PERFORMING ORGANIZATION NAME(S) AND ADDRESS(ES)
NASA Langley Research Center
Hampton, VA 23681-2199

8. PERFORMING ORGANIZATION REPORT NUMBER
L-20800

9. SPONSORING/MONITORING AGENCY NAME(S) AND ADDRESS(ES)
National Aeronautics and Space Administration
Washington, DC 20546-0001

10. SPONSOR/MONITOR'S ACRONYM(S)
NASA

11. SPONSOR/MONITOR'S REPORT NUMBER(S)
NASA-TM-2017-219613

12. DISTRIBUTION/AVAILABILITY STATEMENT
Unclassified
Subject Category 34
Availability: NASA STI Program (757) 864-9658

13. SUPPLEMENTARY NOTES

14. ABSTRACT

An experimental investigation of the effects of distributed surface roughness on boundary-layer transition and turbulent heating has been conducted. Hypersonic wind tunnel testing was performed using hemispherical models with surface roughness patterns simulating those produced by heat shield ablation. Global aeroheating and transition onset data were obtained using phosphor thermography at Mach 6 and Mach 10 over a range of roughness heights and free stream Reynolds numbers sufficient to produce laminar, transitional and turbulent flow. Upstream movement of the transition onset location and increasing heating augmentation over predicted smooth-wall levels were observed with both increasing roughness heights and increasing free stream Reynolds numbers. The experimental heating data are presented herein, as are comparisons to smooth-wall heat transfer distributions from computational flow-field simulations. The transition onset data are also tabulated, and correlations of these data are presented.

15. SUBJECT TERMS
Aerothermodynamcs; Blunt-body; Boundary layer transition; Heat transfer; Roughness

16. SECURITY CLASSIFICATION OF:			**17. LIMITATION OF ABSTRACT**	**18. NUMBER OF PAGES**	**19a. NAME OF RESPONSIBLE PERSON**
a. REPORT	**b. ABSTRACT**	**c. THIS PAGE**			STI Help Desk (email: help@sti.nasa.gov)
U	U	U	UU	181	**19b. TELEPHONE NUMBER** *(Include area code)* (757) 864-9658